nanomaterials

Special Issue Reprint

2D Layered Nanomaterials and Heterostructures for Electronics, Optoelectronics and Sensing

Edited by
Filippo Giannazzo, Federica Bondino, Luca Seravalli and Simonpietro Agnello

mdpi.com/journal/nanomaterials

MDPI

2D Layered Nanomaterials and Heterostructures for Electronics, Optoelectronics and Sensing

2D Layered Nanomaterials and Heterostructures for Electronics, Optoelectronics and Sensing

Guest Editors

Filippo Giannazzo
Federica Bondino
Luca Seravalli
Simonpietro Agnello

MDPI

Basel • Beijing • Wuhan • Barcelona • Belgrade • Novi Sad • Cluj • Manchester

Guest Editors

Filippo Giannazzo
Istituto per la Microelettronica e Microsistemi (IMM)
Consiglio Nazionale della Ricerche (CNR)
Catania
Italy

Federica Bondino
Istituto Officina dei Materiali (IOM)
Consiglio Nazionale della Ricerche (CNR)
Trieste
Italy

Luca Seravalli
Istituto dei Materiali per l'Elettronica ed il Magnetismo (IMEM)
Consiglio Nazionale della Ricerche (CNR)
Parma
Italy

Simonpietro Agnello
Department of Physics and Chemistry Emilio Segré
University of Palermo
Palermo
Italy

Editorial Office
MDPI AG
Grosspeteranlage 5
4052 Basel, Switzerland

This is a reprint of the Special Issue, published open access by the journal *Nanomaterials* (ISSN 2079-4991), freely accessible at: https://www.mdpi.com/journal/nanomaterials/special_issues/913XK3F452.

For citation purposes, cite each article independently as indicated on the article page online and as indicated below:

Lastname, A.A.; Lastname, B.B. Article Title. *Journal Name* **Year**, *Volume Number*, Page Range.

ISBN 978-3-7258-4467-8 (Hbk)
ISBN 978-3-7258-4468-5 (PDF)
https://doi.org/10.3390/books978-3-7258-4468-5

Contents

About the Editors . . . . **vii**

Filippo Giannazzo, Federica Bondino, Luca Seravalli and Simonpietro Agnello
Special Issue: 2D Layered Nanomaterials and Heterostructures for Electronics, Optoelectronics, and Sensing
Reprinted from: *Nanomaterials* **2025**, *15*, 851, https://doi.org/10.3390/nano15110851 . . . . **1**

Fiorenza Esposito, Matteo Bosi, Giovanni Attolini, Francesca Rossi, Roberto Fornari, Filippo Fabbri and Luca Seravalli
Influence of the Carrier Gas Flow in the CVD Synthesis of 2-Dimensional MoS_2 Based on the Spin-Coating of Liquid Molybdenum Precursors
Reprinted from: *Nanomaterials* **2024**, *14*, 1749, https://doi.org/10.3390/nano14211749 . . . . . . **3**

Marianna Španková, Štefan Chromik, Edmund Dobročka, Lenka Pribusová Slušná, Marcel Talacko, Maroš Gregor, et al.
Large-Area MoS_2 Films Grown on Sapphire and GaN Substrates by Pulsed Laser Deposition
Reprinted from: *Nanomaterials* **2023**, *13*, 2837, https://doi.org/10.3390/nano13212837 . . . . . . **17**

Lu Niu, Oliver J. Conquest, Carla Verdi and Catherine Stampfl
Electronic and Optical Properties of 2D Heterostructure Bilayers of Graphene, Borophene and 2D Boron Carbides from First Principles
Reprinted from: *Nanomaterials* **2024**, *14*, 1659, https://doi.org/10.3390/nano14201659 . . . . . . **30**

Yue Su, Peng Chen, Xiangrui Xu, Yufeng Zhang, Weiwei Cai, Gang Peng, et al.
Symmetry-Engineering-Induced In-Plane Polarization Enhancement in Ta_2NiS_5/CrOCl van der Waals Heterostructure
Reprinted from: *Nanomaterials* **2023**, *13*, 3050, https://doi.org/10.3390/nano13233050 . . . . . . **47**

Gennadiy Murastov, Muhammad Awais Aslam, Simon Leitner, Vadym Tkachuk, Iva Plutnarová, Egon Pavlica, et al.
Multi-Layer Palladium Diselenide as a Contact Material for Two-Dimensional Tungsten Diselenide Field-Effect Transistors
Reprinted from: *Nanomaterials* **2024**, *14*, 481, https://doi.org/10.3390/nano14050481 . . . . **56**

Zezhang Yan, Ningsheng Xu and Shaozhi Deng
AC Characteristics of van der Waals Bipolar Junction Transistors Using an MoS_2/WSe_2/MoS_2 Heterostructure
Reprinted from: *Nanomaterials* **2024**, *14*, 851, https://doi.org/10.3390/nano14100851 . . . . **71**

Carsten Strobel, Carlos Alvarado Chavarin, Martin Knaut, Matthias Albert, André Heinzig, Likhith Gummadi, et al.
p-Type Schottky Contacts for Graphene Adjustable-Barrier Phototransistors
Reprinted from: *Nanomaterials* **2024**, *14*, 1140, https://doi.org/10.3390/nano14131140 . . . . . . **78**

Bhishma Pandit, Bhaskar Parida, Hyeon-Sik Jang and Keun Heo
Self-Powered Broadband Photodetector Based on NiO/Si Heterojunction Incorporating Graphene Transparent Conducting Layer
Reprinted from: *Nanomaterials* **2024**, *14*, 551, https://doi.org/10.3390/nano14060551 . . . . **93**

Altaf Hussain Rajpar, Mohamed Bashir Ali Bashir, Ethar Yahya Salih and Emad M. Ahmed
Fabrication and Enhanced Performance Evaluation of TiO_2@Zn/Al-LDH for DSSC Application: The Influence of Post-Processing Temperature
Reprinted from: *Nanomaterials* **2024**, *14*, 920, https://doi.org/10.3390/nano14110920 . . . . **104**

Xinhao Zhang, Shuo Chen, Heqi Ma, Tianyu Sun, Xiangyong Cui, Panpan Huo, et al.
Asymmetric Schottky Barrier-Generated MoS_2/WTe_2 FET Biosensor Based on a Rectified Signal
Reprinted from: *Nanomaterials* **2024**, *14*, 226, https://doi.org/10.3390/nano14020226 . . . . **113**

About the Editors

Filippo Giannazzo

Filippo Giannazzo received an M.Sc. in Physics (1998) and Ph.D. in Materials Science (2002) from the University of Catania (Italy). He joined CNR-IMM in Catania as a researcher in 2006 and has been Research Director since 2020. His scientific interests include: (i) electrical scanning probe microscopy for the study of charge transport in advanced materials for micro- and nano-electronics; (ii) 2D materials (graphene, TMDs) and their heterostructures with WBG semiconductors (SiC, GaN) for high-frequency and energy-efficient electronics.

Federica Bondino

Federica Bondino received an M.Sc. in Physics (1998) and Ph.D. in Physics (2002) from the University of Trieste. She has been a senior researcher at the Consiglio Nazionale delle Ricerche and the scientific director of the synchrotron radiation beamlines BACH since 2015. For over 20 years, she has contributed to the management, development, and maintenance of cutting-edge instrumentation and ultra-high-vacuum beamline end-stations, beamline user support, and experimental research on low-dimensional materials, surfaces, and interfaces using synchrotron radiation.

Luca Seravalli

Luca Seravalli received an M.Sc. in Physics from Trinity College Dublin (Ireland) in 2000 and PhD in Physics from University of Parma (Italy) in 2003. From 2009, he has been a permanent researcher at IMEM-CNR, Italy. From 2001, he has been working on epitaxial growth, characterization, and modelization of semiconductor materials for photonic and electronic applications. He has authored 125 articles, with over 2000 citations. His current interests include CVD growth of 2D materials and MOVPE growth of wide bandgap oxides.

Simonpietro Agnello

Simonpietro Agnello received an M.Sc. (1996) and Ph.D in Physics (2001) from the University of Palermo (Italy). He has been a researcher at the University of Palermo since 2004, and since 2023, he has been a Full Professor in Experimental Physics. His research includes the spectroscopic study of (i) amorphous materials (SiO2) for optoelectronics and harsh environments applications; (ii) doping and thermal stability of 2D materials (graphene, TMDs) for electronics; (iii) defectivity of WBG semiconductors (SiC) for microelectronics and power devices.

nanomaterials

MDPI

Editorial

Special Issue: 2D Layered Nanomaterials and Heterostructures for Electronics, Optoelectronics, and Sensing

Filippo Giannazzo [1,*], Federica Bondino [2], Luca Seravalli [3] and Simonpietro Agnello [4]

[1] Consiglio Nazionale della Ricerche (CNR), Istituto per la Microelettronica e Microsistemi (IMM), Strada VIII, 5, 95121 Catania, Italy
[2] Consiglio Nazionale delle Ricerche (CNR), Istituto Officina dei Materiali (IOM), Area Science Park, S.S. 14 Km. 163, 5, Basovizza, 34149 Trieste, Italy; bondino@iom.cnr.it
[3] Consiglio Nazionale delle Ricerche (CNR), Istituto dei Materiali per l'Elettronica ed il Magnetismo (IMEM), Parco Area delle Scienze 37/a, 43124 Parma, Italy; luca.seravalli@imem.cnr.it
[4] Department of Physics and Chemistry Emilio Segré, University of Palermo, Via Archirafi 36, 90143 Palermo, Italy; simonpietro.agnello@unipa.it
* Correspondence: filippo.giannazzo@imm.cnr.it

Since the first report in 2004 on the electronic properties of graphene exfoliated from graphite [1], the research on two-dimensional materials (2DMs) has grown steadily. To date, hundreds of 2DMs have been investigated experimentally, whereas a database of up to 6000 monolayer structures has recently been compiled through computational studies [2]. Interestingly, the 2DM family covers the entire range of electronic properties, from semimetallic graphene and semiconducting transition metal dichalcogenides (TMDs) to insulating hexagonal boron nitride. Furthermore, van der Waals (vdW) heterostructures with engineered bandgaps have been realized by stacking different layers [3], enabling the demonstration of novel device concepts for electronics/optoelectronic, sensing, quantum, and energy applications.

In this context, this Special Issue, entitled "2D Layered Nanomaterials and Heterostructures for Electronics, Optoelectronics and Sensing", features insightful contributions on the scalable growth of 2DMs, fabrication approaches of vdW heterostructures, advanced characterization methods (optical, vibrational, chemical, electrical), and the theoretical modeling of these heterostructures. Furthermore, it aims to address challenges involved in 2DM integration and device fabrication.

Specifically, the Special Issue includes 10 high-quality, original research papers covering the following topics:

i. Scalable synthesis of molybdenum disulfide (MoS_2) through an advanced chemical vapor deposition (CVD) approach based on liquid Mo precursors [4], as well as by pulsed laser deposition (PLD) on substrates of interest for microelectronics (sapphire, gallium nitride) [5];
ii. First-principles calculations of electronic and optical properties of graphene, borophene, and boron carbide 2D heterostructures [6];
iii. Advanced optical and electronic transport characterization of novel vdW heterostructures (Ta_2NiS_5/CrOCl) [7];
iv. Electronic and optoelectronic devices based on 2DM heterostructures, i.e., novel 2D field effect transistors with a tungsten diselenide (WSe_2) channel and multilayer palladium diselenide ($PdSe_2$) vdW contacts [8]; bipolar transistors based on a MoS_2/WSe_2/MoS_2 heterostructure [9]; photo-transistors and self-powered photodetectors based on graphene/Si [10]; NiO/graphene/Si junctions [11]; photovoltaic devices [12]; and biosensors based on MoS_2/WTe_2 Schottky barriers [13].

https://doi.org/10.3390/nano15110851

This Special Issue spotlights relevant examples of ongoing research directions in the continuously expanding field of 2D materials and aims to serve as inspiration for researchers working in these areas.

Acknowledgments: The Guest Editors of this Special Issue acknowledge the support of European Union (NextGeneration EU), through the MUR-PRIN2022 project "2DIntegratE" (2022RHRZN2).

Conflicts of Interest: The authors declare no conflicts of interest.

References

1. Novoselov, K.S.; Geim, A.K.; Morozov, S.V.; Jiang, D.E.; Zhang, Y.; Dubonos, S.V.; Grigorieva, I.V.; Firsov, A.A. Electric field effect in atomically thin carbon films. *Science* **2004**, *306*, 666. [CrossRef] [PubMed]
2. Zhou, J.; Shen, L.; Costa, M.D.; Persson, K.A.; Ong, S.P.; Huck, P.; Lu, Y.; Ma, X.; Chen, Y.; Tang, H.; et al. DMatPedia, an open computational database of two-dimensional materials from top-down and bottom-up approaches. *Sci. Data* **2019**, *6*, 86. [CrossRef] [PubMed]
3. Geim, K.; Grigorieva, I.V. Van der Waals heterostructures. *Nature* **2013**, *499*, 419. [CrossRef] [PubMed]
4. Esposito, F.; Bosi, M.; Attolini, G.; Rossi, F.; Fornari, R.; Fabbri, F.; Seravalli, L. Influence of the Carrier Gas Flow in the CVD Synthesis of 2-Dimensional MoS_2 Based on the Spin-Coating of Liquid Molybdenum Precursors. *Nanomaterials* **2024**, *14*, 1749. [CrossRef]
5. Španková, M.; Chromik, Š.; Dobročka, E.; Slušná, L.P.; Talacko, M.; Gregor, M.; Pécz, B.; Koos, A.; Greco, G.; Panasci, S.E.; et al. Large-Area MoS_2 Films Grown on Sapphire and GaN Substrates by Pulsed Laser Deposition. *Nanomaterials* **2023**, *13*, 2837. [CrossRef]
6. Niu, L.; Conquest, O.J.; Verdi, C.; Stampfl, C. Electronic and Optical Properties of 2D Heterostructure Bilayers of Graphene, Borophene and 2D Boron Carbides from First Principles. *Nanomaterials* **2024**, *14*, 1659. [CrossRef] [PubMed]
7. Su, Y.; Chen, P.; Xu, X.; Zhang, Y.; Cai, W.; Peng, G.; Zhang, X.; Deng, C. Symmetry-Engineering-Induced In-Plane Polarization Enhancement in Ta_2NiS_5/CrOCl van der Waals Heterostructure. *Nanomaterials* **2023**, *13*, 3050. [CrossRef] [PubMed]
8. Murastov, G.; Aslam, M.A.; Leitner, S.; Tkachuk, V.; Plutnarová, I.; Pavlica, E.; Rodriguez, R.D.; Sofer, Z.; Matković, A. Multi-Layer Palladium Diselenide as a Contact Material for Two-Dimensional Tungsten Diselenide Field-Effect Transistors. *Nanomaterials* **2024**, *14*, 481. [CrossRef]
9. Yan, Z.; Xu, N.; Deng, S. AC Characteristics of van der Waals Bipolar Junction Transistors Using an $MoS_2/WSe_2/MoS_2$ Heterostructure. *Nanomaterials* **2024**, *14*, 851. [CrossRef] [PubMed]
10. Strobel, C.; Chavarin, C.A.; Knaut, M.; Albert, M.; Heinzig, A.; Gummadi, L.; Wenger, C.; Mikolajick, T. p-Type Schottky Contacts for Graphene Adjustable-Barrier Phototransistors. *Nanomaterials* **2024**, *14*, 1140. [CrossRef] [PubMed]
11. Pandit, B.; Parida, B.; Jang, H.-S.; Heo, K. Self-Powered Broadband Photodetector Based on NiO/Si Heterojunction Incorporating Graphene Transparent Conducting Layer. *Nanomaterials* **2024**, *14*, 551. [CrossRef] [PubMed]
12. Rajpar, H.; Bashir, M.B.A.; Salih, E.Y.; Ahmed, E.M. Fabrication and Enhanced Performance Evaluation of TiO_2@Zn/Al-LDH for DSSC Application: The Influence of Post-Processing Temperature. *Nanomaterials* **2024**, *14*, 920. [CrossRef] [PubMed]
13. Zhang, X.; Chen, S.; Ma, H.; Sun, T.; Cui, X.; Huo, P.; Man, B.; Yang, C. Asymmetric Schottky Barrier-Generated MoS_2/WTe_2 FET Biosensor Based on a Rectified Signal. *Nanomaterials* **2024**, *14*, 226. [CrossRef] [PubMed]

nanomaterials

Article

Influence of the Carrier Gas Flow in the CVD Synthesis of 2-Dimensional MoS_2 Based on the Spin-Coating of Liquid Molybdenum Precursors

Fiorenza Esposito [1,2], Matteo Bosi [1], Giovanni Attolini [1], Francesca Rossi [1], Roberto Fornari [1,3], Filippo Fabbri [4,*,†] and Luca Seravalli [1,*,†]

[1] Institute of Materials for Electronics and Magnetism—National Research Council (IMEM-CNR), Parco Area delle Scienze 37/A, 43124 Parma, Italy; fiorenza.esposito@imem.cnr.it (F.E.); matteo.bosi@imem.cnr.it (M.B.); giovanni.attolini@imem.cnr.it (G.A.); francesca.rossi@imem.cnr.it (F.R.); roberto.fornari1@unipr.it (R.F.)

[2] Department of Chemical Science, Life, and Environmental Sustainability, University of Parma, 43124 Parma, Italy

[3] Department of Mathematical, Physical and Computer Sciences, University of Parma, 43124 Parma, Italy

[4] NEST, Istituto Nanoscienze—CNR, Scuola Normale Superiore, Piazza San Silvestro 12, 56127 Pisa, Italy

[*] Correspondence: filippo.fabbri@nano.cnr.it (F.F.); luca.seravalli@imem.cnr.it (L.S.)

[†] These authors contributed equally to this work.

Abstract: Atomically thin molybdenum disulfide (MoS_2) is a two-dimensional semiconductor with versatile applications. The recent adoption of liquid molybdenum precursors in chemical vapor deposition has contributed significantly to the reproducible wafer-scale synthesis of MoS_2 monolayer and few-layer films. In this work, we study the effects of the carrier gas flow rate on the properties of two-dimensional molybdenum disulfide grown by liquid-precursor-intermediate chemical vapor deposition on SiO_2/Si substrates. We characterized the samples using Optical Microscopy, Scanning Electron Microscopy, Raman spectroscopy, and Photoluminescence spectroscopy. We analyzed samples grown with different nitrogen carrier flows, ranging from 150 to 300 sccm, and discussed the effect of carrier gas flows on their properties. We found a correlation between MoS_2 flake lateral size, shape, and number of layers, and we present a qualitative growth model based on changes in sulfur provision caused by different carrier flows. We show how the use of liquid precursors can allow for the synthesis of homogeneous, single-layer flakes up to 100 µm in lateral size by optimizing the gas flow rate. These results are essential for gaining a deeper understanding of the growth process of MoS_2.

Keywords: molybdenum disulfide; liquid molybdenum precursors; chemical vapor deposition; carrier gas; Raman spectroscopy; photoluminescence spectroscopy

1. Introduction

The synthesis of a 2D material is a crucial step because different preparation processes can determine its fundamental material properties [1–6]. Among the various techniques to obtain atomically thin structures from a bottom-up approach, Chemical Vapor Deposition (CVD) has established itself as the most successful, with the recent demonstration that CVD based on metalorganic sources (MOCVD) is the most promising option for wafer-scale synthesis [7–11]. Among 2D materials, molybdenum disulfide (MoS_2) has attracted significant attention due to its unique optical and electrical properties, including a direct bandgap, strong light–matter interaction, and high quantum yield [12]. Various applications for this 2D material in the photonics field have been proposed, such as photodetectors, 2D LEDs, single photon sources, and components of nanophotonic circuits. We refer the reader to several excellent reviews dedicated to this topic [13–15].

The CVD growth of transition metal dichalcogenides is highly sensitive to reaction parameters such as precursor concentration and temperature. Therefore, any modification or uncontrolled fluctuation can significantly influence the reaction kinetics and material quality, leading to poor reproducibility in the synthesis [16]. Liquid molybdenum precursors have been introduced as a viable option to grow 2D MoS_2 by CVD with large flake sizes, proving to be much more reliable than previously used powder precursors, which, despite initial promising results and the simplicity of the process, suffer from serious reproducibility issues [17–21]. This method relies on the sulfurization of a solution containing molybdenum precursors that is deposited by spin-coating on the substrate which is then loaded into the CVD reactor [22,23]. The typical solution is composed of three different components: (i) the water-soluble Mo precursor, (ii) the growth promoter, and (iii) the density gradient medium, which improves adhesion to the substrate surface during spinning. The first two components are mixed in ratios ranging from 1:1 to 8:1 [24,25].

The use of a molybdenum liquid precursor represents a significant modification to the paradigm of the CVD synthesis of two-dimensional materials. With solid precursors, both molybdenum and sulfur are provided to the growth substrate in vapor form, while in the liquid-precursor-intermediate CVD process (LPI-CVD), the solution containing the molybdenum precursor is already present on the growth substrate and undergoes oxidation and solidification during the temperature ramp [25]. This process is somewhat similar to the early work on the sulfurization of the molybdenum layer deposited on the growth substrates, where the primary drawback was that the MoS_2 domains were limited by the initial size of the molybdenum grains in the deposited layer [26]. Although highly efficient outcomes in terms of reproducibility of the process have been obtained with Mo liquid precursors, the dynamic of the growth process has been somewhat overlooked, despite the complexity of the physical and chemical mechanisms involved. For instance, the issue of six-fold defective domains has been noted in the case of WS_2 obtained by LPI-CVD [27]. Similarly, the synthesis of highly tensile-strained MoS_2 monolayers has been demonstrated within a specific temperature range using liquid precursors [28]. Only recently have the different results in terms of material quality using different density gradient media been highlighted [29]. Likewise, Senkic et al. [30] reported variations in the morphology of MoS_2 structures grown with different S:Mo ratios using liquid precursors. Nevertheless, the LPI-CVD has proven to be a successful approach for growing more complex two-dimensional structures, such as patterned $MoSe_2$ [31], highly oriented MoS_2 mono and bilayer structures [17], metal-doped monolayers [32], and van der Waals heterostructures [33]. Since the sulfurization process of liquid precursors spun on the substrate still relies on sulfur vapors being transported to the growth substrate, the flow rate of the inert carrier gas plays a crucial role as it affects both vapor concentration and sulfur precursor transportation. While several studies have focused on the effect of carrier gas in CVD growth using Mo solid precursors [33–35], very few have investigated the effect of carrier gas flow when using liquid precursors.

In this work, we demonstrate that the flow rate of the carrier gas is a critical parameter for the CVD growth of MoS_2 structures, even when using Mo liquid precursors. Unlike the case of the Mo solid precursor, this parameter drastically affects the number of layers and flake sizes but has a lesser impact on the flake shape. At the lowest flow rate, structures with an inhomogeneous number of layers are obtained, featuring a bulk-like center (often pyramidal in shape) and bilayer structures along certain crystallographic directions. At the highest flow rate, the synthesis yields a 100 μm large triangular monolayer with concave edges. Notably, increasing the flow rate decreases the number of layers, reaching the monolayer limit.

2. Materials and Methods

The solution deposited on the substrate consists of a mixture of (i) 1 mL of ammonium heptamolybdate tetrahydrate $(NH_4)_6Mo_7O_{24}\cdot 4H_2O$ (AHT, Sigma-Aldrich (St. Louis, MO, USA), 99.98%) 0.030 mol/L, (ii) 4 mL of NaOH 0.060 mol/L, which acts as a growth promoter, and (iii) 0.5 mL of OptiPrep^{TM}, a density gradient medium containing 60% iodixanol and 40% water. In total, 10 µL of this mixture is then used for spin-coating on a 1 × 1 cm^2 SiO_2/Si substrate (3000 rpm, 30 s) which has been previously treated with O_2 plasma (25 W, 3 min) to improve wettability. The substrate is placed 20 cm away from an alumina boat containing 275 mg of a sulfur solid precursor (Sigma-Aldrich, 99.98%). The growth process is carried out at a temperature of 820 °C (heating rate of 40 °C/min), providing optimal growth conditions, while the low zone containing sulfur powders is independently heated to 180 °C (heating rate of 60 °C/min). The nitrogen carrier gas flow rate, selected for its inert nature and low cost, is kept constant within the range of 150 to 300 sccm during the growth process. Further details on the CVD growth system can be found in [34,35].

The morphology of the MoS_2 flakes is analyzed by scanning electron microscopy (SEM) using a Zeiss Auriga Compact system equipped with a GEMINI Field-Emission column. A statistical analysis of the lateral dimensions of the flakes is performed using SEM images. For each sample, approximately one hundred flakes distributed across different areas of the substrate are considered.

Raman and photoluminescence measurements are carried out with a Renishaw In-Via system, equipped with a confocal microscope, a 532 nm excitation laser, and an 1800 line/mm grating (spectral resolution < 2 cm^{-1}). All the analyses are performed with a 100X objective (NA = 0.85), excitation laser power 500 µW, and an acquisition time of 4 s. The Raman mapping is carried out with a pixel size between 800 nm and 1 µm.

3. Results

We observed that the density and the size of the flakes can be reproducibly controlled by adjusting the carrier gas flow rate. In Figure 1, optical microscopy (OM) and scanning electron microscopy (SEM) images are shown for samples grown under different carrier flows, ranging from 150 to 300 sccm. Lower and higher gas flow rates were also explored, resulting in very small flakes at values below 150 sccm and low-quality 3D structures at higher values.

The concavity of the flakes and thus their shape is directly influenced by the Mo:S ratio. A perfect triangular shape is typically reported in studies using solid precursors, achieved by increasing the sulfur content and growth temperature, whereas greater concavity (multi-apex triangles) is observed when the growth occurs under Mo excess [36]. Statistical measurements of flake concavity show values ranging from 7.5° to 10.2° for carrier flows between 150 and 250 sccm (Figure 2). A higher concavity, reaching 12.5°, was found for the sample with a flow rate of 300 sccm. This analysis suggests that the growth behavior using liquid precursors differs significantly from that observed with solid precursors (such as MoO_3 powders), where carrier gas flow, gas velocity, MoO_3 and S transport, and gas phase pre-reactions greatly influence the growth outcome [37–39]. As shown in Figure 2e, flake concavity remains almost constant for flows up to 250 sccm but increases significantly at 300 sccm.

Figure 3 presents the statistical analysis based on SEM images and the average lateral size of the flakes. By fitting the histograms in Figure 3a–d with Gaussian functions, the average flake sizes were found to be 5.6 ± 0.7 µm, 19.8 ± 2.9 µm, 12.0 ± 3.5 µm, and 76.7 ± 9.1 µm for flows rates of 150 sccm, 200 sccm, 250 sccm, and 300 sccm, respectively. As shown in Figure 3e, data indicate a nonlinear increase in flake size as the flow rate increases from 150 to 300 sccm.

In Figure 4, we present maps of the separation between Raman modes (Δk), a well-established method for determining the number of MoS_2 layers. Monolayer structures exhibit $\Delta k < 19$ cm^{-1}, while bulk structures show $\Delta k > 24$ cm^{-1} [40,41]. Optical reference images of the analyzed flakes, as well as representative Raman spectra, are shown in Figures S1–S3.

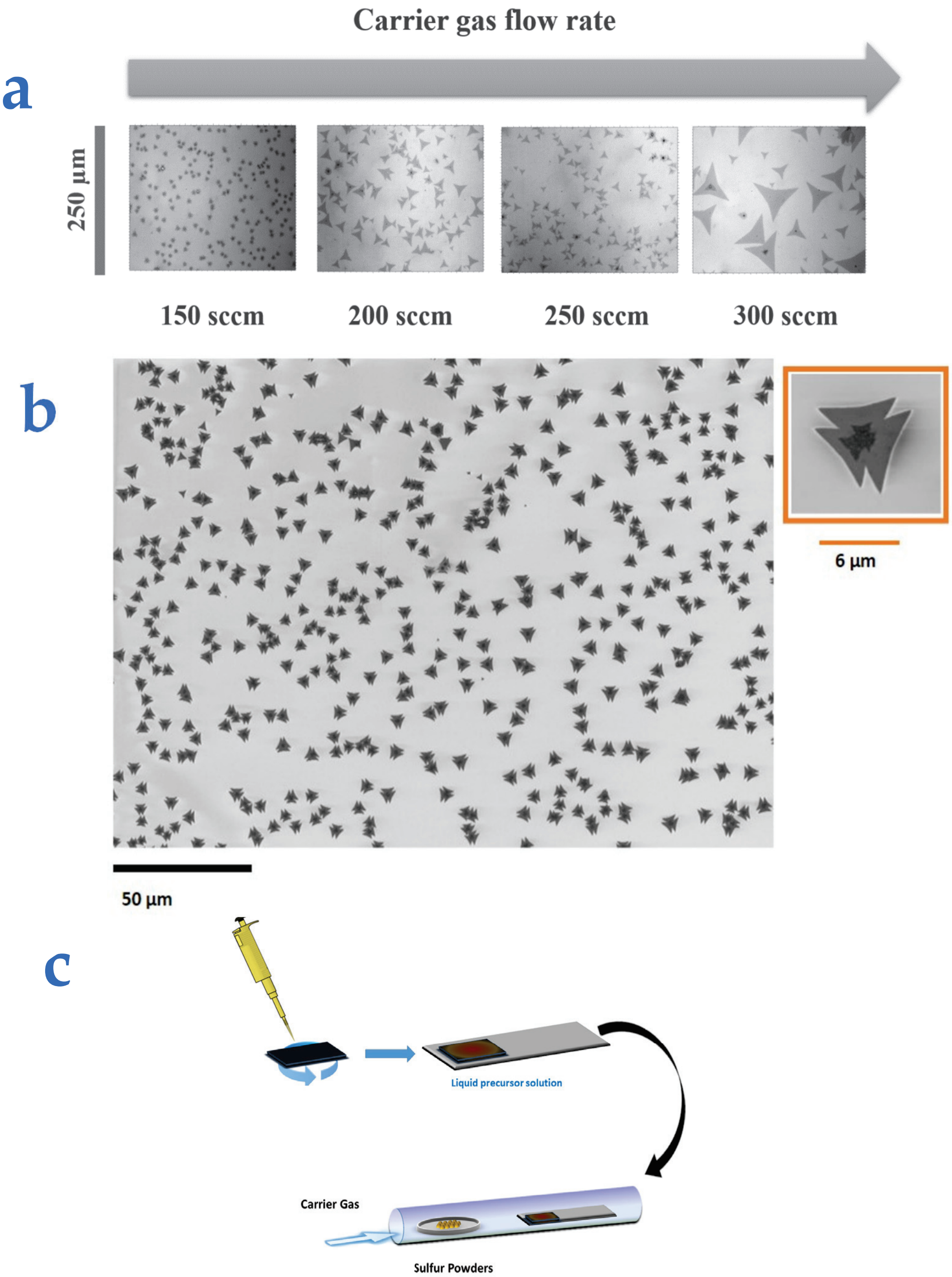

Figure 1. (**a**) Optical microscopy images of flakes at different nitrogen flows. (**b**) SEM image of the sample with at a flow rate of 150 sccm. (**c**) Schematic of the synthesis procedure.

The flakes obtained with a flow of 150 sccm consist of a bulk-like central region and three bilayer lateral structures, as evidenced by the separation of the Raman modes: 26 cm^{-1} in the central region (bulk-like) and 20 cm^{-1} in the lateral areas. The flakes grown with a carrier gas flow rate of 200 sccm and 250 sccm exhibit a homogeneous spatial distribution of Δk. Specifically, Δk is equal to 23 cm^{-1} and 21 cm^{-1} in the case of the 200 sccm and 250 sccm specimens, respectively. These values indicate the presence of few-layer structures. The flakes obtained with a flow of 300 sccm are large, corner-shaped triangular monolayers with $\Delta k = 19$ cm^{-1}. As recently reported [28], the separation of the Raman modes at the corner of the triangular structure is influenced by tensile strain.

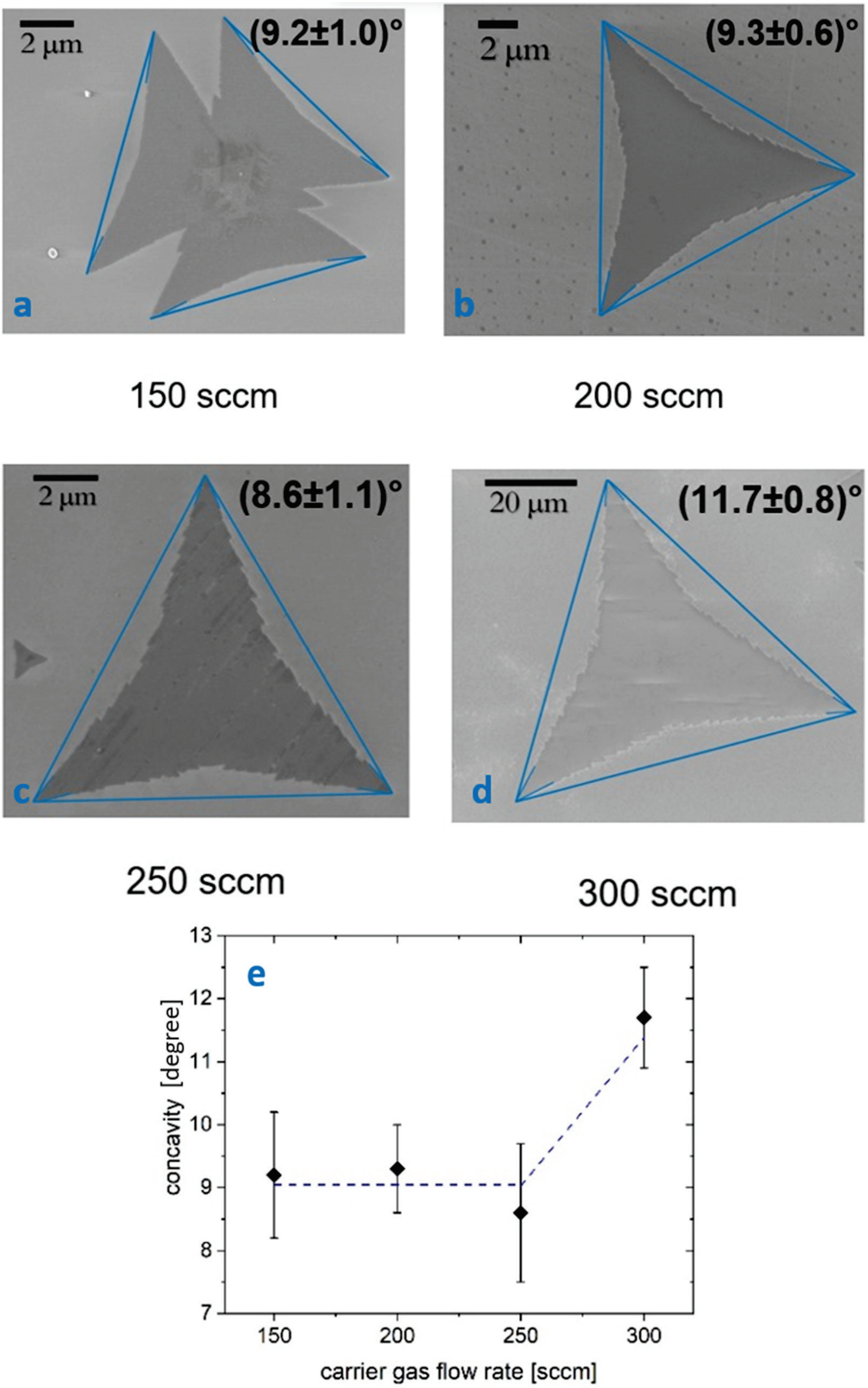

Figure 2. (**a**–**d**) SEM images and flake concavity for flow rates of 150, 200, 250, 300 sccm, respectively. (**e**) Concavity values plotted as a function of flow rate, with the dashed line as a guide for the eye.

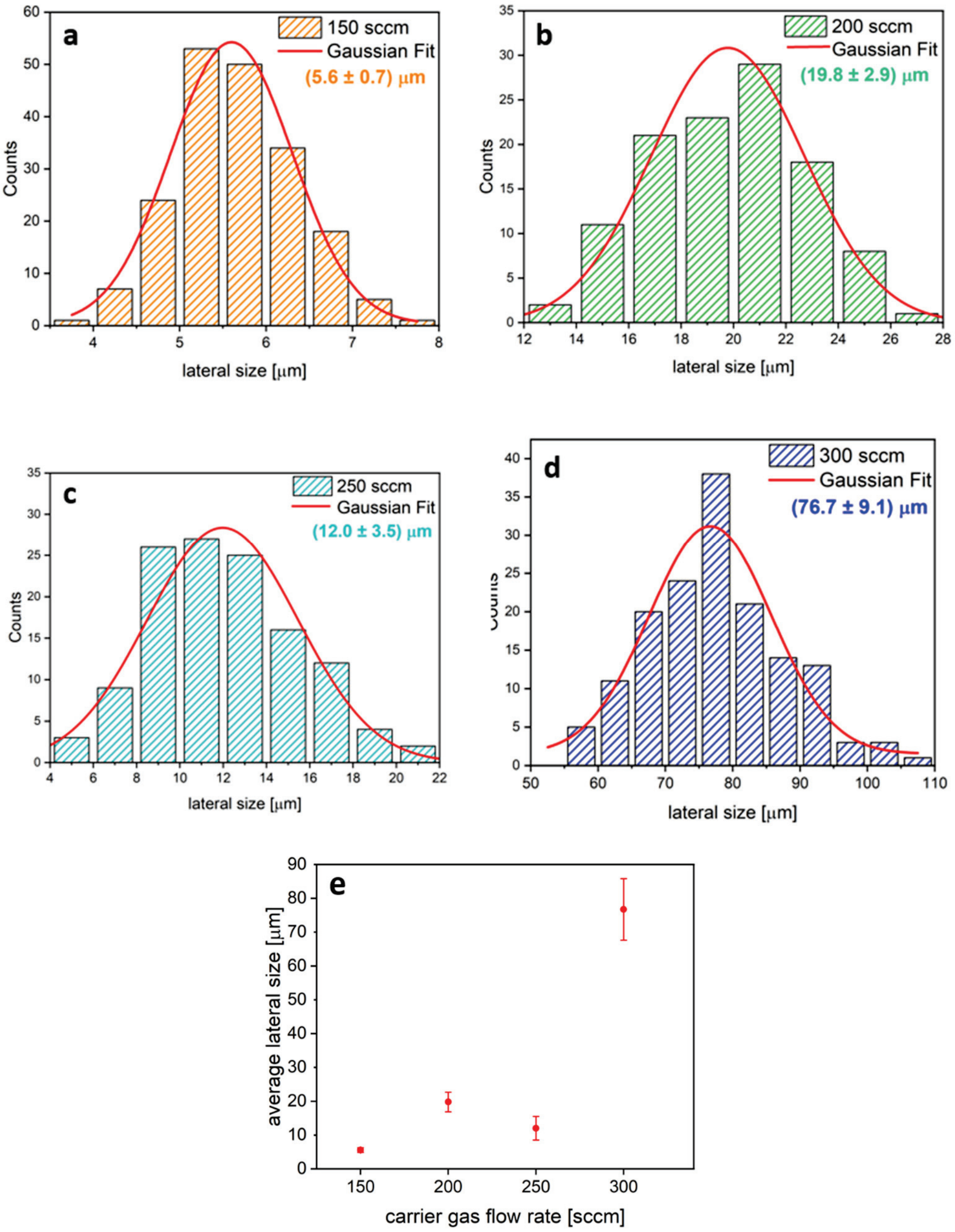

Figure 3. (**a**–**d**) Statistical analysis of the lateral dimensions of MoS_2 flakes at different flow rates (150, 200, 250, 300 sccm). (**e**) Average lateral size of flakes as a function of the carrier flow rate.

Photoluminescence (PL) characterization was performed to analyze the effect of varying carrier gas flow rates on the optical properties [37,38,42].

Figure 5 presents the PL spectra of the triangular structures obtained at different carrier gas flows. For the sample grown at 150 sccm, we report the PL spectrum obtained from the lateral part of the flakes, as the central bulk-like area does not exhibit any light emission. The PL spectra reveal two distinct light emissions, corresponding to the A and B excitonic recombinations of MoS_2 [43–46]. In the samples grown at 150 sccm and 300 sccm, the A exciton peaks at 1.83 eV, whereas the samples obtained at 200 sccm and 250 sccm show a redshift to 1.78 eV. The B exciton consistently peaks at 1.95 eV. Notably, the intensity ratio of A to B varies significantly: it is 2.1 for the 200 sccm and 250 sccm samples, increasing to 8 and 10.2 for the 150 sccm and 300 sccm samples, respectively. The PL intensity ratios and peak positions (Figure 5) confirm the findings from the Raman spectroscopic mapping (Figure 4), indicating that the number of layers varies with the carrier gas flow during the growth process. As the distance between the two Raman peaks decreases—an indication of there being few layers—the integrated area of the exciton A peak in the PL spectrum increases [45]. Both these features suggest the presence of an unstrained MoS_2 monolayer.

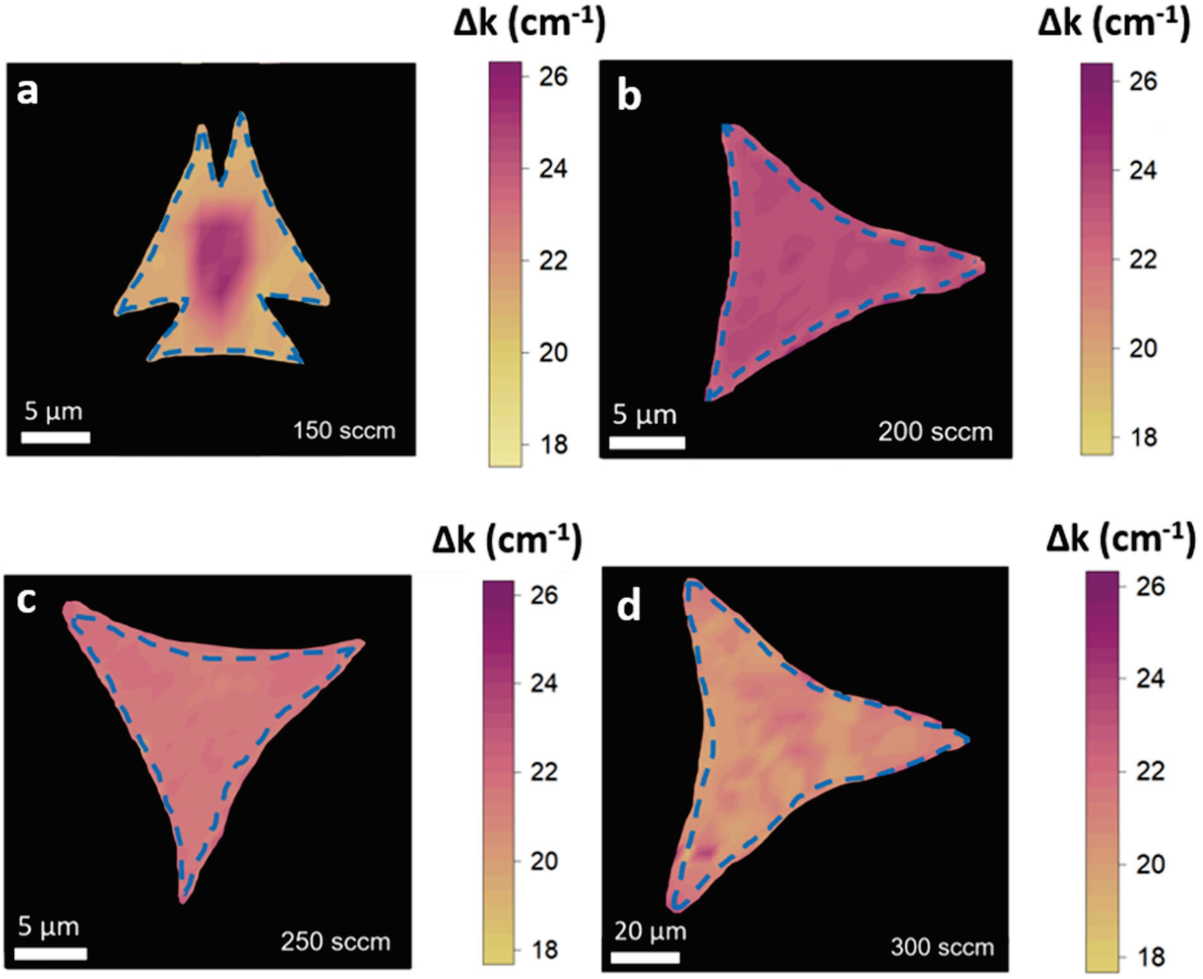

Figure 4. (**a**–**d**) Raman mode separation maps of MoS_2 at flow rates 150-200-250-300 sccm. Yellow areas indicate monolayer and bilayer MoS_2, while pink and purple areas indicate few-layer MoS_2.

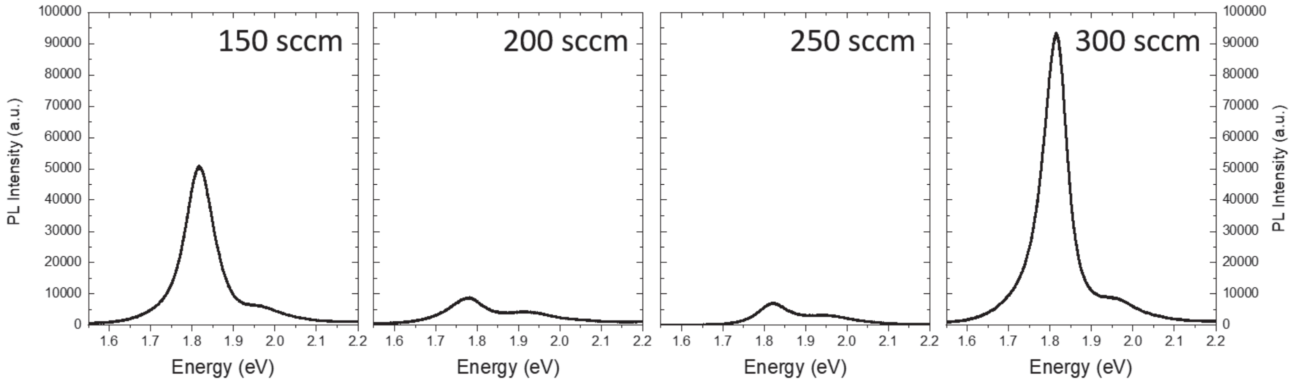

Figure 5. PL spectra for samples at flow rates of 150-200-250-300 sccm.

4. Discussion

Most of the literature on MoS_2 synthesis focuses on solid precursors, which is not directly applicable to our case. Liu et al. [47] demonstrated that increasing the carrier gas flow rate enhances the rate of precursor transport along the growth tube. Furthermore, Cao et al. [48] revealed that the carrier gas flow rate strongly influences the structural and morphological properties of MoS_2 flakes during CVD growth, which subsequently affects their optical properties. In particular, they observed dendritic structures at higher carrier flow rates, while lower carrier flows resulted in triangular shapes. Additionally, it was shown [49] that the concentration of sulfur vapor determines the size and shape of CVD-grown MoS_2 flakes, with the flake shape changing from triangle to hexagon and back to triangle as the sulfur concentration decreased.

The growth process with liquid precursors differs markedly from the typical synthesis of MoS_2 flakes using solid sources in terms of species transport and the reactions involved. Unlike solid Mo powders, the molybdenum available for MoS_2 synthesis with liquid precursors is controlled in a highly reproducible manner by applying a solution spun on the substrate. This method avoids the transport processes of MoO_3 powder in the gas phase, the heterogeneous gas phase reactions between Mo and S, and the uncontrolled MoO_x sub-oxidation processes that usually occur in the gas phase prior to the nucleation on the substrate. All these processes, which occur with solid sources, create a complex relationship between the carrier flow and the concentration of the precursors in both the gas phase and on the substrate surface, potentially leading to reproducibility issues [50,51]. By eliminating the role of gas phase reactions, we hypothesize that all the sulfur evaporating from the source will reach the substrate for the synthesis reactions: no sulfur is lost due to heterogeneous gas phase reactions, as in the case with solid precursors, and no sulfur deposition is experimentally observed in the hot zone of the furnace, between the sulfur boat and the substrate. We highlight that the temperature profile along the tube was measured prior to deposition, and no significant gradients were found in the zone relevant to the deposition. Moreover, uniform gas mixing between sulfur and nitrogen is expected due to the gas flow rate, the high temperature, and the significant distance between the sulfur source and the growth substrate.

The quantity of sulfur available for growth is defined by the solid source temperature and by its dilution in the transport carrier gas. The local concentration of sulfur in the gas stream depends on the flow dynamics of the system, which are influenced by the diameter of the reaction tube, the carrier gas flow rate, the evaporated sulfur, and the temperature profile of the system. The distance between the sulfur source and the substrate may also influence how sulfur is distributed in the gas stream and its local concentration over the liquid precursor. The sulfur available for growth is determined by the number of atoms reaching the substrate surface from the gas phase, primarily defined by the flow dynamics. The sulfur vapor pressure is set by the temperature of the sulfur powder: being in an open tube, the system is in a dynamic equilibrium, and we can assume that the sulfur vapor will never reach its equilibrium pressure. Consequently, the quantity of sulfur evaporating is constant at a given temperature, but its dilution and partial pressure in the gas phase depend on the total amount of the carrier gas: a higher gas flow in standard cubic centimeters per minute results in greater sulfur dilution in the growth tube because the same quantity of sulfur is evaporated and diluted in a larger volume of gas. Thus, we can express the sulfur partial pressure P.P.(S) as inversely proportional to the total flow F_{tot}:

$$P.P.\,(S)\ \sim \frac{1}{F_{tot}}$$

Under our experimental conditions, the flow is laminar (the Reynolds number with a N_2 flow of 300 sccm is approximately 14). The carrier gas flow affects the thickness of the boundary layer between the nutrient gas phase and the substrate surface, influencing sulfur diffusion from the nutrient gas phase to the surface and the diffusion of the reaction byproducts from the surface to the gas phase. The velocity of sulfur diffusion towards the surface is inversely proportional to the boundary layer thickness, which depends on $\frac{1}{\sqrt{F_{tot}}}$ [52,53]. It has also been observed that, in the sulfurization of a molybdenum thin layer deposited by sputtering, the rate-limiting step is the diffusion of sulfur to the surface, highlighting the pivotal role of sulfur diffusion in a system similar to ours and supporting the relevance of the boundary layer model [54,55].

Combining these two dependencies, we can estimate that the sulfur concentration at the substrate surface is proportional to the following:

$$surface\ S\ concentration\ \sim\ P.P.\ (S) \times \frac{1}{boundary\ layer\ thickness}\ \sim\ \frac{1}{F} \times \sqrt{F}\ \sim \frac{1}{\sqrt{F}}$$

We therefore expect a higher sulfur concentration at the substrate surface at low carrier gas flows, and conversely, a lower sulfur surface concentration at higher flows.

In the model proposed here, we make several assumptions derived from previous works using solid molybdenum precursors, particularly regarding the effect of sulfur supply on flake growth. It is important to emphasize that the change in flow rate affects the growth of flakes using solid and liquid precursors in entirely different ways. The transport of molybdenum vapor from solid sources and reactions between MoO_3 and S occurring in the gas phase prior to the synthesis on the flakes do not occur in our system [10,56,57]. By using liquid molybdenum precursors deposited by spin-coating on the growth substrate, the quantity of the molybdenum precursor can be considered constant, independent of other growth parameters. Following the seminal work of Kim et al. [25], during the temperature ramp, the AHT reacts with the residual oxygen in the chamber, creating a mixture of MoO_3 and Na_2MoO_4.

The orientation of the MoS_2 structures may also be affected, as changes in the S:Mo ratio can lead to the synthesis of vertically aligned MoS_2 microscale structures [58]. Additionally, variations in the S:Mo can alter the CVD process, favoring a more layer-by-layer growth mechanism and reducing the desired two-dimensional in-plane enlargement [59].

In Figure 6, we illustrate the effect of the different sulfur provisions on the number of layers and the shape of the obtained MoS_2 structures, based on total carrier flow. Considering the flow dynamic model described above, lower carrier flows result in higher sulfur supply (left panel), leading to MoS_2 structures composed of a central layer-by-layer pyramidal structure with lateral bilayer features [60,61]. A medium sulfur supply (central panel) results in the growth of few-layer structures. Finally, increasing the flow decreases the sulfur provision, resulting in monolayer large-area structures.

The change in sulfur supply transitions the growth regime from kinetic driven (at low flow/high sulfur concentration at the surface) to thermodynamically driven (at higher flow/lower sulfur concentration), which may explain the observed changes in flake shape: at lower flows, the higher concentration of sulfur adatoms arriving at the substrate inhibits the enlargement of existing flakes, as it becomes more favorable to nucleate a new MoS_2 seed rather than enlarging an existing one, thus explaining the formation of pyramid structures and the aggregation of flakes. As the carrier flow increases, the supersaturation of sulfur at the surface decreases and the growth becomes more thermodynamically driven; enlarging existing seeds becomes favorable compared to nucleating new ones, resulting in larger and more regular flakes.

By eliminating the gas phase heterogeneous reactions present when using solid precursors, which depend on many parameters (temperature, distance between the Mo and S powders, position of the substrate, etc.), the growth process with liquid precursors is more controlled and reliable. This may enhance our understanding of MoS_2 growth mechanisms. It should also be noted that, for this reason, results obtained with solid precursors cannot be directly explained by this model.

We also discuss the modifications in the shape of the MoS_2 structures obtained with different sulfur provisions. It is generally observed that concavity increases, and multi-apex triangles are formed if the growth occurs in molybdenum excess [41]. In the case of a lower provision of sulfur, the shape indicates that the CVD process is carried out in a molybdenum-rich environment, as the structures exhibit undergrowth along the sulfur in zig-zag directions [62]. Increasing the sulfur supply leads to a sulfur-rich environment, resulting in concave triangular structures [63].

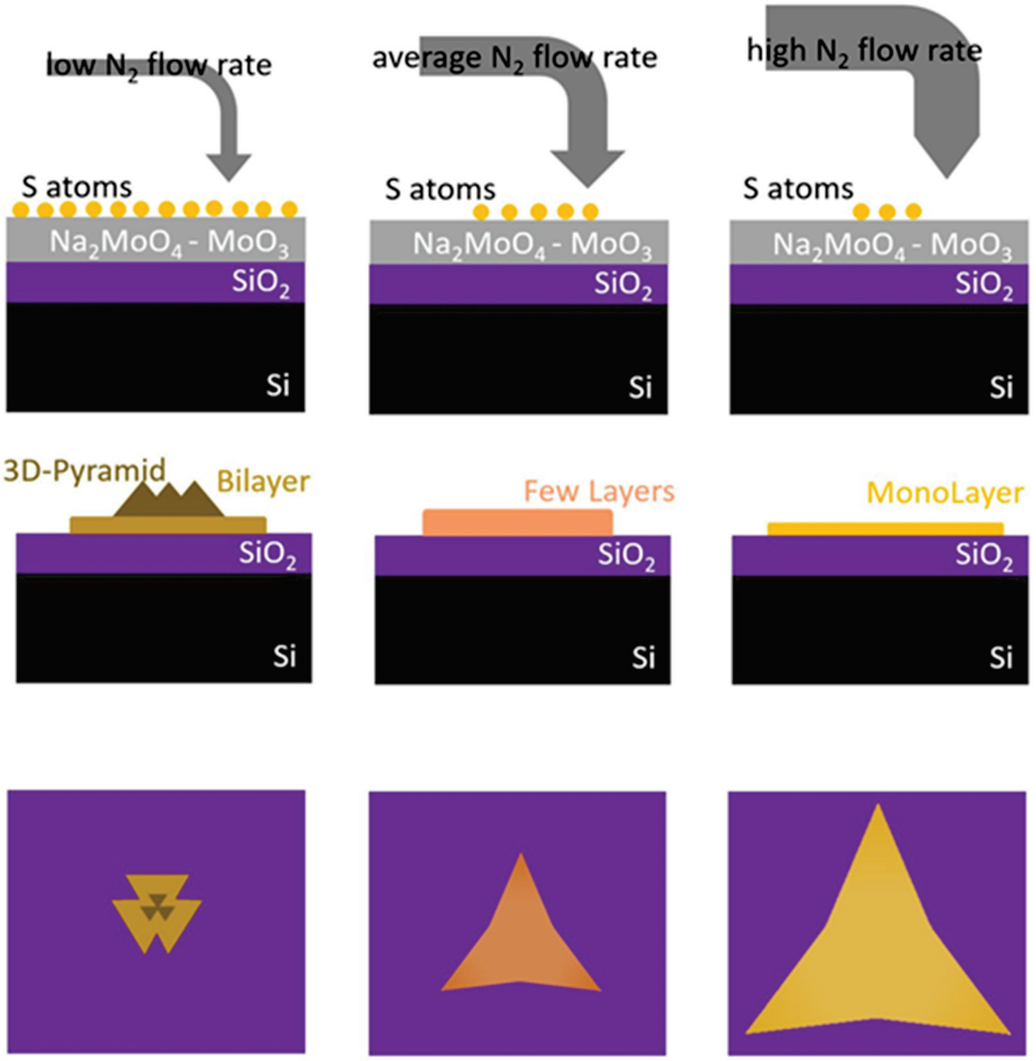

Figure 6. A sketch illustrating the influence of the carrier gas flow rate on sulfur supply, as well as on the shape, size, and number of layers of the flakes, with side and top views of the MoS_2 structures.

The increased concavity in the specimen obtained with a 300 sccm flow rate can be related to a slight decrease in the S:Mo ratio under these conditions, which also induces an increase in the lateral size. Therefore, at higher flows, the increased concavity of flakes suggests that the growth occurs with a slightly lower sulfur supply, corroborating the proposed model regarding sulfur provision. This finding contrasts with what is generally observed with solid precursors, where a higher gas flow rate is reported to increase the provision of sulfur atoms, leading to flakes with reduced concavity and a more regular triangular shape. This discrepancy, as mentioned in the previous section, may be attributed to the very different growth dynamics in the two systems and the absence of gas phase pre-reactions between MoO_3 and S when using solid precursors.

The use of liquid precursors simplifies the growth mechanism of MoS_2 flakes by separating the sulfur supply, which is controlled solely by flow dynamics, from the surface reactions governed by kinetic and thermodynamic processes. This approach also clarifies the influence of sulfur supply on the shape and size of MoS_2 flakes, as it depends only on the total carrier flow, which is proportional to $\frac{1}{\sqrt{F}}$. Our model demonstrates that the S:Mo ratio in the case of liquid precursor CVD simultaneously affects both the number of layers and the size of the MoS_2 structures. At a high sulfur supply (carrier flow = 150 sccm), we obtain small structures characterized by a bulk central region with lateral overgrowth. Conversely, as the sulfur supply decreases, few-layer structures form. When the sulfur reaching the substrate is lower (carrier flow = 300 sccm), monolayer MoS_2 flakes are produced with an average lateral size that is 3.5 times larger than those grown under higher sulfur supply conditions (carrier flow = 200–250 sccm). While our method allows for the growth of large flakes, obtaining a uniform continuous film with our CVD system configuration remains a challenge. To date, this has only been achieved using vertical substrate positioning [64].

To summarize the progress in 2D MoS_2 growth using different approaches, we provide Table 1, where we highlight some relevant parameters from representative articles. Due to the vast number of scientific publications on this material, this table should be considered only as a guideline for standard values commonly found in the literature.

Table 1. Overview of recent studies on 2D-MoS_2 growth, summarizing key parameters from selected publications to provide standard reference values for different growth approaches.

Flake Size (μm)	Mo Precursor	Temperature	Substrate	No. of Layers	Applications	Ref.
continuous	MoO_3 thin film	1000 °C	c-sapphire	Trilayers	Electronics (FET)	[65]
10–50	MoO_3 powders	750 °C	SiO_2/Si	Mono and Bilayers	Photonics	[34]
10–100	MoO_3 powders	700–720 °C	SiO_2/Si	Monolayers	n.a.	[36]
10–20	Liquid	850 °C	c-sapphire	Monolayers	Electronics (FET)	[17]
100–250	Liquid	725 °C	SiO_2/Si	Mono and Bilayers	Electronics (FET)	[19]
100–200	Liquid	820 °C	SiO_2/Si	Monolayers	n.a.	This work

5. Conclusions

We investigated the influence of the carrier gas flow rate on the synthesis of two-dimensional MoS_2 structures using Mo liquid precursors by analyzing the properties of samples grown under identical conditions with varying carrier flows. Our results demonstrate that adjusting the carrier gas flow allows control over the nucleation density, morphology, lateral size, and the number of layers in the MoS_2 flakes. At the lowest flow rate, the resulting structures exhibit an inhomogeneous number of layers, featuring a bulk-like center (predominantly pyramidal) with bilayer structures extending along the Mo zig-zag crystallographic directions. At the highest flow rate, the synthesis yields 100 μm large triangular monolayers with concave edges. These findings are in stark contrast to the results commonly reported for MoS_2 2D structures grown using solid Mo precursors.

We propose a model to explain the effect of different carrier flows on the properties of the flakes, based on changes in sulfur provision: low flows create sulfur-rich conditions, leading to small, layer-by-layer pyramidal structures with lateral bilayers, whereas high flows reduce the S:Mo ratio, resulting in larger, monolayer flakes with greater concavity. This discussion highlights the key differences in the growth process between solid and liquid Mo precursors, emphasizing that carrier gas flow is a critical parameter in the CVD growth of MoS_2 structures. Our study shows that, by optimizing the CVD growth parameters, it is possible to reproducibly achieve monolayer flakes with an average lateral size of about 100 μm.

Supplementary Materials: The following supporting information can be downloaded at: https://www.mdpi.com/article/10.3390/nano14211749/s1, Figure S1: OM images of the flakes analyzed by Raman maps; Figure S2: Representative Raman spectra of MoS_2 for 150-200-250-300 sccm growth processes; Figure S3: Representative Raman spectrum of MoS_2 for 150 sccm growth process.

Author Contributions: Conceptualization, F.E. and L.S.; methodology, F.E., G.A., M.B., F.F. and L.S.; formal analysis, F.E., R.F., F.F. and L.S.; investigation, F.E., F.F. and L.S.; resources, L.S.; data curation,

L.S.; writing—original draft preparation, F.E. and L.S.; writing—review and editing, F.E., M.B., G.A., F.R., R.F., F.F. and L.S.; visualization, F.E. and F.F.; supervision, L.S.; project administration, L.S.; funding acquisition, L.S. All authors have read and agreed to the published version of the manuscript.

Funding: This research was carried out within the PRIN Project "2DIntegrate" (Prot. 2022RHRZN2) funded under the National Recovery and Resilience Plan (NRRP), Mission 4 Component C2 Investment 1.1—Italian Ministry of University and Research funded by the European Union—NextGenerationEU.

Data Availability Statement: The data are available upon reasonable request from the corresponding author.

Acknowledgments: We would like to thank Antonino Picciotto and the technical personnel of the Micro-Nano Facility at Fondazione Bruno Kessler, Povo, Trento, Italy for the preparation of SiO_2/Si substrates.

Conflicts of Interest: The authors declare no conflicts of interest.

References

1. Yu, J.; Li, J.; Zhang, W.; Chang, H. Synthesis of high quality two-dimensional materials via chemical vapor deposition. *Chem. Sci.* **2015**, *6*, 6705–6716. [CrossRef]
2. Singh, A.K.; Kumar, P.; Late, D.J.; Kumar, A.; Patel, S.; Singh, J. 2D Layered Transition Metal Dichalcogenides (MoS_2): Synthesis, Applications and Theoretical Aspects. *Appl. Mater. Today* **2018**, *13*, 242–270. [CrossRef]
3. Yu, J.; Hu, X.; Li, H.; Zhou, X.; Zhai, T. Large-Scale Synthesis of 2D Metal Dichalcogenides. *J. Mater. Chem. C* **2018**, *6*, 4627. [CrossRef]
4. Xiao, X.; Wang, H.; Urbankowski, P.; Gogotsi, Y. Topochemical Synthesis of 2D Materials. *Chem. Soc. Rev.* **2018**, *47*, 8744. [CrossRef] [PubMed]
5. Dong, R.; Zhang, T.; Feng, X. Interface-Assisted Synthesis of 2D Materials: Trend and Challenges. *Chem. Rev.* **2018**, *118*, 6189–6235. [CrossRef]
6. Alam, S.; Chowdhury, M.A.; Shahid, A.; Alam, R.; Rahim, A. Synthesis of emerging two-dimensional (2D) materials—Advances, challenges and prospects. *FlatChem* **2021**, *30*, 100305. [CrossRef]
7. Kim, S.Y.; Kwak, J.; Ciobanu, C.V.; Kwon, S.Y. Recent Developments in Controlled Vapor-Phase Growth of 2D Group 6 Transition Metal Dichalcogenides. *Adv. Mater.* **2019**, *31*, 1804939. [CrossRef]
8. Dumcenco, D.; Ovchinnikov, D.; Marinov, K.; Lazić, P.; Gibertini, M.; Marzari, N.; Sanchez, O.L.; Kung, Y.-C.; Krasnozhon, D.; Chen, M.-W.; et al. Large-Area Epitaxial Monolayer MoS_2. *ACS Nano* **2015**, *9*, 4611–4620. [CrossRef]
9. Seravalli, L.; Bosi, M. A Review on Chemical Vapour Deposition of Two-Dimensional MoS_2 Flakes. *Materials* **2021**, *14*, 7590. [CrossRef]
10. Xia, Y.; Chen, X.; Wei, J.; Wang, S.; Chen, S.; Wu, S.; Ji, M.; Sun, Z.; Xu, Z.; Bao, W.; et al. 2-Inch Growth of Uniform MoS_2 Monolayer for Integrated Circuit Manufacture. *Nat. Mater.* **2023**, *22*, 1324–1331. [CrossRef]
11. Wang, Q.; Tang, J.; Li, X.; Tian, J.; Liang, J.; Li, N.; Ji, D.; Xian, L.; Guo, Y.; Li, L.; et al. Layer-by-Layer Epitaxy of Multi-Layer MoS_2 Wafers. *Natl. Sci. Rev.* **2022**, *9*, nwac077. [CrossRef] [PubMed]
12. Liu, X.; Galfsky, T.; Sun, Z.; Xia, F.; Lin, E.; Lee, Y.-H.; Kéna-Cohen, S.; Menon, V.M. Strong Light–Matter Coupling in Two-Dimensional Atomic Crystals. *Nat. Photonics* **2015**, *9*, 30–34. [CrossRef]
13. Manzeli, S.; Ovchinnikov, D.; Pasquier, D.; Yazyev, O.V.; Kis, A. 2D Transition Metal Dichalcogenides. *Nat. Rev. Mater.* **2017**, *2*, 17033. [CrossRef]
14. Nalwa, H.S. A Review of Molybdenum Disulfide (MoS_2) Based Photodetectors: From Ultra-Broadband, Self-Powered to Flexible Devices. *RSC Adv.* **2020**, *10*, 30529–30602. [CrossRef] [PubMed]
15. Cheng, Y.; Wan, R.; Li, L.; Liu, Z.; Yan, S.; Li, L.; Wang, J.; Gao, Y. Research Progress on Improving the Performance of MoS $_2$ Photodetector. *J. Opt.* **2022**, *24*, 104003. [CrossRef]
16. Ye, Z.; Tan, C.; Huang, X.; Ouyang, Y.; Yang, L.; Wang, Z.; Dong, M. Emerging MoS_2 Wafer-Scale Technique for Integrated Circuits. *Nano-Micro Lett.* **2023**, *15*, 38. [CrossRef]
17. Seo, J.; Lee, J.; Baek, S.; Jung, W.; Oh, N.K.; Son, E.; Park, H. Liquid Precursor-Mediated Epitaxial Growth of Highly Oriented 2D van Der Waals Semiconductors toward High-Performance Electronics. *ACS Appl. Electron. Mater.* **2021**, *3*, 5528–5536. [CrossRef]
18. Zhang, T.; Fujisawa, K.; Zhang, F.; Liu, M.; Lucking, M.C.; Gontijo, R.N.; Lei, Y.; Liu, H.; Crust, K.; Granzier-Nakajima, T.; et al. Universal In Situ Substitutional Doping of Transition Metal Dichalcogenides by Liquid-Phase Precursor-Assisted Synthesis. *ACS Nano* **2020**, *14*, 4326–4335. [CrossRef]
19. Tong, S.W.; Medina, H.; Liao, W.; Wu, J.; Wu, W.; Chai, J.; Yang, M.; Abutaha, A.; Wang, S.; Zhu, C.; et al. Employing a Bifunctional Molybdate Precursor To Grow the Highly Crystalline MoS_2 for High-Performance Field-Effect Transistors. *ACS Appl. Mater. Interfaces* **2019**, *11*, 14239–14248. [CrossRef]
20. Liu, X.; Wang, H.; Yang, D.; Jing, F.; Qiu, H.; Liu, H.; Hu, Z. Embedded Lanthanoid Ions Modulated the Periodic Luminescence of Transition Metal Dichalcogenide Monolayers Prepared from an Aqueous Orecursor. *J. Mater. Chem. C Mater.* **2022**, *10*, 8061–8069. [CrossRef]

21. Qin, Z.; Loh, L.; Wang, J.; Xu, X.; Zhang, Q.; Haas, B.; Alvarez, C.; Okuno, H.; Yong, J.Z.; Schultz, T.; et al. Growth of Nb-Doped Monolayer WS2 by Liquid-Phase Precursor Mixing. *ACS Nano* **2019**, *13*, 10768–10775. [CrossRef] [PubMed]
22. Shen, D.; Jin, Y.; Zhang, Z.; Song, R.; Liu, M.; Li, W.; Li, X.; Wu, R.; Li, B.; Li, J.; et al. Recent Advances in Spin-Coating Precursor Mediated Chemical Vapor Deposition of Two-Dimensional Transition Metal Dichalcogenides. *Precis. Chem.* **2024**, *2*, 282–299. [CrossRef] [PubMed]
23. Guan, H.; Zhao, B.; Zhao, W.; Ni, Z. Liquid-Precursor-Intermediated Synthesis of Atomically Thin Transition Metal Dichalcogenides. *Mater. Horiz.* **2023**, *10*, 1105–1120. [CrossRef]
24. Kang, S.K.; Lee, H.S. Study on Growth Parameters for Monolayer MoS_2 Synthesized by CVD Using Solution-Based Metal Precursors. *Appl. Sci. Converg. Technol.* **2019**, *28*, 159–163. [CrossRef]
25. Kim, H.; Han, G.H.; Yun, S.J.; Zhao, J.; Keum, D.H.; Jeong, H.Y.; Ly, T.H.; Jin, Y.; Park, J.-H.; Moon, B.H.; et al. Role of Alkali Metal Promoter in Enhancing Lateral Growth of Monolayer Transition Metal Dichalcogenides. *Nanotechnology* **2017**, *28*, 36LT01. [CrossRef]
26. Yang, K.Y.; Nguyen, H.T.; Tsao, Y.M.; Artemkina, S.B.; Fedorov, V.E.; Huang, C.W.; Wang, H.C. Large Area MoS_2 Thin Film Growth by Direct Sulfurization. *Sci. Rep.* **2023**, *13*, 8378. [CrossRef]
27. An, G.H.; Yun, S.J.; Lee, Y.H.; Lee, H.S. Growth Mechanism of Alternating Defect Domains in Hexagonal WS 2 via Inhomogeneous W—Precursor Accumulation. *Small* **2020**, *16*, e2003326. [CrossRef] [PubMed]
28. Seravalli, L.; Esposito, F.; Bosi, M.; Aversa, L.; Trevisi, G.; Verucchi, R.; Lazzarini, L.; Rossi, F.; Fabbri, F. Built-in Tensile Strain Dependence on the Lateral Size of Monolayer MoS_2 Synthesized by Liquid Precursor Chemical Vapor Deposition Nanoscale. *Nanoscale* **2023**, *15*, 14669. [CrossRef]
29. Esposito, F.; Bosi, M.; Attolini, G.; Rossi, F.; Panasci, S.E.; Fiorenza, P.; Giannazzo, F.; Fabbri, F.; Seravalli, L. Role of Density Gradients in the Growth Dynamics of 2-Dimensional MoS_2 Using Liquid Phase Molybdenum Precursor in Chemical Vapor Deposition. *Appl. Surf. Sci.* **2023**, *639*, 158230. [CrossRef]
30. Senkić, A.; Bajo, J.; Supina, A.; Radatović, B.; Vujičić, N. Effects of CVD Growth Parameters on Global and Local Optical Properties of MoS_2 Monolayers. *Mater. Chem. Phys.* **2023**, *296*, 127185. [CrossRef]
31. Kang, W.T.; Phan, T.L.; Ahn, K.J.; Lee, I.; Kim, Y.R.; Won, U.Y.; Kim, J.E.; Lee, Y.H.; Yu, W.J. Selective Pattern Growth of Atomically Thin MoSe2Films via a Surface-Mediated Liquid-Phase Promoter. *ACS Appl. Mater. Interfaces* **2021**, *13*, 18056–18064. [CrossRef]
32. Tian, C.; Xiao, R.; Sui, Y.; Feng, Y.; Wang, H.; Zhao, S.; Liu, J.; Gao, X.; Wang, S.; Yu, G. The Controllable Synthesis of Bilayer V Doped WS 2 Based on Liquid Precursor Assisted CVD. *Mater. Lett.* **2023**, *353*, 135292. [CrossRef]
33. Han, G.H.; Neumann, M.; Song, S.; Park, H.W.; Moon, B.H.; Lee, Y.H. Unusual Stacking Sequence of MoS_2 and WS_2 Vertical Heterostructures in One-Pot Chemical Vapor Deposition Growth. *J. Korean Phys. Soc.* **2023**, *82*, 57–67. [CrossRef]
34. Rotunno, E.; Bosi, M.; Seravalli, L.; Salviati, G.; Fabbri, F. Influence of Organic Promoter Gradient on the MoS_2 Growth Dynamics. *Nanoscale Adv.* **2020**, *2*, 2352–2362. [CrossRef]
35. Seravalli, L.; Bosi, M.; Fiorenza, P.; Panasci, S.E.; Orsi, D.; Rotunno, E.; Cristofolini, L.; Rossi, F.; Giannazzo, F.; Fabbri, F. Gold Nanoparticle Assisted Synthesis of MoS_2 Monolayers by Chemical Vapor Deposition. *Nanoscale Adv.* **2021**, *3*, 4826–4833. [CrossRef] [PubMed]
36. Yang, S.Y.; Shim, G.W.; Seo, S.-B.; Choi, S.-Y. Effective Shape-Controlled Growth of Monolayer MoS_2 Flakes by Powder-Based Chemical Vapor Deposition. *Nano Res.* **2017**, *10*, 255–262. [CrossRef]
37. Pei, J.; Yang, J.; Xu, R.; Zeng, Y.H.; Myint, Y.W.; Zhang, S.; Zheng, J.C.; Qin, Q.; Wang, X.; Jiang, W.; et al. Exciton and Trion Dynamics in Bilayer MoS_2. *Small* **2015**, *11*, 6384–6390. [CrossRef]
38. Cadiz, F.; Tricard, S.; Gay, M.; Lagarde, D.; Wang, G.; Robert, C.; Renucci, P.; Urbaszek, B.; Marie, X. Well Separated Trion and Neutral Excitons on Superacid Treated MoS_2 Monolayers. *Appl. Phys. Lett.* **2016**, *108*, 251106. [CrossRef]
39. Splendiani, A.; Sun, L.; Zhang, Y.; Li, T.; Kim, J.; Chim, C.-Y.; Galli, G.; Wang, F. Emerging Photoluminescence in Monolayer MoS_2. *Nano Lett.* **2010**, *10*, 1271–1275. [CrossRef]
40. Lee, C.; Yan, H.; Brus, L.E.; Heinz, T.F.; Hone, J.; Ryu, S. Anomalous Lattice Vibrations of Single- and Few-Layer MoS_2. *ACS Nano* **2010**, *4*, 2695–2700. [CrossRef]
41. Li, H.; Zhang, Q.; Yap, C.C.R.; Tay, B.K.; Edwin, T.H.T.; Olivier, A.; Baillargeat, D. From Bulk to Monolayer MoS_2: Evolution of Raman Scattering. *Adv. Funct. Mater.* **2012**, *22*, 1385–1390. [CrossRef]
42. Golovynskyi, S.; Irfan, I.; Bosi, M.; Seravalli, L.; Datsenko, O.I.; Golovynska, I.; Li, B.; Lin, D.; Qu, J. Exciton and Trion in Few-Layer MoS_2: Thickness- and Temperature-Dependent Photoluminescence. *Appl. Surf. Sci.* **2020**, *515*, 146033. [CrossRef]
43. Amani, M.; Lien, D.H.; Kiriya, D.; Xiao, J.; Azcatl, A.; Noh, J.; Madhvapathy, S.R.; Addou, R.; Santosh, K.C.; Dubey, M.; et al. Near-Unity Photoluminescence Quantum Yield in MoS_2. *Science* **2015**, *350*, 1065–1068. [CrossRef] [PubMed]
44. Birmingham, B.; Yuan, J.; Filez, M.; Fu, D.; Hu, J.; Lou, J.; Scully, M.O.; Weckhuysen, B.M.; Zhang, Z. Spatially-Resolved Photoluminescence of Monolayer MoS_2 under Controlled Environment for Ambient Optoelectronic Applications. *ACS Appl. Nano Mater.* **2018**, *1*, 6226–6235. [CrossRef]
45. Mouri, S.; Miyauchi, Y.; Matsuda, K. Tunable Photoluminescence of Monolayer MoS_2 via Chemical Doping. *Nano Lett.* **2013**, *13*, 5944–5948. [CrossRef]
46. Lu, A.Y.; Martins, L.G.P.; Shen, P.C.; Chen, Z.; Park, J.H.; Xue, M.; Han, J.; Mao, N.; Chiu, M.H.; Palacios, T.; et al. Unraveling the Correlation between Raman and Photoluminescence in Monolayer MoS_2 through Machine-Learning Models. *Adv. Mater.* **2022**, *34*, e2202911. [CrossRef]

47. Liu, H.; Zhu, Y.; Meng, Q.; Lu, X.; Kong, S.; Huang, Z.; Jiang, P.; Bao, X. Role of the Carrier Gas Flow Rate in Monolayer MoS_2 Growth by Modified Chemical Vapor Deposition. *Nano Res.* **2016**, *10*, 643–651. [CrossRef]
48. Cao, Y.; Luo, X.; Han, S.; Yuan, C.; Yang, Y.; Li, Q.; Yu, T.; Ye, S. Influences of Carrier Gas Flow Rate on the Morphologies of MoS_2 Flakes. *Chem. Phys. Lett.* **2015**, *631–632*, 30–33. [CrossRef]
49. Cho, Y.J.; Sim, Y.; Lee, J.H.; Hoang, N.T.; Seong, M.J. Size and Shape Control of CVD-Grown Monolayer MoS_2. *Curr. Appl. Phys.* **2023**, *45*, 99–104. [CrossRef]
50. Lee, Y.H.; Zhang, X.Q.; Zhang, W.; Chang, M.T.; Lin, C.T.; Chang, K.D.; Yu, Y.C.; Wang, J.T.W.; Chang, C.S.; Li, L.J.; et al. Synthesis of Large-Area MoS_2 Atomic Layers with Chemical Vapor Deposition. *Adv. Mater.* **2012**, *24*, 2320–2325. [CrossRef]
51. Zhang, Y.; Zhang, Y.; Ji, Q.; Ju, J.; Yuan, H.; Shi, J.; Gao, T.; Ma, D.; Liu, M.; Chen, Y.; et al. Controlled Growth of High-Quality Monolayer WS2 Layers on Sapphire and Imaging Its Grain Boundary. *ACS Nano* **2013**, *7*, 8963–8971. [CrossRef] [PubMed]
52. Johari, M.H.; Sirat, M.S.; Mohamed, M.A.; Mustaffa, A.F.; Mohmad, A.R. Computational Fluid Dynamics Insights into Chemical Vapor Deposition of Homogeneous MoS_2 Film with Solid Precursors. *Cryst. Res. Technol.* **2023**, *58*, 2300139. [CrossRef]
53. Herman, M.A.; Richter, W.; Sitter, H. *Epitaxy*; Springer Series in Materials Science; Springer: Berlin/Heidelberg, Germany, 2004; Volume 62, ISBN 978-3-642-08737-0.
54. Panasci, S.E.; Koos, A.; Schilirò, E.; Di Franco, S.; Greco, G.; Fiorenza, P.; Roccaforte, F.; Agnello, S.; Cannas, M.; Gelardi, F.M.; et al. Multiscale Investigation of the Structural, Electrical and Photoluminescence Properties of MoS_2 Obtained by MoO_3 Sulfurization. *Nanomaterials* **2022**, *12*, 182. [CrossRef] [PubMed]
55. Kong, D.; Wang, H.; Cha, J.J.; Pasta, M.; Koski, K.J.; Yao, J.; Cui, Y. Synthesis of MoS_2 and $MoSe_2$ Films with Vertically Aligned Layers. *Nano Lett.* **2013**, *13*, 1341–1347. [CrossRef] [PubMed]
56. Pondick, J.V.; Woods, J.M.; Xing, J.; Zhou, Y.; Cha, J.J. Stepwise Sulfurization from MoO_3 to MoS_2 via Chemical Vapor Deposition. *ACS Appl. Nano Mater.* **2018**, *1*, 5655–5661. [CrossRef]
57. Withanage, S.S.; Kalita, H.; Chung, H.-S.; Roy, T.; Jung, Y.; Khondaker, S.I. Uniform Vapor-Pressure-Based Chemical Vapor Deposition Growth of MoS_2 Using MoO_3 Thin Film as a Precursor for Coevaporation. *ACS Omega* **2024**, *3*, 18943–18949. [CrossRef]
58. Kumar, P.; Viswanath, B. Horizontally and Vertically Aligned Growth of Strained MoS_2 Layers with Dissimilar Wetting and Catalytic Behaviors †. *CrystEngComm* **2017**, *19*, 5068–5078. [CrossRef]
59. Kwak, T.; Lee, J.; So, B.; Choi, U.; Nam, O. Growth Behavior of Wafer-Scale Two-Dimensional MoS_2 Layer Growth Using Metal-Organic Chemical Vapor Deposition. *J. Cryst. Growth* **2019**, *510*, 50–55. [CrossRef]
60. Lin, X.; Liu, Y.; Wang, K.; Wei, C.; Zhang, W.; Yan, Y.; Li, Y.J.; Yao, J.; Zhao, Y.S. Two-Dimensional Pyramid-like WS2 Layered Structures for Highly Efficient Edge Second Harmonic Generation. *ACS Nano* **2018**, *12*, 689–696. [CrossRef]
61. Negri, M.; Francaviglia, L.; Kaplan, D.; Swaminathan, V.; Salviati, G.; Fontcuberta I Morral, A.; Fabbri, F. Excitonic Absorption and Defect-Related Emission in Three-Dimensional MoS_2 Pyramids †. *Nanoscale* **2022**, *14*, 1179–1186. [CrossRef]
62. Wang, S.; Rong, Y.; Fan, Y.; Pacios, M.; Bhaskaran, H.; He, K.; Warner, J.H. Shape Evolution of Monolayer MoS_2 Crystals Grown by Chemical Vapor Deposition. *Chem. Mater.* **2014**, *26*, 6371–6379. [CrossRef]
63. Zhu, Z.; You, J.; Zhu, D.; Jiang, G.; Zhan, S.; Wen, J.; Xia, Q. Effect of Precursor Ratio on the Morphological and Optical Properties of CVD-Grown Monolayer MoS_2 Nanosheets. *Mater. Res. Express* **2021**, *8*, 045008. [CrossRef]
64. Wang, S.; Pacios, M.; Bhaskaran, H.; Warner, J.H. Substrate control for large area continuous films of monolayer MoS_2 by atmospheric pressure chemical vapor deposition. *Nanotechnology* **2016**, *27*, 085604.
65. Lin, Y.-C.; Zhang, W.; Huang, J.-K.; Liu, K.-K.; Lee, Y.-H.; Liang, C.-T.; Chu, C.-W.; Li, L.-J. Wafer-Scale MoS2 Thin Layers Prepared by MoO3 Sulfurization. *Nanoscale* **2012**, *4*, 6637–6641. [CrossRef]

nanomaterials

MDPI

Article

Large-Area MoS_2 Films Grown on Sapphire and GaN Substrates by Pulsed Laser Deposition

Marianna Španková [1,*], Štefan Chromik [1], Edmund Dobročka [1], Lenka Pribusová Slušná [1], Marcel Talacko [1], Maroš Gregor [2], Béla Pécz [3], Antal Koos [3], Giuseppe Greco [4], Salvatore Ethan Panasci [4], Patrick Fiorenza [4], Fabrizio Roccaforte [4], Yvon Cordier [5], Eric Frayssinet [5] and Filippo Giannazzo [4]

[1] Institute of Electrical Engineering, Slovak Academy of Sciences, Dúbravská cesta 9, 84104 Bratislava, Slovakia; stefan.chromik@savba.sk (Š.C.); edmund.dobrocka@savba.sk (E.D.); lenka.pribusova-slusna@savba.sk (L.P.S.); marcel.talacko@savba.sk (M.T.)

[2] Faculty of Mathematics, Physics and Informatics, Comenius University Bratislava, 84248 Bratislava, Slovakia; maros.gregor@fmph.uniba.sk

[3] HUN-REN Centre for Energy Research, Institute of Technical Physics and Materials Science, Konkoly-Thege ut 29-33, 1121 Budapest, Hungary; pecz.bela@ek.hun-ren.hu (B.P.); koos.antal@ek.hun-ren.hu (A.K.)

[4] Consiglio Nazionale delle Ricerche—Istituto per la Microelettronica e Microsistemi (CNR-IMM), Strada VIII 5, 95121 Catania, Italy; giuseppe.greco@imm.cnr.it (G.G.); salvatoreethan.panasci@imm.cnr.it (S.E.P.); patrick.fiorenza@imm.cnr.it (P.F.); fabrizio.roccaforte@imm.cnr.it (F.R.); filippo.giannazzo@imm.cnr.it (F.G.)

[5] CNRS, CRHEA, Université Côte d'Azur, 06560 Valbonne, France; yvon.cordier@crhea.cnrs.fr (Y.C.); eric.frayssinet@crhea.cnrs.fr (E.F.)

[*] Correspondence: marianna.spankova@savba.sk

Abstract: In this paper, we present the preparation of few-layer MoS_2 films on single-crystal sapphire, as well as on heteroepitaxial GaN templates on sapphire substrates, using the pulsed laser deposition (PLD) technique. Detailed structural and chemical characterization of the films were performed using Raman spectroscopy, X-ray photoelectron spectroscopy, X-ray diffraction measurements, and high-resolution transmission electron microscopy. According to X-ray diffraction studies, the films exhibit epitaxial growth, indicating a good in-plane alignment. Furthermore, the films demonstrate uniform thickness on large areas, as confirmed by Raman spectroscopy. The lateral electrical current transport of the MoS_2 grown on sapphire was investigated by temperature (T)-dependent sheet resistance and Hall effect measurements, showing a high n-type doping of the semiconducting films (n_s from ~1×10^{13} to ~3.4×10^{13} cm^{-2} from T = 300 K to 500 K), with a donor ionization energy of $E_i = 93 \pm 8$ meV and a mobility decreasing with T. Finally, the vertical current injection across the MoS_2/GaN heterojunction was investigated by means of conductive atomic force microscopy, showing the rectifying behavior of the I-V characteristics with a Schottky barrier height of $\phi_B \approx 0.36$ eV. The obtained results pave the way for the scalable application of PLD-grown MoS_2 on GaN in electronics/optoelectronics.

Keywords: MoS_2; GaN; sapphire substrates; pulsed laser deposition; structural properties; electrical properties

---

1. Introduction

Two-dimensional layered (2D) transition metal dichalcogenides (TMDs), especially molybdenum disulfide (MoS_2), have attracted widespread attention due to their unique electronic, mechanical, and optical properties. Layered MoS_2 consists of a vertical stack of single layers 0.65 nm thick which are held together by van der Waals interactions. Depending on the number of MoS_2 monolayers, it can be possible to tune the bandgap of MoS_2. Monolayer MoS_2 exhibits a large direct bandgap of about 1.8 eV [1], resulting in enhancement in the carrier mobility, which can be utilized for potential applications in next-generation electronic and optoelectronic [2–5] devices. Conventional approaches, such as Scotch-tape-assisted micromechanical exfoliation [6,7] or chemical exfoliation [8],

Nanomaterials **2023**, *13*, 2837. https://doi.org/10.3390/nano13212837

are not suitable for large-area device applications. The chemical vapor deposition (CVD) technique is considered one of the promising techniques for the growth of thin MoS_2 films [9,10]. However, it has some limitations, such as the precise control of the thickness uniformity, the substrate temperature, and the use of multiple precursors [11]. One of the typical physical vapor deposition methods for the fabrication of 2D layered materials is pulsed laser deposition (PLD), which offers several advantages—the capability to produce large-area, few-monolayer-thick, highly crystalline MoS_2 films at relatively low substrate temperatures (the typical substrate temperature for PLD growth is 700 °C), as well as the stoichiometric transfer of the ablated material from the target to the substrate [12–14]. In these studies, 2D MoS_2 thin films have been grown on Al_2O_3, GaN, and SiC-6H substrates. C-plane sapphire (Al_2O_3 (0001)) wafers are the most commonly employed substrates for growth of MoS_2-based 2D materials. This material is a chemically stable hexagonal single crystal, with 60°-rotation symmetry about its c-axis. GaN is a wide bandgap semiconductor and the ideal material of choice for high-frequency transistors (GaN HEMTs technology) and power-switching devices [15–17], as well as for optoelectronic devices (LEDs and laser diodes). MoS_2 and GaN are suitable candidates for 2D/3D heterostructures, as low lattice parameter mismatch between these two materials (<1%) and similar thermal expansion coefficients promise high-quality epitaxial alignment between the materials [18–21].

In this article, we demonstrate the large-area PLD growth of highly uniform, few-monolayer-thick MoS_2 films on c-plane sapphire and heteroepitaxial GaN/sapphire substrates. The films are of excellent crystalline quality and thickness homogeneity, and we were able to prepare them on large-area surfaces, increasing the possibility of using these films for a wide range of applications. Noteworthily, and differently than in previous works [12] where S-enriched MoS_2 targets were used to deposit MoS_2 films with the highest degree of crystallinity but with excess S content, we succeeded in depositing stoichiometric MoS_2 films from a target with a Mo:S ratio of 1:2. Furthermore, thanks to the absence of MoO_3 components in the as-deposited MoS_2 films, no need for additional post-deposition annealing in S is necessary to restore MoS_2 stoichiometry, in contrast to a finding reported in an earlier study [14]. We employed various characterization techniques to investigate the structural and electrical properties of the prepared films. In particular, we provided a detailed analysis of the orientation relationship between the MoS_2 film and the c-sapphire and GaN substrates, for which few results are available in the literature. Furthermore, we provided a detailed electrical investigation of the in-plane transport properties of PLD-grown MoS_2 films on insulating sapphire substrates, extracting key physical parameters like the ionization energy of donors and providing insight into the limiting mechanisms of carrier mobility. To the best of our knowledge, this type of investigation has been not reported so far in PLD-grown MoS_2. The results are useful for benchmarking the electronic quality of the material produced by this approach compared to that of MoS_2 produced by alternative methods.

2. Materials and Methods

Two types of wafers, i.e., single-polished 10 × 10 mm^2 and 0.5 mm thick c-oriented ((0001) plane) sapphire and GaN (0001)/c-sapphire substrates, were used for the MoS_2 growth. The epitaxial GaN films with thicknesses of 4 μm were grown by means of metal–organic chemical vapor deposition on c-sapphire substrates [22].

Few-monolayer (ML)-thick MoS_2 films were prepared via PLD (MBE/PLD-2000 system). The setup consists of a KrF excimer laser with a 248 nm wavelength, mirrors, and a focusing lens. An energy laser pulse of 70 mJ, with a repetition rate of 4 Hz and a laser spot size of 2 mm^2, was applied during the growth process. As a target, a commercially purchased stoichiometric MoS_2 two inches in diameter was used. The target was rotated at a speed of 6 rpm and rastered to avoid pit formation. The distance from the target to the substrate was optimized at 10 cm. The substrate was heated by irradiation from the SiC heater, eliminating the need for direct contact between the heater and the substrate. This is a definite advantage as it allows us to rotate the substrates, enhancing the homogeneity of the deposited films, and the samples do not require any clamping or silver paste. The film growth was carried out at a deposition temperature of 860 °C under 2×10^{-6} Torr background pressure. The 860 °C was the temperature of the thermocouple, which was placed close to the SiC heater so it would show the actual temperature T_S for a non-transparent Si substrate. In the case of a transparent sapphire substrate, this temperature was about 160 °C lower, i.e., in our case, T_S~700 °C. After the film growth, the samples were cooled down to 200 °C at a rate of 50 °C/min before allowing for natural cooling. The final thickness of the MoS_2 films was controlled by the number of pulses; typically, it was in the range between 400 and 800 pulses.

Raman spectroscopy was performed using an Alpha 300R micro-Raman system with a 532 nm excitation laser. The laser beam was focused by a 50× objective lens with a numerical aperture of 0.8. The acquisition time was 5 s, and the laser power was kept below 2 mW for all measurements. All of the spectra were acquired in ambient conditions.

X-ray photoelectron spectroscopy (XPS—Omicron multiprobe system with hemispherical analyzer, Scienta Omicron, Taunusstein, Germany) was performed using monochromatic Al K-alpha X-rays (1486.6 eV). All spectra were measured at an ambient temperature, with photoemission of 45° from the surface.

A Bruker D8 DISCOVER diffractometer equipped with a rotating Cu anode operating at 12 kW was used to determine the crystallographic orientation perpendicular to the film's surface (symmetric $2\theta/\omega$ configuration). To specify the in-plane orientation of the MoS_2 with respect to the substrate, ϕ-scans were carried out. All X-ray measurements were performed in parallel-beam geometry with a Goebel mirror in the primary beam.

High-resolution transmission electron microscopy (HR TEM) analyses were carried out with an aberration-corrected Thermofisher Themis 200 microscope (Thermo Fisher Scientific Inc., Waltham, MA, USA). Cross-sectional TEM specimens of MoS_2/sapphire and MoS_2/GaN/sapphire were prepared by a Ga FIB (focused ion beam) and finished at 2 kV. During the FIB process, a platinum coating was deposited in order to defend the lamella from the energetic gallium ions. We also evaporated an amorphous carbon layer, as we wanted to avoid close contact between the MoS_2 and platinum particles.

The sheet resistance, carrier density, and mobility of the MoS_2 grown on the sapphire substrate were evaluated by four-point probe and Hall effect measurements in the van der Pauw configuration. For this purpose, Ni(20 nm)/Au(80 nm) contacts were deposited by sputtering at the four corners of square-shaped (1 cm × 1 cm) MoS_2/sapphire samples. Ohmic contacts on MoS_2 were obtained with as-deposited Ni/Au stacks. The vertical current injection at the MoS_2/GaN interface was probed at the nanoscale by conductive atomic force microscopy (C-AFM) with a DI3100 system by Bruker with Nanoscope V electronics, using Pt-coated conductive tips.

3. Results

We performed characterization using Raman spectroscopy in order to verify the thicknesses and properties of our MoS_2 films (Figure 1a,b). Raman spectroscopy serves as a strong tool to determine the vibrational modes of TMDs. The characteristic Raman modes $E^1{}_{2g}$ and A_{1g} are the most intense signals for the 2H-MoS_2 phase and can be used to determine the number of MoS_2 layers. This number depends on the difference $\Delta\omega$ between the $E^1{}_{2g}$ and A_{1g} peak wavenumbers. We obtained values of $\Delta\omega$~22.5–22.7 cm^{-1} and ~24.2 cm^{-1} for the MoS_2 films shown in Figure 1a,b, corresponding to two to three monolayers (prepared by 400 laser pulses) and five monolayers (prepared by 800 laser pulses) of MoS_2, respectively. The thickness uniformity of the MoS_2 films was determined from arrays of 40 × 40 Raman spectra collected from an area measuring 10 × 10 μm.

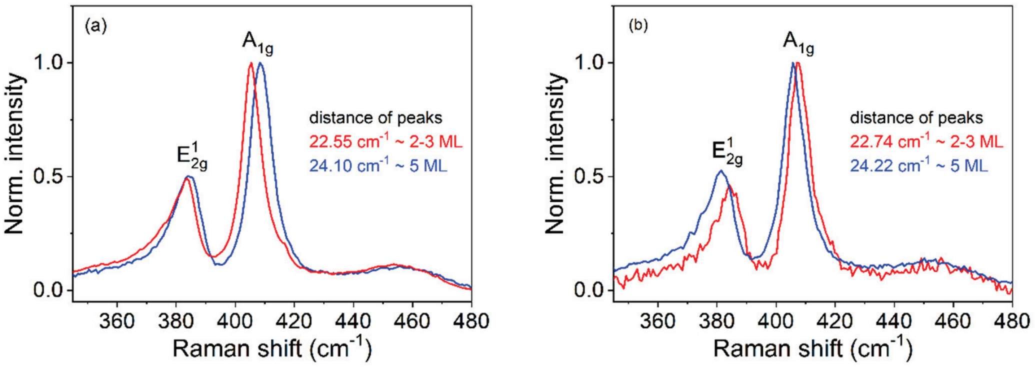

Figure 1. Normalized Raman spectra of MoS_2 deposited on sapphire (**a**) and on GaN/sapphire (**b**), with various pulse numbers. The two characteristic in-plane ($E^1{}_{2g}$) and out-of-plane (A_{1g}) vibrational modes are labeled.

Figure 2a,c show two representative color maps of the Δω values extracted from the arrays of spectra measured on MoS_2/sapphire and MoS_2/GaN surfaces, respectively. Figure 2b,d are the histograms of the Δω values in the two maps, from which a very narrow distribution can be observed. The same results were obtained at different positions of the samples' surfaces, demonstrating a high degree of thickness uniformity over a large area. Raman analyses demonstrated that MoS_2 films with nearly identical thicknesses were obtained by PLD on the sapphire and GaN/sapphire substrates.

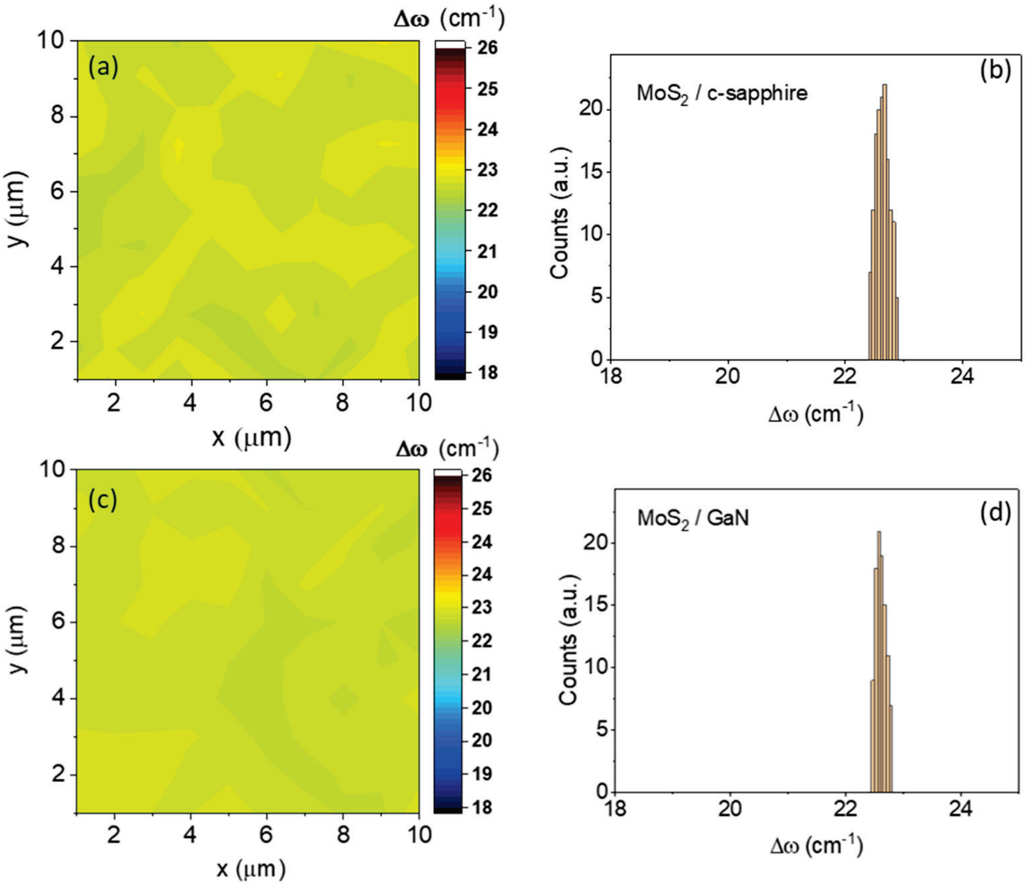

Figure 2. Raman mapping images and histograms of the differences (Δω) between the $E^1{}_{2g}$ and A_{1g} peaks collected on 10 μm × 10 μm scan areas on the MoS_2 2–3 ML in thickness and grown on c-sapphire (**a**,**b**) and (**c**,**d**) GaN/c-sapphire substrates.

High-resolution images taken in TEM mode and based on the lattice spacings show 2–3 monolayers of MoS_2 grown on c-sapphire, as well as on GaN/c-sapphire (Figures 3a and 4a). Figures 3b and 4b show cross-sectional scanning transmission electron microscopy (STEM) images taken with a high-angle annular dark field (HAADF) detector, called Z contrast. In the HAADF STEM image mode, Mo atoms, possessing a higher atomic number Z, exhibit significantly enhanced brightness, allowing for the detection of MoS_2 layers. The image in Figure 4b shows 2–3 ML of MoS_2 in close contact to GaN; there is no oxide or amorphous layer on the top of GaN.

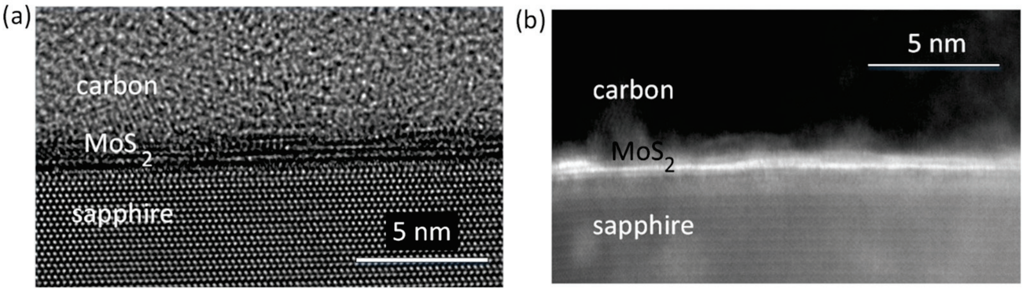

Figure 3. (**a**) HREM image in TEM mode shows 2–3 ML of the MoS_2 grown on c-sapphire. (**b**) In the HAADF STEM image mode, the Mo appears very bright (**b**).

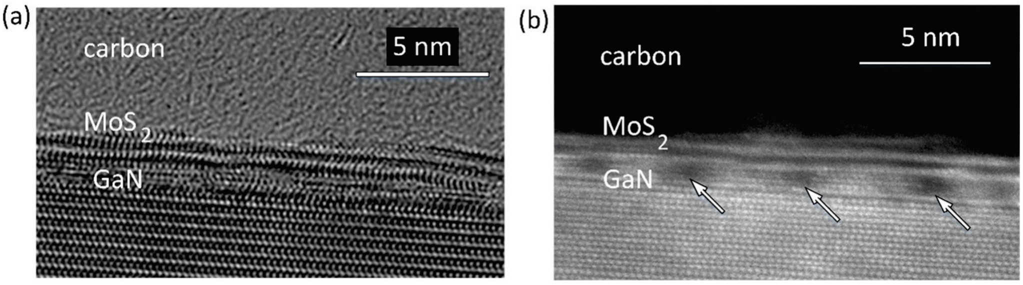

Figure 4. HREM TEM (**a**) and HAADF STEM (**b**) images of the MoS_2 2–3 ML in thickness and grown on GaN/c-sapphire. Locally, there are other small GaN islands on the surface of the perfect GaN covered by the MoS_2. The observed periodic dark spots, denoted by arrows, indicate empty voids between the islands.

However, the periodic darker regions observed inside the GaN suggest the presence of potential damage or structural imperfections.

XPS was used to measure the chemical composition and stoichiometry of the MoS_2 samples. The evaluated atomic concentrations obtained from the survey spectrum confirmed the ideal stoichiometry of the MoS_2 films grown on both types of substrates, and we registered carbon on the top of the surface originating from elements of the atmosphere and substrate (Figure 5). The Shirley background subtraction procedure was applied on the high-resolution spectra taken from the samples, and peak fitting was carried out through the selection of Gaussian–Lorentzian functions (Figure 6).

Peak deconvolutions of the spectra revealed binding energies at 228.72 eV and 231.98 eV, corresponding to Mo^{4+} $3d_{5/2}$ and $3d_{3/2}$ orbitals of 2H-MoS_2, respectively. The peak at 226.14 eV was assigned to the S 2s orbital. Additional peaks were observed from the doublet peak of MoS_2, S $2p_{3/2}$, and S $2p_{1/2}$ detected at 161.2 eV and 163.2 eV, respectively. The presence of the Mo 3d and S 2p states confirmed the formation of 2H MoS_2 [23].

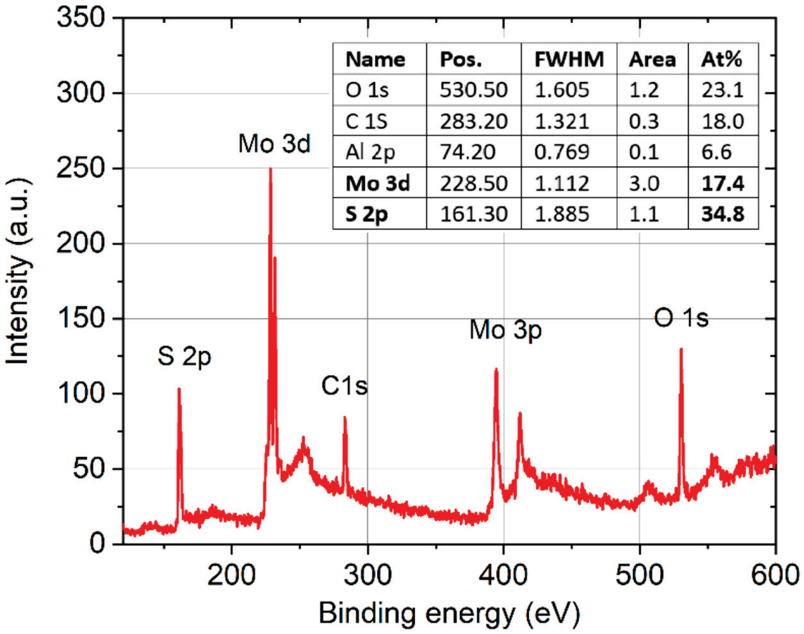

Name	Pos.	FWHM	Area	At%
O 1s	530.50	1.605	1.2	23.1
C 1S	283.20	1.321	0.3	18.0
Al 2p	74.20	0.769	0.1	6.6
Mo 3d	228.50	1.112	3.0	**17.4**
S 2p	161.30	1.885	1.1	**34.8**

Figure 5. Typical XPS survey spectrum of an MoS_2/c-sapphire. The films were deposited in a stoichiometric composition (Mo:S = 1:2) without any significant chemical shift (inset).

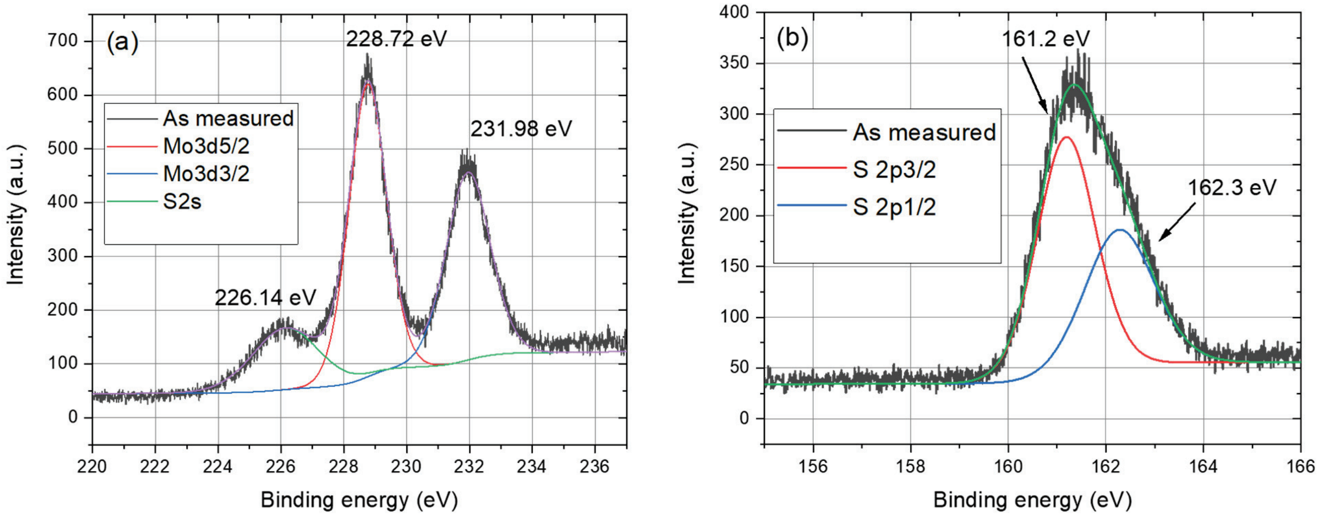

Figure 6. Deconvolutions of XPS Mo 3d (**a**) and S 2p (**b**) spectra of a 3-monolayer-thick MoS_2 grown on c-sapphire.

XRD analyses confirmed the preferential growth (with the c-axis perpendicular to the substrate plane) of the MoS_2 films grown on c-sapphire as well as on GaN/c-sapphire substrates (Figure 7a). The standard $2\theta/\omega$ diffraction pattern presented in Figure 7a reveals an extremely wide diffraction, 0002, of MoS_2. However, the rocking curves (Figure 7b) recorded at different values of 2θ around the tabulated value 14.378° were surprisingly narrow; the values of the full width at half maximum (FWHM) varied between 0.3° and 0.4°. This indicates a very strange shape of the 0002 diffraction spot, which was elongated in reciprocal space (RS) along the direction perpendicular to the sample's surface. This was confirmed by an RS map of the diffraction 0002, as shown in Figure 8. The map is presented with the dimensionless linear coordinates h and l, introduced in RS in parallel and perpendicular directions with respect to the sample's surface. They have the units $1/d_{11\bar{2}0}$ and $1/d_{0001}$, respectively, where d_{hkil} is the interplanar distance of the corresponding lattice planes $hkil$ of the GaN. The advantage of the parameters h and l is that they acquire integer values at the diffraction spots of the substrate and make the interpretation and evaluation of the measurements quite easy. Note that, for greater clarity and better insight, the horizontal dimension of the map was 15 times enlarged with respect to its actual value.

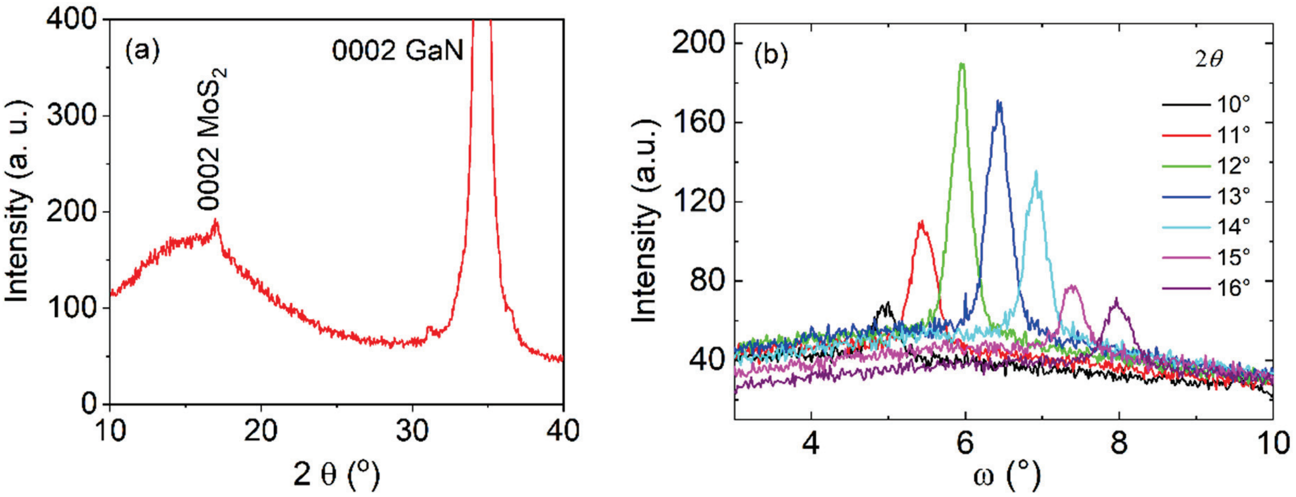

Figure 7. 2θ/ω diffraction pattern of a 5-monolayer-thick MoS_2 film deposited on GaN/c-sapphire (**a**). Rocking curves taken from the 0002 diffraction of the MoS_2 at different 2θ values (**b**). The FWHM of the rocking curves reached a value of about 0.3–0.4°. (FWHM 0002 GaN = 0.11 °).

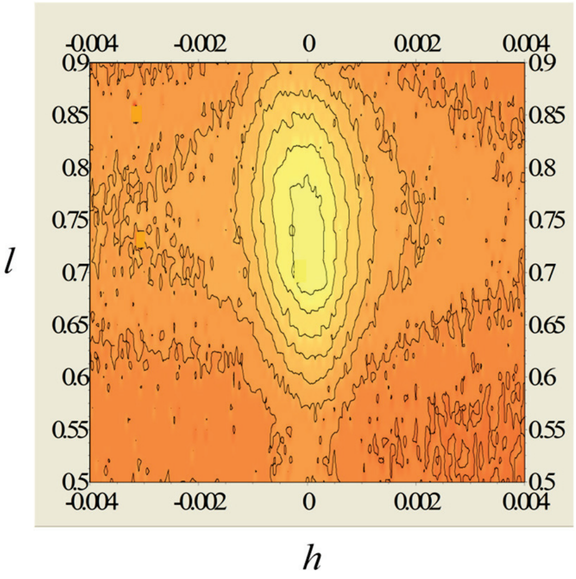

Figure 8. Reciprocal space maps around 0002 Bragg diffraction of the MoS_2 on GaN/c-sapphire for $\phi = 0°$.

The in-plane orientation relationship between the film and the substrate was examined through ϕ-scans of the strongest diffraction, $10\bar{1}3$, of the hexagonal MoS_2 (Figure 9a,b). A ϕ-scan of the $10\bar{1}4$ diffraction of the sapphire was also recorded. Six maxima of MoS_2 were detected, indicating the presence of a biaxial texture. The hexagonal MoS_2 lattice was rotated by an angle of 30° to the sapphire lattice (Figure 9a), and the crystallographic orientation can be described as MoS_2 (0001) $[10\bar{1}0] \parallel$ sapphire (0001) $[2\bar{1}\bar{1}0]$. A similar situation occurred in the case of MoS_2 grown on the GaN/c-sapphire substrate. To reveal the orientation relationship of the in-plane ordered MoS_2 with respect to the GaN/c-sapphire, the ϕ-scan from the $10\bar{1}1$ diffraction of the GaN layer was measured beside the ϕ-scan of the $10\bar{1}4$ diffraction of the sapphire (Figure 9b). In this case, the in-plane relationship between the MoS$_2$ and the GaN/c-sapphire substrate (Figure 9c) was MoS$_2$ (0001) $\left[10\bar{1}0\right]$ $\|$ GaN (0001) $\left[10\bar{1}0\right]$ $\|$ sapphire (0001) $\left[2\bar{1}\bar{1}0\right]$. To evaluate the "perfection" of the in-plane ordering, the FWHM values of the φ-scans of the $10\bar{1}3$ MoS$_2$ diffraction were estimated for the sapphire and the GaN/sapphire substrates. The obtained FWHM values were 9° and 8°, respectively, indicating the similar quality of the MoS$_2$ films grown on different substrates. For reference, the FWHMs of the φ-scans for the $10\bar{1}4$ sapphire and the $10\bar{1}1$ GaN diffractions were approximately 0.2° and 0.3°, respectively.

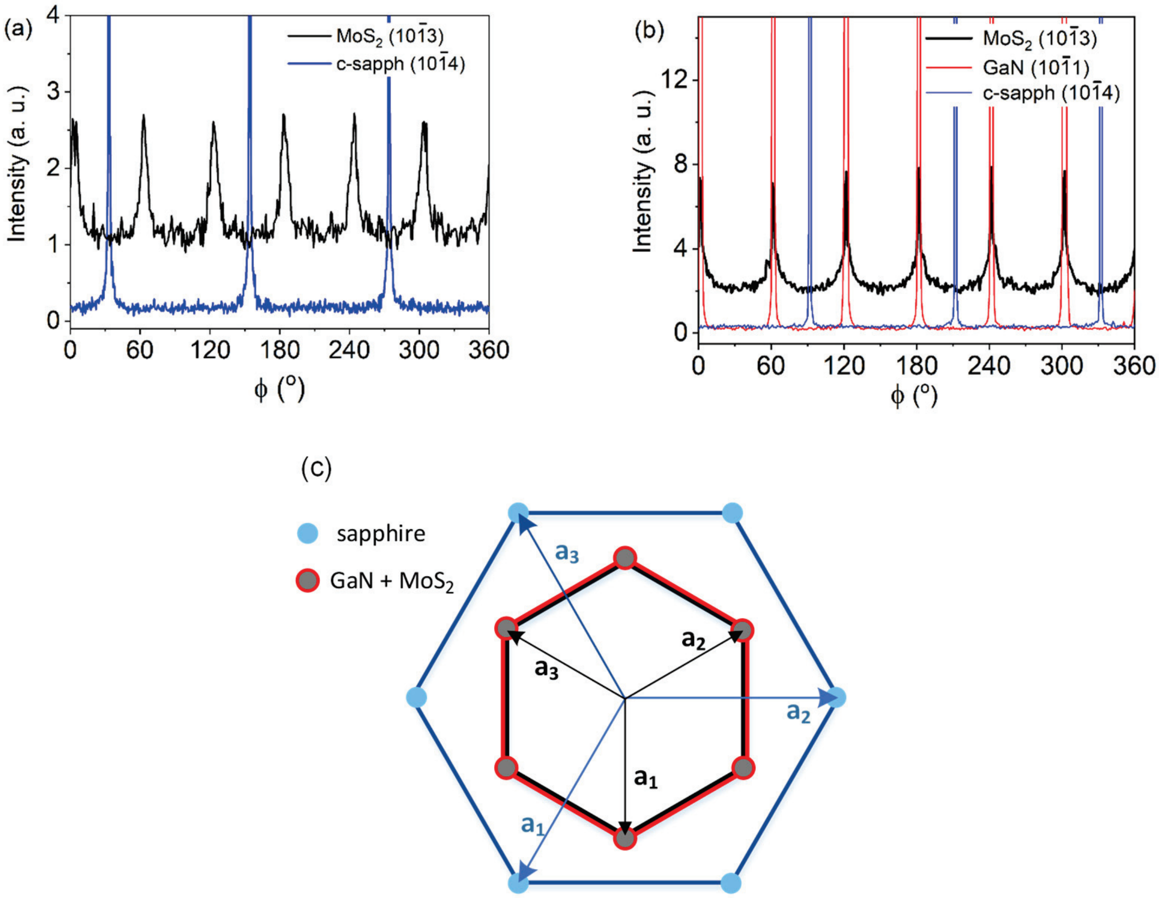

Figure 9. ϕ -scans of the $(10\bar{1}3)$ MoS$_2$ planes. In-plane ordering observed in cases of MoS$_2$ films grown on both c-sapphire (**a**) and GaN/c-sapphire (**b**) substrates. Schematic representation of the orientation relationship between c-plane sapphire, GaN, and MoS$_2$. Vectors $\mathbf{a_1}$, $\mathbf{a_2}$, and $\mathbf{a_3}$ represent crystallographic axes in the (0001) plane of the sapphire, the GaN and MoS$_2$ lattice (**c**).

Electrical characterizations were finally carried out on the MoS$_2$ films grown on the sapphire and GaN/sapphire substrates. Firstly, the sheet resistance, carrier density, and mobility of PLD-grown MoS$_2$ on the insulating sapphire substrate were evaluated by four-point probe and Hall effect measurements in the van der Pauw configuration (see the schematic in Figure 10a). After preliminarily checking that the as-deposited Ni/Au pads provided Ohmic contacts onto MoS$_2$ (see the insert in Figure 10b), the temperature dependence of the sheet resistance (R_{sh}) was evaluated in a range from T = 300 to 500 K. As illustrated in Figure 10b, a monotonic decrease in R_{sh} from ≈375 kΩ/sq to ≈150 kΩ/sq was observed with the increase in temperature in this range, as is consistent with the expected semiconducting behavior of the MoS$_2$ film. Furthermore, the Hall effect measurements, with an applied magnetic field B = 1000 G, showed an increase in the sheet electron density from $n_s \approx 1 \times 10^{13}$ cm^{-2} to $n_s \approx 3.4 \times 10^{13}$ cm^{-2}. This was in the same temperature range (Figure 10c, left axis) that was ascribed to the ionization of shallow donors with energy levels located below the MoS$_2$ conduction band. To evaluate the ionization energy E_i of these donor levels (i.e., their energy distance from the bottom of the conduction band $E_i = E_c - E_D$), we employed the neutrality equation for the approximation of a highly n-type doped semiconductor with a low level of acceptor compensation ($N_D >> N_A$) [24]:

$$n_s \approx \sqrt{\frac{N_D N_c}{2}} \exp\left(-\frac{E_i}{2k_B T}\right) \propto T^{\frac{3}{4}} \exp\left(-\frac{E_i}{2k_B T}\right) \quad (1)$$

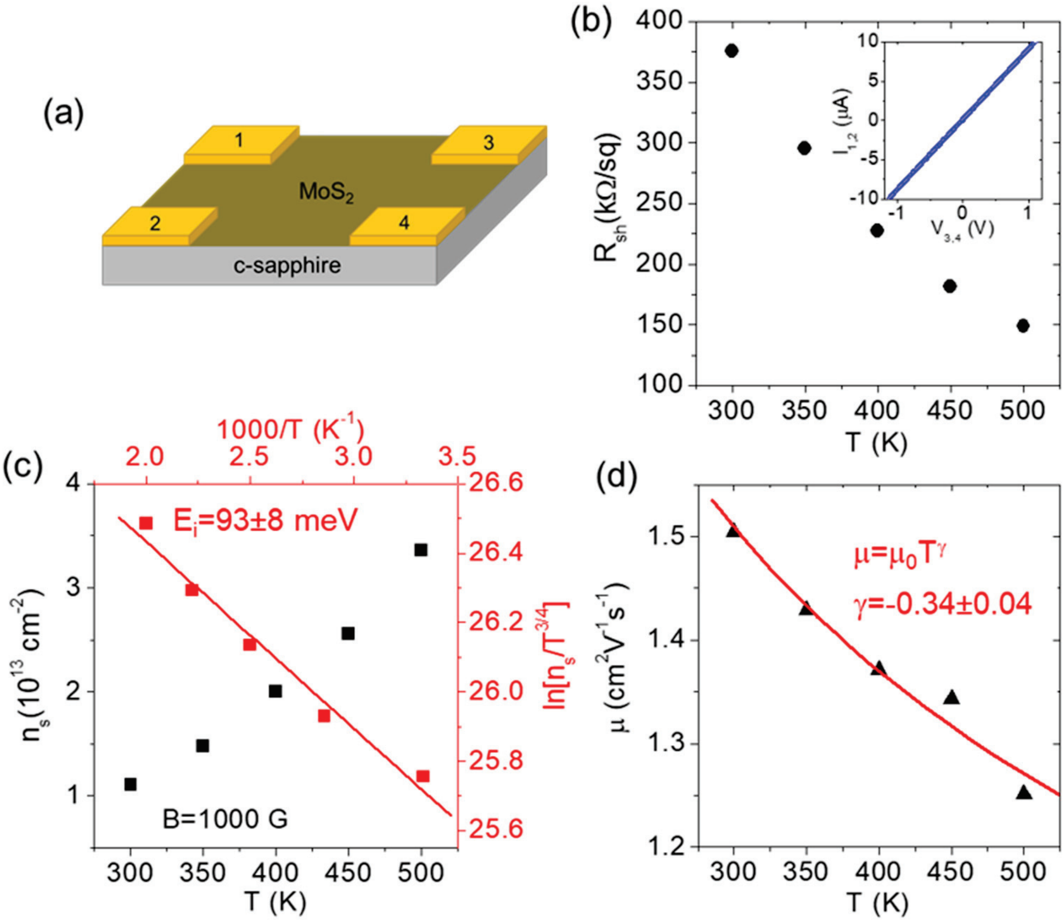

Figure 10. Schematic of the van der Pauw structure used for sheet resistance and Hall effect measurement on the PLD-grown MoS_2 film on a sapphire substrate (**a**). Temperature-dependent sheet resistance R_{sh} measurement. The ohmic behavior of the as-deposited Ni/Au contacts at the four corners of the MoS_2 film is shown in the insert (**b**). Sheet electron density n_s as a function of the temperature T evaluated by Hall effect measurements, with a magnetic field B = 1000 G. Red symbols show the Arrhenius plot of $\ln[n_s/T^{3/4}]$ (right scale) vs. 1000/T (upper scale). The linear fit (red line) from which the ionization energy $E_i = 93 \pm 3$ meV of the donor levels responsible for n-type doping in PLD-grown MoS_2 was evaluated (**c**). Hall electron mobility is represented by μ as a function of temperature T, and fits with the relation $\mu = \mu_0 T^{\gamma}$, from which $\gamma \approx -0.34$ was evaluated (**d**).

Here, k_B is the Boltzmann constant, N_D is the donor density, and N_C is the effective electron density in the MoS_2 conduction band, which depends on the temperature as $N_c \propto T^{3/2}$. Such an approximation of a negligible compensation is justified, in part, by the nearly ideal stoichiometry of the PLD-grown MoS_2, without any MoO_3 contributions, as was deduced from the XPS analyses shown in Figures 5 and 6. In fact, MoO_3 residues in the deposited films have recently been demonstrated to act with p-type doping levels, causing a significant compensation for the natural n-type doping of MoS_2 [25]. Based on Equation (1), an Arrhenius plot of $\ln[n_s T^{-3/4}]$ vs. 1000/T is provided in right and top axis of Figure 10c, and the ionization energy $E_i = 93 \pm 8$ meV was obtained from the slope of the linear fit.

Finally, the temperature dependence of the electron mobility μ was evaluated from the combination of the R_{sh} and n_s results, according to the relation $\mu = 1/(qn_sR_{sh})$. A slight decrease in μ from ≈ 1.5 cm^{2}V^{-1}s^{-1} to ≈ 1.25 cm^{2}V^{-1}s^{-1} was observed by increasing T from 300 to 500 K, as illustrated in Figure 10d. To obtain a deeper insight into the scattering mechanisms responsible for this decreasing trend in mobility, a fitting of the experimental data with the power function:

$$\mu = \mu_0 T^{\gamma} \tag{2}$$

was also carried out (red line in Figure 10d), from which a value of the exponent $\gamma = -0.34 \pm 0.04$ was deduced. According to the literature results, the electron mobility in MoS_2 films is limited by two main scattering mechanisms depending on the sample temperature, i.e., the charged impurity scattering (which dominates at lower temperatures) and phonon scattering (which dominates at higher temperatures). Both the charged-impurities-limited mobility (μ_{CI}) and phonon-limited mobility (μ_{ph}) contributions are typically described by a power function of the temperature T (see Equation (2)), with positive and negative γ values, respectively [26]. In particular, the theoretically predicted values of γ for optical-phonon-limited mobility could range from $\gamma = -1.69$ for monolayer MoS_2 to $\gamma = -2.6$ for bulk crystals [27]. Clearly, the negative value of $\gamma = -0.34$, obtained by fitting of the experimental results, was significantly lower than these theoretical expectations. This indicates that, although phonon scattering played an important role, other competitive mechanisms contributed to limiting the electron mobility of our PLD-grown MoS_2. These may include not only charged impurity scattering, but also scattering by defects (such as grain boundaries of MoS_2 domains), which can account for this lower temperature dependence of electron mobility.

After investigating the lateral current transport in the thin MoS_2 films supported by the insulating sapphire substrate, we evaluated the vertical current injection across the 2D/3D semiconductor heterojunction formed by n-type MoS_2 with n-type GaN. To this aim, local current-voltage (I-V_{tip}) characteristics were acquired by applying a dc bias ramp between a nanometric-sized (r_{tip} = 5nm) Pt-coated AFM tip in contact with MoS_2 and a large metal contact, consisting of a Ni(20 nm)/Au(80 nm) stack, deposited on the bare GaN surface, as is schematically illustrated in the inset of Figure 11a. This Ni/Au stack was not subjected to any thermal annealing in order to avoid the eventual structural modification of MoS_2. In this configuration, for geometric reasons, the I-V characteristics were sensitive to local current injection through the Pt/MoS_2/GaN vertical heterojunction, whereas current flow in the GaN layer and through the large metal contact introduced a series resistance contribution. Figure 11a shows a set of four I-V characteristics collected at different positions on the deposited MoS_2 film. All of the curves exhibited rectifying behavior, with negligible current under negative polarization and current onset at the same forward bias. These characteristics are very reproducible under negative and small positive bias (V_{tip} < 1V), indicating the high uniformity of the MoS_2/GaN heterostructure. The main difference can be observed at a higher positive bias, which is related to series resistance contributions. A representative I-V curve is presented on a semi-log scale at a low forward bias in Figure 11b, from which a linear increase in the current over two orders of magnitude can be observed from V = 0 to 0.25 V. This is followed by a bending, which is associated with series resistance. In this low-bias regime, we can assume that current injection from the Pt tip to MoS_2 can be ruled by direct tunneling (assumption justified by the high doping of MoS_2 deduced in Figure 10c), whereas the MoS_2 heterojunction with n-GaN can be described as a Schottky junction using the thermionic emission equation:

$$I = A^* A_{tip} \exp\left(-\frac{q\phi_B}{k_B T}\right) \exp\left(\frac{qV_{tip}}{nk_B T}\right) \tag{3}$$

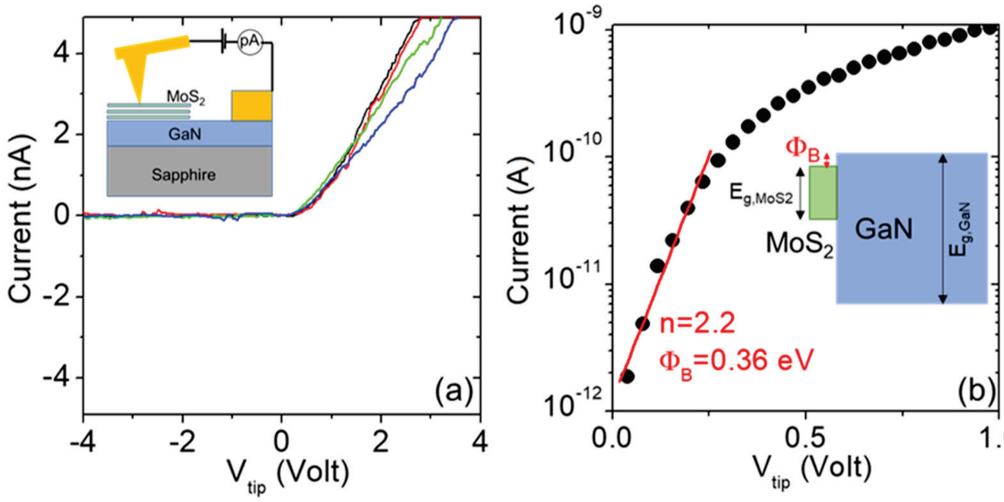

Figure 11. (**a**) Local I-V_{tip} characteristics collected by C-AFM at different positions on the MoS_2/GaN heterostructures. Insert: schematic of the C-AFM setup for local current measurements. (**b**) Semi-log scale plot of a representative I-V_{tip} characteristic in the low-forward-bias regime, and fitting with the thermionic emission equation. Insert: schematic band diagram of the MoS_2/GaN heterojunction.

In this equation, A_{tip} is the tip contact area, $A^* = 26.9$ A cm^{-2} K^{-2} is the Richardson constant of GaN, k_B is the Boltzmann constant, ϕ_B is the Schottky barrier height at the MoS_2/GaN interface, and n is the ideality factor. In particular, a value of n = 2.2 was extracted from the slope of the linear fit in Figure 11b, and a barrier height of $\phi_B = 0.36$ eV was evaluated from the intercept with the current axis. This ϕ_B value corresponds to a small conduction band discontinuity between n-type MoS_2 and n-GaN, as is consistent with the results reported in several recent investigations of this heterostructure [28,29]. The deviation of the ideality factor from n = 1 indicates the presence of non-idealities at the heterojunction.

4. Conclusions

In summary, we grew large-area epitaxial MoS_2 films from 2 to 5 monolayers thick on c-sapphire and on GaN/c-sapphire substrates by means of pulsed laser deposition. The high thickness uniformity of the MoS_2 was demonstrated by Raman intensity mapping. The atomic concentrations determined from the XPS survey spectrum confirmed the ideal stoichiometry of the films. The $2\theta/\omega$ diffraction revealed the growth of the MoS_2 with the c-axis perpendicular to the substrate plane, and the FWHM values measured on the 0002 MoS_2 diffraction were in the range of 0.3–0.4°. The ϕ-scan measurements showed a high degree of in-plane ordering in both the MoS_2 films grown on c-sapphire as well as on GaN/c-sapphire substrates. Temperature-dependent characterization of the sheet resistance, carrier density, and mobility on MoS_2 deposited on the sapphire substrate provided insights into the current transport mechanisms in these ultra-thin films, such as the ionization energy of the donors and the scattering phenomena limiting carrier mobility. Finally, we used C-AFM to measure the vertical current across the MoS_2/GaN heterojunctions and observed a rectifying I-V behavior, with a low Schottky barrier of $\phi_B = 0.36$ eV, which was estimated by fitting these curves under forward polarization of the tip. Current–voltage characteristics collected at different positions on the film indicated the high uniformity of the MoS_2/GaN heterostructure. The obtained results represent significant progress in the advancement of large-area device fabrication and application.

Author Contributions: Conceptualization, M.Š. and Š.C.; writing—original draft, M.Š. and F.G.; writing—review and editing, M.Š., E.D., B.P. and Y.C.; investigation, E.D., L.P.S., M.T., M.G., B.P., A.K., G.G., S.E.P., P.F. and E.F.; formal analysis, M.T., G.G., S.E.P. and P.F.; project administration, F.R. and F.G.; funding acquisition, Š.C., B.P. and F.G. All authors have read and agreed to the published version of the manuscript.

Funding: These results were achieved within the Project "ETMOS—Epitaxial Transition Metal dichalcogenides Onto wide bandgap hexagonal Semiconductors for advanced electronics". The work was also supported by the Slovak Grant Agency for Science, VEGA 2/0140/22, Slovak Research and Development Agency, APVV-19-0303. F.G. and B.P. acknowledge funding for travel from the CNR/HAS (2023-25) bilateral project GHOST-III. B.P. thanks the financial support of NKFIH TKP2021-NKTA-05. F.G. acknowledges funding from MUR under the PRIN project "2DIntegratE" (2022RHRZN2).

Data Availability Statement: The data are available upon reasonable request from the corresponding author.

Conflicts of Interest: The authors declare no conflict of interest.

References

1. Mak, K.F.; Lee, C.; Hone, J.; Shan, J.; Heinz, T.F. Atomically Thin MoS 2: A New Direct-Gap Semiconductor. *Phys. Rev. Lett.* **2010**, *105*, 136805. [CrossRef]
2. Wang, Q.H.; Kalantar-Zadeh, K.; Kis, A.; Coleman, J.N.; Strano, M.S. Electronics and Optoelectronics of Two-Dimensional Transition Metal Dichalcogenides. *Nat. Nanotechnol.* **2012**, *7*, 699–712. [CrossRef] [PubMed]
3. Baugher, B.W.H.; Churchill, H.O.H.; Yang, Y.; Jarillo-Herrero, P. Optoelectronic Devices Based on Electrically Tunable p–n Diodes in a Monolayer Dichalcogenide. *Nat. Nanotechnol.* **2014**, *9*, 262–267. [CrossRef] [PubMed]
4. Ugeda, M.M.; Bradley, A.J.; Shi, S.-F.; da Jornada, F.H.; Zhang, Y.; Qiu, D.Y.; Ruan, W.; Mo, S.-K.; Hussain, Z.; Shen, Z.-X.; et al. Giant Bandgap Renormalization and Excitonic Effects in a Monolayer Transition Metal Dichalcogenide Semiconductor. *Nat. Mater.* **2014**, *13*, 1091–1095. [CrossRef]
5. Radisavljevic, B.; Kis, A. Mobility Engineering and a Metal–Insulator Transition in Monolayer MoS2. *Nat. Mater.* **2013**, *12*, 815–820. [CrossRef] [PubMed]
6. Splendiani, A.; Sun, L.; Zhang, Y.; Li, T.; Kim, J.; Chim, C.-Y.; Galli, G.; Wang, F. Emerging Photoluminescence in Monolayer MoS $_2$. *Nano Lett.* **2010**, *10*, 1271–1275. [CrossRef] [PubMed]
7. Lee, C.; Yan, H.; Brus, L.E.; Heinz, T.F.; Hone, J.; Ryu, S. Anomalous Lattice Vibrations of Single- and Few-Layer MoS $_2$. *ACS Nano* **2010**, *4*, 2695–2700. [CrossRef]
8. Coleman, J.N.; Lotya, M.; O'Neill, A.; Bergin, S.D.; King, P.J.; Khan, U.; Young, K.; Gaucher, A.; De, S.; Smith, R.J.; et al. Two-Dimensional Nanosheets Produced by Liquid Exfoliation of Layered Materials. *Science* **2011**, *331*, 568–571. [CrossRef]
9. Lee, Y.-H.; Zhang, X.-Q.; Zhang, W.; Chang, M.-T.; Lin, C.-T.; Chang, K.-D.; Yu, Y.-C.; Wang, J.T.-W.; Chang, C.-S.; Li, L.-J.; et al. Synthesis of Large-Area MoS_2 Atomic Layers with Chemical Vapor Deposition. *Adv. Mater.* **2012**, *24*, 2320–2325. [CrossRef]
10. Yu, Y.; Li, C.; Liu, Y.; Su, L.; Zhang, Y.; Cao, L. Controlled Scalable Synthesis of Uniform, High-Quality Monolayer and Few-Layer MoS2 Films. *Sci. Rep.* **2013**, *3*, 1866. [CrossRef]
11. Liu, H.; Ansah Antwi, K.K.; Ying, J.; Chua, S.; Chi, D. Towards Large Area and Continuous MoS_2 Atomic Layers via Vapor-Phase Growth: Thermal Vapor Sulfurization. *Nanotechnology* **2014**, *25*, 405702. [CrossRef]
12. Serrao, C.R.; Diamond, A.M.; Hsu, S.-L.; You, L.; Gadgil, S.; Clarkson, J.; Carraro, C.; Maboudian, R.; Hu, C.; Salahuddin, S. Highly Crystalline MoS_2 Thin Films Grown by Pulsed Laser Deposition. *Appl. Phys. Lett.* **2015**, *106*, 052101. [CrossRef]
13. Siegel, G.; Venkata Subbaiah, Y.P.; Prestgard, M.C.; Tiwari, A. Growth of Centimeter-Scale Atomically Thin MoS_2 Films by Pulsed Laser Deposition. *APL Mater.* **2015**, *3*, 056103. [CrossRef]
14. Ho, Y.-T.; Ma, C.-H.; Luong, T.-T.; Wei, L.-L.; Yen, T.-C.; Hsu, W.-T.; Chang, W.-H.; Chu, Y.-C.; Tu, Y.-Y.; Pande, K.P.; et al. Layered MoS_2 Grown on *c* -Sapphire by Pulsed Laser Deposition. *Phys. Status Solidi RRL Rapid Res. Lett.* **2015**, *9*, 187–191. [CrossRef]
15. Baliga, B.J. Gallium Nitride Devices for Power Electronic Applications. *Semicond. Sci. Technol.* **2013**, *28*, 074011. [CrossRef]
16. Fletcher, A.S.A.; Nirmal, D. A Survey of Gallium Nitride HEMT for RF and High Power Applications. *Superlattices Microstruct.* **2017**, *109*, 519–537. [CrossRef]
17. Giannazzo, F.; Panasci, S.E.; Schilirò, E.; Greco, G.; Roccaforte, F.; Sfuncia, G.; Nicotra, G.; Cannas, M.; Agnello, S.; Frayssinet, E.; et al. Atomic Resolution Interface Structure and Vertical Current Injection in Highly Uniform MoS_2 Heterojunctions with Bulk GaN. *Appl. Surf. Sci.* **2023**, *631*, 157513. [CrossRef]
18. Ruzmetov, D.; Zhang, K.; Stan, G.; Kalanyan, B.; Bhimanapati, G.R.; Eichfeld, S.M.; Burke, R.A.; Shah, P.B.; O'Regan, T.P.; Crowne, F.J.; et al. Vertical 2D/3D Semiconductor Heterostructures Based on Epitaxial Molybdenum Disulfide and Gallium Nitride. *ACS Nano* **2016**, *10*, 3580–3588. [CrossRef]
19. O'Regan, T.P.; Ruzmetov, D.; Neupane, M.R.; Burke, R.A.; Herzing, A.A.; Zhang, K.; Birdwell, A.G.; Taylor, D.E.; Byrd, E.F.C.; Walck, S.D.; et al. Structural and Electrical Analysis of Epitaxial 2D/3D Vertical Heterojunctions of Monolayer MoS_2 on GaN. *Appl. Phys. Lett.* **2017**, *111*, 051602. [CrossRef]
20. Lee, E.W.; Lee, C.H.; Paul, P.K.; Ma, L.; McCulloch, W.D.; Krishnamoorthy, S.; Wu, Y.; Arehart, A.R.; Rajan, S. Layer-Transferred MoS_2/GaN PN Diodes. *Appl. Phys. Lett.* **2015**, *107*, 103505. [CrossRef]
21. Moun, M.; Kumar, M.; Garg, M.; Pathak, R.; Singh, R. Understanding of MoS2/GaN Heterojunction Diode and Its Photodetection Properties. *Sci. Rep.* **2018**, *8*, 11799. [CrossRef] [PubMed]

22. Frayssinet, E.; Beaumont, B.; Faurie, J.P.; Gibart, P.; Makkai, Z.; Pécz, B.; Lefebvre, P.; Valvin, P. Micro Epitaxial Lateral Overgrowth of GaN/Sapphire by Metal Organic Vapour Phase Epitaxy. *MRS Internet J. Nitride Semicond. Res.* **2002**, *7*, e8. [CrossRef]
23. Ganta, D.; Sinha, S.; Haasch, R.T. 2-D Material Molybdenum Disulfide Analyzed by XPS. *Surf. Sci. Spectra* **2014**, *21*, 19–27. [CrossRef] [PubMed]
24. Sze, S.M.; Ng, K.K. *Physics of Semiconductor Devices*, 1st ed.; Wiley: Hoboken, NJ, USA, 2006; ISBN 978-0-471-14323-9.
25. Giannazzo, F.; Panasci, S.E.; Schilirò, E.; Roccaforte, F.; Koos, A.; Nemeth, M.; Pécz, B. Esaki Diode Behavior in Highly Uniform MoS_2 /Silicon Carbide Heterojunctions. *Adv. Mater. Interfaces* **2022**, *9*, 2200915. [CrossRef]
26. Tu, H.-W.; Shih, C.-C.; Lin, C.-L.; Yu, M.-Z.; Lai, J.-J.; Luo, J.-C.; Lin, G.-L.; Jian, W.-B.; Watanabe, K.; Taniguchi, T.; et al. High Field-Effect Performance and Intrinsic Scattering in the Two-Dimensional MoS2 Semiconductors. *Appl. Surf. Sci.* **2021**, *564*, 150422. [CrossRef]
27. Baugher, B.W.H.; Churchill, H.O.H.; Yang, Y.; Jarillo-Herrero, P. Intrinsic Electronic Transport Properties of High-Quality Monolayer and Bilayer MoS_2. *Nano Lett.* **2013**, *13*, 4212–4216. [CrossRef]
28. Tangi, M.; Mishra, P.; Ng, T.K.; Hedhili, M.N.; Janjua, B.; Alias, M.S.; Anjum, D.H.; Tseng, C.-C.; Shi, Y.; Joyce, H.J.; et al. Publisher's Note: "Determination of Band Offsets at GaN/Single-Layer MoS2 Heterojunction" [Appl. Phys. Lett. **109**, 032104 (2016)]. *Appl. Phys. Lett.* **2016**, *109*, 079901. [CrossRef]
29. Zhang, Z.; Qian, Q.; Li, B.; Chen, K.J. Interface Engineering of Monolayer MoS_2 /GaN Hybrid Heterostructure: Modified Band Alignment for Photocatalytic Water Splitting Application by Nitridation Treatment. *ACS Appl. Mater. Interfaces* **2018**, *10*, 17419–17426. [CrossRef]

nanomaterials

Article

Electronic and Optical Properties of 2D Heterostructure Bilayers of Graphene, Borophene and 2D Boron Carbides from First Principles

Lu Niu [1], Oliver J. Conquest [1,*], Carla Verdi [1,2] and Catherine Stampfl [1,*]

[1] School of Physics, The University of Sydney, Sydney, NSW 2006, Australia
[2] School of Mathematics and Physics, The University of Queensland, Brisbane, QLD 4072, Australia
* Correspondence: oliver.conquest@sydney.edu.au (O.J.C.); catherine.stampfl@sydney.edu.au (C.S.)

Abstract: In the present work the atomic, electronic and optical properties of two-dimensional graphene, borophene, and boron carbide heterojunction bilayer systems (Graphene–BC_3, Graphene–Borophene and Graphene–B_4C_3) as well as their constituent monolayers are investigated on the basis of first-principles calculations using the HSE06 hybrid functional. Our calculations show that while borophene is metallic, both monolayer BC_3 and B_4C_3 are indirect semiconductors, with band-gaps of 1.822 eV and 2.381 eV as obtained using HSE06. The Graphene–BC_3 and Graphene–B_4C_3 bilayer heterojunction systems maintain the Dirac point-like character of graphene at the K-point with the opening of a very small gap (20–50 meV) and are essentially semi-metals, while Graphene–Borophene is metallic. All bilayer heterostructure systems possess absorbance in the visible region where the resonance frequency and resonance absorption peak intensity vary between structures. Remarkably, all heterojunctions support plasmons within the range 16.5–18.5 eV, while Graphene–B_4C_3 and Graphene–Borophene exhibit a π-type plasmon within the region 4–6 eV, with the latter possessing an additional plasmon at the lower energy of 1.5–3 eV. The dielectric tensor for Graphene–B_4C_3 exhibits complex off-diagonal elements due to the lower P3 space group symmetry indicating it has anisotropic dielectric properties and could exhibit optically active (chiral) effects. Our study shows that the two-dimensional heterostructures have desirable optical properties broadening the potential applications of the constituent monolayers.

Keywords: graphene; borophene; BC_3; B_4C_3; two-dimensional; heterostructure; van der Waals; DFT; optical; dielectric

1. Introduction

Graphene is well-known to have excellent electrical conductivity, desirable mechanical and thermal properties, and high light transmittance in the visible light–infrared region. It also has an extremely high quantum efficiency for light-matter interactions and is strongly optically nonlinear. It has therefore found applications in e.g., electronics, energy storage, biomedical and other fields [1]. Relative to conventional plasmonic materials, graphene possesses highly confined plasmons with much longer lifetimes. Also, graphene plasmons are active in an extended wavelength range, namely, the mid-infrared and terahertz regime. This wavelength range overlaps with the feature signals of most organic and biomolecules, which has broadened graphene's applications towards plasmonic biological and chemical sensors [2] in addition to plasmonic waveguides, and infrared photodetectors. Moreover, the properties can be tuned by forming graphene-hybrid materials, finding applications in biosensors, chemical sensors, optical sensors, and other types of sensors [3].

In other areas, however, the use of graphene has been limited due to its zero-value band gap. One of the methods used to expand the application of graphene is to form heterostructures. Stacking different two-dimensional (2D) materials together can form double-layer or even multi-layer artificial materials that are maintained by van der Waals interactions [4]. Such materials are known as van der Waals heterojunctions. A wide range of physical properties can be obtained by such stacking, making van der Waals heterojunctions even more important than the 2D material itself. There are vast numbers of 2D materials, and with forming heterostructures thereof, a diverse range of electrical, photonic, plasmonic, mechanical, and chemical properties can be theoretically predicted through ab initio calculations and machine learning [5,6], and experimentally engineered [7,8].

Recently, the prospect of developing plasmonic devices employing 2D semiconductors has attracted considerable attention [9,10]. Plasmonic modes in each class of van der Waals semiconductors have their own peculiarities, along with potential technological capabilities. Recently, graphene-like BC_3 has been synthesized experimentally [11–13] and is found to be semiconducting with an indirect band gap. Calculations have shown that nanostructures of graphene-like BC_3 possess desirable absorbance in the visible region and by changing the size of the nanostructure, the resonance peak position of the absorption spectrum can be effectively regulated [14]. Recent studies have also predicted a stable B_4C_3 monolayer which is even more stable than the previously synthesized BC_3 monolayer [15]. Boron carbides are known for their exceptional hardness, thermal stability, and chemical inertness. The emergence of 2D boron carbides adds a new dimension to the study of these materials, offering novel properties and opportunities for technological innovation [16,17].

Borophene is another 2D material of high current interest. This monolayer allotrope of boron forms several structures and is characterized by its unique atomic structure and exceptional electronic properties, which has opened new avenues for innovation in the areas of electronics, energy storage, catalysis, plasmonics, superconductivity, and sensors [11]. One particularly intriguing aspect of borophene's versatility lies in its ability to form heterojunctions—interfaces between different borophene structures or between borophene and other materials. Borophene-graphene heterostructures have been realized [18] where they have shown good stability and ability to function as a humidity sensor, exhibiting a sensitivity about 700 times higher than that of pristine graphene, and 27 times higher than that of borophene. Also, recently both lateral and vertical integration of borophene with graphene has been achieved [19], as has the formation of bi-layer (α-phase) borophene on the Ag(111) surface [20].

The synergistic combination of graphene's exceptional electrical conductivity, mechanical strength, and flexibility with boron carbide's high hardness, thermal stability, and chemical resistance, and with borophene's attractive electronic properties, hold tremendous potential for a wide range of applications spanning from electronics and optoelectronics to energy storage and sensing. As research in this field continues to advance, the development of scalable synthesis methods, the elucidation of structure-property relationships, and the exploration of novel applications will be key focal points. To date, there is little known about the physical properties of graphene-based bilayer heterojunctions with borophene and boron-carbide materials. This motivates the present work to gain an understanding of these heterojunctions, through the study of their electronic and optical properties on the basis of first-principles calculations. Such understanding is crucial for their future technological application, where the unique properties of these materials can be harnessed.

The paper is organised as follows: in Section 2 the calculation method is described, followed by the Results and Discussion in Section 3. Herein we describe the physical properties of the monolayers and heterostructures, including band structure, density of states, electron density difference distributions, Schottky barriers and the optical properties. This is followed by the Conclusions in Section 4.

2. Calculation Method

We perform first-principle calculations using density functional theory (DFT) as implemented in the Vienna Ab initio Simulation Package (VASP) [21–23]. The projector augmented wave (PAW) method pseudopotentials are used to account for the electron-ion interactions [24]. For the structural optimization calculations, we use the generalized gradient approximation (GGA) of Perdew-Burke-Ernzerhof (PBE) as the exchange-correlation functional [25]. The Becke-Johnson damped D3(BJ) dispersion correction is also included to account for long-range van der Waals (vdW) interactions [26–28]. A Γ-centered **k**-point sampling mesh of 11 × 11 × 1 (23 × 23 × 1 for the smaller graphene unit cell, see Figure S1) and a plane wave energy cutoff of 450 eV are used. Electronic convergence criteria are set to 10^{-6} eV and systems are allowed to relax until all forces on each atom are below 0.01 eV/Å. For smearing of the electronic states we used the Gaussian smearing method implemented in VASP.

For the calculation of electronic properties, the PBE exchange-correlation functional is known to underestimate band-gap energies so we also use the screened hybrid exchange-correlation functional of Heyd, Scuseria, and Ernzerhof (HSE06) which gives more accurate band-gap energies [29–31]. All density of states (DOS) calculations use a Γ-centered **k**-point sampling mesh of 33 × 33 × 1 and Gaussian smearing of the electronic states with a broadening value of 0.1 eV. The HSE06 exchange-correlation functional is also used for the calculation of optical properties, in particular, the frequency-dependent dielectric function with a Γ-centered **k**-point sampling mesh of 17 × 17 × 1 and 65 × 65 × 1. The complex frequency-dependent dielectric function, $\epsilon(\omega)$, is given by Equation (1), where $\epsilon_1(\omega)$ and $\epsilon_2(\omega)$ are the real and imaginary parts, respectively, and ω is the frequency in eV:

$$\epsilon(\omega) = \epsilon_1(\omega) + i\epsilon_2(\omega) \tag{1}$$

In Equation (1) the imaginary part of the dielectric function, $\epsilon_2(\omega)$, is given by:

$$\epsilon_2(\omega) = \mathrm{Im}\,\epsilon_{\alpha\beta}(\omega) = \frac{4\pi^2 e^2}{\Omega} \lim_{q\to 0} \frac{1}{q^2} \sum_{c,v,\mathbf{k}} 2\omega_{\mathbf{k}}\delta(E_{c\mathbf{k}} - E_{v\mathbf{k}} - \omega) \times \langle \mu_{c\mathbf{k}+\mathbf{e}_\alpha q} | \mu_{v\mathbf{k}} \rangle \langle \mu_{v\mathbf{k}} | \mu_{c\mathbf{k}+\mathbf{e}_\beta q} \rangle \tag{2}$$

where **k** is the electron wavevector, $\omega_{\mathbf{k}}$ is the **k**-point weight, q is the Bloch vector for the incident wave and Ω is the unit cell volume [32,33]. Here v and c are the valence and conduction bands indices, respectively. The $\mu_{v\mathbf{k}/c\mathbf{k}}$ terms are the cell periodic parts of the orbitals and $\mathbf{e}_{\alpha/\beta}$ are the unit vectors for the three Cartesian directions. Lastly, $E_{c\mathbf{k}}$ is the c^{th} conduction band energy and $E_{v\mathbf{k}}$ is the v^{th} valence band energy.

The real part of the dielectric function is obtained by applying the Kramers-Kronig transformation to the imaginary part of the dielectric function in Equation (2):

$$\epsilon_1(\omega) = \mathrm{Re}\,\epsilon_{\alpha\beta}(\omega) = \delta_{\alpha\beta} + \frac{2}{\pi} P \int_0^\infty \mathrm{d}\omega' \frac{\omega' \epsilon_2(\omega')}{\omega'^2 - \omega^2 + i\eta} \tag{3}$$

where P is the principal value and η (here $\eta = 0.1$) is the complex shift.

Using the dielectric function we also calculate the absorption coefficient, $\alpha(\omega)$, given in Equation (4), where c is the speed of light.

$$\alpha(\omega) = \frac{\sqrt{2}\omega}{c} \left[\left(\epsilon_1^2(\omega) + \epsilon_2^2(\omega) \right)^{\frac{1}{2}} - \epsilon_1(\omega) \right]^{\frac{1}{2}} \tag{4}$$

The loss function, $L(\omega)$, is calculated using the expression:

$$L(\omega) = \frac{\epsilon_2(\omega)}{\epsilon_1^2(\omega) + \epsilon_2^2(\omega)} \tag{5}$$

For the calculation of the refractive index $n(\omega)$, extinction coefficient $k(\omega)$ and reflectivity $R(\omega)$ we use Equations (6), (7) and (8), respectively. In Equation (8), n is the refractive index and k is the extinction coefficient.

$$n(\omega) = \left[\frac{\sqrt{\epsilon_1^2 + \epsilon_2^2} + \epsilon_1}{2} \right]^{\frac{1}{2}} \tag{6}$$

$$k(\omega) = \left[\frac{\sqrt{\epsilon_1^2 + \epsilon_2^2} - \epsilon_1}{2} \right]^{\frac{1}{2}} \quad (7)$$

$$R(\omega) = \frac{(n-1)^2 + k^2}{(n+1)^2 + k^2} \quad (8)$$

We note that the dielectric tensor contains the combined dielectric response of the 2D material and the vacuum so that the magnitude of ϵ_1 and ϵ_2 depend linearly on the thickness of the vacuum [34,35]. In the present work, for all systems, the vacuum region is 11 Å.

The interlayer binding energies (E_b) of the bilayer heterostructures are calculated using Equation (9), where E_H is the total energy of the heterostructure, $E_{\mathrm{BC}/B}$ is the total energy of the isolated boron-carbide (/borophene) monolayer and E_G is the total energy of the Graphene monolayer.

$$E_\mathrm{b} = E_\mathrm{H} - E_{\mathrm{BC}/B} - E_\mathrm{G} \quad (9)$$

The charge density difference ($\Delta\rho(\mathbf{r})$) for the heterostructure systems is calculated using Equation (10). The $\rho_\mathrm{AB}(\mathbf{r})$ term is the total charge density of the heterostructure system and $\rho_\mathrm{A/B}(\mathbf{r})$ are the total charge densities of the isolated monolayers making up the heterostructure.

$$\Delta\rho(\mathbf{r}) = \rho_\mathrm{AB}(\mathbf{r}) - \rho_\mathrm{A}(\mathbf{r}) - \rho_\mathrm{B}(\mathbf{r}) \quad (10)$$

3. Results and Discussion

3.1. Monolayer Properties

We start by investigating the structural and electronic properties of the three monolayers, namely BC_3, B_4C_3 and borophene. The graphene monolayer is also investigated as it always forms one layer of the heterostructure systems. The optimized structures of BC_3, B_4C_3, borophene and graphene are shown in Figure 1. The monolayer allotrope of borophene has been predicted to have various low-energy structures with the β_{12}, χ_3 and α' structures having been synthesised experimentally [36]. For this study we chose to investigate the α' structure of borophene, not only because it has been synthesised experimentally, but also because it has been shown to have the most favourable cohesive energy from GGA level ab initio calculations [37].

The structural properties and band gap energies of the monolayer systems are shown in Table 1. For graphene the lattice constant is calculated to be $a = 2.467$ Å, while those of borophene, BC_3 and B_4C_3 are 5.051 Å, 5.169 Å and 4.690 Å, respectively. In agreement with previous calculations, graphene is a semi-metal, borophene is metallic, while BC_3 and B_4C_3 are indirect semiconductors [38,39] with calculated indirect band-gaps of 1.822 eV (0.634 eV) and 2.381 eV (1.647 eV) as obtained by the HSE06 (PBE), respectively. In Figure S2 the optimisation of the lattice constants for the monolayers are shown and the band structures of the four monolayer systems are shown in Figure 2.

Table 1. Optimized lattice constants, inter-atomic distances, and band gaps of monolayer BC_3, borophene, B_4C_3, and graphene. Here, a is the lattice parameter with $a = b$ for all systems, B-B, C-C, and B-C are the boron-boron, carbon-carbon, and boron-carbon bond lengths. Borophene and B_4C_3 have B-B and B-C bonds of different lengths, these are identified by labels l_1 ... l_7 in Figure 1. The band gap E_g is calculated using the PBE and HSE06 exchange-correlation functionals, values in brackets are from previous theoretical studies. "Nature" indicates the electronic character of the system with "indirect" referring to an indirect semiconductor.

System	a ($a = b$) (Å)	B-B (Å)	C-C (Å)	B-C (Å)	$E_{\mathrm{g-PBE}}$ (eV)	$E_{\mathrm{g-HSE06}}$ (eV)	Nature
BC_3	5.169	-	1.421	1.563	0.634 (0.62–0.66) [38,40,41]	1.822 (1.83) [41]	indirect

Table 1. *Cont.*

System	a $(a = b)$ (Å)	B-B (Å)	C-C (Å)	B-C (Å)	$E_{g-\mathrm{PBE}}$ (eV)	$E_{g-\mathrm{HSE06}}$ (eV)	Nature
Borophene	5.051	1.689 (l_1) 1.672 (l_2) 1.707 (l_3)	-	-	-	-	metallic
B_4C_3	4.690	1.689 (l_4)	-	1.592 (l_5) 1.517 (l_6) 1.548 (l_7)	1.647	2.381 (2.39) [42]	indirect
Graphene	2.467	-	1.424	-	-	-	semimetal

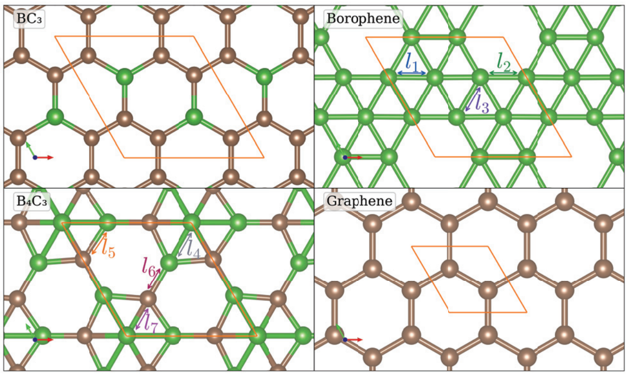

Figure 1. Optimized atomic structures of BC_3, borophene, B_4C_3 and graphene. Boron and carbon atoms are denoted by the green and brown spheres, respectively. Borophene has three unique bonds indicated by l_1, l_2 and l_3, while B_4C_3 has four unique bonds indicated by l_4, l_5, l_6 and l_7. The unit cells are highlighted in orange.

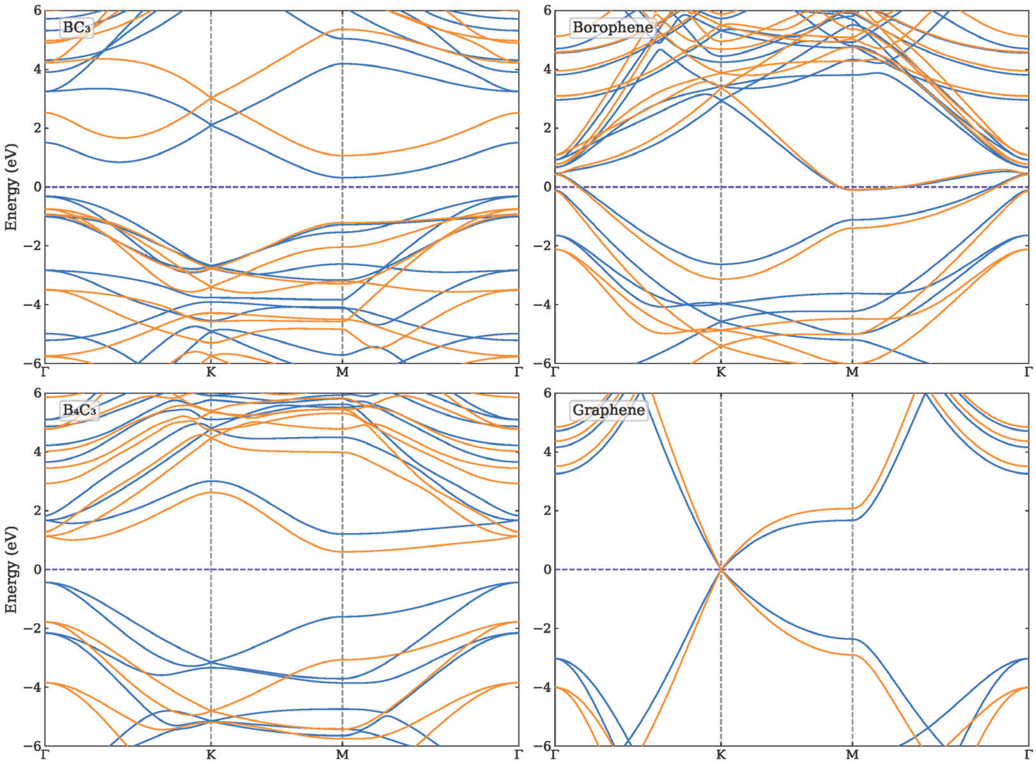

Figure 2. Band structure of the four monolayer systems, BC_3, B_4C_3, borophene and graphene as calculated using the PBE (blue) and HSE06 (orange) functionals. The Fermi level is indicated by the purple dashed line.

3.2. Heterostructures

3.2.1. Structural Properties

We now turn to determining the structure of the bilayer heterojunctions, which are composed of monolayer graphene stacked with monolayer BC_3, borophene, and B_4C_3 (namely, Graphene–BC_3, Graphene–Borophene and Graphene–B_4C_3), respectively. To create the heterostructues we use a (2 × 2) cell. For each system, we considered various lateral coordinations (positions) of these layers. Specifically, "Hollow", "Bridge" and "Top" coordinations for the Graphene–BC_3 bilayer systems, and "Hollow 1", "Hollow 2", "Bridge" and "Top" coordinations for the Graphene–Borohene and Graphene–B_4C_3 bilayer systems. We studied the relative energies, optimized lattice constants, and inter-planar distances for all structures. Details about this procedure are given in Figures S3–S6. Due to the weak van der Waals interaction between the layers, the difference in energies of the lateral positions is very small, with the values given in Table S1.

The results show that the energetically most favourable lateral position for the Graphene–BC_3 system is the "Hollow" coordination stacking configuration. This means that each atom in BC_3 is projected onto the center of a hexagon in graphene as shown in Figure 3. The bilayer system Graphene–Borophene and Graphene–B_4C_3 have the "Top" coordination stacking configuration as the energetically most favourable one. In this arrangement, each hexagon without an atom in the bottom layer is projected onto the center of a hexagon in graphene, but not every hexagon center in graphene aligns with a hexagon without an atom from the bottom layer (see Figure 3).

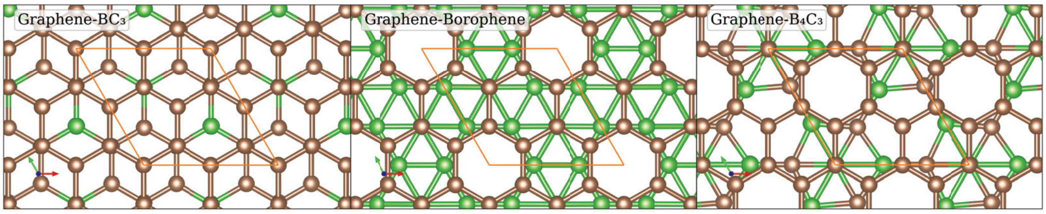

Figure 3. Top view of the optimized atomic structures of Graphene–BC_3, Graphene–Borophene, and Graphene–B_4C_3. Boron and carbon atoms are denoted by the green and brown spheres, respectively. The unit cell is indicated by the orange parallelogram.

It can be seen from Table 2 that Graphene–Borophene is metallic, while Graphene–BC_3 and Graphene–B_4C_3 are semi-metals. Out of all the heterostructure systems, a maximum (tensile) strain of 3.33% is present for B_4C_3. For the bilayer system Graphene–BC_3, graphene is under tensile strain and BC_3 is under compressive strain. For the bilayer system Graphene–Borophene, a slight tensile strain is present for Graphene, while borophene experiences compressive strain. For the bilayer system Graphene–B_4C_3, there is compressive strain in Graphene, while B_4C_3 is under a larger tensile strain. Generally, tensile strain tends to narrow the band gap, reducing it and increasing conductivity [43]. Conversely, compressive strain tends to widen the band gap, thereby decreasing conductivity [44].

Table 2. Optimized structural properties for each bilayer heterojunction system. Namely, the lowest energy lateral coordination (or position) of the stacking relative to graphene, the optimized lattice constant a, strain relative to the respective monolayer, S_G and $S_{BC/B}$, inter-planar distance d_{IL} and electronic nature. A negative and positive value of the percentage strain corresponds to a compressive and tensile strain, respectively.

System	Coordination	a ($a = b$) (Å)	S_G	$S_{BC/B}$	d_{IL} (Å)	Nature
Graphene–BC_3	Hollow	5.044	2.23%	−2.42%	3.372	semi-metal
Graphene–Borophene	Top	4.979	0.91%	−1.43%	3.505	metallic
Graphene–B_4C_3	Top	4.846	−1.78%	3.33%	3.514	semi-metal

3.2.2. Charge Density Difference

The charge density difference distributions for the heterostructure systems are shown in Figure 4 as calculated using Equation (10) by subtracting the charge density of the monolayers from the charge density of the heterostructure system. It is clear from the side view (middle panels) in Figure 4 that in all cases there is charge depletion from the graphene layer (top layer) and accumulation in the alternate monolayer. The largest charge redistribution is found for Graphene–BC_3. This is consistent with the smaller interlayer distance, due to the hollow site relative coordination rather than the top site, as for the Graphene–Bororphene and Graphene–B_4C_3 heterostructures. We also observe that atoms in the lower layers which directly coordinate with a carbon atom in the graphene layer have the largest charge accumulation regions. In contrast, the carbon atoms in the graphene layer with bridge or hollow coordination to the atoms of the lower layer show the largest regions of charge depletion. This gives rise to the patterns in the charge accumulation/depletion regions shown in the top and bottom views of Figure 4. Therefore, we find the relative coordination between the bilayer heterostructures has a direct impact on their electronic properties. For the Graphene–B_4C_3 heterostructure, quite striking is the 3-fold rotational symmetry as seen from the top and bottom views (upper and lower plots of the rightmost panel).

In the next sections the band structure and density of states are investigated to further characterise the electronic structure of these heterostructure systems.

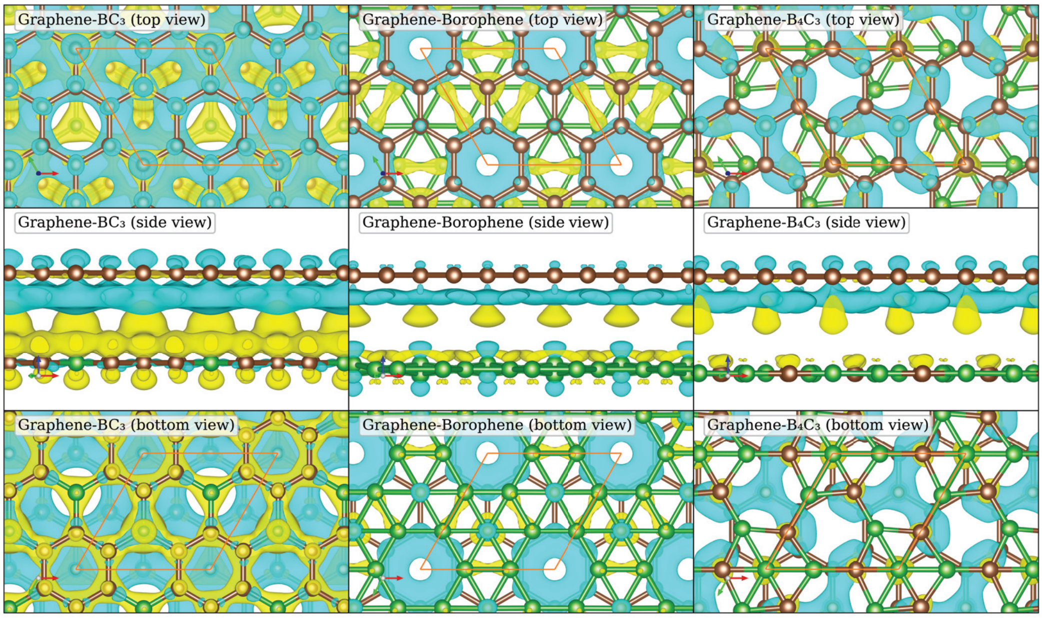

Figure 4. Charge density difference ($\Delta\rho(\mathbf{r})$, calculated using Equation (10)) between the monolayers and the heterostructures. Regions of charge accumulation are shown in yellow and regions of charge depletion are shown in blue. The isosurface level is 1.5×10^{-4} a_0^{-3} and the top layer is always graphene. The unit cell is indicated by the orange parallelogram.

3.2.3. Band Structure and Density of States

For the bilayer systems, the band structures and total density of states (DOS) are shown in Figures 5–7 as calculated using the HSE06 and PBE functionals. The corresponding atom-projected (or partial) PDOS are presented in Figures S9–S11. The band structures for the other lateral positions considered for the Graphene–Borophene and Graphene–B_4C_3 systems are shown in Figures S7 and S8, where there is a small difference between them.

The Graphene–Borophene system exhibits metallic behaviour due to the small occupancy of states at the K-point which are mainly carbon related as seen from the PDOS in Figure S9. Graphene–B_4C_3 appears to have kept the character of the respective monolayers, displaying essentially semi-metal behaviour with the B_4C_3 states located away from the Fermi level (i.e. above ≈1.2 eV and below ≈−0.8 eV) as seen from the PDOS in Figure S10. It is notable that the Graphene–BC_3 heterojunction exhibits a sizeable density-of-states just above the Fermi level (see Figure S11) which is related to the relatively flat band near the M-point and along K to Γ in the Brillouin zone. For these bilayer systems, the main difference between the PBE and HSE06 appears to be the raising and lowering of conduction and valence bands of the HSE06, respectively, relative to those obtained by the PBE functional. At the K-point the graphene bands exhibit a very small band-gap opening of 20 meV and 50 meV for Graphene–B_4C_3 and Graphene–BC_3, respectively.

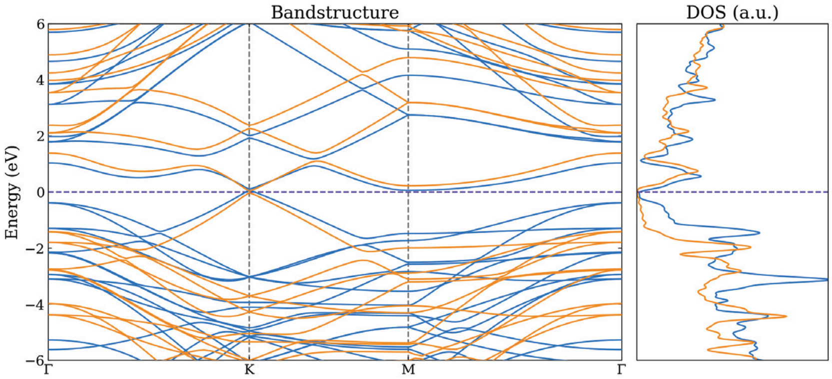

Figure 5. Band structure and total DOS for Graphene–BC_3 as calculated using the PBE (blue) and HSE06 (orange) functionals. The Fermi level is indicated by the purple dashed line.

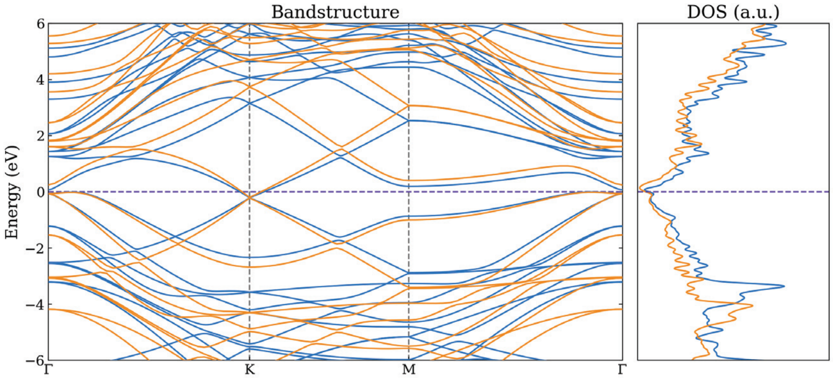

Figure 6. Band structure and total DOS for Graphene–Borophene as calculated using the PBE (blue) and HSE06 (orange) functionals. The Fermi level is indicated by the purple dashed line.

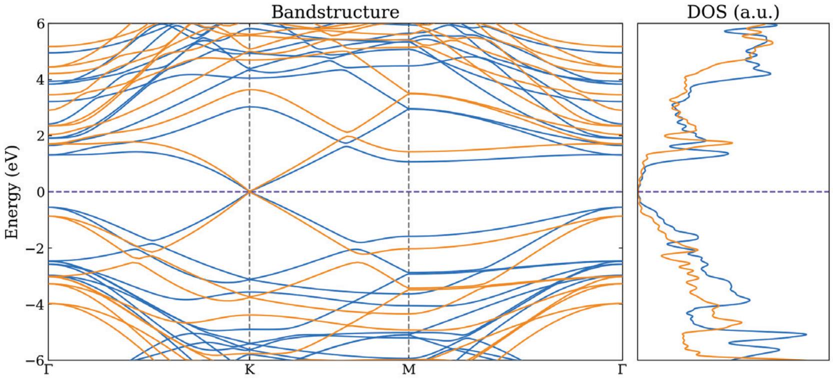

Figure 7. Band structure and total DOS for Graphene–B_4C_3 as calculated using the PBE (blue) and HSE06 (orange) functionals. The Fermi level is indicated by the purple dashed line.

3.2.4. Schottky Barrier Height

The graphene/boron-carbide bilayer structures can function as a Schottky diode. A high Schottky barrier will block the reverse (metal-to-semiconductor) current, realizing the rectification effect of a diode. Based on the Schottky–Mott model (shown in Figure 8, left), at the metal–semiconductor interface [45] in n-type materials the Schottky barrier (Φ_n) is defined as the energy difference between the Fermi level (E_F) and the conduction band minimum (E_C), that is, $\Phi_n = E_C - E_F$. Similarly, in p-type materials the Schottky barrier (Φ_p) is defined as the energy difference between the Fermi level (E_F) and the VBM (E_V), that is, $\Phi_p = E_F - E_V$ [46,47]. The sum of two types of Schottky barriers is approximately equal to the band gap value (E_g) of the semiconductor, that is, $\Phi_n + \Phi_p = E_g$. For the Graphene–B_4C_3 system as illustrated in Figure 8, right, we find $\Phi_n = 1.42$ eV (1.07 eV) for the HSE06 (PBE) and $\Phi_p = 0.87$ eV (0.55 eV) for the HSE06 (PBE) signifying the heterojunction forms a p-type Schottky barrier since $\Phi_p < \Phi_n$. For the Graphene–BC_3 heterostructure bilayer, we find $\Phi_n = 0.19$ eV (0.003 eV) for the HSE06 (PBE) and $\Phi_p = 1.42$ eV (0.39 eV) for the HSE06 (PBE) signifying an n-type Schottky barrier. For device applications a smaller Schottky barrier height or even an Ohmic contact is preferred to reduce contact resistance.

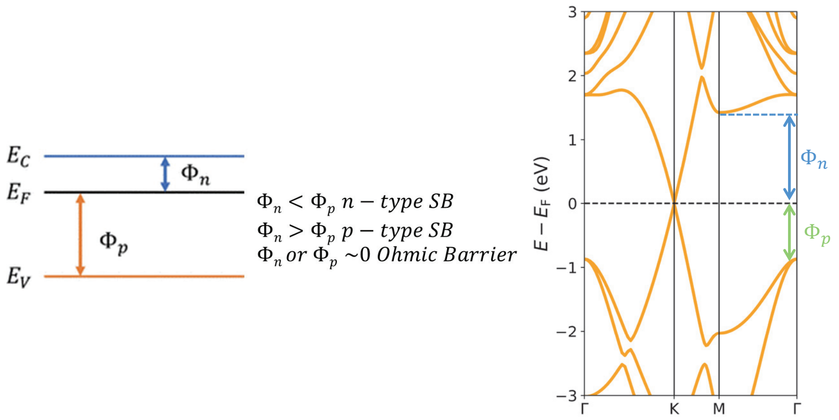

Figure 8. Left: schematic of the Schottky-Mott model showing the valence and conduction band energies, the Fermi energy, and n-type and p-type Schottky barriers labelled E_V, E_C, E_F, Φ_n, and Φ_p, respectively. **Right**: Example for the HSE06 calculated Graphene–B_4C_3 heterojunction showing the determined Schottky barrier height from the band structure.

3.3. Optical Properties

Having determined the atomic and electronic properties of the bilayer systems, the optical properties are now investigated. In particular, the real part (ϵ_1) and imaginary part (ϵ_2) of the dielectric function are calculated, and from them the other optical properties can be determined (cf. Equations (4)–(8)). ϵ_1 is a measure of the strength of the dynamical screening effects arising from charge excitations, while ϵ_2 is a measure of light absorption as a consequence of neutral and plasmonic charge excitations. A negative value of the real part of the dielectric function indicates metallic character for the corresponding ranges of the electromagnetic spectrum.

It is first important to establish the appropriate **k**-point set to yield converged results. For graphene, we tested a number of **k**-point meshes, and found that 129 × 129 × 1 yielded converged results as shown in Figure S12, in good agreement with previous results [48]. We therefore used this **k**-point sampling density for the other single monolayers (whose unit cells are (2 × 2) relative to graphene), namely a 65 × 65 × 1 **k**-point set. The dielectric function for all the monolayers is shown in Figure S13 where the results are consistent with previous calculations, namely: graphene [48], BC_3 [14,49], B_4C_3 [42] and borophene [50,51]. The response of the structures to light is highly dependent on the polarisation direction of incoming light, as seen by the anisotropic character of the in- and out-of-plane directions of the dielectric function. For in-plane, the well-known π plasmon of graphene can be seen emerging around 4 eV and the $\pi - \sigma$ plasmon emerges at around 14 eV. The other monolayer systems also have a π-like plasmon which emerges for B_4C_3 around 3 eV, for BC_3 around 2 eV and borophene around 1 eV. It can furthermore be seen from Figure S13 for the real part of the dielectric function in the out-of-plane direction for borophene, that a plasmon emerges at 9.8 eV as evidenced by the negative value which becomes positive around 10.5 eV.

As previously reported, the latter three monolayers, remarkably, exhibit visible light absorption which is also indicated by the in-plane imaginary part of the dielectric function seen in Figure S13. The static dielectric constants (real part of the dielectric constant at zero energy) for BC_3 are 4.0 eV for in-plane polarization and 1.4 eV for out-of-plane polarization as obtained by the PBE. These values can be compared to 4.86 eV for in-plane polarization and 1.59 eV for out of plane polarization as obtained by Ref. [49] using the PBE functional. For B_4C_3 the in-plane static dielectric constant is 3.9 eV and the out-of-plane is calculated to be 1.5 eV. We note these values reflect the combined monolayer-vacuum system. In Figure S14 the corresponding optical properties are shown for the monolayer systems.

Before we present the results for the three heterostructure bilayer systems, we first perform a convergence check for the number of unoccupied bands to include in the calculation of the dielectric function. Figure S15 shows the results for the representative system Graphene–B_4C_3. It can be seen that 128 bands yield well-converged results and we hereafter use this value for all the bilayer calculations. Further tests of the energy convergence criteria are reported in Figure S16.

The results for the dielectric function of the Graphene–Borophene heterojunction are shown in Figure 9 as obtained using both the PBE and HSE06 functionals. It can firstly be seen that, in comparison to the PBE results, the HSE06 yields a blue shift of the features to higher energies. The real part exhibits characteristics of both graphene and borophene with the presence of plasmons emerging around the same energies of the respective monolayers (i.e., 5 eV (4 eV), 2 eV (1 eV) for HSE06 (PBE) respectively). There is, however, a significant difference in the out-of-plane dielectric function compared to the monolayer systems. Firstly, it can be noticed that the borophene related plasmon that emerges at around 9.8 eV in the monolayer, has shifted to higher energies and now appears at around 17 eV (HSE06) 14 eV (PBE) with a plasmon resonance frequency at about 18 eV (HSE06) 15 eV (PBE), as determined by the energy at which the real part of the dielectric function changes from negative to positive. Also, a new feature with two peaks occurs around 2–5 eV (1–4 eV) for the HSE06 (PBE) for both the real and imaginary parts of the dielectric function. This feature in the imaginary part is attributed to interband transitions involving B- and G-derived states about the K-point and along the direction towards the M- and Γ-points—a similar feature appears for the other bilayer heterojunctions, albeit showing just one main peak. For in-plane polarization, the first main peak of ϵ_2 happens in the visible range, and is related to $\pi - \pi^*$ transitions. The main peaks along the out-of-plane direction are broad and occur in the energy range between 9–18.5 eV (8–17.5 eV) for the HSE06 (PBE), being related to $\pi - \sigma^*$ and $\pi^* - \sigma$ transitions.

In Figure 10 the results for the dielectric function of the Graphene–BC_3 heterostructure are shown, as obtained using both the PBE and HSE06. In contrast to the Graphene–Borophene system, the real part of the dielectric function is positive for all the energy range considered. There are however energies at which it goes to zero, namely in the region 2.5–5 eV and from 13 eV (15 eV) onwards for the PBE (HSE06). When ϵ_1 is zero but not negative, it suggests the system is close to the resonance but has not fully entered the regime where strong optical reflection or plasmonic modes are dominant, as those would typically require $\epsilon_1 < 0$. Also different to the Graphene–Borophene system is the sizeable in-plane value of both ϵ_1 and ϵ_2 in the region 10–15 eV. Similar to the Graphene–Borophene system, however, is the negative out-of-plane real part of the dielectric function at around 16–17 eV (14–15 eV) from HSE06 (PBE) indicating the presence of a plasmon. Interestingly, monolayer BC_3 does not exhibit this feature (unlike borophene), and it is thus presumably related to the $\pi - \sigma$-type plasmon present for graphene at $\approx$15 eV but which involves transitions between states involving both monolayers. For in-plane polarization, the first main peaks of ϵ_2 occur in the visible range, and are related to $\pi - \pi^*$ transitions. The main peaks along the out-of-plane direction are broad and are in the energy range between 11–17 eV (9–16 eV) for the HSE06 (PBE), being related to $\pi - \sigma^*$ and $\pi^* - \sigma$ transitions.

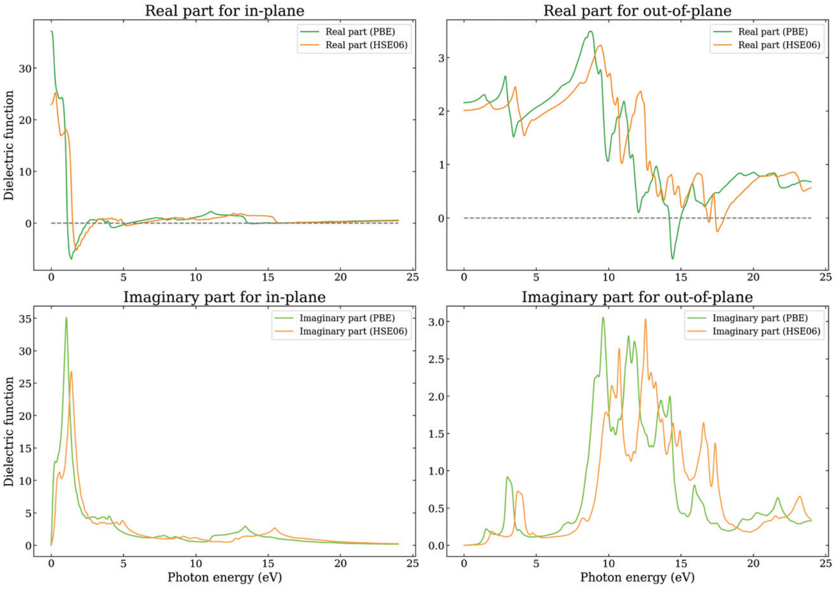

Figure 9. The real and imaginary parts of the in-plane and out-of-plane dielectric function as a function of photon energy as calculated using the PBE and HSE06 functionals for the Graphene–Borophene heterostructure.

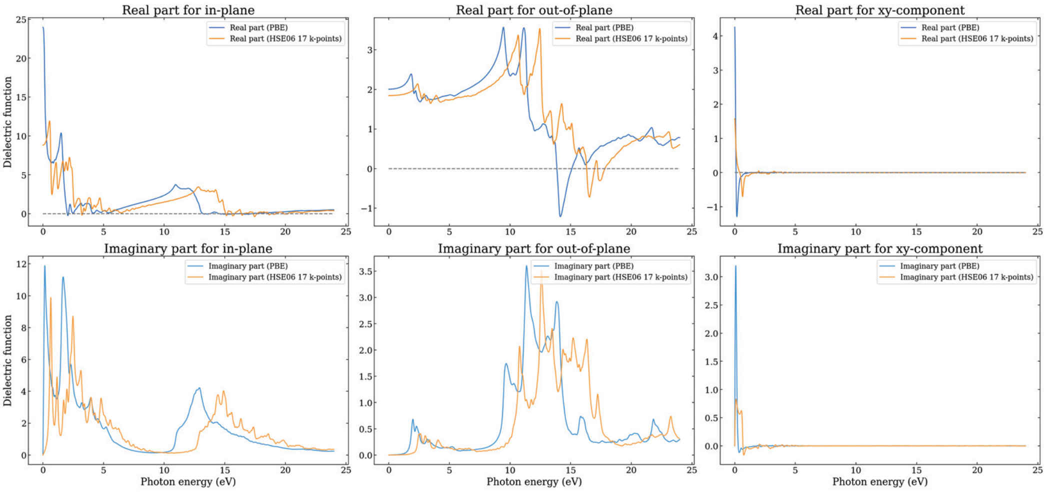

Figure 10. The real and imaginary parts of the in-plane and out-of-plane dielectric function as a function of photon energy as calculated using the PBE and HSE06 functionals for the Graphene–BC_3 heterostructure.

Interestingly, and in contrast to Graphene–Borophene, the dielectric tensor for this system contains complex non-zero off-diagonal components, as seen in Figure 10 for the xy component. Figure S17 shows all of the components, in which it is observed that components $xy = -yx, xz = -zx, yz = -zy$. The dielectric tensor describes the response of a material to an external electric field, that is, it characterizes how the polarization of the material changes in response to the applied electric field. For an incident photon, the dielectric tensor components describe the response of the material to the photon's electric field component along different directions, e.g., the element ϵ_{xy} and ϵ_{yx} describe the response to an electric field applied along the x-direction, resulting in polarization along the y-direction and vice versa. It is clear that the components are however non-zero only at very low energy and are small in value.

In Figure 11 the results for the dielectric function of the Graphene–B_4C_3 heterostructure are shown, as obtained using both the PBE and HSE06. It can be seen that the real part of the dielectric function for the in-plane component is negative in the region 5–6 eV HSE06 (4–5 eV PBE) and 17–18 eV HSE06 (15–16 PBE) thus hosting plasmons in the ultraviolet. The out-of-plane component also displays negative values about 17–18 eV HSE06 (14.5–15.5 eV PBE). Similarly to Graphene–B_4C_3 for in-plane polarization, the first main peaks of ϵ_2 are also in the visible range, and the main peaks along the out-of-plane direction are broad and occur in the energy range between 10–18 eV (9–17 eV) for the HSE06 (PBE).

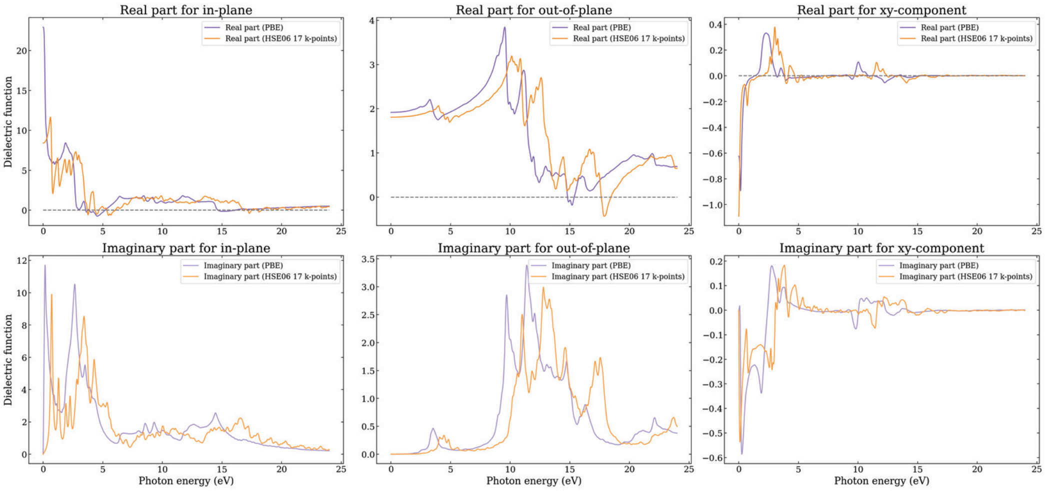

Figure 11. The real and imaginary parts of the in-plane and out-of-plane dielectric function as a function of photon energy as calculated using the PBE and HSE06 functionals for the Graphene–B_4C_3 heterostructure.

Similar to Graphene–BC_3, the dielectric tensor for this system contains complex non-zero off-diagonal components, as seen in Figure 11. Figure S18 shows all of the components where $xy = -yx, xz = -zx, yz = -zy$. In this case the dielectric function is non-zero for a considerable range of energies, i.e., from 0–5 eV and from 10–15 eV. The Graphene–B_4C_3 system has a P3 space group which has 3-fold rotational symmetry along the c (z-coordiante)-axis and it lacks mirror symmetry planes perpendicular to this axis or within the a, b (x, y plane). This lower symmetry allows for the presence of off-diagonal elements in the dielectric tensor. This means that the dielectric response of the material with this space group can exhibit anisotropic coupling between different crystallographic directions. The presence of complex off-diagonal elements in the dielectric tensor of a material with the P3 space group indicates that the material has anisotropic and possibly chiral optical properties, which could lead to effects like optical activity. It furthermore indicates Graphene–B_4C_3 dissipates energy differently depending on the direction of the electric field.

In order to further explore the optical properties of the heterostructure bilayers, the absorption coefficient, loss function, reflectivity, refractive index, and extinction coefficient are calculated. Figure 12 shows the absorbance and loss function for the three systems for in-plane and out-of-plane polarizations. In Figures S19–S23 all the components are shown. The absorbance threshold corresponds to where the imaginary part of the dielectric function, $\epsilon_2(\omega)$, shows its first peak. For all systems the adsorption coefficient starts very low and increases with energy, consistent with the lowest direct transition energies in the band structure. It is clear that there is absorption in the visible region of the spectrum (1.7–3.3 eV). It is noticeable that the Graphene–Borophene heterostructure has a significantly greater absorbance than the other two systems where it rises sharply around 1 eV. This can be attributed to transitions between the flat region of valence band about the Γ point and the low lying conduction band in the same region of the Brillouin zone. The Graphene–BC_3 heterostructure exhibits a similar sharp rise beginning at a slightly higher energy of around 2.5 eV, followed by Graphene–B_4C_3 at around 3.5 eV due to transitions between the relatively flat valence and conduction bands along the Γ-M direction.

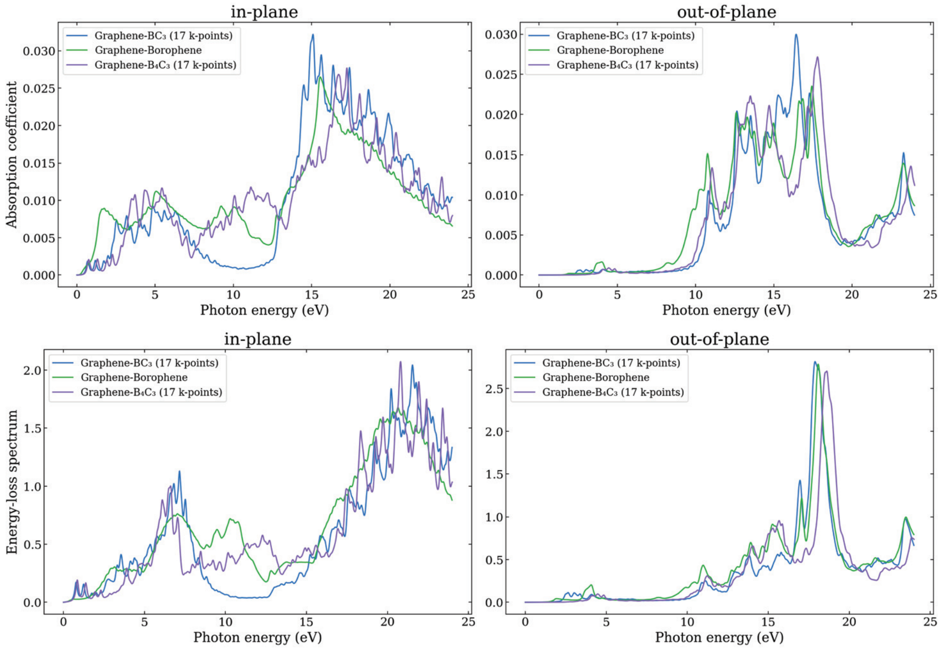

Figure 12. The in-plane and out-of-plane adsorption coefficient (upper) and energy loss spectrum (lower) as a function of photon energy as calculated using the HSE06 functional.

The loss function in Figure 12 presents a sharp feature at low energy, related to Dirac-like plasmons, for the Graphene–BC_3 and Graphene–B_4C_3 structures which is absent for the Graphene–Borophene bilayer. The broader features from 3–8 eV can be attributed to π-like plasmons. We note that individual interband transitions presumably coexist with the plasmons forming a broad background. The coexistence of individual transitions and plasmons in the same energy range lead to a coupling of the two types of excitations, and hence finite plasmon lifetimes as well as interband transitions [52]. The features in the loss function for energies around 15 eV where there is onset of a sharp increase may be associated with $\pi - \sigma$-type plasmons, where for all three bilayer heterostructures there is a plasmon supported at around this energy (as indicated by the negative real part of the out-of-plane component of the dielectric function).

In Figure 13 the reflectivity and refractive index are shown for the three heterostructures, as obtained using the HSE06, for polarization in the in-plane and out-of-plane directions. All of the components for each heterostructure are shown in Figures S25–S27. The refractive index is related to the real and imaginary parts of the dielectric constant. It can be seen that the trends in refractive index are similar to ϵ_1, which indicates that the effect of the real part of the dielectric function on the refractive index plays the leading role. The refractive index determines how much the path of light is bent, or refracted, when entering a material. For visible light, most transparent materials have refractive indices between 1 and 2. The absolute refractive index of an optical medium is defined as the ratio of the speed of light in vacuum and the phase velocity (speed at which the crests of the wave move) of light in a material. Given that it is possible for the phase velocity to travel faster than the speed of light in vacuum, the refractive index can be less than 1. For frequencies near the plasmon resonance in 2D materials, the refractive index can drop below one due to the strong interaction between light and the plasmonic oscillations.

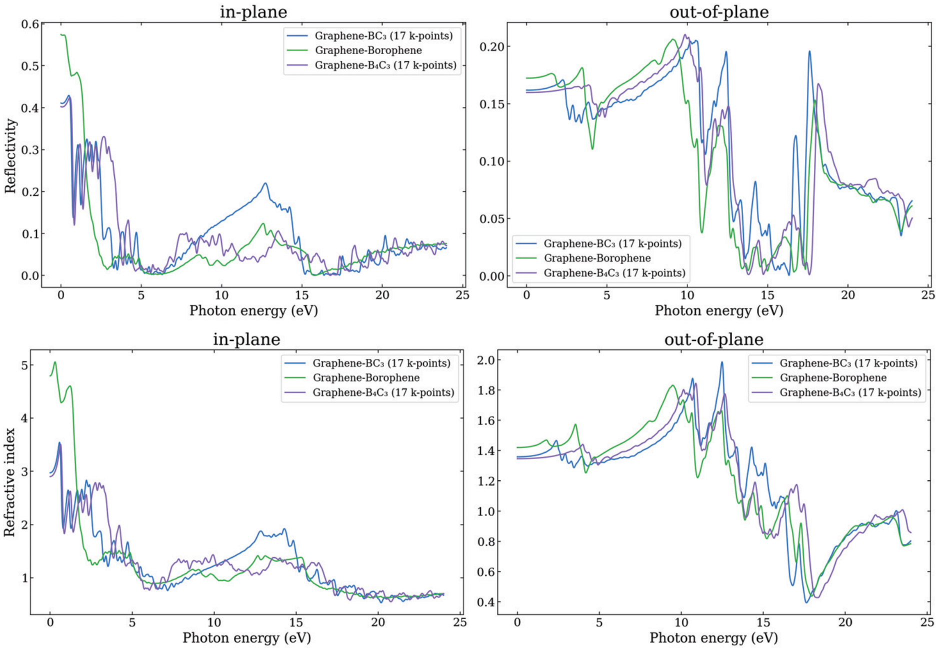

Figure 13. The in-plane and out-of-plane reflectivity (upper) and refractive index (lower) as a function of photon energy as calculated using the HSE06 functional.

It can be seen that the refractive index for in-plane polarization is close to, and less than one for energies in the range of ∼5–7 eV and greater than ∼17 eV for all three systems, while the out-of-plane refractive index is close to or less than one for energies greater than about 14 eV. This means that in these ranges of the electromagnetic spectrum, the structures are highly transparent, and it is in the region of where the plasmons occur.

The extinction coefficient (see Figure S23) for out-of-plane polarization displays a broad maximum from zero up to around 13 eV, while the in-plane polarization exhibits a maximum value in the region from 0–2, 0–2.5 and 0–3 eV, for the Graphene–Borophene, Graphene–BC_3 and Graphene–B_4C_3 heterostructures, respectively. There is also a broad peak in the region of around 7–15 eV. This means that in these energy regions, photons will be absorbed very fast.

4. Conclusions

In the present work, the atomic, electronic, and optical properties of Graphene–Borophene, Graphene–BC_3 and Graphene–B_4C_3 bilayer heterostructure systems have been investigated using first-principles calculations employing the HSE06 and PBE functionals. We find all systems have a small binding energy between the layers showing that graphene interacts weakly with the monolayers via the van der Waals interaction. The Graphene–Borophene bilayer is found to be metallic, while Graphene–BC_3 and Graphene–B_4C_3 structures maintain the characteristic linear bands of Graphene about the K-point with only very small band gap opening (20–50 meV). The calculated optical properties show absorbance in the visible region of the spectrum for all heterostructures with Graphene–Borophene exhibiting the strongest absorption. All heterostructures support plasmons with Graphene–Borophene exhibiting two at low energy, one emerging at 2 eV and the other around 5 eV. The Graphene–B_4C_3 bilayer heterostructure is found to have non-negligible off-diagonal elements in the dielectric tensor over a range of energies which suggests it could exhibit interesting optically active (chiral) effects.

Supplementary Materials: The following supporting information can be downloaded at: https://www.mdpi.com/article/10.3390/nano14201659/s1, Figure S1: **k**-point convergence; Figure S2: Monolayer lattice parameters; Figure S3: Heterostructure lattice paramaters; Table S1: Heterostructure lateral position tests; Figure S4: Graphene–BC_3 interlayer distance; Figure S5: Graphene–Borophene interlayer distance; Figure S6: Graphene–B_4C_3 interlayer distance; Figure S7: Graphene–Borophene PBE band structure; Figure S8: Graphene–B_4C_3 PBE band structure; Figure S9: Graphene–Borophene projected density of states; Figure S10: Graphene–B_4C_3 projected density of states; Figure S11: Graphene–BC_3 projected density of states; Figure S12: Dielectric function **k**-point convergence for graphene; Figure S13: Monolayer dielectric functions; Figure S14: Monolayer optical properties; Figure S15: Dielectric function band convergence; Figure S16: Dielectric function energy criteria convergence; Figure S17: Graphene–BC_3 dielectric tensor components; Figure S18: Graphene–B_4C_3 dielectric tensor components; Figure S19: Heterostructure adsorption coefficient; Figure S20: Heterostructure loss function; Figure S21: Heterostructure reflectivity; Figure S22: Heterostructure refractive index; Figure S23: Heterostructure extinction coefficient.

Author Contributions: Conceptualization, C.S.; Methodology, C.V., C.S., O.J.C. and L.N.; Software, L.N.; Validation, L.N., O.J.C. and C.V.; Formal Analysis, L.N.; Investigation, L.N.; Resources, C.S.; Data Curation, L.N.; Writing—Original Draft Preparation, C.S., O.J.C., C.V. and L.N.; Writing—Review & Editing, C.S., O.J.C. and C.V.; Visualization, L.N.; Supervision, C.S., C.V. and O.J.C.; Project Administration, C.S., C.V. and O.J.C. All authors have read and agreed to the published version of the manuscript.

Funding: C.V. thanks the Australian Research Council for financial support (DE220101147).

Data Availability Statement: The original data presented in the study are openly available in the GitHub repository Photonico/Graphene-BC_20230622 (accessed on 14 October 2024) at https://github.com/Photonico/Graphene-BC_20230622.

Acknowledgments: This research was undertaken with the assistance of resources from the National Computational Infrastructure (NCI Australia), an NCRIS enabled capability supported by the Australian Government.

Conflicts of Interest: The authors declare no conflict of interest.

References

1. Janavika, K.; Thangaraj, R.P. Graphene and its Application: A Review. *Mater. Today Proc.* **2023**. [CrossRef]
2. Sakthivel, R.; Keerthi, M.; Chung, R.J.; He, J.H. Heterostructures of 2D Materials and Their Applications in Biosensing. *Prog. Mater. Sci.* **2023**, *132*, 101024. [CrossRef]
3. Zhang, Z.; Lee, Y.; Haque, M.F.; Leem, J.; Hsieh, E.Y.; Nam, S. Plasmonic Sensors Based on Graphene and Graphene Hybrid Materials. *Nano Converg.* **2022**, *9*, 28. [CrossRef]
4. Novoselov, K.S.; Mishchenko, A.; Carvalho, A.; Castro Neto, A. 2D Materials and van der Waals Heterostructures. *Science* **2016**, *353*, aac9439. [CrossRef] [PubMed]
5. Thygesen, K.S. Calculating Excitons, Plasmons, and Quasiparticles in 2D Materials and van der Waals Heterostructures. *2D Mater.* **2017**, *4*, 022004. [CrossRef]
6. He, H.; Wang, Y.; Qi, Y.; Xu, Z.; Li, Y.; Wang, Y. From Prediction to Design: Recent Advances in Machine Learning for the Study of 2D Materials. *Nano Energy* **2023**, *118*, 108965. [CrossRef]
7. Lin, Y.C.; Torsi, R.; Younas, R.; Hinkle, C.L.; Rigosi, A.F.; Hill, H.M.; Zhang, K.; Huang, S.; Shuck, C.E.; Chen, C.; et al. Recent Advances in 2D Material Theory, Synthesis, Properties, and Applications. *ACS Nano* **2023**, *17*, 9694–9747. [CrossRef]
8. Elbanna, A.; Jiang, H.; Fu, Q.; Zhu, J.F.; Liu, Y.; Zhao, M.; Liu, D.; Lai, S.; Chua, X.W.; Pan, J.; et al. 2D Material Infrared Photonics and Plasmonics. *ACS Nano* **2023**, *17*, 4134–4179. [CrossRef]
9. Agarwal, A.; Vitiello, M.S.; Viti, L.; Cupolillo, A.; Politano, A. Plasmonics with Two-Dimensional Semiconductors: From Basic Research to Technological Applications. *Nanoscale* **2018**, *10*, 8938–8946. [CrossRef]
10. Qiu, B.; Zhao, X.; Hu, G.; Yue, W.; Ren, J.; Yuan, X. Optical Properties of Graphene/MoS2 Heterostructure: First Principles Calculations. *Nanomaterials* **2018**, *8*, 962. [CrossRef]
11. Yanagisawa, H.; Tanaka, T.; Ishida, Y.; Matsue, M.; Rokuta, E.; Otani, S.; Oshima, C. Phonon Dispersion Curves of a BC_3 Honeycomb Epitaxial Sheet. *Phys. Rev. Lett.* **2004**, *93*, 177003. [CrossRef] [PubMed]
12. Yanagisawa, H.; Tanaka, T.; Ishida, Y.; Rokuta, E.; Otani, S.; Oshima, C. Phonon Dispersion Curves of Stable and Metastable BC_3 Honeycomb Epitaxial Sheets and their Chemical Bonding: Experiment and Theory. *Phys. Rev. B* **2006**, *73*, 045412. [CrossRef]
13. Tanaka, H.; Kawamata, Y.; Simizu, H.; Fujita, T.; Yanagisawa, H.; Otani, S.; Oshima, C. Novel Macroscopic BC_3 Honeycomb Sheet. *Solid State Commun.* **2005**, *136*, 22–25. [CrossRef]
14. Chen, J.; Cheng, X.L.; Zhang, H. Plasmon Excitation in BC_3 Nanostructures from First Principles. *Plasmonics* **2019**, *14*, 109–116. [CrossRef]
15. Tian, X.; Xuan, X.; Yu, M.; Mu, Y.; Lu, H.G.; Zhang, Z.; Li, S.D. Predicting Two-Dimensional Semiconducting Boron Carbides. *Nanoscale* **2019**, *11*, 11099–11106. [CrossRef]

16. Luo, X.; Yang, J.; Liu, H.; Wu, X.; Wang, Y.; Ma, Y.; Wei, S.H.; Gong, X.; Xiang, H. Predicting Two-Dimensional Boron-Carbon Compounds by the Global Optimization Method. *J. Am. Chem. Soc.* **2011**, *133*, 16285–16290. [CrossRef] [PubMed]
17. Fan, D.; Lu, S.; Guo, Y.; Hu, X. Two-Dimensional Stoichiometric Boron Carbides with Unexpected Chemical Bonding and Promising Electronic Properties. *J. Mater. Chem. C* **2018**, *6*, 1651–1658. [CrossRef]
18. Hou, C.; Tai, G.; Liu, B.; Wu, Z.; Yin, Y. Borophene-Graphene Heterostructure: Preparation and Ultrasensitive Humidity Sensing. *Nano Res.* **2021**, *14*, 2337–2344. [CrossRef]
19. Liu, X.; Hersam, M.C. Borophene-Graphene Heterostructures. *Sci. Adv.* **2019**, *5*, eaax6444. [CrossRef]
20. Liu, X.; Li, Q.; Ruan, Q.; Rahn, M.S.; Yakobson, B.I.; Hersam, M.C. Borophene Synthesis Beyond the Single-Atomic-Layer Limit. *Nat. Mater.* **2022**, *21*, 35–40. [CrossRef]
21. Kresse, G.; Hafner, J. Ab initio Molecular Dynamics for Liquid Metals. *Phys. Rev. B* **1993**, *47*, 558. [CrossRef] [PubMed]
22. Kresse, G.; Furthmüller, J. Efficiency of ab-initio Total Energy Calculations for Metals and Semiconductors using a Plane-Wave Basis Set. *Comput. Mater. Sci.* **1996**, *6*, 15–50. [CrossRef]
23. Kresse, G.; Furthmüller, J. Efficient Iterative Schemes for Ab initio Total-Energy Calculations Using a Plane-Wave Basis Set. *Phys. Rev. B* **1996**, *54*, 11169–11186. [CrossRef]
24. Kresse, G.; Joubert, D. From Ultrasoft Pseudopotentials to the Projector Augmented-Wave Method. *Phys. Rev. B* **1999**, *59*, 1758. [CrossRef]
25. Perdew, J.P.; Burke, K.; Ernzerhof, M. Generalized Gradient Approximation Made Simple. *Phys. Rev. Lett.* **1996**, *77*, 3865–3868. [CrossRef]
26. Becke, A.D.; Johnson, E.R. A Density-Functional Model of the Dispersion Interaction. *J. Chem. Phys.* **2005**, *123*, 154101. [CrossRef] [PubMed]
27. Grimme, S.; Antony, J.; Ehrlich, S.; Krieg, H. A Consistent and Accurate Ab Initio Parametrization of Density Functional Dispersion Correction (DFT-D) for the 94 Elements H-Pu. *J. Chem. Phys.* **2010**, *132*, 154104. [CrossRef]
28. Grimme, S.; Ehrlich, S.; Goerigk, L. Effect of the Damping Function in Dispersion Corrected Density Functional Theory. *J. Comput. Chem.* **2011**, *32*, 1456–1465. [CrossRef]
29. Saßnick, H.D.; Cocchi, C. Electronic Structure of Cesium-Based Photocathode Materials From Density Functional Theory: Performance of PBE, SCAN, and HSE06 Functionals. *Electron. Struct.* **2021**, *3*, 027001. [CrossRef]
30. Heyd, J.; Scuseria, G.E.; Ernzerhof, M. Hybrid functionals based on a screened Coulomb potential. *J. Chem. Phys.* **2003**, *118*, 8207–8215. [CrossRef]
31. Krukau, A.V.; Vydrov, O.A.; Izmaylov, A.F.; Scuseria, G.E. Influence of the exchange screening parameter on the performance of screened hybrid functionals. *J. Chem. Phys.* **2006**, *125*, 224106. [CrossRef] [PubMed]
32. Wooten, F. *Optical Properties of Solids*; Academic Press: New York, NY, USA, 1972.
33. Gajdoš, M.; Hummer, K.; Kresse, G.; Furthmüller, J.; Bechstedt, F. Linear Optical Properties in the Projector-Augmented Wave Methodology. *Phys. Rev. B* **2006**, *73*, 045112. [CrossRef]
34. Weng, J.; Gao, S.P. A Honeycomb-Like Monolayer of HfO_2 and the Calculation of Static Dielectric Constant Eliminating the Effect of Vacuum Spacing. *Phys. Chem. Chem. Phys.* **2018**, *20*, 26453–26462. [CrossRef] [PubMed]
35. Laturia, A.; Van de Put, M.L.; Vandenberghe, W.G. Dielectric Properties of Hexagonal Boron Nitride and Transition Metal Dichalcogenides: From Monolayer to Bulk. *Npj 2D Mater. Appl.* **2018**, *2*, 6. [CrossRef]
36. Kaneti, Y.V.; Benu, D.P.; Xu, X.; Yuliarto, B.; Yamauchi, Y.; Golberg, D. Borophene: Two-dimensional Boron Monolayer: Synthesis, Properties, and Potential Applications. *Chem. Rev.* **2022**, *122*, 1000–1051. [CrossRef]
37. Wu, X.; Dai, J.; Zhao, Y.; Zhuo, Z.; Yang, J.; Zeng, X.C. Two-Dimensional Boron Monolayer Sheets. *ACS Nano* **2012**, *6*, 7443–7453. [CrossRef]
38. Zhang, Y.; Wu, Z.F.; Gao, P.F.; Fang, D.Q.; Zhang, E.H.; Zhang, S.L. Strain-Tunable Electronic and Optical Properties of BC_3 Monolayer. *RSC Adv.* **2018**, *8*, 1686–1692. [CrossRef]
39. Nosheen, U.; Jalil, A.; Ilyas, S.Z.; Illahi, A.; Khan, S.A.; Hassan, A. First-Principles Insight into a B_4C_3 Monolayer as a Promising Biosensor for Exhaled Breath Analysis. *J. Electron. Mater.* **2022**, *51*, 6568–6578. [CrossRef]
40. Behzad, S. Mechanical Control of the Electro-Optical Properties of Monolayer and Bilayer BC_3 by Applying the In-Plane Biaxial Strain. *Surf. Sci.* **2017**, *665*, 37–42. [CrossRef]
41. Zhang, H.; Liao, Y.; Yang, G.; Zhou, X. Theoretical Studies on the Electronic and Optical Properties of Honeycomb BC_3 monolayer: A Promising Candidate for Metal-free Photocatalysts. *ACS Omega* **2018**, *3*, 10517–10525. [CrossRef]
42. Chang, H.; Tu, K.; Zhang, X.; Zhao, J.; Zhou, X.; Zhang, H. B_4C_3 Monolayer with Impressive Electronic, Optical, and Mechanical Properties: A Potential Metal-Free Photocatalyst for CO_2 Reduction under Visible Light. *J. Phys. Chem. C* **2019**, *123*, 25091–25101. [CrossRef]
43. Roldán, R.; Castellanos-Gomez, A.; Cappelluti, E.; Guinea, F. Strain Engineering in Semiconducting Two-Dimensional Crystals. *J. Phys. Condens. Matter* **2015**, *27*, 313201. [CrossRef] [PubMed]
44. Boukhvalov, D.; Katsnelson, M.; Lichtenstein, A. Hydrogen on Graphene: Electronic Structure, Total Energy, Structural Distortions and Magnetism from First-Principles Calculations. *Phys. Rev. B* **2008**, *77*, 035427. [CrossRef]
45. Tung, R.T. The Physics and Chemistry of the Schottky Barrier Height. *Appl. Phys. Rev.* **2014**, *1*. [CrossRef]
46. Guo, Y.; Wang, F.Q.; Wang, Q. An All-Carbon vdW Heterojunction Composed of Penta-Graphene and Graphene: Tuning the Schottky Barrier by Electrostatic Gating or Nitrogen Doping. *Appl. Phys. Lett.* **2017**, *111*, 073503. [CrossRef]

47. Liu, B.; Zhao, Y.Q.; Yu, Z.L.; Wang, L.Z.; Cai, M.Q. Tuning the Schottky Rectification in Graphene-Hexagonal Boron Nitride-Molybdenum Disulfide Heterostructure. *J. Colloid Interface Sci.* **2018**, *513*, 677–683. [CrossRef]
48. Warmbier, R.; Quandt, A. Plasmonic and Dielectric Properties of Ideal Graphene. *Comput. Mater. Sci.* **2016**, *114*, 18–22. [CrossRef]
49. Mortazavi, B.; Shahrokhi, M.; Raeisi, M.; Zhuang, X.; Pereira, L.F.C.; Rabczuk, T. Outstanding Strength, Optical Characteristics and Thermal Conductivity of Graphene-Like BC_3 and BC_6N Semiconductors. *Carbon* **2019**, *149*, 733–742. [CrossRef]
50. Huang, Y.; Shirodkar, S.N.; Yakobson, B.I. Two-Dimensional Boron Polymorphs for Visible Range Plasmonics: A First-Principles Exploration. *J. Am. Chem. Soc.* **2017**, *139*, 17181–17185. [CrossRef]
51. Adamska, L.; Sharifzadeh, S. Fine-Tuning the Optoelectronic Properties of Freestanding Borophene by Strain. *ACS Omega* **2017**, *2*, 8290–8299. [CrossRef]
52. Li, P.; Ren, X.; He, L. First-Principles Calculations and Model Analysis of Plasmon Excitations in Graphene and Graphene/hBN Heterostructure. *Phys. Rev. B* **2017**, *96*, 165417. [CrossRef]

nanomaterials

MDPI

Communication

Symmetry-Engineering-Induced In-Plane Polarization Enhancement in Ta_2NiS_5/CrOCl van der Waals Heterostructure

Yue Su [1,2], Peng Chen [3], Xiangrui Xu [1], Yufeng Zhang [1], Weiwei Cai [1], Gang Peng [2], Xueao Zhang [1,*] and Chuyun Deng [2,*]

[1] College of Physical Science and Technology, Xiamen University, Xiamen 361005, China
[2] College of Science, National University of Defense Technology, Changsha 410073, China
[3] Songshan Lake Materials Laboratory, Dongguan 523808, China
* Correspondence: xazhang@xmu.edu.cn (X.Z.); dengchuyun@nudt.edu.cn (C.D.)

Abstract: Van der Waals (vdW) interfaces can be formed via layer stacking regardless of the lattice constant or symmetry of the individual building blocks. Herein, we constructed a vdW interface of layered Ta_2NiS_5 and CrOCl, which exhibited remarkably enhanced in-plane anisotropy via polarized Raman spectroscopy and electrical transport measurements. Compared with pristine Ta_2NiS_5, the anisotropy ratio of the Raman intensities for the B_{2g}, ^2A_g, and ^3A_g modes increased in the heterostructure. More importantly, the anisotropy ratios of conductivity and mobility in the heterostructure increased by one order of magnitude. Specifically speaking, the conductivity ratio changed from ~2.1 (Ta_2NiS_5) to ~15 (Ta_2NiS_5/CrOCl), while the mobility ratio changed from ~2.7 (Ta_2NiS_5) to ~32 (Ta_2NiS_5/CrOCl). Such prominent enhancement may be attributed to the symmetry reduction caused by lattice mismatch at the heterostructure interface and the introduction of strain into the Ta_2NiS_5. Our research provides a new perspective for enhancing artificial anisotropy physics and offers feasible guidance for future functionalized electronic devices.

Keywords: Ta_2NiS_5/CrOCl; symmetry engineering; van der Waals heterostructure; enhanced anisotropy; angle-dependent Raman spectrum; electrical transport

1. Introduction

Low-symmetry two-dimensional (2D) materials exhibit significant anisotropy in optical, electrical, and thermal properties due to their asymmetric lattice structures, which has attracted widespread attention in the past decade [1–4]. Phosphorus (BP), one of the most famous low-symmetry materials, has been widely used in polarization optoelectronics, sensing, and energy storage [5–7]. Moreover, symmetry engineering and artificial anisotropy offer a new degree of freedom to modulate the original physical properties of 2D materials toward improved functional performance. Recently, a study reported a novel symmetry reduction method that employs van der Waals (vdW) interfaces to achieve artificial anisotropy enhancement in ReS_2 [8]. In this sense, vdW heterostructures can offer a simple and effective approach to reduce the symmetry of 2D materials.

VdW heterostructure interfaces serve as a platform for studying exotic physical properties, which can be easily prepared via the combination and stacking process of diverse layered materials [9]. When lattice mismatch in a heterostructure occurs at a specific angle, moiré patterns can be observed at the interface, which triggers novel physical phenomena that are absent in the parent materials [10,11]. For instance, in a WSe_2/BP heterostructure, WSe_2 and BP form periodic moiré patterns via vdW forces, resulting in the in-plane polarization of isotropic WSe_2. In addition, lattice mismatch at the heterostructure interface introduces strain within the material. By applying uniaxial tensile strain, the structural symmetry of MoS_2 can be altered, enabling it to successfully exhibit anisotropic characteristics [12]. However, introducing in-plane polarization in highly symmetrical materials

Nanomaterials **2023**, *13*, 3050. https://doi.org/10.3390/nano13233050

https://www.mdpi.com/journal/nanomaterials

results in a lower anisotropy ratio. Therefore, we enhance the anisotropic differences in low-symmetry materials via symmetry engineering.

Ta_2NiS_5, a low-symmetry ternary transition metal chalcogenide, has attracted widespread attention due to its applications in electronics, optoelectronics, and biosensing [13–17]. Unlike single-element or binary anisotropic materials such as BP, $PtSe_2$, and WTe_2, ternary chalcogenides consist of three elements and can adjust their physical properties via stoichiometric variation [18–20]. However, the anisotropy ratio of Ta_2NiS_5 makes it difficult to reach the requirements of practical applications. Therefore, we chose to further enhance the anisotropy of Ta_2NiS_5 via symmetry engineering. CrOCl is a low-symmetry antiferromagnetic insulator with inherent ferromagnetism, large spin polarization, a high Curie temperature, and an ultralow exfoliation energy [21–23]. As a means of achieving polarized electronic devices, using an insulating substrate for modulation can simplify the model and avoid the influence of interlayer charge transfer on the electrical properties of the device. Researchers have successfully used CrOCl as a substrate and introduced artificial anisotropy into isotropic materials via symmetry engineering including MoS_2/CrOCl and WSe_2/CrOCl heterostructures [12,24]. Therefore, utilizing CrOCl as a substrate to reduce the symmetry of 2D materials is a recognized and viable approach.

In this work, we report a noteworthy enhancement effect on the in-plane anisotropy of Ta_2NiS_5 via vdW symmetry engineering. The experimental results of angle-resolved Raman spectroscopy demonstrated that the anisotropy enhancement occurred in the B_{2g}, ${}^2A_g$, and ${}^3A_g$ modes of the Ta_2NiS_5/CrOCl heterostructure. The angle-dependent electrical transport results indicate that the anisotropy ratio of conductivity and mobility in the heterostructure increased compared with that in pristine Ta_2NiS_5. The Ta_2NiS_5/CrOCl heterostructure possesses strong anisotropic electrical properties, which can be utilized for direction-sensitive electronic devices. Our research provides a new sight for symmetry engineering in nanoelectronics.

2. Materials and Methods

We prepared Ta_2NiS_5 and CrOCl flakes (Figure S1) from bulk crystals (Onway Technology Co., Ltd., Shanghai, China) via mechanical exfoliation and constructed Ta_2NiS_5/CrOCl vdW heterostructures using dry transfer via transfer equipment with a 2D location adjustment platform and optical microscope. Due to the anisotropic properties of both Ta_2NiS_5 and CrOCl, we aligned the *a*-axis of Ta_2NiS_5 with the *a*-axis of CrOCl when constructing the heterostructure. We used polarization Raman spectroscopy to determine the lattice orientation of the material (Figures S2 and S3). Simultaneously, we combined the literature findings to confirm that the long-axis of Ta_2NiS_5 was the *a*-axis, while the long-axis of CrOCl was referred to as the *a*-axis [22,25]. In order to enhance the interlayer coupling of the heterostructure and remove the residual adhesive on the heterostructure surface, we annealed the heterostructure at 325 °C for 1 h. Six pairs of electrodes with Cr/Au (10/70 nm) were fabricated using electron-beam lithography (Raith, Pittsburgh, Germany) and PVD75 e-beam evaporation (Kurt J. Lesker, Pittsburgh, Jefferson Hills, UT, USA). For the Raman spectroscopy (WITEC, Ulm, Germany), we employed a 532 nm laser source and a 100× microscope objective. In the parallel configuration, the incident light polarization (e_i) was parallel to the scattered light polarization (e_s), while in the vertical configuration, e_i was vertical to e_s. We defined the direction as 0° when the *a*-axis of Ta_2NiS_5 was parallel to the incident light direction. The laser spot size was less than 500 nm. To avoid sample damage, the laser power was adjusted to less than 1 mw. The electrical characterization of the Ta_2NiS_5 and Ta_2NiS_5/CrOCl heterostructures was carried out with a probe station (Lake Shore, Westerville, OH, USA) equipped with a semiconductor analyzer system (Keithley, Cleveland, OH, USA).

3. Results

We chose a ternary transition-metal chalcogenide, Ta_2NiS_5, and an insulator, CrOCl, as the building blocks of the interface because the compounds have similar rotational and mirror symmetries. The Ta_2NiS_5 and CrOCl crystal structures are illustrated in Figure 1a,b, both belonging to an orthorhombic structure [23]. When Ta_2NiS_5 and CrOCl are stacked to form a heterostructure, stripe moiré patterns occur at the Ta_2NiS_5/CrOCl interface (Figure 1c). The generation of moiré patterns further alters the electrical and optical properties of the heterostructure [26]. Unlike the moiré patterns in twisted graphene, the stripe moiré patterns originate from the lattice mismatch at the Ta_2NiS_5/CrOCl interface, and it may induce in-plane polarization at this interface via strain [27,28]. In a MoS_2/CrOCl heterostructure, this stripe moiré pattern is ascribed to the lattice mismatch between MoS_2 and CrOCl, resulting in the strain in the MoS_2 [9,12].

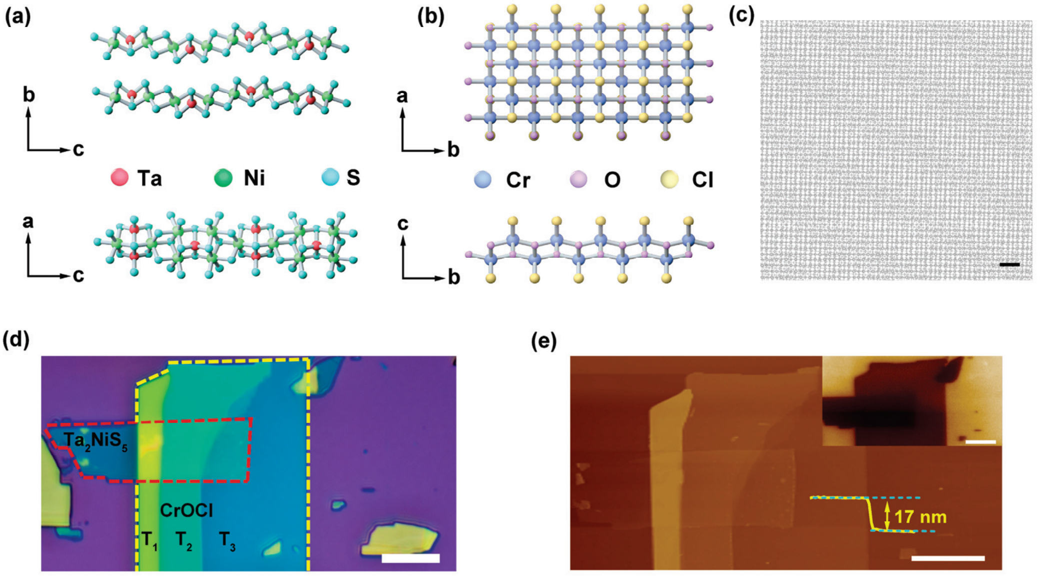

Figure 1. Characterizations of Ta_2NiS_5/CrOCl heterostructure. Schematic illustrations of the crystal lattice structure for (**a**) Ta_2NiS_5 and (**b**) CrOCl. (**c**) Stripe moiré pattern simulation diagram of heterointerface. The scale bar is 1 nm. (**d**) Optical image and (**e**) AFM of Ta_2NiS_5/CrOCl heterostructure. The thickness of Ta_2NiS_5 is 9.2 nm, and the thicknesses of the T_1, T_2, and T_3 of CrOCl are approximately 61, 27.5, and 17 nm. The inset shows the KPFM image of Ta_2NiS_5/CrOCl heterostructure. The scale bars in (**d**,**e**) are both 10 µm.

Figure 1d shows the optical image of the Ta_2NiS_5/CrOCl heterostructure. The red-marked region indicates Ta_2NiS_5, and the yellow-marked region represents multiple thicknesses of CrOCl. Figure 1e corresponds to the atomic force microscope (AFM) image, which provides a higher-resolution view. It can be observed that the surface of the heterostructure is smooth. No crack or fold exists in the overlapping area, indicating the high quality of the interface. The inset is the Kelvin probe force microscopy (KPFM) image of the Ta_2NiS_5/CrOCl heterostructure. The KPFM image exhibits a highly uniform potential distribution in the overlapping regions, and a significant potential discrepancy can be seen.

We employed angular-resolved polarized Raman spectroscopy to investigate the symmetry of the Ta_2NiS_5 and Ta_2NiS_5/CrOCl heterostructures, aiming to uncover the influence of symmetry engineering on the in-plane polarization intensity. For Ta_2NiS_5, it has a B_{2g} and three A_g vibration modes. The force vectors correspond to a twisting motion for the B_{2g} mode and stretching motions for the ${}^2A_g$ and ${}^3A_g$ modes [13]. The polarization plots of each Raman mode are shown in Figure 2a,b. The B_{2g}, ${}^2A_g$, and ${}^3A_g$ modes of pristine Ta_2NiS_5 and the Ta_2NiS_5/CrOCl heterostructure exhibit four-lobed shapes. Under the parallel polarization configuration, the B_{2g} mode intensity of pristine Ta_2NiS_5 had a 90° variation period, while its intensities achieved the maxima at $\alpha \approx 40^{\circ}$, 130°, 220°, and 310°. The B_{2g} mode intensities achieved the maxima in the Ta_2NiS_5/CrOCl heterostructure at $\alpha \approx 40^{\circ}$ and 220° with the sub-maxima at $\alpha \approx 30^{\circ}$ and 310°. The anisotropy ratio of B_{2g} intensity increased from 4.6 (Ta_2NiS_5) to 9 (Ta_2NiS_5/CrOCl). Similar behavior was observed in the $^{3}A_g$ mode, where the maximum intensities occurred at $\alpha \approx 170°$, and 350° for both pristine Ta_2NiS_5 and the heterostructure, with sub-maxima at $\alpha \approx 80°$, and 260° in the heterostructure. The anisotropy ratio of the $^{3}A_g$ intensities increased from 2 (Ta_2NiS_5) to 3.3 (Ta_2NiS_5/CrOCl). Meanwhile, the $^{2}A_g$ mode reached its maximum intensities at $\alpha \approx 165°$ and 345° in both pristine Ta_2NiS_5 and the Ta_2NiS_5/CrOCl heterostructure, with sub-maxima at $\alpha \approx 45°$ and 135°. The anisotropy ratio increased from 3.8 (Ta_2NiS_5) to 5.9 (Ta_2NiS_5/CrOCl). By comparing the Raman spectroscopy results of Ta_2NiS_5 and the Ta_2NiS_5/CrOCl heterostructure, it can be clearly observed that the asymmetry of Ta_2NiS_5 was enhanced by constructing the heterostructure.

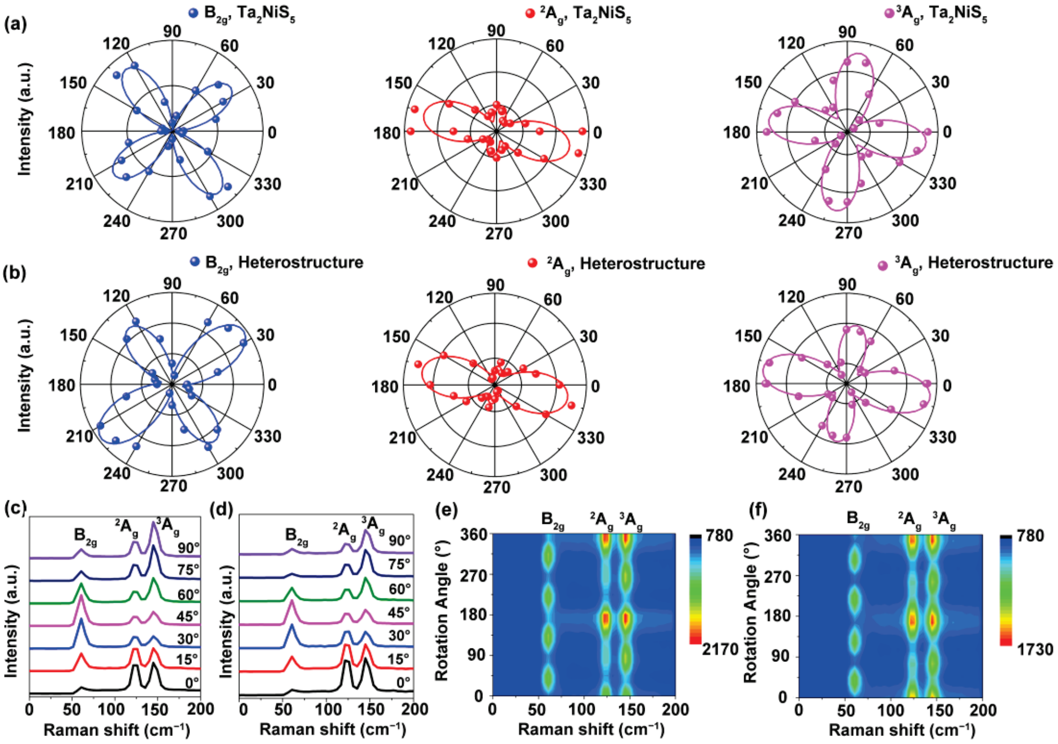

Figure 2. Polarized Raman spectra of Ta_2NiS_5/CrOCl heterostructure under parallel-polarized configuration. The polar plots of (**a**) Ta_2NiS_5 and (**b**) Ta_2NiS_5/CrOCl heterostructure for B_{2g}, $^{2}A_g$, and $^{3}A_g$ intensities in a rotation period. Raman spectra for different polarized angles of (**c**) Ta_2NiS_5 and (**d**) Ta_2NiS_5/CrOCl heterostructure. Contour maps of angular-dependent Raman spectra of (**e**) Ta_2NiS_5 and (**f**) Ta_2NiS_5/CrOCl heterostructure.

As shown in Figure 2c, the B_{2g}, $^{2}A_g$, and $^{3}A_g$ of pristine Ta_2NiS_5 along the *a*-axis are located at 61.6, 123.7, and 146.1 cm^{-1}. The Raman frequencies of Ta_2NiS_5 and Ta_2NiS_5/CrOCl along the *a*- and *c*-axes are exhibited in Figure 2d and Table S1, wherein all the Raman frequencies of the heterostructure shift along both the *a*-axis and *c*-axis compared with those of the Ta_2NiS_5. Figure 2e,f shows the contour maps of the Raman intensity varying with the angle for Ta_2NiS_5 and the heterostructure, respectively. By comparing the Raman spectra of Ta_2NiS_5 and Ta_2NiS_5/CrOCl, it can be observed that the Raman frequency shift occurred in the heterostructure. The Raman frequency is influenced by temperature, doping, material thickness, and strain [18,29–31]. In our comparative experiments, the same Ta_2NiS_5 thickness and test temperature were used, and CrOCl was used as an insulator, eliminating the influence of doping. Therefore, we suspect that the Raman shift was mainly caused by strain. When Ta_2NiS_5 and CrOCl form a vdW heterostructure, the mismatch of their lattice constants leads to lattice reconstruction, reducing the symmetry of Ta_2NiS_5 and enhancing the polarization. Meanwhile, the lattice mismatch may also cause strain within Ta_2NiS_5, further affecting the symmetry of the observed Raman modes in it. The B_{2g}, $^{2}A_g$, and $^{3}A_g$ modes represent the distortion and stretching movements of the Raman force vector. When Ta_2NiS_5 is strained, the Raman frequencies and symmetries of these modes change accordingly, consistent with the experimental phenomena we observed.

In order to further compare the enhancement effect of anisotropy on Ta_2NiS_5, we characterized the Ta_2NiS_5/CrOCl heterostructure via angle-dependent electrical transport measurements. Figure 3a shows a schematic diagram of the Ta_2NiS_5/CrOCl device, where we define 0° as the angle when the electrode E1 is parallel to the *a*-axis of Ta_2NiS_5. The side view of the device structure is shown in Figure S4. The electrode was deposited on Ta_2NiS_5. The channel length was 15 μm, and the angle between adjacent electrodes was 30°. Figure 3b,d displays the optical microscope image, AFM image, and height map image of the Ta_2NiS_5/CrOCl device. The prepared heterostructure exhibits uniform quality distribution, free of wrinkles and residue, showcasing a high-quality vdW interface. The thicknesses of Ta_2NiS_5 and CrOCl were 5.8 nm and 37.2 nm, respectively. The I-V curves were measured between distinct diagonal contacts at various temperatures. We tested the temperature-dependent resistance curves of Ta_2NiS_5 and the Ta_2NiS_5/CrOCl heterostructure along the *a*-axis (Figure 3e). With the increase in temperature, the resistance of the *a*-axis decreased, showing typical semiconductor characteristics, which were similar to those of the pristine Ta_2NiS_5. Figure 3f presents the I_{ds}–V_{ds} curves of the Ta_2NiS_5/CrOCl heterostructure at different angles at room temperature. The currents at different angles show significant anisotropy.

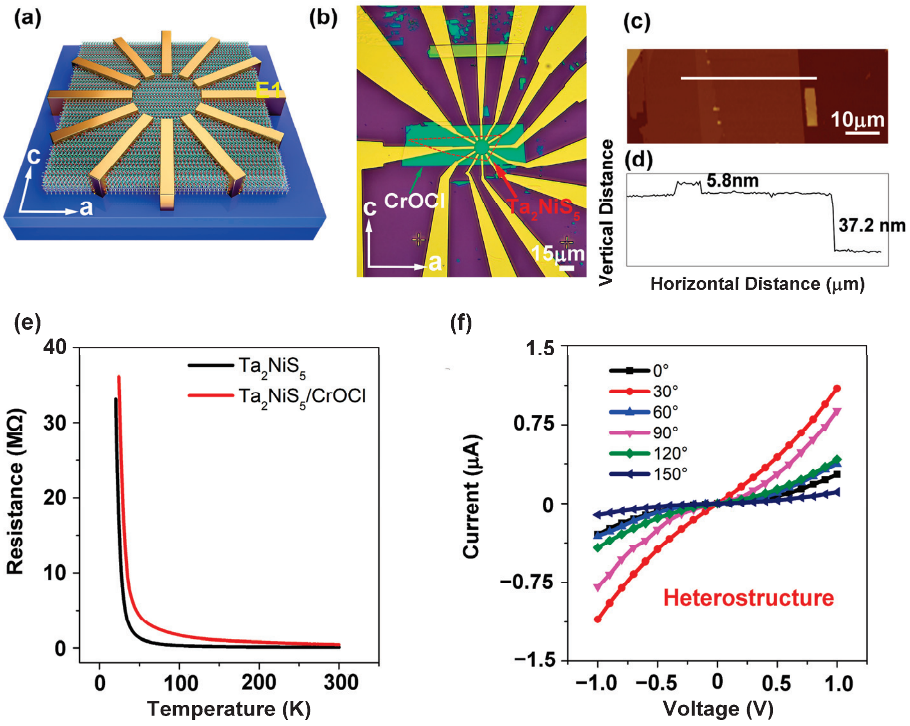

Figure 3. Characterization of Ta_2NiS_5/CrOCl device. (**a**) Schematic view of device structure. The (**b**) optical image and (**c**) AFM image of Ta_2NiS_5/CrOCl device. (**d**) Height map of Ta_2NiS_5/CrOCl device that scanned along the white area in (**c**). (**e**) Temperature-dependent resistance curves of Ta_2NiS_5 and Ta_2NiS_5/CrOCl heterostructure along *a*-axis. (**f**) I_{ds}–V_{ds} curves of Ta_2NiS_5/CrOCl heterostructure with different angles at room temperature.

To further describe the electrical anisotropy of the heterostructure, we characterized the conductivity and mobility of the Ta_2NiS_5 and Ta_2NiS_5/CrOCl devices. At a certain angle θ, the conductivity of anisotropic materials can be expressed as [32]:

$$\sigma_\theta = \sigma_a sin^2\theta + \sigma_c cos^2\theta \tag{1}$$

where σ_θ represents the conductivity of the sample in the θ direction, σ_a and σ_c denote the conductivity along the *a*- and *c*-axes, respectively. We measured the electrical conductivity at 80–300 K, as shown in Figure 4a and Table S2. The pristine Ta_2NiS_5 exhibited mirror symmetry, so its electrical transport properties exhibited two-fold rotational symmetry along the *a*-axis and *c*-axis [13]. The electrical conductivity reached its maximum along the *a*-axis and achieved its minimum along the *c*-axis. The anisotropy ratio of pristine Ta_2NiS_5 was approximately 2.1 (Figure 4c), which is similar to the reported value of 1.78–1.41 (80–300 K) in the literature [13]. Figure 4b displays a polar plot of the electrical conductivity of Ta_2NiS_5/CrOCl at 80–200 K, indicating clear anisotropy in conductance. The angle-dependent conductance exhibits typical two-fold symmetry. The σ_{max} occur at θ = 52° and 232°, while the σ_{min} are present at θ = 142° and 322°. The deviation of the polar axis might be attributed to lattice mismatch at the interface of the heterostructure, leading to a change in the periodic symmetry of the lattice. Similar phenomena have also been observed in other heterostructures [8,33]. Figure 4c shows the comparison of the anisotropy ratio ($\sigma_{max}/\sigma_{min}$) of the electrical conductivity of Ta_2NiS_5 and Ta_2NiS_5/CrOCl at different temperatures. The anisotropic ratio is approximately 15, which is one order higher than that of the pristine Ta_2NiS_5 (~2.1).

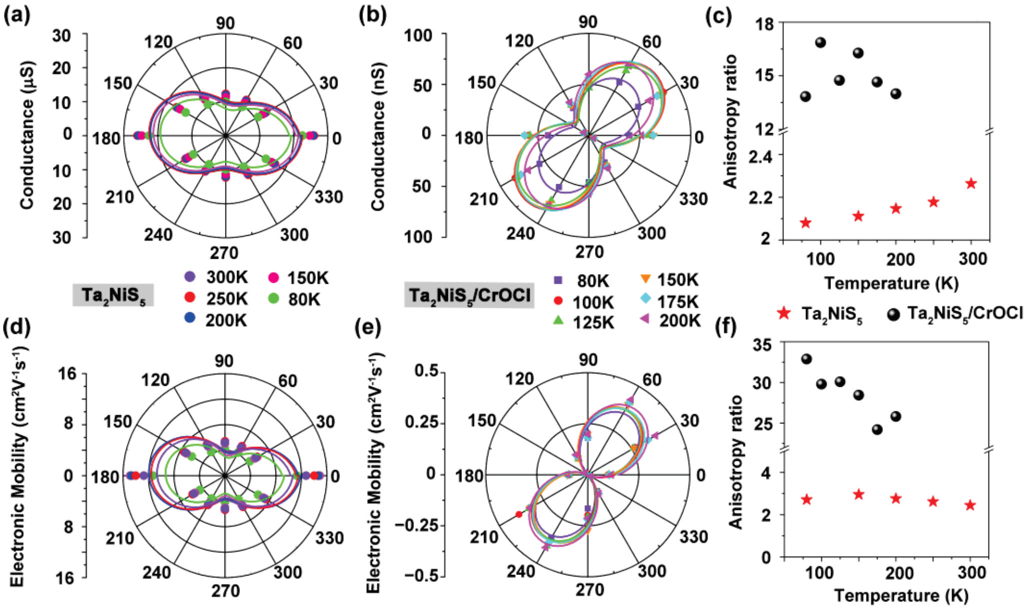

Figure 4. Electrical anisotropy of Ta_2NiS_5 and Ta_2NiS_5/CrOCl devices. Angle-dependent DC conductance of (**a**) Ta_2NiS_5 and (**b**)Ta_2NiS_5/CrOCl heterostructure at different temperatures. Angle-dependent electron mobility of (**d**) Ta_2NiS_5 and (**e**) Ta_2NiS_5/CrOCl heterostructure at different temperatures. (**c**) Conductivity σ and (**f**) mobility μ ratio of Ta_2NiS_5 and Ta_2NiS_5/CrOCl heterostructure at different temperatures.

The corresponding angle-resolved transfer characteristics for Ta_2NiS_5/CrOCl are shown in Figure S5. The transfer curves at different temperatures and angles demonstrate considerable discrepancies. The anisotropic carrier mobility of Ta_2NiS_5/CrOCl was estimated according to the equation [34]:

$$\mu = \left(\frac{dI_{ds}}{dV_g}\right)\left(\frac{L}{WC_iV_{ds}}\right) \tag{2}$$

where L and W represent the length and width of the channel. $C_i = \varepsilon_0\varepsilon_r/d$ is the gate capacitance, ε_0 is the vacuum dielectric constant, ε_r is the relative dielectric constant of SiO_2 (for Ta_2NiS_5) and CrOCl (for Ta_2NiS_5/CrOCl), and d is the thickness of SiO_2 (for Ta_2NiS_5) and CrOCl (for Ta_2NiS_5/CrOCl). dI_{ds}/dV_g represents the maximum slope of the linear region in the transfer curve. The carrier mobility of pristine Ta_2NiS_5 exhibits a similar dependence on angles to conductivity (Figure 4d). The anisotropy ratio (*a*/*c*-axis) of the mobility is approximately 2.7 (Figure 4f, red). The angle-resolved field-effect carrier mobilities are shown in Figure 4e. The maximum mobility occurs at 53° (233°), whereas the minimum is at 143° (323°), giving an anisotropic mobility ratio (μ_{max}/μ_{min}) of approximately 32 at 80 K. The anisotropic ratio of mobility decreases with the increase in temperature. At 200 K, the mobilities anisotropic ratio is approximately 25 (Figure 4f, black). The anisotropic ratio of mobilities in the heterostructure is enhanced by one order of magnitude compared with that of the pristine Ta_2NiS_5. The experimental results of electrical transport once again demonstrate that via symmetry engineering, we successfully enhanced the in-plane anisotropy in Ta_2NiS_5.

Based on the above experimental results, we conclude that the in-plane anisotropy enhancement of $Ta_2NiS_5/CrOCl$ might be attributed to the following reasons. The cause of enhanced anisotropy may be attributed to the reduction in lattice symmetry induced by the vdW interface constructed via symmetry engineering. Recent studies also indicate that constructing a vdW interface can reduce lattice symmetry [35,36]. By utilizing the symmetric engineering of functionalized heterointerfaces with anisotropic vdW dielectric SiP_2, in-plane polarization was induced within the isotropic single-layer MoS_2, resulting in anisotropic conductivity and photoluminescence [37]. Hangyel et al. studied the in-plane anisotropy of graphene induced by strong interlayer interactions with vdW epitaxially grown on MoO_3 layers [38]. The in-plane conductivity anisotropy of graphene is 1.43. By constructing a BP/Bi_2Se_3 heterostructure, anisotropic optical properties were generated within the isotropic Bi_2Se_3, with the anisotropic ratio of polarization Raman intensity reaching up to 12 [39]. The stripe moiré patterns simulated at the $Ta_2NiS_5/CrOCl$ interface also reveal that the lattice mismatch led to a decrease in the symmetry of the heterostructure. Furthermore, all the Raman frequencies shifted in the heterostructure compared with those of pristine Ta_2NiS_5, and the Raman frequency shift could be related to strain, excluding the effects of temperature, doping, and thickness. We speculate that the anisotropy enhancement of Ta_2NiS_5 may be caused by the strain induced by lattice mismatch at the vdW interface. It has been confirmed in $MoS_2/CrOCl$ heterostructures that lattice mismatch between MoS_2 and CrOCl results in uniaxial strain in the MoS_2 [12]. In addition, Ni et al. predicted that under smaller in-plane strain, anisotropy can be observed in SnSe/GeSe [40]. Thus, we infer that the enhancement of anisotropy in $Ta_2NiS_5/CrOCl$ might be attributed to the vdW-interface-induced symmetry reduction and the strain.

4. Conclusions

In conclusion, by constructing vdW heterostructures via symmetric engineering, we demonstrated the enhancement of anisotropy in the $Ta_2NiS_5/CrOCl$ heterostructure via polarized Raman spectroscopy and electrical transport measurements. Angle-resolved polarized Raman spectroscopy revealed that the polarized intensities of the B_{2g}, ^2A_g, and ^3A_g modes in the heterostructure were enhanced. The anisotropy ratios for the B_{2g}, ^2A_g, and ^3A_g modes increase from 4.6, 3.8, and 2 in the pristine Ta_2NiS_5 to 9, 5.9, and 3.3 in the $Ta_2NiS_5/CrOCl$ heterostructure, respectively. The angle-dependent electrical transport measurements prove that the anisotropic ratio of conductivity and mobility in the heterostructure increased by one order of magnitude compared with those of the pristine Ta_2NiS_5. The anisotropy ratio of conductivity was enhanced from ~2.1 (Ta_2NiS_5) to ~15 ($Ta_2NiS_5/CrOCl$), and the anisotropy ratio of mobility was enhanced from ~2.7 (Ta_2NiS_5) to ~32 ($Ta_2NiS_5/CrOCl$). The reason for this anisotropic enhancement may have contributed to the lattice mismatch and strain. This study provides inspiration to study symmetry-related van der Waals heterostructures and pave the way to novel nano-electronic devices.

Supplementary Materials: The following supporting information can be downloaded at https://www.mdpi.com/article/10.3390/nano13233050/s1. Figure S1: Photograph of Ta_2NiS_5 and CrOCl; Figure S2: The angle-dependent Raman spectra of CrOCl flake in parallel configuration; Figure S3: The angle-dependent Raman spectra of CrOCl flake in perpendicular configuration;

Figure S4: Schematic diagram of Ta_2NiS_5/CrOCl device in side view; Figure S5: Transfer characteristic curves of Ta_2NiS_5/CrOCl device; Table S1: Comparison of Raman frequencies of Ta_2NiS_5 and Ta_2NiS_5/CrOCl; Table S2: Comparison of the anisotropy ratios of Ta_2NiS_5 and Ta_2NiS_5/CrOCl heterostructure.

Author Contributions: Conceptualization, Y.S. and C.D.; investigation, Y.S. and P.C.; methodology, Y.S.; software, X.X.; formal analysis, Y.S. and C.D.; resources, G.P., X.Z. and C.D.; data curation, Y.S.; writing—original draft preparation, Y.S.; writing—review and editing, C.D., Y.Z. and X.Z.; supervision, C.D. and X.Z.; project administration, G.P. and W.C. All authors have read and agreed to the published version of the manuscript.

Funding: This research was funded by the National Natural Science Foundation of China (NSFC) (grant nos. 11874423 and 11404399).

Data Availability Statement: The data presented in this study are available upon request from the corresponding authors.

Acknowledgments: The authors thank Xiao Guo from the Institute of Physics, the Chinese Academy of Sciences, for his guidance on the discussion of the data and revising of the manuscript.

Conflicts of Interest: The authors declare no conflict of interest. All authors have read and agreed to the published version of the manuscript.

References

1. Zhong, M.; Meng, H.; Liu, S.; Yang, H.; Shen, W.; Hu, C.; Yang, J.; Ren, Z.; Li, B.; Liu, Y.; et al. In-Plane Optical and Electrical Anisotropy of 2D Black Arsenic. *ACS Nano* **2021**, *15*, 1701–1709. [CrossRef] [PubMed]
2. Yan, Y.; Xiong, W.; Li, S.; Zhao, K.; Wang, X.; Su, J.; Song, X.; Li, X.; Zhang, S.; Yang, H.; et al. Direct Wide Bandgap 2D $GeSe_2$ Monolayer toward Anisotropic UV Photodetection. *Adv. Opt. Mater.* **2019**, *7*, 1900622. [CrossRef]
3. Xia, F.; Wang, H.; Jia, Y. Rediscovering black phosphorus as an anisotropic layered material for optoelectronics and electronics. *Nat. Commun.* **2014**, *5*, 4458. [CrossRef] [PubMed]
4. Yang, S.; Yang, Y.; Wu, M.; Hu, C.; Shen, W.; Gong, Y.; Huang, L.; Jiang, C.; Zhang, Y.; Ajayan, P.M. Highly In-Plane Optical and Electrical Anisotropy of 2D Germanium Arsenide. *Adv. Funct. Mater.* **2018**, *28*, 1707379. [CrossRef]
5. Qiu, M.; Sun, Z.T.; Sang, D.K.; Han, X.G.; Zhang, H.; Niu, C.M. Current progress in black phosphorus materials and their applications in electrochemical energy storage. *Nanoscale* **2017**, *9*, 13384–13403. [CrossRef]
6. Islam, A.; van den Akker, A.; Feng, P.X.L. Anisotropic Thermal Conductivity of Suspended Black Phosphorus Probed by Opto-Thermomechanical Resonance Spectromicroscopy. *Nano Lett.* **2018**, *18*, 7683–7691. [CrossRef]
7. Liu, H.W.; Hu, K.; Yan, D.F.; Chen, R.; Zou, Y.Q.; Liu, H.B.; Wang, S.Y. Recent Advances on Black Phosphorus for Energy Storage, Catalysis, and Sensor Applications. *Adv. Mater.* **2018**, *30*, 1800295. [CrossRef]
8. Zhu, W.; Wei, X.; Yan, F.; Lv, Q.; Hu, C.; Wang, K. Broadband polarized photodetector based on p-BP/n-ReS_2 heterojunction. *J. Semicond.* **2019**, *40*, 092001. [CrossRef]
9. Akamatsu, T.; Ideue, T.; Zhou, L.; Dong, Y.; Kitamura, S.; Yoshii, M.; Yang, D.; Onga, M.; Nakagawa, Y.; Watanabe, K.; et al. A van der Waals interface that creates in-plane polarization and a spontaneous photovoltaic effect. *Science* **2021**, *372*, 68–72. [CrossRef]
10. Bai, Y.; Zhou, L.; Wang, J.; Wu, W.; McGilly, L.J.; Halbertal, D.; Lo, C.F.B.; Liu, F.; Ardelean, J.; Rivera, P.; et al. Excitons in strain-induced one-dimensional moire potentials at transition metal dichalcogenide heterojunctions. *Nat. Mater.* **2020**, *19*, 1068–1073. [CrossRef]
11. Wang, L.; Shih, E.-M.; Ghiotto, A.; Xian, L.; Rhodes, D.A.; Tan, C.; Claassen, M.; Kennes, D.M.; Bai, Y.; Kim, B.; et al. Correlated electronic phases in twisted bilayer transition metal dichalcogenides. *Nat. Mater.* **2020**, *19*, 861–866. [CrossRef] [PubMed]
12. Zheng, X.; Wei, Y.; Zhang, X.; Wei, Z.; Luo, W.; Guo, X.; Liu, J.; Peng, G.; Cai, W.; Huang, H.; et al. Symmetry Engineering Induced In-Plane Polarization in MoS_2 through Van der Waals Interlayer Coupling. *Adv. Funct. Mater.* **2022**, *28*, 2202658. [CrossRef]
13. Li, L.; Gong, P.; Wang, W.; Deng, B.; Pi, L.; Yu, J.; Zhou, X.; Shi, X.; Li, H.; Zhai, T. Strong In-Plane Anisotropies of Optical and Electrical Response in Layered Dimetal Chalcogenide. *ACS Nano* **2017**, *11*, 10264–10272. [CrossRef]
14. Su, Y.; Deng, C.; Liu, J.; Zheng, X.; Wei, Y.; Chen, Y.; Yu, W.; Guo, X.; Cai, W.; Peng, G.; et al. Highly in-plane anisotropy of thermal transport in suspended ternary chalcogenide Ta_2NiS_5. *Nano Res.* **2022**, *15*, 6601–6606. [CrossRef]
15. Tan, C.; Yu, P.; Hu, Y.; Chen, J.; Huang, Y.; Cai, Y.; Luo, Z.; Li, B.; Lu, Q.; Wang, L.; et al. High-Yield Exfoliation of Ultrathin Two-Dimensional Ternary Chalcogenide Nanosheets for Highly Sensitive and Selective Fluorescence DNA Sensors. *J. Am. Chem. Soc.* **2015**, *137*, 10430–10436. [CrossRef]
16. Duan, Q.; Yang, L.; He, Y.; Chen, L.; Li, J.; Miao, L.; Zhao, C. Layered Ta_2NiS_5 Q-Switcher for Mid-Infrared Fluoride Fiber Laser. *IEEE Photonics J.* **2021**, *13*, 1–4. [CrossRef]
17. Mu, K.; Chen, H.; Li, Y.; Zhang, Y.; Wang, P.; Zhang, B.; Liu, Y.; Zhang, G.; Song, L.; Sun, Z. Electronic structures of layered Ta_2NiS_5 single crystals revealed by high-resolution angle-resolved photoemission spectroscopy. *J. Mater. Chem. C* **2018**, *6*, 3976–3981. [CrossRef]

18. Luo, Z.; Maassen, J.; Deng, Y.; Du, Y.; Garrelts, R.P.; Lundstrom, M.S.; Ye, P.D.; Xu, X. Anisotropic in-plane thermal conductivity observed in few-layer black phosphorus. *Nat. Commun.* **2015**, *6*, 8572. [CrossRef] [PubMed]
19. Yin, S.; Zhang, W.; Tan, C.; Chen, L.; Chen, J.; Li, G.; Zhang, H.; Zhang, Y.; Wang, W.; Li, L. Thermal Conductivity of Few-Layer PtS_2 and $PtSe_2$ Obtained from Optothermal Raman Spectroscopy. *J. Phys. Chem. C* **2021**, *125*, 16129–16135. [CrossRef]
20. Chen, Y.; Peng, B.; Cong, C.; Shang, J.; Wu, L.; Yang, W.; Zhou, J.; Yu, P.; Zhang, H.; Wang, Y.; et al. In-Plane Anisotropic Thermal Conductivity of Few-Layered Transition Metal Dichalcogenide Td-WTe_2. *Adv. Mater.* **2019**, *31*, e1804979. [CrossRef]
21. Miao, N.; Xu, B.; Zhu, L.; Zhou, J.; Sun, Z. 2D Intrinsic Ferromagnets from van der Waals Antiferromagnets. *J. Am. Chem. Soc.* **2018**, *140*, 2417–2420. [CrossRef] [PubMed]
22. Zhang, T.; Wang, Y.; Li, H.; Zhong, F.; Shi, J.; Wu, M.; Sun, Z.; Shen, W.; Wei, B.; Hu, W.; et al. Magnetism and Optical Anisotropy in van der Waals Antiferromagnetic Insulator CrOCl. *ACS Nano* **2019**, *13*, 11353–11362. [CrossRef] [PubMed]
23. Qing, X.; Li, H.; Zhong, C.; Zhou, P.; Dong, Z.; Liu, J. Magnetism and spin exchange coupling in strained monolayer CrOCl. *Phys. Chem. Chem. Phys.* **2020**, *22*, 17255–17262. [CrossRef] [PubMed]
24. Wei, Z.; Zheng, X.; Wei, Y.; Zhang, X.; Luo, W.; Liu, J.; Peng, G.; Huang, H.; Lv, T.; Zhang, X.; et al. Van der Waals Interlayer Coupling Induces Distinct Linear Dichroism in WSe_2 Photodetectors. *Adv. Opt. Mater.* **2022**, *11*, 2201962. [CrossRef]
25. Feng, Y.; Chen, R.; He, J.; Qi, L.; Zhang, Y.; Sun, T.; Zhu, X.; Liu, W.; Ma, W.; Shen, W.; et al. Visible to mid-infrared giant in-plane optical anisotropy in ternary van der Waals crystals. *Nat. Commun.* **2023**, *14*, 6739. [CrossRef]
26. Tang, K.; Qi, W. Moire-Pattern-Tuned Electronic Structures of van der Waals Heterostructures. *Adv. Funct. Mater.* **2020**, *30*, 2002672. [CrossRef]
27. Sunku, S.S.; Ni, G.X.; Jiang, B.Y.; Yoo, H.; Sternbach, A.; McLeod, A.S.; Stauber, T.; Xiong, L.; Taniguchi, T.; Watanabe, K.; et al. Photonic crystals for nano-light in moire graphene superlattices. *Science* **2018**, *362*, 1153–1156. [CrossRef]
28. Yoo, H.; Engelke, R.; Carr, S.; Fang, S.; Zhang, K.; Cazeaux, P.; Sung, S.H.; Hovden, R.; Tsen, A.W.; Taniguchi, T.; et al. Atomic and electronic reconstruction at the van der Waals interface in twisted bilayer graphene. *Nat. Mater.* **2019**, *18*, 448–453. [CrossRef]
29. Wei, Y.; Wei, Z.; Zheng, X.; Liu, J.; Chen, Y.; Su, Y.; Luo, W.; Peng, G.; Huang, H.; Cai, W.; et al. Stress Effects on Temperature-Dependent In-Plane Raman Modes of Supported Monolayer Graphene Induced by Thermal Annealing. *Nanomaterials* **2021**, *11*, 2751. [CrossRef]
30. Yoon, D.; Son, Y.-W.; Cheong, H. Strain-Dependent Splitting of the Double-Resonance Raman Scattering Band in Graphene. *Phys. Rev. Lett.* **2011**, *106*, 155502. [CrossRef]
31. Ferrari, A.C.; Basko, D.M. Raman spectroscopy as a versatile tool for studying the properties of graphene. *Nat. Nanotechnol.* **2013**, *8*, 235–246. [CrossRef] [PubMed]
32. Qiu, G.; Du, Y.; Charnas, A.; Zhou, H.; Jin, S.; Luo, Z.; Zemlyanov, D.Y.; Xu, X.; Cheng, G.J.; Ye, P.D. Observation of Optical and Electrical In-Plane Anisotropy in High-Mobility Few-Layer $ZrTe_5$. *Nano Lett.* **2016**, *16*, 7364–7369. [CrossRef] [PubMed]
33. Gao, X.G.; Chen, G.X.; Li, D.K.; Li, X.K.; Liu, Z.B.; Tian, J.G. Modulation of photothermal anisotropy using black phosphorus/rhenium diselenide heterostructures. *Nanoscale* **2018**, *10*, 10844–10849. [CrossRef] [PubMed]
34. Tian, Z.; Guo, C.; Zhao, M.; Li, R.; Xue, J. Two-Dimensional SnS: A Phosphorene Analogue with Strong In-Plane Electronic Anisotropy. *ACS Nano* **2017**, *11*, 2219–2226. [CrossRef] [PubMed]
35. Chaudhary, K.; Tamagnone, M.; Rezaee, M.; Bediako, D.K.; Ambrosio, A.; Kim, P.; Capasso, F. Engineering phonon polaritons in van der Waals heterostructures to enhance in-plane optical anisotropy. *Sci. Adv.* **2019**, *5*, 7171. [CrossRef] [PubMed]
36. Xiao, M.; Yang, H.; Shen, W.; Hu, C.; Zhao, K.; Gao, Q.; Pan, L.; Liu, L.; Wang, C.; Shen, G.; et al. Symmetry-Reduction Enhanced Polarization-Sensitive Photodetection in Core-Shell SbI_3/Sb_2O_3 van der Waals Heterostructure. *Small* **2020**, *16*, e1907172. [CrossRef]
37. Li, Z.; Huang, J.; Zhou, L.; Xu, Z.; Qin, F.; Chen, P.; Sun, X.; Liu, G.; Sui, C.; Qiu, C.; et al. An anisotropic van der Waals dielectric for symmetry engineering in functionalized heterointerfaces. *Nat. Commun.* **2023**, *14*, 5568. [CrossRef] [PubMed]
38. Kim, H.; Kim, J.H.; Kim, J.; Park, J.; Park, K.; Baek, J.-H.; Shin, J.-C.; Lee, H.; Son, J.; Ryu, S.; et al. In-plane anisotropy of graphene by strong interlayer interactions with van der Waals epitaxially grown MoO_3. *Sci. Adv.* **2023**, *9*, eadg6696. [CrossRef]
39. Mao, N.; Zhang, S.; Wu, J.; Tian, H.; Wu, J.; Xu, H.; Peng, H.; Tong, L.; Zhang, J. Investigation of black phosphorus as a nano-optical polarization element by polarized Raman spectroscopy. *Nano Res.* **2018**, *11*, 3154–3163. [CrossRef]
40. Ni, H.; Li, M.; Hu, Y.; Mao, C.; Xue, L.; Zeng, H.; Yan, Z.; Wu, Y.; Zheng, C. Two-dimensional SnSe/GeSe van der Waals heterostructure with strain-tunable electronic and optical properties. *J. Phys. Chem. Solids* **2019**, *131*, 223–229. [CrossRef]

nanomaterials

Article

Multi-Layer Palladium Diselenide as a Contact Material for Two-Dimensional Tungsten Diselenide Field-Effect Transistors

Gennadiy Murastov [1,†], Muhammad Awais Aslam [1,†], Simon Leitner [1], Vadym Tkachuk [2], Iva Plutnarová [3], Egon Pavlica [2], Raul D. Rodriguez [4], Zdenek Sofer [3] and Aleksandar Matković [1,*]

[1] Department Physics, Mechanics and Electrical Engineering, Montanuniversität Leoben, Franz Josef Strasse 18, 8700 Leoben, Austria; simon.leitner@stud.unileoben.ac.at (S.L.)
[2] Laboratory of Organic Matter Physics, University of Nova Gorica, Vipavska 13, SI-5000 Nova Gorica, Slovenia; vadym.tkachuk@ung.si (V.T.); egon.pavlica@ung.si (E.P.)
[3] Department of Inorganic Chemistry, University of Chemistry and Technology Prague, Technická 5, 166 28 Prague, Czech Republic; plutnari@vscht.cz (I.P.); zdenek.sofer@vscht.cz (Z.S.)
[4] Research School of Chemistry & Applied Biomedical Sciences, Tomsk Polytechnic University, Lenina ave. 30, 634034 Tomsk, Russia; raul@tpu.ru
* Correspondence: aleksandar.matkovic@unileoben.ac.at
† These authors contributed equally to this work.

Abstract: Tungsten diselenide (WSe_2) has emerged as a promising ambipolar semiconductor material for field-effect transistors (FETs) due to its unique electronic properties, including a sizeable band gap, high carrier mobility, and remarkable on–off ratio. However, engineering the contacts to WSe_2 remains an issue, and high contact barriers prevent the utilization of the full performance in electronic applications. Furthermore, it could be possible to tune the contacts to WSe_2 for effective electron or hole injection and consequently pin the threshold voltage to either conduction or valence band. This would be the way to achieve complementary metal–oxide–semiconductor devices without doping of the channel material.This study investigates the behaviour of two-dimensional WSe_2 field-effect transistors with multi-layer palladium diselenide ($PdSe_2$) as a contact material. We demonstrate that $PdSe_2$ contacts favour hole injection while preserving the ambipolar nature of the channel material. This consequently yields high-performance *p*-type WSe_2 devices with $PdSe_2$ van der Waals contacts. Further, we explore the tunability of the contact interface by selective laser alteration of the WSe_2 under the contacts, enabling pinning of the threshold voltage to the valence band of WSe_2, yielding pure *p*-type operation of the devices.

Keywords: palladium diselenide; tungsten diselenide; tungsten selenium oxide; semi-metal; laser treatment; contact engineering; field-effect transistor; pMOS; van der Waals electronics; 2D materials

1. Introduction

Two-dimensional (2D) materials, and especially 2D semiconductors, are emerging as ever-more promising platforms to be added into very-large-scale integration (VLSI) technologies [1,2]. This is driven by the shrinking pitch sizes required to achieve higher integration density, energy efficiency, and speed of electronic circuits [3,4]. To achieve this feat, comprehensive studies have been undertaken to offer 2D channel materials and insulators [5,6] with performance parameters comparable to those of silicon-based technologies. Both traditional (Al_2O_3/HfO_2) and 2D insulators have shown promising results in developing complex architectures [7,8]. Similarly, a huge library of 2D semiconductors is available for the purpose of choosing *p*-type, *n*-type, or ambipolar channel materials [9,10]. In this regard, ambipolar WSe_2 has garnered keen interest in the scientific community due to its potential applications towards complementary metal–oxide–semiconductor (CMOS) technology, solar cells, water splitting, light emitting, and gas sensing [11–15]. Moreover, patterned nanoribbons of WSe_2 have been shown to offer high electrical performance and the possibility to be coupled with metallic nanoparticles, which offers exciting possibilities in optoelectronic applications and tunable catalysis [16,17]. Like other 2D materials, the properties of WSe_2 can be tuned via thickness [18], plasma treatment [19], strain [20], and choice of contacts [21,22].

However, the development of technology-relevant metal–semiconductor interfaces remains a significant bottleneck for the integration of 2D semiconductors into VLSI [1,23]. This is also true for achieving high-quality contacts to ambipolar WSe_2. The existing metal electrode deposition technologies cause the degradation of the 2D materials at the contact interface by the formation of metal-induced gap states (MIGS) and defect-induced gap states. In turn, these gap states result in the formation of large barriers at the junctions, consequently lowering the device performance and increasing energy consumption [24,25]. In addition to the creation of potential barriers, MIGS also alter transport fundamentally by changing transmission around the transport gap. An example of this can be seen in metallization-induced change of the quantum limits of contact resistance in one-dimensional contacts to semiconducting graphene nanoribbons [26]. There have been several efforts to find suitable contact materials and contact deposition methods to realise the full potential of 2D material-based circuits. These include the use of edge contacts [27,28], low-work-function metals [29], ultra-high vacuum evaporation [30], buffer layers [31], self-assembled dipolar monolayers [32], and dry stamping of metal electrodes [33,34]. In particular, metallised edge contacts are commonly the best-performing technology in large-area 2D material-based devices [27,28]. However, this is not the case for one-dimensional (1D) or quasi-1D nanostructures of 2D materials such as nanoribbons and nanowires, as phosphorene nanodevices with edge contacts [35,36].

More recently, semi-metallic contacts such as bismuth, antimony, and graphene have shown promising results [37–39]. However, semi-metal depositions involve heating of the substrate up to 100 °C to achieve a particular orientation of the metal (Sb $01\bar{1}\bar{2}$ on MoS_2), which tends to introduce defects into heat-sensitive 2D semiconductors with ambipolar functionality, such as WSe_2 [40,41] and black phosphorus [42]. In case of graphene contacts, the growth of graphene films as top electrodes would require very high temperatures [43], hindering direct growth as the incorporation path to the back-end-of-line (BEoL) processes. However, ambipolar 2D materials are critical for CMOS electronic applications. It is essential to develop contacts which preserve the ambipolar behaviour while providing sufficient on-state currents and I_{ON}/I_{OFF} ratios relevant for technological aspects. To address this challenge, significant efforts have been made, including the use of In and Pd contacts to WSe_2 [44,45].

The use of $PdSe_2$ as a contact material was first demonstrated by Oyedele et al., who employed defective $Pd_{17}Se_{15}$ as contacts with $PdSe_2$ to demonstrate a low Schottky barrier [46] and later by Seo et al. for the realization of $PdSe_2$-based CMOS devices [47]. $PdSe_2$ has also been used to contact MoS_2 in a junction field-effect transistor as a top gate due to its promising optoelectronic properties which include long-wavelength infrared photo responsivity [48–51]. With a layer-dependent bandgap in the infrared region, $PdSe_2$ itself is a unique member of the transition metal dichalcogenide family with potential uses in optoelectronic devices [52]. It behaves as a semi-metal for thicknesses above 20 nm and transforms to a semi-conducting state for thinner layers [53,54]. Large-area $PdSe_2$ can be grown at temperatures as low as 250 °C [55], unlike graphite, which makes it critical for BEoL integration as a van der Waals electrode material. Moreover, graphite contacts dope the WSe_2 towards a dominant n-type electrical response, therefore disrupting the ambipolar nature of WSe_2 [56].

In this work, we propose $PdSe_2$ contacts to WSe_2 which demonstrate high I_{ON}/I_{OFF} ratio and high on-state currents while maintaining the intrinsic ambipolar behaviour of the channel material. To further tune the behaviour of our devices, we propose localised laser treatment of WSe_2 at the contact regions to demonstrate dominant p-type FETs with high threshold voltage stability. This can allow for the co-integration of p-type and ambipolar devices in a circuit without the need to change the contact material nor the need to introduce any dopants into the channel.

2. Materials and Methods

2.1. $PdSe_2$ Crystal Growth

$PdSe_2$ crystals were synthesised by direct reaction of elements in a quartz glass ampoule. Powder palladium (99.99%, −100 mesh, Safina, Prague-Vestec, Czech Republic) and selenium granules (99.9999%, 2–4 mm granules, Wuhan Xinrong New Material Co., Wuhan, China) corresponding to 3 g of $PdSe_2$ were placed in a quartz ampoule (25 × 100 mm) with additional selenium corresponding to 1% in excess. The ampoule was melt sealed under a high vacuum (1×10^{-3} Pa) using an oxygen–hydrogen torch and placed in muffle furnace. The ampoule was heated at 850 °C using a heating rate of 1 °C/min, and after 12 h it was cooled to room temperature at a cooling rate of 0.1 °C/min. The ampoule with formed $PdSe_2$ crystals was opened in an argon-filled glove box.

2.2. Device Fabrication

Using laser lithography (DaLi, Cerklje, Slovenia) and thermal evaporation, 45 nm/5 nm stripe-like Au/Cr electrodes were patterned onto a 300 nm SiO_2/Si substrate. hBN flakes were used as a bottom gate oxide on top of one the Au pads. Multi-layer $PdSe_2$ or crystal (kish) graphite flakes were placed on top of the WSe_2 flakes as source and drain electrodes. Flakes of 2D materials were mechanically exfoliated from bulk single crystals using commercially available Nitto tape and polydimethylsiloxane (PDMS) Gel–Pak–DGL–X4. The flakes were selected based on optical contrast and transferred one by one to build up the devices. The thickness of the hBN used for the devices was approximately 20 nm, considering a value for the relative dielectric constant of ϵ_r = 3.5 [57]. Further, optical microscopy, atomic force microscopy (AFM), and Raman spectroscopy measurements were performed to confirm the layer thickness, uniformity, and exact device geometries.

2.3. Electrical Characterization

Room temperature (RT) and low-temperature (78 K) electrical characterizations were performed using a Keithley 2636A Source Meter (Tektronix GmbH, Koeln, Germany) attached to an Instec probe station (Boulder, CO, USA). The samples were contacted via Au-coated Ti electrical cantilever microprobes. The Instec's mK2000 temperature controller was used to monitor the temperature with a resolution of 0.01 K. The cooling and heating rates were 20 °C/min and 10 °C/min, respectively.

2.4. FET Figures of Merit (FOM) Extraction and Device Modelling

The off-state current (I_{OFF}) was defined as the minimum in $I_D(V_G)$ curves, while the on-state current (I_{ON}) was defined as the maximum obtained in $I_D(V_G)$ for the electron or hole branch. The maximum current is limited by the amount of the electrostatic field that can be applied through the back gate, and I_{ON} was estimated 5 to 8 V away from the threshold voltage (V_{th}). The threshold voltage was estimated by extrapolation of the linear fit to the point of intersection of the I_D = 0 A line. The linear fit was performed in the V_G region shifted by 2 V from the onset voltage point (V_{on}) and by 4 V to 5 V from the V_{on}. The onset voltage point was defined as the V_G point from which the I_D continuously increases from the gate leakage levels (usually 0.5–2 × 10^{-11} A). The middle of the region between V_{on} and V_{th} was used to estimate the sub-threshold swing (SS) values.

Modelling of the FET output curves was performed using the ideal transistor operating in the linear regime, shifted by the V_{th} via a capacitor at the gate. To model the non-ideal and non-linear behaviour of the contacts, a linear resistor and a Schottky diode were added in series to the ideal transistor. The current through the transistor was described as: $I_D = (\mu C_{ox} W/L) \cdot ((V_G - V_{th}) \cdot V_{FET} + (V_{FET}^2/2))$. Here, V_{FET} corresponds to the fraction of the total V_D bias that is experienced by the ideal transistor, C_{ox} is the area-specific gate dielectric capacitance, and μ is the intrinsic mobility. Upon reaching the limit of the linear regime — defined as the maximum $I_D(V_{FET})$ value of the model — the maximum current level was kept independent of the V_{FET}, describing the saturation of the device. The ohmic component of the contact resistance is defined by a linear resistor, with its corresponding potential drop described as $V_{ohmic} = R_{ohmic} \cdot I_D$. The non-linear component of the contact resistance is described by: $V_{junction} = V_{thermal}\ln(1 + I_D/I_0))$. Here, $V_{thermal} = k_B T/e$ and k_B stands for the Boltzmann's constant, T is fixed to the set temperature of the experiment, and e is the unit charge. I_0 represents the reverse current of the Schottky diode. Considering that $V_D = V_{FET} + V_{ohmic} + V_{junction}$ the system is solved in a self-consistent manner using three fitting parameters: μ, R_{ohmic}, and I_0. In the first fitting iteration, the parameters are assumed to be independent of V_G and are fitted to the sequence of the electrical output curves for the hole or the electron branch. In the second iteration, for each V_G the parameters are allowed to vary by ±20% from the previously determined values. The contact resistance is further expressed as a device width-scaled (W) value: $WR_C = W((V_{ohmic} + V_{junction})/I_D)$.

2.5. Laser Treatment of WSe_2

The freshly exfoliated channel WSe_2 was laser-treated (532 nm, 100× objective) under ambient conditions using a motorised sample stage. The laser modification of WSe_2 was performed prior to the transfer of $PdSe_2$ contacts. The laser power was set to 50 mW. A point-to-point scan was carried out with a resolution of 0.2 µm, and a fixed exposure time of 0.1 s for each point.

2.6. AFM and In Operando KPFM Measurements

Horiba/AIST-NT Omegascope (Lille, France) AFM system was used for the AFM topography measurements, with Nunano SPARK 350 Pt probes (spring constant of 42 Nm^{-1}, resonant frequency 330 kHz, and tip radius of 30 nm). Topography images were processed in the open-source software Gwyddion v2.56 [58], applying zero-order line correction and three-point plane averaging.

In operando Kelvin Probe Force Microscopy (KPFM) measurements were carried out on $PdSe_2$-contacted devices under the ambient conditions. To prevent device degradation during prolonged ambient operation, the devices for the KPFM experiments were top capped by an additional 10 nm thick hBN flake. For the device biasing during the KPFM measurements, a Keithley 2636A Source Meter was used, and the device ground (source) was connected to the ground of the KPFM feedback loop. KPFM was operated in a frequency-modulated two-pass regime with a second-pass lift height of 8 nm, yielding a total of about 18 nm distance between the probe and the hBN capped channel. To extract electrostatic potential drops across the channel of an operating device, a single line in the middle of the device was repeatedly scanned while the external bias was applied. To compensate for the work function and stray field differences, each potential drop is normalised to the cross-sections recorded with V_D = 0 V, following the procedure detailed in Ref. [32].

2.7. Raman Spectroscopy

Raman spectroscopy measurements were performed using a Horiba LabRam HR Evolution confocal Raman spectrometer (Lille, France) with 1800 lines/mm gratings. A 532 nm laser was used with an excitation power in the range of 0.1–3.2 mW. The laser spot was focused by a 100×, 0.9 NA objective.

3. Results and Discussions

3.1. Electrical Characteristics of WSe_2 FETs with Graphite and $PdSe_2$ Electrodes

Figure 1a depicts a schematic representation of the 2D layer stacks along with optical images of the typical devices with graphite (Gr) and $PdSe_2$ contacts. Figure 1b,c present in a semi-log scale the device width-scaled electrical transfer curves, source–drain current as a function of the applied local back gate bias $I_D(V_G)$, comparing the two different types of van der Waals contacts (Gr and $PdSe_2$) to multilayered WSe_2. For each transfer curve, five subsequent forward and backward V_G sweeps were carried out at 2 V/s. In both cases, a small hysteresis of 200 mV was observed. The measurements were carried out at 78 K to minimise charge-trap-related effects and unintentional doping effects from the trapped water and air at the interfaces [16,59,60]. Graphite-contacted devices showed a dominant *n*-type behaviour which was previously reported and attributed to the band alignment that favours electron injection from the graphite towards the channel material [56,61]. In Figure 1b, the second device (Device 2) also exhibits notably high current in the hole branch, however, the threshold voltage remains closer to the electron branch, as expected for the efficient electron injection from graphite electrodes [56].

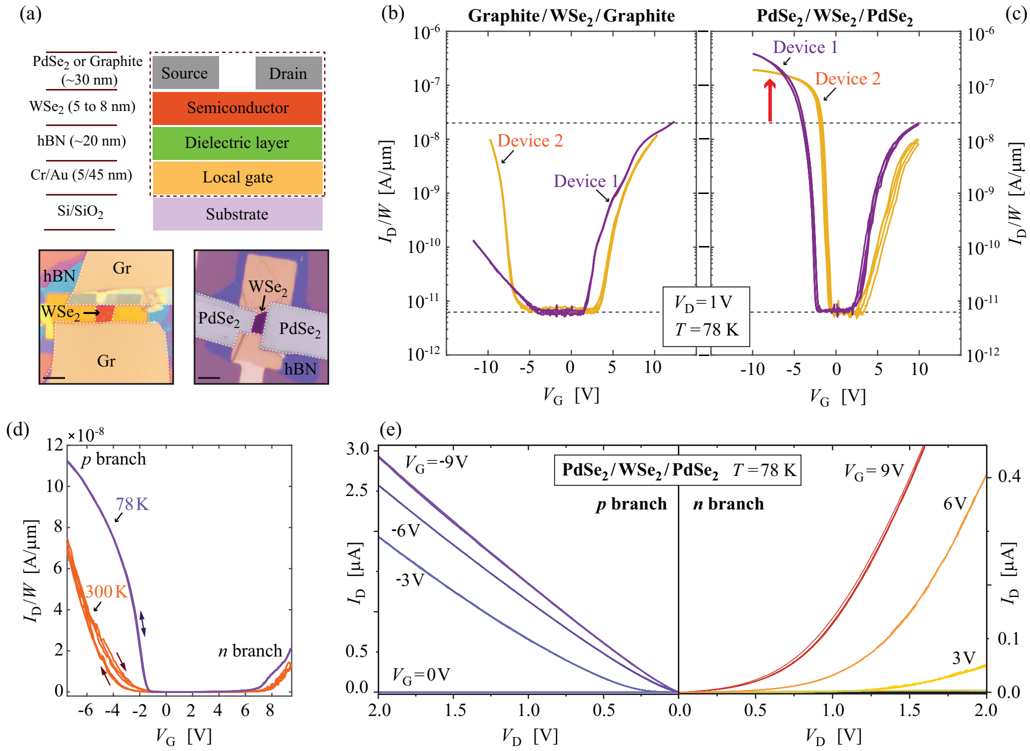

Figure 1. Electrical characteristics of graphite- and $PdSe_2$-contacted WSe_2 FETs: (**a**) Schematic representation of device configuration with optical images of WSe_2 FETs (scale bar: 10 µm). (**b**,**c**) Semi-log electrical transfer curves of devices with graphite (Gr) and $PdSe_2$ contacts, respectively. The I_D in (**b**,**c**) is scaled by the mean width of the channels to allow for better comparison of the current values between the different devices. The horizontal dashed lines that interconnect (**b**,**c**) serve as a guide to see the reached on- and off-state current levels. The red arrow in (**c**) indicates over an order of magnitude larger current of the hole branch in the case of $PdSe_2$ contacts. (**d**) Comparison of the device width-scaled electrical transfer curves ($PdSe_2$ contacted device) measured at 300 K (orange) and 78 K (purple), presented in linear scale. The arrows indicate the direction of the V_G sweep, highlighting an increase in the hysteresis observed at 300 K. (**e**) Output curves for the hole and electron branches at 78 K (2×10^{-2} mbar) of a device with $PdSe_2$ contacts. Note that the current values for the *n*-branch are approximately one order of magnitude lower than for the *p*-branch. The different colored lines in (**e**) represent the curves at the different values of V_G, as indicated in the figure.

The main difference in the electrical transfer curves between Gr and $PdSe_2$-contacted devices occurs at the negative V_G values, i.e., in the hole branch. In contrast to graphite-contacted devices, when $PdSe_2$ is used as a contact, the FETs were found to exhibit dominant *p*-type behaviour and an increased device performance for both electron and hole branches. This is explained by the favoured level alignment of the $PdSe_2$ with the hole branch of the WSe_2 due to the higher work function of $PdSe_2$ in comparison to graphite. The I_{ON}/I_{OFF} ratio for $PdSe_2$ ($\sim 4 \times 10^4$) was one order of magnitude better than that of graphite contacts.

Horizontal dashed lines that interconnect Figure 1b,c serve as a guide to help compare the current levels. For the WSe_2 devices reported in the literature, the I_{ON}/I_{OFF} ratio varies over several orders of magnitude [11]: from 10^2 (e.g., $NbSe_2$ contacts to the *n*-branch [56]) up to 10^9 with more elaborate device architectures and high-k dielectrics [18]. With respect to the electrode engineering to access the *p*-branch, $NbSe_2$- and Pt-contacted WSe_2 were reported to reach the values in the range 10^4–10^7 [18,56].

Furthermore, $PdSe_2$-contacted devices maintained an intrinsic behaviour which is evident by an almost equidistant V_{on} for both electron and hole branches with reference to $V_G = 0$ V. This was not the case for graphite-contacted devices where larger V_G was required to reach the on state of the *p*-branch compared to the *n*-branch, therefore indicating a disruption in the intrinsic doping levels. On average, we observe a V_{on} for the hole branch to be at (-4.5 ± 0.9) V and at (-1.9 ± 1.3) V respectively for the Gr and $PdSe_2$ contacts; similar values for the V_{on} were observed for the electron branch: (2.5 ± 1.7) V and (3.0 ± 0.8) V respectively for the Gr and $PdSe_2$ contacts.

A comparison between 300 K and 78 K width-scaled transfer curves of a $PdSe_2$-contacted device is presented in Figure 1d. The temperature primarily impacts the phonon-related carrier scattering in the channel, the Schottky junction-related potential drop, and gate dielectric interface charge trap states. Consequently, at lower temperatures we observe an overall increase in the drain currents and mobilities for both branches (by a factor of $\sim$2 comparing 78 K and 300 K), quenching of the hysteresis with respect to the forward and backward V_G sweeping, and a minor reduction in the V_{th} values.

Figure 1e represents the electrical output curves for the $PdSe_2$-contacted channel; the source–drain current as a function of the applied source–drain bias is $I_D(V_D)$. Especially at more negative V_G values (on state of the *p*-branch), the electrical output curves of the *p*-branch exhibit linear behaviour. For the *n*-branch, the overall I_D values are about one order of magnitude lower than that of the *p*-branch and show significant deviation from the linear behaviour at lower V_D values regardless of the applied V_G. All of these observations indicate that a significantly larger barrier exists for the electron than for the hole injection from $PdSe_2$ into WSe_2. At low temperatures, within the applied V_D range and for V_G more than 0.5 V away from the V_{th}, we did not observe the current saturation. However, within the same bias range at room temperature, saturation can be achieved (see Figure 2).

3.2. Contact Resistance of the $PdSe_2$/WSe_2 Interface

The contact resistance of the interface between $PdSe_2$ and WSe_2 was evaluated independently by two approaches: parameter extraction via device modelling and direct measurements by in operando KPFM. In the first approach, we have modelled the sequence of the electrical output data by applying an equivalent electrical scheme as shown in Figure 2a (see also Section 2). The system was solved in a self-consistent manner and fitted to the set of output curves either for the hole or for the electron branch, as presented in Figure 2b,c. Parameters of the ohmic (R_{ohmic}) and non-linear Schottky component (I_0) of the contact resistance were extracted, and width-scaled contact resistance (WR_C) was expressed considering specific points of operation (fixed V_D, V_G, and, consequently, I_D values). We obtain $WR_C = (2.84 \pm 0.53) \times 10^6$ Ωµm for the hole branch and $WR_C = (3.72 \pm 0.69) \times 10^8$ Ωµm for the electron branch. The values are reported for the operation at 300 K, with V_G set 5 V away from the V_{th} in both cases of the hole and the electron branches, and under 1.5 V of source–drain bias. In particular, the need to include the non-linear Schottky element in the model is evident in a strong downward bending of the output curves at lower V_D, as pointed out by the red arrows in Figure 2c. Especially in the electron branch case, at lower I_D the contact resistance and the entire device operation is Schottky junction-dominated, and almost all of the applied V_D is taken by this junction as the most resistive element in the circuit. At higher I_D, the $V_{junction}$ still dominates over V_{ohmic} by a factor of 5 to 10.

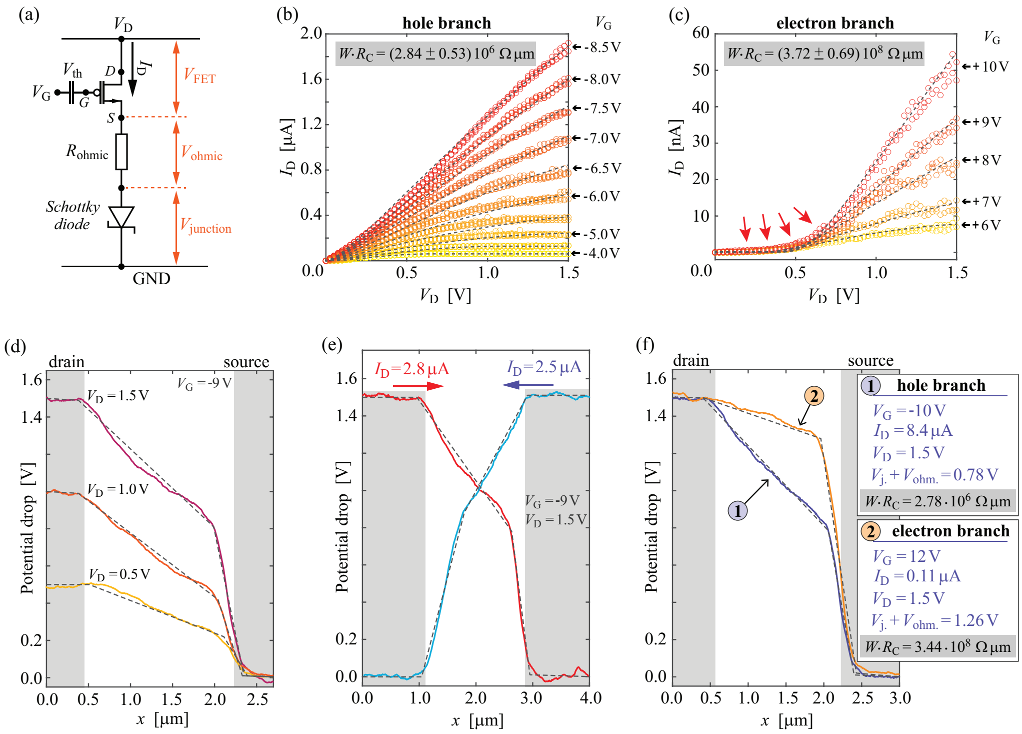

Figure 2. Contact resistance of the $PdSe_2/WSe_2$ interface: (**a**) Equivalent electrical scheme used for the self-consistent modelling of the output curves. (**b**,**c**) Electrical output curves of a $PdSe_2/WSe_2/PdSe_2$ device measured at 300 K for the hole and electron branches, respectively. Different colored circles represent the measured I_D values at set different V_G as indicated in the right corner of the sub-panels (**b**,**c**). The dashed lines are a model for the entire data set. Red arrows in (**c**) indicate a severe downward bending of the output curves at lower V_D. Contact resistance values (WR_C) extracted by modelling the curves from (**b**,**c**) are indicated in each sub-panel. (**d**–**f**) In operando KPFM potential profiles recorded as single lines across the channel, measured under ambient conditions. Solid lines present the work function difference corrected potential drops, and the dashed lines are linear fits to the experimental curves. (**d**) A sequence of the potential drops with varied V_D. (**e**) Alternating the source and drain contacts, which demonstrates that the steep potential drop is related to the grounded electrode. (**f**) Comparison of the potential drops at V_D = 1.5 V, with V_G setting the device in an on state of the hole and electron branches, labelled with (1) and (2), respectively. Insets in (**f**) provide the operation points and the extracted WR_C values from the KPFM measurements.

In the second approach to evaluating the contact resistance of the $PdSe_2/WSe_2$ interface, we have used in operando KPFM. This technique measures the electric potential several nanometres above the channel during device operation. Therefore, it resolves the potential drops between the electrodes, and allows independent distinguishing of the potential drops that correspond to the drain (not observed in our case), the channel, and the source [16,32]. An example of the potential drop profiles is presented in Figure 2d in the hole branch on state and for varied V_D between 0.5 V and 1.5 V. Four regions are clearly distinguishable in the potential drop profiles: flat potential values corresponding to the source and drain regions of the scan, a monotone drop of the potential along the channel, and a much steeper drop at the contact to the source electrode. Linear fits to these elements are presented by dashed black lines. The steeper drop connected to the transition between the channel-related potential drop and the source contact region is directly related to the $V_{\text{junction}} + V_{\text{ohmic}}$ in the device model. Knowing the I_D values during the potential drop profile measurements and the width of the device, it is possible to express the observed junction-related potential drop as the width-scaled contact resistance.

Figure 2e presents the potential drop profiles when the connections between the source and the drain are exchanged, effectively reversing the current flow direction. We observe that the contact resistance associated potential drop is connected to the grounded source electrode, i.e., that the $PdSe_2/WSe_2$ interface is rectifying. This proves the predominant Schottky nature of the contact resistance, as also suggested by the model.

Lastly, when biased under very similar operation points as in the case of the contact resistance extraction from the electrical output data sets (Figure 2f), we obtain the following device width-scaled contact resistance values obtained from in operando KPFM: $WR_C = 2.78 \times 10^6$ Ωμm for the hole-branch and $WR_C = 3.44 \times 10^8$ Ωμm for the electron branch.

The obtained WR_C values imply that $PdSe_2$ is an effective hole injector. This is seen from the two orders of magnitude larger contact resistance of the electron branch under similar operation conditions. Furthermore, the contact resistance of the $PdSe_2/WSe_2$ interface for *p*-type operation performs similar to the commonly employed evaporated metallic contacts [62,63] while preserving the intrinsic doping levels and the ambipolar nature of the WSe_2. Reported values for WSe_2 contact resistance range from 10^8 Ω μm to 10^5 Ω μm with electrostatic gating and down to 10^4 Ω μm for electrolyte gating that can induce very high density states in WSe_2 [45,56,62]. Some of the lowest values reported for the contact resistance (1.1×10^5 Ω μm) are with Pt electrodes, where MIGS cannot be excluded at the electrode interface [45].

3.3. Optimizing Contact Interface via Laser-Driven Oxidation of WSe_2

Recent work has shown that the application of mild oxygen plasma can be an effective way to reduce the Schottky barrier in multilayer WSe_2 FETs [64–66]. The plasma treatment causes the formation of a conductive tungsten selenium oxide (WSe_yO_x). The oxide was found to form in a layer-by-layer manner [64,65], effectively generating a WSe_yO_x/WSe_2 heterostructure that acts as a facilitator for the hole injection [66,67]. However, it is important to protect the channel active area during the plasma treatment to avoid device degradation. We wanted to investigate if a laser-based approach could open a way to achieve similar modification of WSe_2, as with the mild plasma treatment. An advantage of the laser-driven oxidation approach is straightforward patterning by laser scanning. Using laser irradiation (532 nm, 50 mW) under ambient conditions, we have observed a similar oxidation process of WSe_2.

To explore the influence of the WSe_yO_x layer on the contact properties between WSe_2 and $PdSe_2$, we have irradiated an area of the WSe_2 flake that is slightly larger than the contact area with $PdSe_2$. After the laser treatment, $PdSe_2$ flakes were transferred and used as contacts. Figure 3a(*i*–*iii*) show the schematic representation of the laser treatment and the device assembly process for the WSe_yO_x-modified contacts. Figure 3b(*i*–*iii*) represent the corresponding optical images of the flake and the final device, where only one side of the flake was treated by the laser. Figure 3c presents a zoomed-in region of the interface to highlight the parts of the ablated layers, oxidised layers, and remaining pristine WSe_2 layers.

AFM was performed to observe the morphological and height changes due to laser treatment. The results are presented in Figure 4a,b. AFM image before laser treatment shows large bubbles formed at the interface between WSe_2 and hBN, as well as between hBN and SiO_2 interface. This is expected for 2D material heterostructures assembled under ambient conditions and using PDMS stamps due to the entrapment of air and water [68–70]. Such interfaces result in localised charge-trap and scattering centres, and a flat interface is desired to achieve better performance [71,72]. Interestingly, laser treatment resulted in the removal and migration of these bubbles from the scan area, even at the regions not directly exposed to the laser irradiation. This is illustrated in Figure 4b. Such behaviour can be attributed to the self-cleaning property of 2D materials under a systematic sweep of the laser spot which allows local heating and migration of the trapped water/air bubbles at the interfaces [71,72]. The arrows in Figure 4b represent the direction of laser sweeping, and the dashed rectangle indicates the laser-exposed area. Figure 4a,b (bottom) show the change in height of the flake before and after the treatment. The resultant height corresponds to a thickness of 3.9 nm. This indicates the ablation of about five mono-layers of WSe_2, and the remaining flake effectively forms a WSe_yO_x/WSe_2 heterostructure. Combined with Raman spectroscopy data (Figure 4c) we estimate that after the laser treatment, about three layers of WSe_2 remain, with about 2 nm of WSe_yO_x formed on top [64–66]. Raman spectroscopy was also performed to verify the crystal quality of the laser-modified flakes. Figure 4c presents the Raman spectra before and after the laser treatment of a WSe_2 flake. The increase in the Raman intensity of the A_{1g} mode (shown in the inset) after the treatment validates the thinning of WSe_2 with the oxidation of top layers. Such an increase in the intensity of the peaks is related to the thinning of WSe_2 and an increase in the phonon lifetime [45,73]. An increase in phonon lifetime should be also observed in the according change in the device-apparent field-effect mobility. However, for both treated and the untreated devices, the apparent hole mobilities were within the sample-to-sample variation.

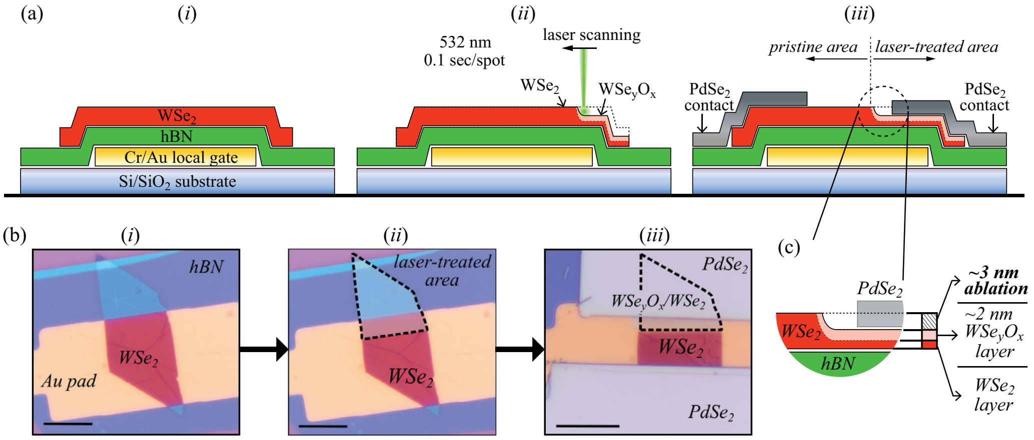

Figure 3. Laser treatment of WSe_2: ((**a**) *i*–*iii*) Schematic cross-section of the laser-treated devices (not to scale), presenting the laser treatment process of the electrode interface step by step. ((**b**) *i*–*iii*) Optical micrographs (scale 5 μm) of a representative device corresponding to each fabrication step in ((**a**) *i*–*iii*). ((**a**,**b**) *i*) The heterostack of WSe_2/hBN on a local gate electrode prior to the laser treatment, and ((**a**,**b**) *ii*) after the top part of the WSe_2 flake was scanned by the laser (exposed part of the WSe_2 flake is indicated by the dashed lines). ((**a**,**b**) *iii*) The same device after stamping of $PdSe_2$ contacts. In the presented case, only one side of the channel–electrode interface was laser-treated. (**c**) A zoom in on the schematic in ((**a**) *iii*) highlighting the part of the ablated WSe_2 layer, part of the oxidised WSe_yO_x layer, and the unmodified part of the WSe_2 layer.

3.4. Electrical Characteristics of WSe_2 FETs with $WSe_2/WSe_yO_x/PdSe_2$ Electrode Interface

Figure 5a represents the electrical transfer curves for the WSe_2 device with both source and drain electrode interfaces modified by the laser treatment. The device showed a notable decrease in I_{ON}. However, highly stable *p*-type devices were realised with respect to V_{th} variations between subsequent sweeps at room temperature operation and also under varied V_G sweeping rates. V_{th} for the hole branch of the WSe_yO_x-modified contacts was found to be at (-0.42 ± 0.06) V, which is about four times lower than the $PdSe_2/WSe_2$ interface. More importantly, the sample-to-sample-, forward/backward sweep-, and multiple sweep-related variations in the V_{th} value are almost completely reduced. The dominant *p*-type behaviour with the quenching of the electron branch can be associated with WSe_yO_x, which acts as an efficient hole injection layer [66,67]. The WSe_yO_x/WSe_2 layer also extends beyond the contact regions into the channel (for about 1 μm) to ensure that the contact is not made directly with the unmodified WSe_2. Consequently, WSe_yO_x could also introduce interface traps in the channel active area. To test this, we have probed the stability of the devices by examining the hysteresis voltage (V_H), as a difference in the V_{th} between the forward and backward sweeping electrical transfer curves. V_H values for the varied V_G sweep rates are shown in Figure 5b. The device remained stable at high sweeping rates (up to 15 V/s) with a negligible hysteresis of 55 mV. An increase in the hysteresis of up to 150 mV was noted at low sweeping rates. The hysteresis values correspond well to the pristine $PdSe_2/WSe_2/PdSe_2$ devices, indicating that the WSe_yO_x layers did not affect device stability. The observed hysteresis is likely related to the interface between hBN and WSe_2 or is inherent to the WSe_2 layers.

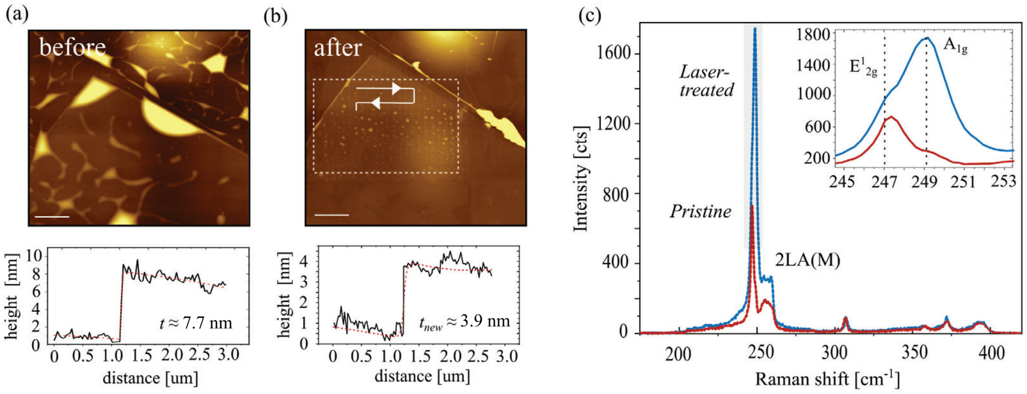

Figure 4. Topography changes and Raman investigation of laser-treated WSe_2: (**a**) Atomic force microscopy (AFM) image of a WSe_2 flake on hBN before laser exposure with the corresponding line profile (height) of the flake. The predominant morphological features are water/air bubbles trapped at the WSe_2/hBN and hBN/SiO_2 interfaces. (**b**) The same area as in (**a**) treated with a 50 mW 532 nm laser beam. The exposed region is marked with a dashed rectangle, and the laser scanning direction is indicated with an arrow. The corresponding height profiles are presented at the bottom of the topography images. (**a**,**b**) Lateral scale bar 2 µm, z-scale 25 nm. (**c**) Raman spectrum before and after laser irradiation, recorded with 5 mW, 532 nm, and 5 × 10 s acquisition parameters. The main WSe_2 peaks are preserved and enhanced in intensity after the laser treatment. Inset (**b**) presents a zoomed-in region of the main $E^1{}_{2g}$ and A_{1g} modes.

Two-dimensional semiconductors commonly show large variations in the V_{th} at varying drain voltages which also impacts the device stability [6,74,75]. To test this, we subjected our device to a V_D ranging from 0.5 V to 2.0 V. The device maintained the same V_{th} for forward and backward sweeps with a V_D-independent hysteresis of 98 mV. The subthreshold swing (SS) values were also significantly improved from 200 mV/dec for the non-treated to 100 mV/dec for the treated devices. It is worth mentioning that these devices operated without a top encapsulation and therefore, a high-k dielectric encapsulation, optimization of the hBN thickness, and integration into dual-gate geometries can further improve WSe_2 FET performance. The obtained SS values, especially for the laser-treated devices, perform better than commonly reported back-gate implemented FETs, where the SS values range from 2500 mV/dec to 400 mV/dec [11,18,20]. Some of the lowest reported SS values for WSe_2 devices (95 mV/dec) were achieved by utilizing 20 nm of HfO_2 as the gate insulator and *p*-branch matching Pt contacts [45].

We have also fabricated asymmetric devices where only one side of the channel was treated with the laser (as also shown in Figure 3). An example of the electrical transfer curves observed for such devices is presented in Figure 5d. A large hysteresis window was observed, which directly depends on the choice of the drain electrode, i.e., the device exhibits rectifying behaviour with respect to the induced hysteresis. For the case where the laser-treated region was used as a drain, a stable *p*-branch was realised with negligible hysteresis, represented by a solid black curve in Figure 5d. A pronounced hysteresis of 2 V was only present for the *n*-branch. This was observed to be in stark contrast to the behaviour of the same device when the non-treated region was used as the drain. In that case, a *p*-branch hysteresis of 4 V was observed. In both cases, the hysteresis was stable for multiple forward–backward sweeps as indicated by the arrows. Such behaviour can be associated with large differences between the number of carriers available underneath the contact regions. As one end of the channel is intentionally favouring hole injection and prohibiting electron injection, the other stays in its original form. Such large and stable rectifying hysteretic behaviour could be employed in novel concepts as computing in memory and self-reconfiguring electronics [76,77].

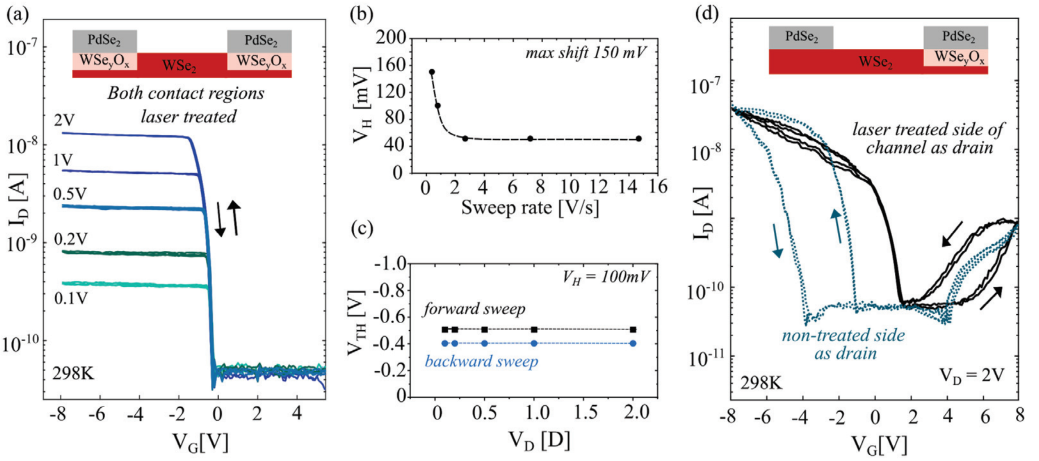

Figure 5. Electrical response of $WSe_2/WSe_yO_x/PdSe_2$ electrode interface: (**a**) Semi-log scale electrical transfer curves of a WSe_2 device with both source and drain electrode interfaces treated by a laser prior to stamping $PdSe_2$ contacts measured at 298 K, 2×10^{-2} mbar. (**b**) V_H plot as a function of a scan speed (measured at 298 K, 2×10^{-2} mbar). (**c**) Position of the V_{th} for both forward and backward V_G sweeping with varied V_D. The difference indicates the hysteresis (V_H) is independent of V_D. (**d**) Semi-log scale electrical transfer curves for an asymmetric WSe_2 FET with only one contact pad treated by the laser. The dotted lines represent the drain electrode connected to the non-treated $PdSe_2$ contact side, while source and drain were swapped for the solid black line. The arrows indicate the V_G sweeping direction.

4. Conclusions

In summary, we have introduced $PdSe_2$ contacts to WSe_2 FETs that enable effective hole injection, enhanced *p*-type performance, and preserve the intrinsic ambipolar response of WSe_2. $PdSe_2$ contacts allow essentially hysteresis-free electrical response while maintaining high on-state currents and I_{ON}/I_{OFF} ratio enhancement by one order of magnitude in comparison to graphite-contacted devices. Considering the low temperatures required for the $PdSe_2$ growth, it is a promising electrode candidate especially when considering the potential that $PdSe_2$ brings for the upscaling of 2D-material-based electronics and the incorporation of ambipolar WSe_2 to post-CMOS architectures.

We extended the study to also contact laser-treated WSe_2, where the laser irradiation induces the formation of a conductive WSe_yO_x layer at the electrode interface. In this case, we observed highly stable *p*-type behaviour of the devices with a two-fold improvement in the subthreshold swing, stabilization of the V_{th} for the hole branch. Interestingly, if only one electrode interface is modified by the laser treatment, asymmetric WSe_2 FETs were achieved, which exhibited pronounced and stable hysteretic behaviour of only one (electron or hole) branch. The hysteresis was dependent on the direction of applied drain voltage. Such device response can be used to design in-memory computing and reconfigurable electronic concepts based purely on 2D interfaces.

Author Contributions: G.M. and M.A.A. conceived the idea for the study. M.A.A. and A.M. performed data analysis and wrote the manuscript. G.M. and S.L. prepared the 2D material heterostacks and carried out the experiments. I.P. and Z.S. provided the $PdSe_2$ crystals. V.T. and E.P. fabricated the gold pad substrates. R.D.R. supervised Raman and AFM measurements. S.L. and A.M. performed the experiments and data analysis/modelling related to the extraction of the contact resistance. A.M. acquired the main funding for the study. All authors have read and agreed to the published version of the manuscript.

Funding: This work is supported by the Austrian Science Fund (FWF) under grants no. I4323-N36 and Y1298-N. A.M. acknowledges the support provided by the ERC grant POL_2D_PHYSICS (101075821).

Z.S. was supported by ERC–CZ program (project LL2101) from Ministry of Education Youth and Sports (MEYS) and used large infrastructure from project reg. No. CZ.02.1.01/0.0/0.0/15_003/0000444 financed by the EFRR. R.D.R. acknowledges the Russian Science Foundation grant 23-42-00081. V.T. and E.P. acknowledge funding by the Slovenian Research and Innovation Agency (ARIS) under research program P1–0055. The authors acknowledge infrastructure support of the Montanuniversitaet Leoben (Raman AFM TERS lab).

Data Availability Statement: The data generated within this study and the samples related to this study are available from the corresponding author upon reasonable request.

Conflicts of Interest: The authors declare no conflicts of interest.

References

1. Cao, W.; Bu, H.; Vinet, M.; Cao, M.; Takagi, S.; Hwang, S.; Ghani, T.; Banerjee, K. The future transistors. *Nature* **2023**, *620*, 501–515. [CrossRef]
2. Zhu, K.; Wen, C.; Aljarb, A.A.; Xue, F.; Xu, X.; Tung, V.; Zhang, X.; Alshareef, H.N.; Lanza, M. The development of integrated circuits based on two-dimensional materials. *Nat. Electron.* **2021**, *11*, 775–785. [CrossRef]
3. Ahmad, W.; Gong, Y.; Abbas, G.; Khan, K.; Khan, M.; Ali, G.; Shuja, A.; Tareen, A.K.; Khan, Q.; Li, D. Evolution of low-dimensional material-based field-effect transistors. *Nanoscale* **2021**, *10*, 5162–5186. [CrossRef] [PubMed]
4. Rawat, A.; Gupta, A.K.; Rawat, B. Performance projection of 2D material-based CMO inverters for sub-10-nm channel length. *IEEE Trans. Electron. Devices* **2021**, *68*, 3622–3629. [CrossRef]
5. Fiori, G.; Bonaccorso, F.; Iannaccone, G.; Palacios, T.; Neumaier, D.; Seabaugh, A.; Banerjee, S.K.; Colombo, L. Electronics based on two-dimensional materials. *Nat. Nanotechnol.* **2014**, *9*, 768–779. [CrossRef]
6. Li, J.; Chen, X.; Zhang, D.W.; Zhou, P. Van-der-Waals heterostructure based field effect transistor application. *Crystals* **2017**, *8*, 8. [CrossRef]
7. Illarionov, Y.Y.; Knobloch, T.; Jech, M.; Lanza, M.; Akinwande, D.; Vexler, M.I.; Mueller, T.; Lemme, M.C.; Fiori, G.; Schwierz, F.; et al. Insulators for 2D nanoelectronics: The gap to bridge. *Nat. Commun.* **2020**, *118*, 3385. [CrossRef]
8. Arora, A.; Ganapathi, K.L.; Dixit, T.; Miryala, M.; Masato, M.; Rao, M.S.R.; Krishnan, A. Thickness-Dependent Nonlinear Electrical Conductivity of Few-Layer Muscovite Mica. *Phys. Rev. Appl.* **2022**, *17*, 064042. [CrossRef]
9. Zhou, J.; Lin, J.; Huang, X.; Zhou, Y.; Chen, Y.; Xia, J.; Wang, H.; Xie, Y.; Yu, H.; Lei, J.; et al. A library of atomically thin metal chalcogenides. *Nature* **2018**, *556*, 355–359. [CrossRef]
10. Di Bartolomeo, A. Emerging 2D materials and their van der Waals heterostructures. *Nanomaterials* **2020**, *10*, 579. [CrossRef]
11. Cheng, Q.; Pang, J.; Sun, D.; Wang, J.; Zhang, S.; Liu, F.; Chen, Y.; Yang, R.; Liang, N.; Lu, X.; et al. WSe_2 2D p-type semiconductor-based electronic devices for information technology: Design, preparation, and applications. *InfoMat* **2020**, *102*, 656–697. [CrossRef]
12. Kumar, R.; Goel N.; Hojamberdiev, M.; Kumar, M. Transition metal dichalcogenides-based flexible gas sensors. *Sens. Actuator A Phys.* **2020**, *303*, 111875. [CrossRef]
13. Sumesh, C.K.; Peter, S.C. Two-dimensional semiconductor transition metal based chalcogenide based heterostructures for water splitting applications. *Dalton Trans.* **2019**, *48*, 12772–12802. [CrossRef]
14. Maniyar, A.; Choudhary, S. Visible region absorption in TMDs/phosphorene heterostructures for use in solar energy conversion applications. *RSC Adv.* **2020**, *10*, 31730–31739. [CrossRef]
15. Wang, C.; Yang, F.; Gao, Y. The highly-efficient light-emitting diodes based on transition metal dichalcogenides: From architecture to performance. *Nanoscale Adv.* **2020**, *2*, 4323–4340. [CrossRef]
16. Aslam, M.A.; Tran, T.H.; Supina, A.; Siri, O.; Meunier, V.; Watanabe, K.; Taniguchi, T.; Kralj, M.; Teichert, C.; Sheremet, E.; et al. Single-crystalline nanoribbon network field effect transistors from arbitrary two-dimensional materials. *npj 2D Mater. Appl.* **2022**, *6*, 76. [CrossRef]
17. Murastov, G.; Aslam, M.A.; Tran, T.H.; Lassnig, A.; Watanabe, K.; Taniguchi, T.; Wurster, S.; Nachtnebel, M.; Teichert, C.; Sheremet, E.; et al. Photoinduced edge-specific nanoparticle decoration of two-dimensional tungsten diselenide nanoribbons. *Commun. Chem.* **2023**, *6*, 166. [CrossRef]
18. Pudasaini, P.R.; Oyedele, A.; Zhang, C.; Stanford, M.G.; Cross, N.; Wong, A.T.; Hoffman, A.N.; Xiao, K.; Duscher, G.; Mandrus, D.G.; et al. High-performance multilayer WSe_2 field-effect transistors with carrier type control. *Nano Res.* **2018**, *11*, 722–730. [CrossRef]
19. Nan, H.; Zhou, R.; Gu, X.; Xiao, S.; Ostrikov, K.K. Recent advances in plasma modification of 2D transition metal dichalcogenides. *Nanoscale* **2019**, *11*, 19202–19213. [CrossRef] [PubMed]
20. Kozhakhmetov, A.; Stolz, S.; Tan, A.M.Z.; Pendurthi, R.; Bachu, S.; Turker, F.; Alem, N.; Kachian, J.; Das, S.; Hennig, R.G.; et al. Controllable p-type doping of 2D WSe_2 via vanadium substitution. *Adv. Funct. Mater.* **2021**, *31*, 2105252. [CrossRef]
21. Grützmacher, S.; Heyl, M.; Nardi, M.V.; Koch, N.; List-Kratochvil, E.J.W.; Ligorio, G. Local Manipulation of the Energy Levels of 2D TMDCs on the Microscale Level via Microprinted Self-Assembled Monolayers. *Adv. Mater. Interf.* **2023**, *10*, 2300276. [CrossRef]
22. Pang, Y.-D.; Wu, E.-X.; Xu, Z.-H.; Hu, X.-D.; Wu, S.; Xu, L.-Y.; Liu, J. Effect of electrical contact on performance of WSe_2 field effect transistors. *Chin. Phys. B* **2021**, *30*, 068501. [CrossRef]

23. Liu, Y.; Duan, X.; Shin, H.-J.; Park, S.; Huang, Y.; Duan, X. Promises and prospects of two-dimensional transistors. *Chin. Phys. B* **2021**, *519*, 43–53. [CrossRef] [PubMed]
24. Liao, W.; Zhao, S.; Li, F.; Wang, C.; Ge, Y.; Wang, H.; Wang, S.; Zhang, H. Interface engineering of two-dimensional transition metal dichalcogenides towards next-generation electronic devices: Recent advances and challenges. *Nanoscale Horiz.* **2020**, *5*, 787–807. [CrossRef] [PubMed]
25. Rai, A.; Movva, H.C.P.; Roy, A.; Taneja, D.; Chowdhury, S.; Banerjee, S.K. Progress in contact, doping and mobility engineering of MoS2: An atomically thin 2D semiconductor. *Crystals* **2018**, *8*, 316. [CrossRef]
26. Poljak, M.; Matić, M. Metallization-induced quantum limits of contact resistance in graphene nanoribbons with one-dimensional contacts. *Materials* **2021**, *14*, 3670. [CrossRef] [PubMed]
27. Jain, A.; Szabó, Á.; Parzefall, M.; Bonvin, E.; Taniguchi, T.; Watanabe, K.; Bharadwaj, P.; Luisier, M.; Novotny, L. One-dimensional edge contacts to a monolayer semiconductor. *Nano Lett.* **2019**, *19*, 6914–6923. [CrossRef]
28. Cheng, Z.; Yu, Y.; Singh, S.; Price, K.; Noyce, S.G.; Lin, Y.-C.; Cao, L.; Franklin, A.D. Immunity to contact scaling in MoS_2transistors using in situ edge contacts. *Nano Lett.* **2019**, *19*, 5077–5085. [CrossRef] [PubMed]
29. Das, S.; Chen, H.-Y.; Penumatcha, A.V.; Appenzeller, J. High performance multilayer MoS_2 transistors with scandium contacts. *Nano Lett.* **2013**, *13*, 100–105. [CrossRef] [PubMed]
30. English, C.D.; Shine, G.; Dorgan, V.E.; Saraswat, K.C.; Pop, E. Improved contacts to MoS_2 transistors by ultra-high vacuum metal deposition. *Nano Lett.* **2016**, *16*, 3824–3830. [CrossRef]
31. Kwon, G.; Choi, Y.; Lee, H.; Kim, H.; Jeong, J.; Jeong, K.; Baik, M.; Kwon, H.; Ahn, J.; Lee, E.; et al. Interaction-and defect-free van der Waals contacts between metals and two-dimensional semiconductors. *Nat. Electron.* **2022**, *5*, 241–247. [CrossRef]
32. Matković, A.; Petritz, A.; Schider, G.; Krammer, M.; Kratzer, M.; Karner-Petritz, E.; Fian, A.; Gold, H.; Gärtner, M.; Terfort, A.; et al. Interfacial band engineering of MoS_2/gold interfaces using pyrimidine-containing self-assembled monolayers: Toward contact-resistance-free bottom-contacts. *Adv. Electron. Matter.* **2020**, *6*, 2000110. [CrossRef]
33. Liu, Y.; Guo, J.; Zhu, E.; Liao, L.; Lee, S.-J.; Ding, M.; Shakir, I.; Gambin, V.; Huang, Y.; Duan, X. Approaching the Schottky–Mott limit in van der Waals metal–semiconductor junctions. *Nature* **2018**, *557*, 696–700. [CrossRef] [PubMed]
34. Liu, G.; Tian, Z.; Yang, Z.; Xue, Z.; Zhang, M.; Hu, X.; Wang, Y.; Yang, Y.; Chu, P.K.; Mei, Y.; et al. Graphene-assisted metal transfer printing for wafer-scale integration of metal electrodes and two-dimensional materials. *Nat. Electron.* **2022**, *5*, 275–280. [CrossRef]
35. Poljak, M.; Matić, M.; Župančić, T.; Zeljko, A. Lower limits of contact resistance in phosphorene nanodevices with edge contacts. *Nanomaterials* **2022**, *12*, 656. [CrossRef] [PubMed]
36. Poljak, M.; Matić, M. Optimum Contact Configurations for Quasi-One-Dimensional Phosphorene Nanodevices *Nanomaterials* **2023**, *13*, 1759. [CrossRef] [PubMed]
37. Shen; Su, P.C.; Lin, C.; Chou, Y.; Cheng, A.S.; Park, C.C.; Chiu, J.H.; Lu, M.H.; Tang, A.Y.; Tavakoli, H.L.; M, M.; et al. Ultralow contact resistance between semimetal and monolayer semiconductors. *Nature* **2021**, *593*, 211–217. [CrossRef] [PubMed]
38. Mootheri, V.; Arutchelvan, G.; Banerjee, S.; Sutar, S.; Leonhardt, A.; Boulon, M.; Huyghebaert, C.; Houssa, M.; Asselberghs, I.; Radu, I.; et al. Graphene based Van der Waals contacts on MoS_2 field effect transistors. *2D Mater.* **2020**, *8*, 015003. [CrossRef]
39. Ryu, H.; Kim, D.; Kwon, J.; Park, S.K.; Lee, W.; Seo, H.; Watanabe, K.; Taniguchi, T.; Kim, S.; van der Zande, A.M.; et al. Fluorinated Graphene Contacts and Passivation Layer for MoS_2 Field Effect Transistors. *Adv. Electron. Matter.* **2022**, *8*, 2101370. [CrossRef]
40. Li, Z.; Wang, Y.; Jiang, J.; Liang, Y.; Zhong, B.; Zhang, H.; Yu, K.; Kan, G.; Zou, M. Temperature-dependent Raman spectroscopy studies of 1–5-layer WSe_2. *Nano Res.* **2020**, *13*, 591–595. [CrossRef]
41. Liu; Tan, Y.; Chou, C.; Nayak, H.; Wu, A.; Ghosh, D.; Chang, R.; Hao, H.Y.; Wang, Y.; Kim, X.; S, J.; et al. Thermal oxidation of WSe_2 nanosheets adhered on SiO_2/Si substrates. *Nano Lett.* **2015**, *15*, 4979–4984. [CrossRef]
42. Illarionov, Y.Y.; Waltl, M.; Rzepa, G.; Knobloch, T.; Kim, J.-S.; Akinwande, D.; Grasser, T. Highly-stable black phosphorus field-effect transistors with low density of oxide traps. *npj 2D Mater. Appl.* **2017**, *1*, 23. [CrossRef]
43. Wang, J.-B.; Ren, Z.; Hou, Y.; Yan, X.-L.; Liu, P.-Z.; Zhang, H.; Zhang, H.-X.; Guo, J.-J. A review of graphene synthesis at low temperatures by CVD methods. *New Carbon Mater.* **2020**, *35*, 193–208. [CrossRef]
44. Liu, W.; Kang, J.; Sarkar, D.; Khatami, Y.; Jena, D.; Banerjee, K. Role of metal contacts in designing high-performance monolayer n-type WSe_2 field effect transistors. *Nano Lett.* **2013**, *13*, 1983–1990. [CrossRef] [PubMed]
45. Zhang, L.; Zhang, Y.; Sun, X.; Jia, K.; Zhang, Q.; Wu, Z.; Yin, H. High-performance multilayer WSe_2 p-type field effect transistors with Pd contacts for circuit applications. *J. Mater. Sci. Mater. Electron.* **2021**, *32*, 17427–17435. [CrossRef]
46. Oyedele, A.D.; Yang, S.; Feng, T.; Haglund, A.V.; Gu, Y.; Puretzky, A.A.; Briggs, D.; Rouleau, C.M.; Chisholm, M.F.; Unocic, R.R.; et al. Defect-mediated phase transformation in anisotropic two-dimensional $PdSe_2$ crystals for seamless electrical contacts. *J. Am. Chem. Soc.* **2019**, *141*, 8928–8936. [CrossRef] [PubMed]
47. Seo, J.-E.; Park, E.; Das, T.; Kwak, J.Y.; Chang, J. Demonstration of $PdSe_2$ CMOS Using Same Metal Contact in $PdSe_2$ n-/p-MOSFETs through Thickness-Dependent Phase Transition. *Adv. Electron. Mater.* **2022**, *8*, 2200485. [CrossRef]
48. Long, M.; Wang, Y.; Wang, P.; Zhou, X.; Xia, H.; Luo, C.; Huang, S.; Zhang, G.; Yan, H.; Fan, Z.; et al. Palladium diselenide long-wavelength infrared photodetector with high sensitivity and stability. *Adv. Electron. Mater.* **2019**, *13*, 2511–2519. [CrossRef] [PubMed]

49. Gu, Y.; Cai, H.; Dong, J.; Yu, Y.; Hoffman, A.N.; Liu, C.; Oyedele, A.D.; Lin, Y.C.; Ge, Z.; Puretzky, A.A.; et al. Two-dimensional palladium diselenide with strong in-plane optical anisotropy and high mobility grown by chemical vapor deposition. *Adv. Mater.* **2020**, *32*, 1906238. [CrossRef]
50. Sun, J.; Shi, H.; Siegrist, T.; Singh, D.J. Electronic, transport, and optical properties of bulk and mono-layer $PdSe_2$. *Appl. Phys. Lett.* **2015**, *107*, 153902. [CrossRef]
51. Liang, Q.; Wang, Q.; Zhang, Q.; Wei, J.; Lim, S.X.; Zhu, R.; Hu, J.; Wei, W.; Lee, C.; Sow, C.; et al. High-performance, room temperature, ultra-broadband photodetectors based on air-stable $PdSe_2$. *Adv. Mater.* **2019**, *31*, 1807609. [CrossRef]
52. Wang, Y.; Pang, J.; Cheng, Q.; Han, L.; Li, Y.; Meng, X.; Ibarlucea, B.; Zhao, H.; Yang, F.; Liu, H.; et al. Applications of 2D-layered palladium diselenide and its van der Waals heterostructures in electronics and optoelectronics. *Nano–Micro Lett.* **2021**, *13*, 143. [CrossRef]
53. Liang, Q.; Chen, Z.; Zhang, Q.; Wee, A.T.S. Pentagonal 2D transition metal dichalcogenides: $PdSe_2$ and beyond. *Adv. Funct. Mater.* **2022**, *32*, 2203555. [CrossRef]
54. Oyedele, A.D.; Yang, S.; Liang, L.; Puretzky, A.A.; Wang, K.; Zhang, J.; Yu, P.; Pudasaini, P.R.; Ghosh, A.W.; Liu, Z.; et al. PdSe2: Pentagonal two-dimensional layers with high air stability for electronics. *J. Am. Chem. Soc.* **2017**, *139*, 14090–14097. [CrossRef] [PubMed]
55. Withanage, S.S.; Khondaker, S.I. Low pressure CVD growth of 2D $PdSe_2$ thin film and its application in $PdSe_2$-$MoSe_2$ vertical heterostructure. *2D Mater.* **2022**, *9*, 025025. [CrossRef]
56. Sata, Y.; Moriya, R.; Masubuchi, S.; Watanabe, K.; Taniguchi, T.; Machida, T. n-and p-type carrier injections into WSe_2 with van der Waals contacts of two-dimensional materials. *Jpn. J. Appl. Phys.* **2017**, *56*, 04CK09. [CrossRef]
57. Laturia, A.; Van de Put, M.L.; Vandenberghe, W.G. Dielectric properties of hexagonal boron nitride and transition metal dichalcogenides: From monolayer to bulk. *npj 2D Mater. Appl.* **2018**, *2*, 6. [CrossRef]
58. Nečas, D.; Klapetek, P. Gwyddion: An open-source software for SPM data analysis. *Open Phys.* **2012**, *10*, 181–188. [CrossRef]
59. Zhou, L.; Ge, C.; Yang, H.; Sun, Y.; Zhang, J. A high-pressure enhanced coupling effect between graphene electrical contacts and two-dimensional materials thereby improving the performance of their constituent FET devices. *J. Mater. Chem. C* **2019**, *7*, 15171–15178. [CrossRef]
60. Watson, A.J.; Lu, W.; Guimarães, M.H.D.; Stöhr, M. Transfer of large-scale two-dimensional semiconductors: Challenges and developments. *2D Mater.* **2021**, *8*, 032001. [CrossRef]
61. Pan, Y.; Rahaman, M.; He, L.; Milekhin, I.; Manoharan, G.; Aslam, M.A.; Blaudeck, T.; Willert, A.; Matković, A.; Madeira, T.I.; et al. Exciton tuning in monolayer WSe_2 via substrate induced electron doping. *Nanoscale Adv.* **2022**, *4*, 5102–5108. [CrossRef]
62. Allain, A.; Kang, J.; Banerjee, K.; Kis, A. Electrical contacts to two-dimensional semiconductors. *Nat. Mater.* **2015**, *14*, 1195–1205. [CrossRef]
63. Wang, Y.; Chhowalla, M. Making clean electrical contacts on 2D transition metal dichalcogenides. *Nat. Rev. Phys.* **2022**, *4*, 101–112. [CrossRef]
64. Lee, K.; Ngo, T.D.; Lee, S.; Shin, H.; Choi, M.S.; Hone, J.; Yoo, W.J. Effects of Oxygen Plasma Treatment on Fermi-Level Pinning and Tunneling at the Metal–Semiconductor Interface of WSe_2 FETs. *Adv. Electron. Mater.* **2023**, *9*, 2200955. [CrossRef]
65. Ngo, T.D.; Choi, M.S.; Lee, M.; Ali, F.; Hassan, Y.; Ali, N.; Liu, S.; Lee, C.; Hone, J.; Yoo, W.J. Selective Electron Beam Patterning of Oxygen-Doped WSe_2 for Seamless Lateral Junction Transistors. *Adv. Sci.* **2022**, *9*, 2202465. [CrossRef] [PubMed]
66. Moon, I.; Lee, S.; Lee, M.; Kim, C.; Seol, D.; Kim, Y.; Kim, K.H.; Yeom, G.Y.; Teherani, J.T.; Hone, J.; et al. The device level modulation of carrier transport in a 2D WSe_2 field effect transistor via a plasma treatment. *Nanoscale* **2019**, *11*, 17368–17375. [CrossRef]
67. Kang, W.–M.; Lee, S.T.; Cho, I.–T.; Park, T.H.; Shin, H.; Hwang, C.S.; Lee, C.; Park, B.–G.; Lee, J.–H. Multi-layer WSe_2 field effect transistor with improved carrier-injection contact by using oxygen plasma treatment. *Solid-State Electron.* **2018**, *140*, 2–7.
68. Li, Q.; Song, J.; Besenbacher, F.; Dong, M. Two-dimensional material confined water. *Acc. Chem. Res.* **2015**, *48*, 119–127. [CrossRef] [PubMed]
69. Jain, A.; Bharadwaj, P.; Heeg, S.; Parzefall, M.; Taniguchi, T.; Watanabe, K.; Novotny, L. Minimizing residues and strain in 2D materials transferred from PDMS. *Nanotechnology* **2018**, *29*, 265203. [CrossRef]
70. Wang, W.; Clark, N.; Hamer, M.; Carl, A.; Tovari, E.; Sullivan-Allsop, S.; Tillotson, E.; Gao, Y.; de Latour, H.; Selles, F.; et al. Clean assembly of van der Waals heterostructures using silicon nitride membranes. *Nat. Electron.* **2023**, *6*, 981–990. [CrossRef]
71. Purdie, D.G.; Pugno, N.M.; Taniguchi, T.; Watanabe, K.; Ferrari, A.C.; Lombardo, A. Cleaning interfaces in layered materials heterostructures. *Nat. Commun.* **2018**, *9*, 5387. [CrossRef] [PubMed]
72. Jeon, D.; Kim, H.; Gu, M.; Kim, T. Imaging Fermi-level hysteresis in nanoscale bubbles of few-layer MoS_2. *Commun. Mater.* **2023**, *4*, 62. [CrossRef]
73. Zhang, R.; Drysdale, D.; Koutsos, V.; Cheung, R. Controlled layer thinning and p-type doping of WSe_2 by vapor XeF_2. *Adv. Funct. Mater.* **2017**, *27*, 1702455. [CrossRef]
74. Park, W.; Pak, Y.; Jang, H.Y.; Nam, J.H.; Kim, T.H.; Oh, S.; Choi, Sung M.; Kim, Y.; Cho, B. Improvement of the bias stress stability in 2D MoS_2 and WS_2 transistors with a TiO_2 interfacial layer. *Nanomaterials* **2019**, *9*, 1155. [CrossRef] [PubMed]
75. Ye, M.; Zhang, D.; Yap, Y.K. Recent advances in electronic and optoelectronic devices based on two-dimensional transition metal dichalcogenides. *Electronics* **2017**, *6*, 43. [CrossRef]

76. Fei, W.; Trommer, J.; Lemme, M.C.; Mikolajick, T.; Heinzig, A. Emerging reconfigurable electronic devices based on two-dimensional materials: A review. *InfoMat* **2022**, *4*, e12355. [CrossRef]
77. Feng, C.; Wu, W.; Liu, H.; Wang, J.; Wan, H.; Ma, G.; Wang, H. Emerging Opportunities for 2D Materials in Neuromorphic Computing. *Nanomaterials* **2023**, *13*, 2720. [CrossRef]

nanomaterials

MDPI

Communication

AC Characteristics of van der Waals Bipolar Junction Transistors Using an MoS_2/WSe_2/MoS_2 Heterostructure

Zezhang Yan, Ningsheng Xu and Shaozhi Deng *

State Key Laboratory of Optoelectronic Materials and Technologies, Guangdong Province Key Laboratory of Display Material and Technology, School of Electronics and Information Technology, Sun Yat-sen University, Guangzhou 510275, China; yanzzh3@mail2.sysu.edu.cn (Z.Y.); stsxns@mail.sysu.edu.cn (N.X.)

* Correspondence: stsdsz@mail.sysu.edu.cn

Abstract: Two-dimensional layered materials, characterized by their atomically thin thicknesses and surfaces that are free of dangling bonds, hold great promise for fabricating ultrathin, lightweight, and flexible bipolar junction transistors (BJTs). In this paper, a van der Waals (vdW) BJT was fabricated by vertically stacking MoS_2, WSe_2, and MoS_2 flakes in sequence. The AC characteristics of the vdW BJT were studied for the first time, in which a maximum common emitter voltage gain of around 3.5 was observed. By investigating the time domain characteristics of the device under various operating frequencies, the frequency response of the device was summarized, which experimentally proved that the MoS_2/WSe_2/MoS_2 BJT has voltage amplification capability in the 0–200 Hz region. In addition, the phase response of the device was also investigated. A phase inversion was observed in the low-frequency range. As the operating frequency increases, the relative phase between the input and output signals gradually shifts until it is in phase at frequencies exceeding 2.3 kHz. This work demonstrates the signal amplification applications of the vdW BJTs for neuromorphic computing and wearable healthcare devices.

Keywords: two-dimensional material; van der Waals; vertically stacked; bipolar junction transistor; AC characteristics

1. Introduction

Bipolar junction transistors (BJTs), as some of the important semiconductor devices, have attracted great attention in past decades. They contain three separately doped regions, which are defined as the collector, base, and emitter. Two-dimensional (2D) materials offer significant opportunities for the construction of high-performance BJTs owing to their unique interlayered van der Waals (vdW) bonding characteristics [1–3]. By employing mechanical exfoliation or chemical vapor deposition (CVD), monolayer or multilayer 2D materials, including hexagonal boron nitride (h-BN) [4,5], transition metal dichalcogenides (TMDs) [6–9], and graphene [10–12], can be easily obtained. These ultrathin 2D materials provide possibilities for fabricating vdW BJTs with base regions of atomic thicknesses.

In the past few years, several 2D-material-based BJTs, such as BP/MoS_2/BP [13–16], Cu_9S_5/PtS_2/WSe_2 [17], and MoS_2/WSe_2/MoS_2 [18–20], have been fabricated successively. The static characteristics of these devices have been extensively studied, and they show promising application potential in the fields of photodetection [21,22], gas sensing [23,24], and biosensing [25]. However, the AC characteristics of vdW BJTs fabricated from 2D materials have not been reported yet, which is crucial for determining a device's ability to process alternating signals.

In this paper, we report on a vdW BJT that was constructed by vertically stacking MoS_2, WSe_2, and MoS_2 flakes in sequence. The static and AC characteristics of the device were investigated in a common emitter configuration. A maximum voltage gain of around 3.5 was observed in the low-frequency range. As the operating frequency increased, the voltage gain gradually decreased to unity at 200 Hz, and the relative phase between input and output signals gradually changed from 180° to 0° at 2.3 kHz. This systematic investigation of vdW BJTs provides a direct understanding of the electrical behavior of such devices under alternating current conditions, which could potentially aid in the utilization of the vdW BJTs in wearable healthcare devices and future neuromorphic applications.

2. Materials and Methods

2.1. Device Fabrication

A controlled multistep dry transfer process was employed to fabricate the vdW BJT [26]. Firstly, the WSe_2 and MoS_2 flakes were exfoliated from the bulk crystals supplied by HQ Graphene Company (Groningen, The Netherlands). Then, using the dry transfer technique, MoS_2, WSe_2 and MoS_2 sheets were stacked onto a clean 300 nm SiO_2/Si substrate in sequence. In this case, the top and bottom MoS_2 sheets were separated by the middle WSe_2 flake. Thirdly, maskless lithography was utilized to define the locations of the metal electrodes and thermal evaporation was employed to deposit Cr/Ag metals with thicknesses of 10 nm and 100 nm. Finally, the device underwent a two-hour annealing process in an argon atmosphere at 300 °C to eliminate the photoresistant residues and potentially facilitate Ag diffusion into the underlying MoS_2 flakes, thereby reducing the contact resistance [27].

2.2. Characterization

AFM (NTEGRA Spectra, NT-MDT, Moscow, Russia) and Raman spectroscopy (In Via Reflex, Renishaw, Wotton-under-Edge, Gloucestershire, UK) instruments were employed to characterize the height profile and composition of the vdW BJT. A semiconductor parameter analyzer (B1500A, Agilent Technologies, Santa Clara, CA, USA) was used to investigate the static characteristics of the device. The AC performance of the vdW BJT was measured using an oscilloscope (DPO 7354C, Tektronix, Portland, OR, USA) and an arbitrary waveform generator (DG4062, RIGOL, Beijing, China).

3. Results and Discussion

Figure 1a,b show the schematic diagram and the optical image of the vertically stacked $MoS_2/WSe_2/MoS_2$ BJT. Here, the top MoS_2 sheet acts as the collector (C) while the bottom MoS_2 sheet serves as the emitter (E). The multilayer WSe_2 sheet was designed for the base (B) region. Figure 1c shows the height profile of the device. Apparently, the thicknesses of bottom MoS_2, middle WSe_2, and top $MoS_2$are 13 nm, 3.5 nm, and 63.9 nm, respectively. To analyze the composition of the device, Raman spectra were obtained for the individual 2D materials as well as their overlap regions, as shown in Figure 1d. From the bottom MoS_2, Raman peaks at 383.7 and 408.8 cm^{-1} can be observed. The two Raman peaks have a relatively large separation of 25.1 cm^{-1}, confirming the multilayer nature of the MoS_2 material [28,29]. The peaks at 249.8 and 258.3 cm^{-1} for the WSe_2 flake are ascribed to the E_{2g}^1 mode and the A_{1g} mode [30]. In addition, the Raman spectra of the three flake overlap region are the sum of the Raman peaks of the MoS_2 and WSe_2 flakes, thereby confirming the successful fabrication of the vertically stacked heterostructure [31].

The static performance of the vdW BJT in common base mode was initially investigated. In this case, the base was grounded, whereas the base–collector and base–emitter junctions were separately reverse-biased and forward-biased. The band diagram of the vdW BJT operating in the forward-active operating mode is depicted in Figure 2a. Figure 2b shows the relationship between the base–emitter voltage (V_{BE}) and the emitter current (I_E) at various fixed collector–base voltages (V_{CB}). With the increase in V_{BE}, the depletion region of the base–emitter junction narrows, facilitating an enhanced diffusion of electrons from emitter to base. Hence, I_E increased with a larger V_{BE}. Figure 2c illustrates the output characteristic of the vdW BJT. The V_{BE} can effectively affect the collector current (I_C), since it can influence the electrons diffusing from the emitter. The electrons were transferred into the collector, constituting the main component of the I_C. The common base current gain (α) was determined to be around 1.01 at V_{BE} = 5 V by calculating the ratio of I_C and I_E. Figure 2d shows the output performance of the vdW BJT operating in common emitter mode. At low V_{CE} values, the collector current shows an approximately linear increase with the V_{CE}, indicating the saturation region of the device [13]. Beyond the saturation region, changes in V_{CE} have minimal impact on the I_C. Instead, the I_C is primarily influenced by variations in V_{BE}. This region is defined as the active region of the device. A maximum current gain ($\beta = I_C/I_B$) of approximately 9 can be obtained at V_{BE} = 0.4 V under the common emitter configuration, as shown in Figure 2d. It is noteworthy that the $MoS_2/WSe_2/MoS_2$ BJT has a relatively low on/off ratio, which may be attributed to the ultrathin base region. The negatively biased base–collector junction introduces an extra electric field perpendicular to the base–emitter junction, thereby diminishing the device's on/off ratio [19,23].

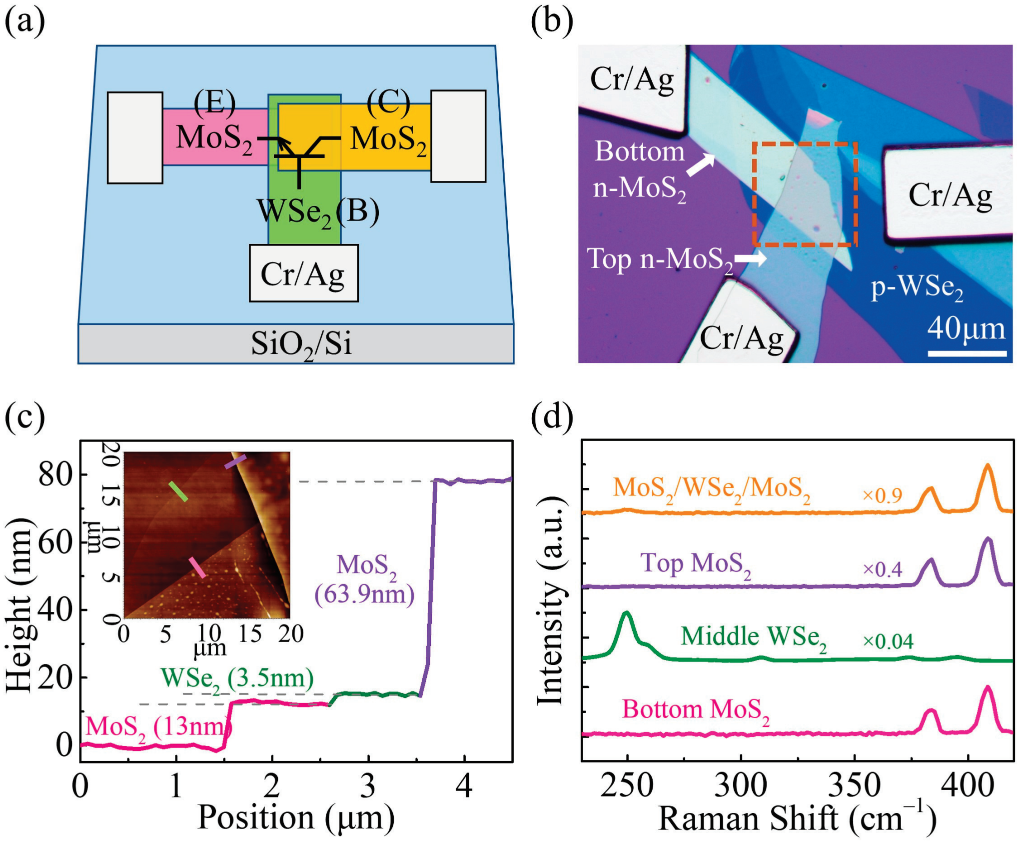

Figure 1. (**a**) Schematic illustration of the vdW BJT. (**b**) Optical microscope image of the vdW BJT. The inside of the dashed brown square represents the three flake overlapped region. (**c**) Height profile of the device. The dashed lines indicate the horizontal position of the steps. The inset illustrates the corresponding AFM image. (**d**) Raman spectra of the bottom MoS_2, middle WSe_2, top MoS_2, and $MoS_2/WSe_2/MoS_2$ three flake overlap regions.

Since the device showed excellent static performance, the AC characteristics of the vdW BJT operating in common emitter mode were investigated. The schematic diagram of the electrical connection is shown in Figure 3a. Here, a DC voltage (V_{BE} = 5.8 V) and a small AC voltage (v_i) were applied to the base–emitter junction. The base–collector junction was reverse-biased by connecting the collector to another power supply (V_{CE} = 34 V) through a load resistor (R_L = 22 MΩ). An oscilloscope was used to monitor the input and output waveforms of the device in real time. Figure 3b illustrates the time domain characteristics of the device operating at 1 Hz. Here, an AC voltage v_i with an amplitude of 0.2 V is superimposed on the V_{BE}, which causes the voltage applied on the base–emitter junction to fluctuate sinusoidally above and below its DC bias level. The resulting variation in I_B causes the output current change. Therefore, an output AC signal with an amplitude approximately 3.5 times higher than the input AC signal can be observed in the collector region.

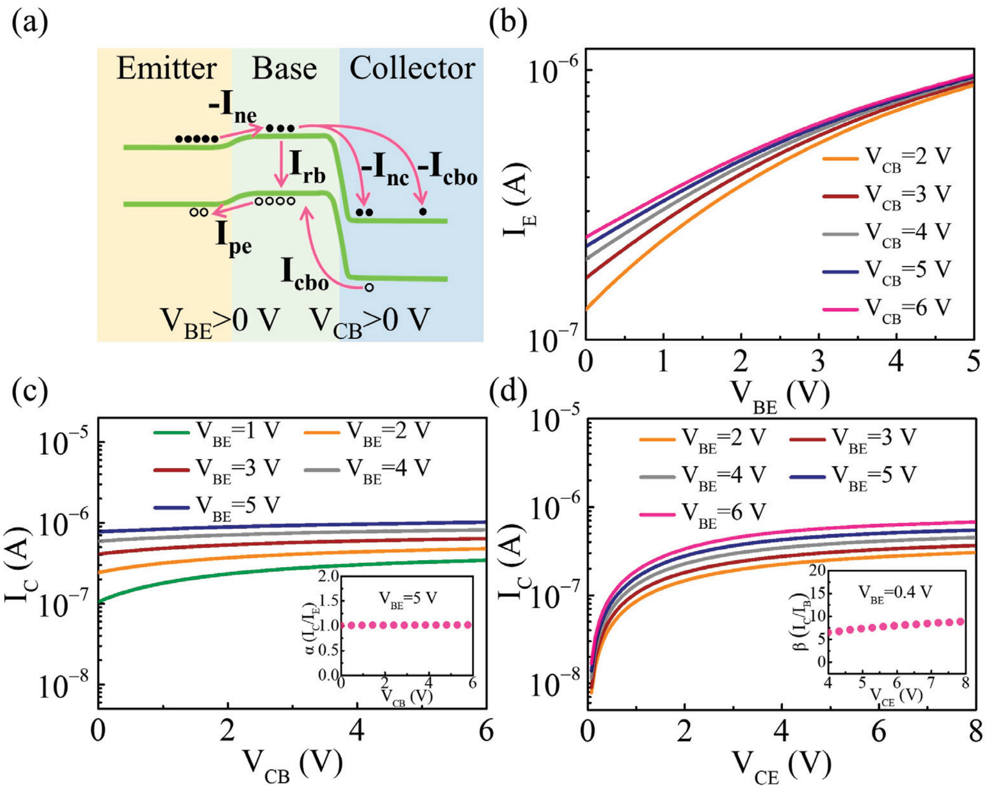

Figure 2. (**a**) Band diagram of the vdW BJT operating in forward-active operating mode. The orange, green, and blue areas indicate the emitter, base, and collector region of the device, respectively. (**b**) The relationship between I_E and V_{BE} at various fixed V_{CB} values. (**c**) The relationship between I_C and V_{CB} at various values of V_{BE}. Inset shows α as a function of V_{CB} at a fixed V_{BE} = 5 V. (**d**) The relationship between I_C and V_{CE} at various fixed V_{BE} values. Inset shows β as a function of V_{CE} at a fixed V_{BE} = 0.4 V.

The time domain characteristics of the vdW BJT operating at other frequencies were also investigated. The representative results, such as for the device operating at 50 Hz and 1 kHz, are shown in Figure 3c,d. It is worth mentioning that the voltage in the collector region was higher than that in the base region throughout the experiment, which indicates that the BJT remained in forward-active operating mode at all times. Figure 4a summarizes the common emitter voltage gain versus the operating frequency. With the increase in operating frequency, the amplitude of the output voltage signal gradually decreases until the voltage gain falls to unity at 200 Hz, indicating that the device has voltage amplification capability in the 0–200 Hz region. Figure 4b illustrates the phase response of the device. The output signal at the collector region is 180° out of phase with the input signal in the low-frequency range. As the operating frequency increases, the relative phase between the input and output signals begins to shift until the output signal is in phase with the input signal at 2.3 kHz.

Further, the frequency response of the β value can be evaluated according to the time domain characteristics of the device operating at different frequencies, as illustrated in Figure 3b–d. Here, the output current (i_C) of the device can be determined from the output signal (u_o) by applying the formula $i_C = (V_{CE} - u_o)/R_L$. As the operating frequency continuously increases, the amplitude of i_C is unchanged at first and then gradually decreases when the operating frequency exceeds 1 Hz. However, the input current (i_B) is almost unaffected by the operating frequency. Therefore, the β value changing with the frequency is consistent with the trend of i_C changing with the frequency; that is, it decreases as the operating frequency increases. In addition, to investigate the repeatability of the AC performance of the device, several other vdW BJTs with similar configurations were fabricated and investigated. All devices exhibited similar AC characteristics. The typical test results are shown in Figure S1 of the Supplementary Materials. The performance of the 2D-material-based n-p-n BJTs reported in the literature is summarized in Table 1 [14,18–20,23,25].

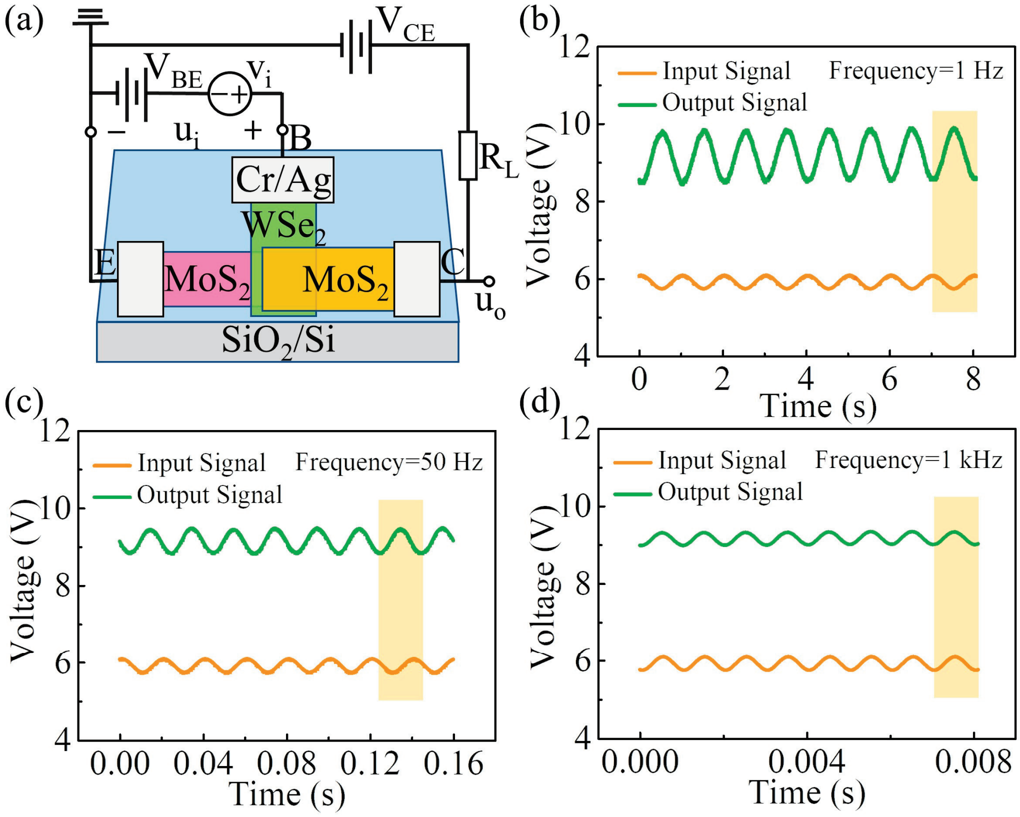

Figure 3. (**a**) Schematic diagram of the electric connection of the vdW BJT in common emitter mode. (**b**–**d**) Time domain characteristics of the vdW BJT operating at 1 Hz, 50 Hz, and 1 kHz, respectively. The yellow area demonstrates the relative phase between the input and output signals during one cycle of the sinusoidal signal.

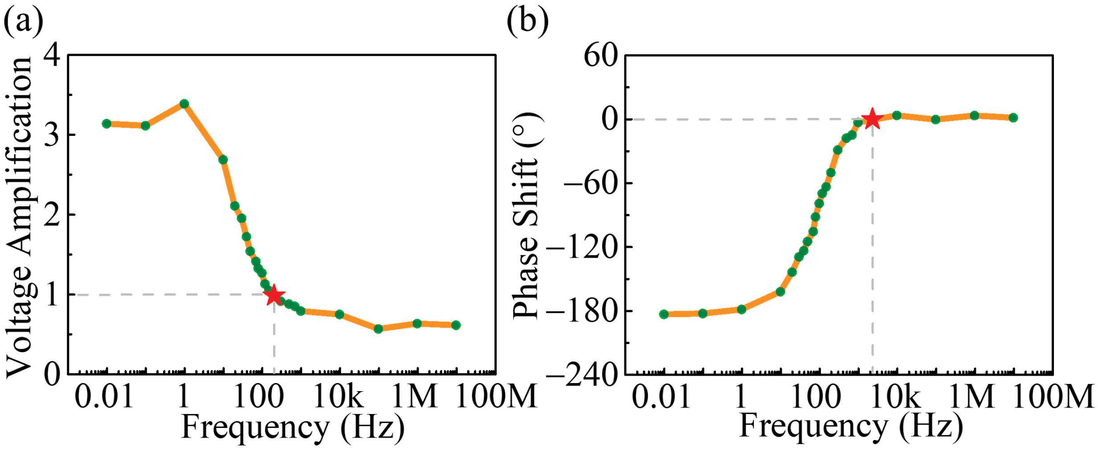

Figure 4. (**a**) The frequency response of the device. The red star represents the frequency corresponding to a voltage amplification of 1. (**b**) The phase response of the device. The red star represents the frequency when the input and output signals are in phase. The green dots represent experimental test results and are connected by orange lines.

Table 1. Comparison of device performance results between this work and various previously reported 2D-material-based n-p-n BJTs [14,18–20,23,25].

Materials	Structure	On Current (μA)	α (DC)	β (DC)	Cutoff Frequency (Hz)	Voltage Gain	Ref.
$MoS_2/WSe_2/MoS_2$	Vertical	0.67	1.01	9	~200	3.5	This work
$MoS_2/WSe_2/MoS_2$	Vertical	0.001	0.97	12	/	/	[19]
$MoS_2/WSe_2/MoS_2$	Vertical	0.054	~1	150	/	/	[18]
$MoTe_2/GeSe/MoTe_2$	Vertical	0.014	0.95	29.3	/	/	[25]
$WS_2/GeSe/WS_2$	Vertical	7.48	1.11	20.7	/	/	[23]
MoS_2/WSe2/MoS_2	In-plane	0.001	/	3	/	/	[20]
$MoS_2/BP/MoS_2$	Lateral	0.06	0.98	41	/	/	[14]

4. Conclusions

In summary, a vdW BJT was fabricated by vertically stacking MoS_2, WSe_2, and MoS_2 flakes in sequence. The static characteristics of the device were investigated in common emitter and common base modes, demonstrating excellent current modulation and saturation characteristics. The AC performance of the device in common emitter mode was also investigated. A phase inversion from output to input with a maximum voltage gain of around 3.5 was obtained in the low-frequency range. As the operating frequency increases, the voltage gain gradually decreases to unity at 200 Hz and the relative phase between the input and output signals gradually changes to 0° at 2.3 kHz. This work demonstrates the AC characteristics of the vdW BJT and experimentally proves the device's ability to process alternating signals. If the issues of device array fabrication and device-to-device variation can be further addressed, this will significantly promote the application of vdW BJTs as neuromorphic devices and wearable healthcare devices.

Supplementary Materials: The following supporting information can be downloaded at https://www.mdpi.com/article/10.3390/nano14100851/s1: Figure S1. (a) Optical microscope image of the $MoS_2/WSe_2/MoS_2$ BJT. (b–d) Time domain characteristics of the device operating at 1 Hz, 100 Hz, and 1 kHz, respectively. (e) The frequency response of the device. (f) The phase response of the device.

Author Contributions: S.D. and N.X. proposed and supervised the project. Z.Y. carried out the experiments and analyzed the data. Z.Y., N.X. and S.D. discussed and interpreted the results. Z.Y. and S.D. wrote the manuscript. All authors have read and agreed to the published version of the manuscript.

Funding: This research was funded by the National Key Basic Research Program of China (grant numbers 2019YFA0210200 and 2019YFA0210203), the Science and Technology Department of Guangdong Province, and the Fundamental Research Funds for the Central Universities.

Data Availability Statement: The data presented in this article are available upon request from the corresponding author.

Conflicts of Interest: The authors declare no conflict of interest.

References

1. Liu, Y.; Weiss, N.O.; Duan, X.D.; Cheng, H.C.; Huang, Y.; Duan, X.F. Van der Waals heterostructures and devices. *Nat. Rev. Mater.* **2016**, *1*, 16042. [CrossRef]
2. Frisenda, R.; Molina-Mendoza, A.J.; Mueller, T.; Castellanos-Gomez, A.; Van, D. Atomically thin p–n junctions based on two-dimensional materials. *Chem. Soc. Rev.* **2018**, *47*, 3339–3358. [PubMed]
3. Castellanos-Gomez, A.; Duan, X.F.; Fei, Z.; Gutierrez, H.R.; Huang, Y.; Huang, X.Y.; Quereda, J.; Qian, Q.; Sutter, E.; Sutter, P. Van der Waals heterostructures. *Nat. Rev. Methods Primers* **2022**, *2*, 58. [CrossRef]
4. Park, J.H.; Park, J.C.; Yun, S.J.; Kim, H.; Luong, D.H.; Kim, S.M.; Choi, S.H.; Yang, W.; Kong, J.; Kim, K.K.; et al. Large-Area Monolayer Hexagonal Boron Nitride on Pt Foil. *ACS Nano* **2014**, *8*, 8520–8528. [CrossRef]
5. Ismach, A.; Chou, H.; Ferrer, D.A.; Wu, Y.P.; McDonnell, S.; Floresca, H.C.; Covacevich, A.; Pope, C.; Piner, R.; Kim, M.J.; et al. Toward the Controlled Synthesis of Hexagonal Boron Nitride Films. *ACS Nano* **2012**, *6*, 6378–6385. [CrossRef] [PubMed]
6. Li, H.; Yin, Z.Y.; He, Q.Y.; Li, H.; Huang, X.; Lu, G.; Fam, D.W.H.; Tok, A.I.Y.; Zhang, Q.; Zhang, H. Fabrication of Single- and Multilayer MoS_2 Film-Based Field-Effect Transistors for Sensing NO at Room Temperature. *Small* **2012**, *8*, 63–67. [CrossRef]

7. Rhyee, J.S.; Kwon, J.; Dak, P.; Kim, J.H.; Kim, S.M.; Park, J.; Hong, Y.K.; Song, W.G.; Omkaram, I.; Alam, M.A.; et al. High-Mobility Transistors Based on Large-Area and Highly Crystalline CVD-Grown $MoSe_2$ Films on Insulating Substrates. *Adv. Mater.* **2016**, *28*, 2316–2321. [CrossRef]
8. Campbell, P.M.; Tarasov, A.; Joiner, C.A.; Tsai, M.Y.; Pavlidis, G.; Graham, S.; Ready, W.J.; Vogel, E.M. Field-effect transistors based on wafer-scale, highly uniform few-layer p-type WSe_2. *Nanoscale* **2016**, *8*, 2268–2276. [CrossRef]
9. Zhou, J.D.; Lin, J.H.; Huang, X.W.; Zhou, Y.; Chen, Y.; Xia, J.; Wang, H.; Xie, Y.; Yu, H.M.; Lei, J.C.; et al. A library of atomically thin metal chalcogenides. *Nature* **2018**, *556*, 355–359. [CrossRef]
10. Novoselov, K.S.; Geim, A.K.; Morozov, S.V.; Jiang, D.; Zhang, Y.; Dubonos, S.V.; Grigorieva, I.V.; Firsov, A.A. Electric field effect in atomically thin carbon films. *Science* **2004**, *306*, 666–669. [CrossRef]
11. Guo, W.; Wu, B.; Wang, S.; Liu, Y.Q. Controlling Fundamental Fluctuations for Reproducible Growth of Large Single-Crystal Graphene. *ACS Nano* **2018**, *12*, 1778–1784. [CrossRef] [PubMed]
12. Guo, W.; Jing, F.; Xiao, J.; Zhou, C.; Lin, Y.W.; Wang, S. Oxidative-Etching-Assisted Synthesis of Centimeter-Sized Single-Crystalline Graphene. *Adv. Mater.* **2016**, *28*, 3152–3158. [CrossRef] [PubMed]
13. Aftab, S.; Eom, J. Van der Waals 2D layered-material bipolar transistor. *2D Mater.* **2019**, *6*, 035005. [CrossRef]
14. Su, B.W.; Zhang, X.L.; Yao, B.W.; Guo, H.W.; Li, D.K.; Chen, X.D.; Liu, Z.B.; Tian, J.G. Laser Writable Multifunctional van der Waals Heterostructures. *Small* **2020**, *16*, e2003593. [CrossRef] [PubMed]
15. Lee, G.; Pearton, S.J.; Ren, F.; Kim, J. Two-Dimensionally Layered p-Black Phosphorus/n-MoS_2/p-Black Phosphorus Heterojunctions. *ACS Appl. Mater. Interfaces* **2018**, *10*, 10347–10352. [CrossRef] [PubMed]
16. Su, B.W.; Yao, B.W.; Zhang, X.L.; Huang, K.X.; Li, D.K.; Guo, H.W.; Li, X.K.; Chen, X.D.; Liu, Z.B.; Tian, J.G. A gate-tunable symmetric bipolar junction transistor fabricated via femtosecond laser processing. *Nanoscale Adv.* **2020**, *2*, 1733–1740. [CrossRef] [PubMed]
17. Yang, S.J.; Pi, L.J.; Li, L.; Liu, K.L.; Pei, K.; Han, W.; Wang, F.K.; Zhuge, F.W.; Li, H.Q.; Cheng, G.; et al. 2D Cu_9S_5/PtS_2/WSe_2 Double Heterojunction Bipolar Transistor with High Current Gain. *Adv. Mater.* **2021**, *33*, 2106537. [CrossRef]
18. Lee, G.; Pearton, S.J.; Ren, F.; Kim, J. 2D Material-Based Vertical Double Heterojunction Bipolar Transistors with High Current Amplification. *Adv. Electron. Mater.* **2019**, *5*, 1800745. [CrossRef]
19. Liu, L.W.; Xu, N.S.; Zhang, Y.; Zhao, P.; Chen, H.J.; Deng, S.Z. Van der Waals Bipolar Junction Transistor Using Vertically Stacked Two-Dimensional Atomic Crystals. *Adv. Funct. Mater.* **2019**, *29*, 1807893. [CrossRef]
20. Lin, C.Y.; Zhu, X.D.; Tsai, S.H.; Tsai, S.P.; Lei, S.D.; Shi, Y.M.; Li, L.J.; Huang, S.J.; Wu, W.F.; Yeh, W.K.; et al. Atomic-Monolayer Two-Dimensional Lateral Quasi-Heterojunction Bipolar Transistors with Resonant Tunneling Phenomenon. *ACS Nano* **2017**, *11*, 11015–11023. [CrossRef] [PubMed]
21. Li, H.; Ye, L.; Xu, J.B. High-Performance Broadband Floating-Base Bipolar Phototransistor Based on WSe_2/BP/MoS_2 Heterostructure. *ACS Photonics* **2017**, *4*, 823–829. [CrossRef]
22. Lv, L.; Zhuge, F.W.; Xie, F.J.; Xiong, X.J.; Zhang, Q.F.; Zhang, N.; Huang, Y.; Zhai, T.Y. Reconfigurable two-dimensional optoelectronic devices enabled by local ferroelectric polarization. *Nat. Commun.* **2019**, *10*, 3331. [CrossRef]
23. Afzal, A.M.; Iqbal, M.Z.; Dastgeer, G.; Nazir, G.; Mumtaz, S.; Usman, M.; Eom, J. WS_2/GeSe/WS_2 Bipolar Transistor-Based Chemical Sensor with Fast Response and Recovery Times. *ACS Appl. Mater. Interfaces* **2020**, *12*, 39524–39532. [CrossRef] [PubMed]
24. Liu, L.W.; Xu, N.S.; Ke, Y.L.; Chen, H.J.; Zhang, Y.; Deng, S.Z. Sensing by Surface Work Function Modulation: High Performance Gas Sensing using van der Waals Stacked Bipolar Junction Transistor. *Sens. Actuators B-Chem.* **2021**, *345*, 130340. [CrossRef]
25. Dastgeer, G.; Shahzad, Z.M.; Chae, H.; Kim, Y.H.; Ko, B.M.; Eom, J. Bipolar Junction Transistor Exhibiting Excellent Output Characteristics with a Prompt Response against the Selective Protein. *Adv. Funct. Mater.* **2022**, *32*, 2204781. [CrossRef]
26. Yan, Z.; Xu, N.; Deng, S. Realization of High Current Gain for Van der Waals MoS_2/WSe_2/MoS_2 Bipolar Junction Transistor. *Nanomaterials* **2024**, *14*, 718. [CrossRef] [PubMed]
27. Abraham, M.; Mohney, S.E. Annealed Ag contacts to MoS_2 field-effect transistors. *J. Appl. Phys.* **2017**, *122*, 115306. [CrossRef]
28. Jiang, Y.R.; Wang, R.Q.; Li, X.P.; Ma, Z.N.; Li, L.; Su, J.; Yan, Y.; Song, X.H.; Xia, C.X. Photovoltaic Field-Effect Photodiodes Based on Double van der Waals Heterojunctions. *ACS Nano* **2021**, *15*, 14295–14304. [CrossRef] [PubMed]
29. Thakur, D.; Sato, Y.; Sabarigresan, M.; Ramadurai, R.; Balakrishnan, V. Enhanced optical emission at MoS_2-WS_2 heterostructure interface with n-N junction. *Appl. Surf. Sci.* **2022**, *606*, 154923. [CrossRef]
30. Xiao, J.W.; Zhang, Y.; Chen, H.J.; Xu, N.S.; Deng, S.Z. Enhanced Performance of a Monolayer MoS_2/WSe_2 Heterojunction as a Photoelectrochemical Cathode. *Nano-Micro Lett.* **2018**, *10*, 60. [CrossRef]
31. Zhu, J.Q.; Yue, X.F.; Chen, J.J.; Wang, J.; Wan, J.; Bao, W.Z.; Hu, L.G.; Liu, R.; Cong, C.X.; Qiu, Z.J. Ultrasensitive Phototransistor Based on Laser-Induced P-Type Doped WSe_2/MoS_2 Van der Waals Heterojunction. *Appl. Sci.* **2023**, *13*, 6024. [CrossRef]

nanomaterials

Article

p-Type Schottky Contacts for Graphene Adjustable-Barrier Phototransistors

Carsten Strobel [1,*], Carlos Alvarado Chavarin [2], Martin Knaut [1], Matthias Albert [1], André Heinzig [1], Likhith Gummadi [1], Christian Wenger [2,3] and Thomas Mikolajick [1]

[1] Institute of Semiconductors and Microsystems, Chair of Nanoelectronics, Technische Universität Dresden, Nöthnitzer Straße 64, 01187 Dresden, Germany; martin.knaut@tu-dresden.de (M.K.); matthias.albert@tu-dresden.de (M.A.); andre.heinzig@tu-dresden.de (A.H.); likhith.gummadi@mailbox.tu-dresden.de (L.G.); thomas.mikolajick@tu-dresden.de (T.M.)
[2] IHP—Leibniz-Institut für Innovative Mikroelektronik, Im Technologiepark 25, 15236 Frankfurt (Oder), Germany; alvarado@ihp-microelectronics.com (C.A.C.); wenger@ihp-microelectronics.com (C.W.)
[3] Semiconductor Materials, Brandenburg University of Technology Cottbus-Senftenberg, Platz der Deutschen Einheit 1, 03046 Cottbus, Germany
* Correspondence: carsten.strobel@tu-dresden.de; Tel.: +49-35146333151

Abstract: The graphene adjustable-barriers phototransistor is an attractive novel device for potential high speed and high responsivity dual-band photodetection. In this device, graphene is embedded between the semiconductors silicon and germanium. Both n-type and p-type Schottky contacts between graphene and the semiconductors are required for this device. While n-type Schottky contacts are widely investigated, reports about p-type Schottky contacts between graphene and the two involved semiconductors are scarce. In this study, we demonstrate a p-type Schottky contact between graphene and p-germanium. A clear rectification with on–off ratios of close to 10^3 (±5 V) and a distinct photoresponse at telecommunication wavelengths in the infrared are achieved. Further, p-type silicon is transferred to or deposited on graphene, and we also observe rectification and photoresponse in the visible range for some of these p-type Schottky junctions. These results are an important step toward the realization of functional graphene adjustable-barrier phototransistors.

Keywords: phototransistor; GABT; graphene; p-type; silicon; germanium; high responsivity; high speed; dual-band; photodetection

1. Introduction

High-speed photodetectors are a key building block in fiber optic communication systems, which primarily operate in the wavelength range from 1.3 to 1.55 µm [1]. Such devices are the main components in several applications such as long-haul data transition, local area networks, board-to-board, chip-to-chip, and intrachip interconnects. Photodiodes currently dominate the field of high-speed photodetection in the infrared wavelength range at telecommunication standards. Bandwidths of 170 GHz and responsivities of 0.27 A W^{-1} have been demonstrated with indium phosphide (InP) based photodiodes [2]. In 2021, the ultimate and benchmark photodetector performance was achieved with a p-i-n photodiode based on epitaxially grown germanium. A 3-dB bandwidth of 265 GHz and a responsivity of 0.3 A W^{-1} was verified [3]. Graphene (Gr) has also been employed for ultra-high speed (500 GHz) and tunable photodetectors but with moderate responsivity [4]. Another special feature of optical devices made of graphene is their potential absorption up to the THz range through surface plasmon resonance [5]. Novel in-fiber graphene-based devices with increased responsivities have also been reported [6]. Although today's phototransistors have higher sensitivity than photodiodes, their speed is lower. For example, a responsivity of 10^7 A W^{-1} has been demonstrated with a graphene-based phototransistor utilizing PbS quantum dots [7]. However, the bandwidth of this phototransistor is only 100 Hz. The development of photodetectors with high responsivity and high speed in the visible and short-wave infrared (SWIR) persists as a major challenge in optoelectronics. To tackle this challenge, a novel device called a graphene adjustable-barriers transistor (GABT) was proposed in 2022 [8]. The device can best be used as a high-performance dual-band phototransistor (photo-GABT) with sensitivity in the infrared and visible spectral range [9]. In this application scenario, ultra-high responsivities above 10^8 A W^{-1} and a high speed with cutoff frequencies of more than 1 GHz are predicted [9]. Two device designs are conceivable. The first is an n-Si/Gr/p-Ge structure, while the second is a p-Si/Gr/n-Ge composition. As will be discussed later in this paper, the first design maximizes the device's speed at telecommunication wavelengths in the infrared and is, therefore, called the IR configuration. In contrast, the second design allows for higher speeds at shorter wavelengths in the visible range and is, therefore, termed the VIS configuration. Although Gr/n-Ge [10,11] and n-Si/Gr junctions [12–15], which are part of the two photo-GABT designs, are widely examined, this is not the case for Gr/p-Ge and p-Si/Gr. Nonetheless, p-type Schottky junctions between Gr and p-Ge as well as Gr and p-Si are essential for the device operation of the various photo-GABT designs. For the first IR configuration with n-Si/Gr/p-Ge, the challenge is to fabricate a rectifying Gr/p-Ge junction. It is often argued that there could be no rectification at such a junction due to the orientation of the graphene and p-Ge work functions. This hypothesis seems to be confirmed by a study by Song et al. [16]. On the contrary, a significant p-type Schottky junction behavior was found even between n-Ge and graphene when Gr is grown directly on Ge [17]. This is attributed to the n- to p-type conversion of the entire Ge substrate due to the formation of a large density of acceptor defects during the graphene growth process. However, in this case, the area of the junction was in the nanometer scale, which limits the current density and application scenarios.

In the present study, we demonstrate for the first time a large area p-type Schottky junction between Gr and p-Ge with Gr transferred to the semiconductor. Rectification was observed for much larger device dimensions of up to 100×100 μm^2. For the VIS configuration of the photo-GABT formed by a p-Si/Gr/n-Ge structure, a p-type Schottky junction between Gr and p-Si is required. While such p-type Schottky diodes were frequently implemented with Gr transferred on top of p-Si [18], investigations on devices with p-Si transferred or deposited on top of Gr are missing. This is also addressed in the present study. We will show I-V curves in the dark and under illumination for such silicon-on-graphene Schottky diodes. A clear rectification and photoresponse are observed for the selected p-Si/Gr devices. The Schottky barrier heights are deduced from I-V-T measurements. These results are an important milestone in realizing the first graphene adjustable-barrier phototransistor prototype devices.

2. Materials and Methods

Gallium-doped germanium wafers with a resistivity of 2–4 Ohm·cm (Siegert Wafer, Aachen, Germany) were used as the substrate for the Gr/p-Ge devices. The thickness of the p-Ge wafer is 500 μm. A cleaning procedure containing acetone, hydrogen peroxide, hydrofluoric acid, and RCA clean (Sigma Aldrich, Taufkirchen, Germany) was applied to reduce organic and metallic impurities from the wafer surface. Silicon dioxide was deposited by chemical vapor deposition with a thickness of 100 nm. An area of 50×50 μm^2 was exposed from SiO_2 by photolithography and subsequent hydrofluoric acid treatment (5%, 3 min). The 100 nm thick tungsten metallization was realized by photolithography, RF sputtering, and lift-off technique. Next, commercially available monolayer graphene (Graphenea, San Sebastian, Spain) was transferred on top of p-Ge by a poly(methyl methacrylate) (PMMA) assisted wet transfer approach. Another photolithography was applied to pattern Gr using an oxygen plasma treatment. Finally, titanium and aluminum were deposited on the backside of the substrate by electron beam evaporation. A picture of the fabricated devices is shown in Appendix A (Figure A2).

The p-Si/Gr test structure with the silicon transfer approach utilizes a silicon wafer (Siegert Wafer, Aachen, Germany) and a thermally grown SiO_2 insulator. Tungsten and Gr were produced and patterned with photolithography similar to the p-Ge/Gr devices. To fabricate the transferred p-Si slice, a 500 µm thick, single-side polished monocrystalline silicon wafer (Siegert Wafer, Aachen, Germany) was covered with 10 nm of aluminum and 100 nm of ZnO:Al on the textured side of the wafer. The wafer was then annealed at 600 °C for 5 min to form an Al back surface field. Afterward, the wafer was cut by wire sawing to a size of $550 \times 550\ \mu m^2$ and transferred to the target location by means of micromanipulators. Thereby, the polished side of the p-Si slice points toward the underlying graphene.

The p-Si/Gr devices with p-Si deposited on Gr utilize a similar base technology for the framework (substrate + SiO_2 + W + Gr) as described above. However, p-Si is sputter deposited from a polysilicon target (5N, Boron, 0.5 Ohm·cm, FHR Anlagenbau, Ottendorf-Okrilla, Germany). The fast annealing of p-Si takes place in an RTP tool at 1273 K with a heating rate of 2 K/s. The slow annealing is conducted in a furnace from ATV Technologie GmbH (Vaterstetten, Germany) at 1273 K with a heating rate of 10 K/min. The top contact consisted of Al/ZnO:Al and was brought up by photolithography.

The electrical characterization was conducted using a Keithley SCS 4200 semiconductor analyzer (Cleveland, Ohio, United States) connected to a vacuum probe station. To illuminate the devices with a wavelength of 450 nm, a mounted GaN-LED with 23 mW/cm^2 maximum optical output power (Thorlabs GmbH, Bergkirchen, Germany) was used. The input power at the device was monitored by a PM400K5 optical power meter from Thorlabs GmbH. When illuminated with 1550 nm wavelength, a mounted LED with 260 mW/cm^2 maximum optical output power was used.

3. Results and Discussion

3.1. Design Considerations of the Proposed Photo-GABT and Its Potential Performance

Figure 1 shows the three-dimensional device architecture of the novel photo-GABT device with the IR-(n-Si/Gr/p-Ge) and VIS configuration (p-Si/Gr/n-Ge). In the IR-design, graphene is embedded between an n-type silicon top semiconductor with an increased band gap of 1.1 eV and a p-type germanium bottom semiconductor with a low bandgap of 0.67 eV. The illumination takes place through the transparent conductive front contact, acting as drain electrode (D), and made of, e.g., ZnO:Al. A silicon dioxide layer is used to isolate the square-shaped source metallization from bulk germanium.

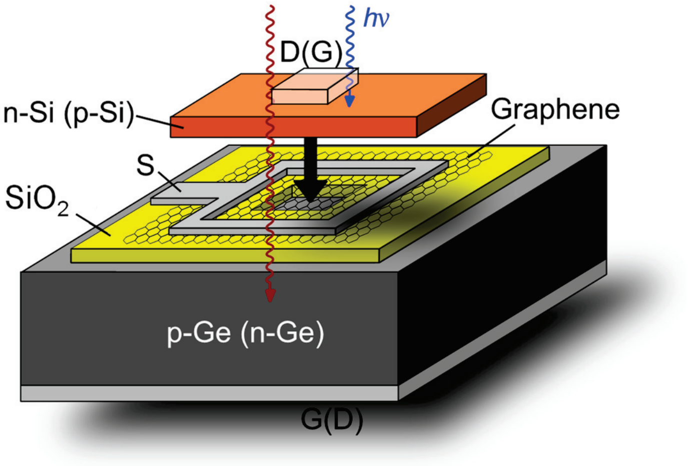

Figure 1. Structure of the photo-GABT's IR configuration (VIS configuration) with a p-type (n-type) germanium bottom semiconductor and an n-type (p-type) silicon top semiconductor. S—source, D—drain, G—gate, hv—photon energy.

To explain the functionality of the new photo-GABT, we can look at the band diagram of the device (Figure 2). In this configuration, an inverse band bending with a Schottky barrier $q\Phi_G$ at the valence band forms between the gate semiconductor p-Ge and graphene

(Figure 2a). Thus, this junction represents a p-type Schottky contact with barrier $q\Phi_G$, while the n-Si/Gr junction is an n-type Schottky contact with barrier $q\Phi_D$. In the OFF-state of the phototransistor, the large drain Schottky barrier $q\Phi_D$ restricts the current across the drain-source junction, as indicated by the small red arrow. Note that in this situation, the drain-source voltage V_{DS} itself is not capable of modulating the graphene Fermi energy level due to electrostatic screening by the thick depleted n-Si layer. This requires a drain semiconductor thickness larger than 300 nm. The ON-state (Figure 2b) is triggered by SWIR illumination. The light of, e.g., 1550 nm wavelength is transmitted through the n-Si with a wider bandgap and then absorbed in the p-Ge gate semiconductor with a smaller bandgap. Within the graphene/p-Ge space charge region, the absorbed light generates electron-hole pairs, which are separated by the potential gradient of the Schottky junction. Thus, electrons move toward and accumulate in graphene and also shift the graphene Fermi energy level toward the conduction band E_C. This leads to a decreasing drain Schottky barrier $q\Phi_D$, and the current across the drain-source junction increases (big red arrow, Figure 2b). A similar shift of the Gr Fermi energy level and subsequent reduction in the drain Schottky barrier height, triggered by a gate voltage instead of illumination, was demonstrated for the barristor device [19]. Calculations indicate a potentially ultra-high responsivity of 2.8×10^8 AW^{-1} for the photo-GABT operation under SWIR illumination (see Appendix A, Figure A1). Furthermore, the potential speed of the device is calculated to be beyond 1 GHz (see Appendix A). Such a potentially high-speed and high-responsivity device is unique amongst today's photodetection technologies.

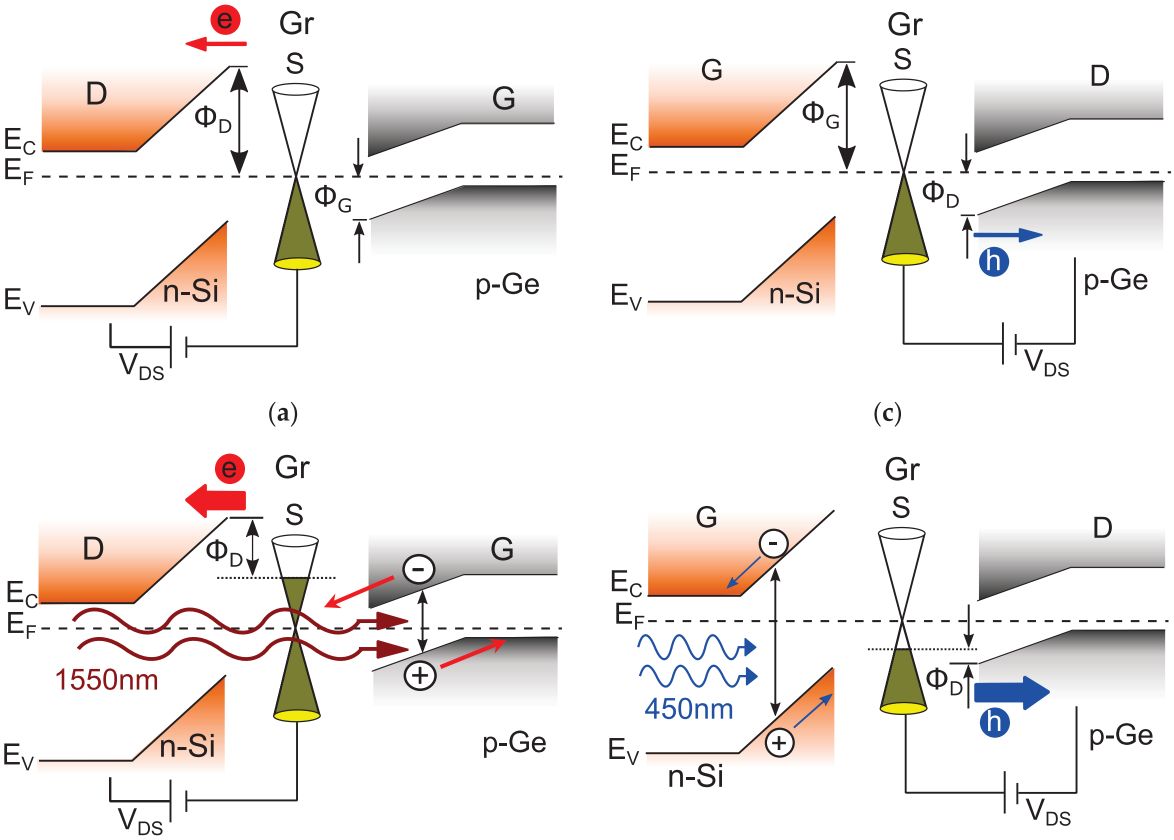

(a) (c)

(b) (d)

Figure 2. Simplified band diagrams of the photo-GABT operation states for different cases/conditions (**a**) SWIR operation in the OFF-state with the Schottky barriers Φ_G and Φ_D. (**b**) ON-state with infrared illumination of 1550 nm wavelength. (**c**) VIS operation in the OFF-state with the Schottky barriers Φ_G and Φ_D. (**d**) ON-state with illumination at 450 nm wavelength.

Apart from the outstanding responsivity and speed, another potential feature of the photo-GABT is the possibility of dual-band operation independent of the configuration. To be specific, the photo-GABT can also operate in the visible spectral range (VIS, λ = 380–750 nm). For example, Figure 2c,d show the OFF- and ON-states of the photo-GABT under 450 nm illumination, respectively. In this case, the roles of the semiconductors are switched, and now n-Si acts as the gate, while p-Ge is the drain terminal. In the OFF-state without illumination (Figure 2c), the negatively biased drain features only a small hole current across the drain Schottky barrier Φ_D, as indicated by the thin blue arrow. In the ON-state (Figure 2d), the blue light illumination of, e.g., 450 nm generates electron-hole pairs within the n-Si gate semiconductor. These electron-hole pairs are then separated in the n-Si/Gr space charge region, and the holes move toward graphene. The accumulation of holes in Gr decreases the Fermi energy level toward the valence band, and their drain Schottky barrier height $q\Phi_D$ is also lowered. Thus, a large current across this barrier is enabled, as indicated by the big blue arrow in Figure 2d. As the device operation in the VIS range relies on hole transport, exhibiting lower mobility, the speed of the photo-GABT might be slightly reduced compared to the operation in the SWIR range. If the maximum speed is required in the VIS range, the device structure can be inverted to the VIS configuration (p-Si/Gr/n-Ge), as already described in Ref. [9]. In this case, the challenge is the fabrication of p-type Schottky contacts between p-Si on top of graphene, while for the IR configuration (n-Si/Gr/p-Ge), p-type Schottky contacts for Gr on top of p-Ge are required. In the following section, initial results on p-type Schottky contacts between silicon, germanium, and graphene are presented.

3.2. p-Type Schottky Junctions for the Photo-GABT

3.2.1. Graphene on p-Germanium

The I-V plot of the Gr/p-Ge junction in the dark and under illumination with a wavelength of 1550 nm is shown in Figure 3a. The black curve (dark I-V) reveals a clear rectification with an on–off ratio at ±5 V of approximately 5×10^2 ($\pm 2.9 \times 10^2$). The biasing of the junction is illustrated in the inset of Figure 3a. Together with the measurement, this verifies the p-type Schottky contact behavior. When illuminated with a wavelength of 1550 nm, a distinct photoresponse under the reverse bias of the Gr/p-Ge diode can be observed. The responsivity of this non-optimized diode is approximately 1×10^{-4} A W^{-1}. The I-V curves were also measured as a function of temperature (see Figure 3b) in order to extract the Schottky barrier height. Thereby, the diode current of a p-type Schottky diode is described by [17]:

$$I = -I_0\left(e^{-\frac{q(V-R_S I)}{nkT}} - 1\right) \tag{1}$$

where I is the current, q is the elementary charge, V is the voltage applied to graphene, R_s is the series resistance, n is the diode ideality factor, k is the Boltzmann constant, T is the temperature, and I_0 is given by the following equation:

$$I_0 = AA^* T^2 e^{-\Phi_{B0}/kT} \tag{2}$$

where A, A^*, and Φ_{B0} represent the junction area, the Richardson constant of the semiconductor, and the Schottky barrier height, respectively. A conventional Richardson plot can be used to evaluate the Schottky barrier height by taking the natural logarithm of Equation (2):

$$ln\left(\frac{I_0}{T^2}\right) = ln(AA^*) - \frac{q\Phi_{B0}}{kT} \tag{3}$$

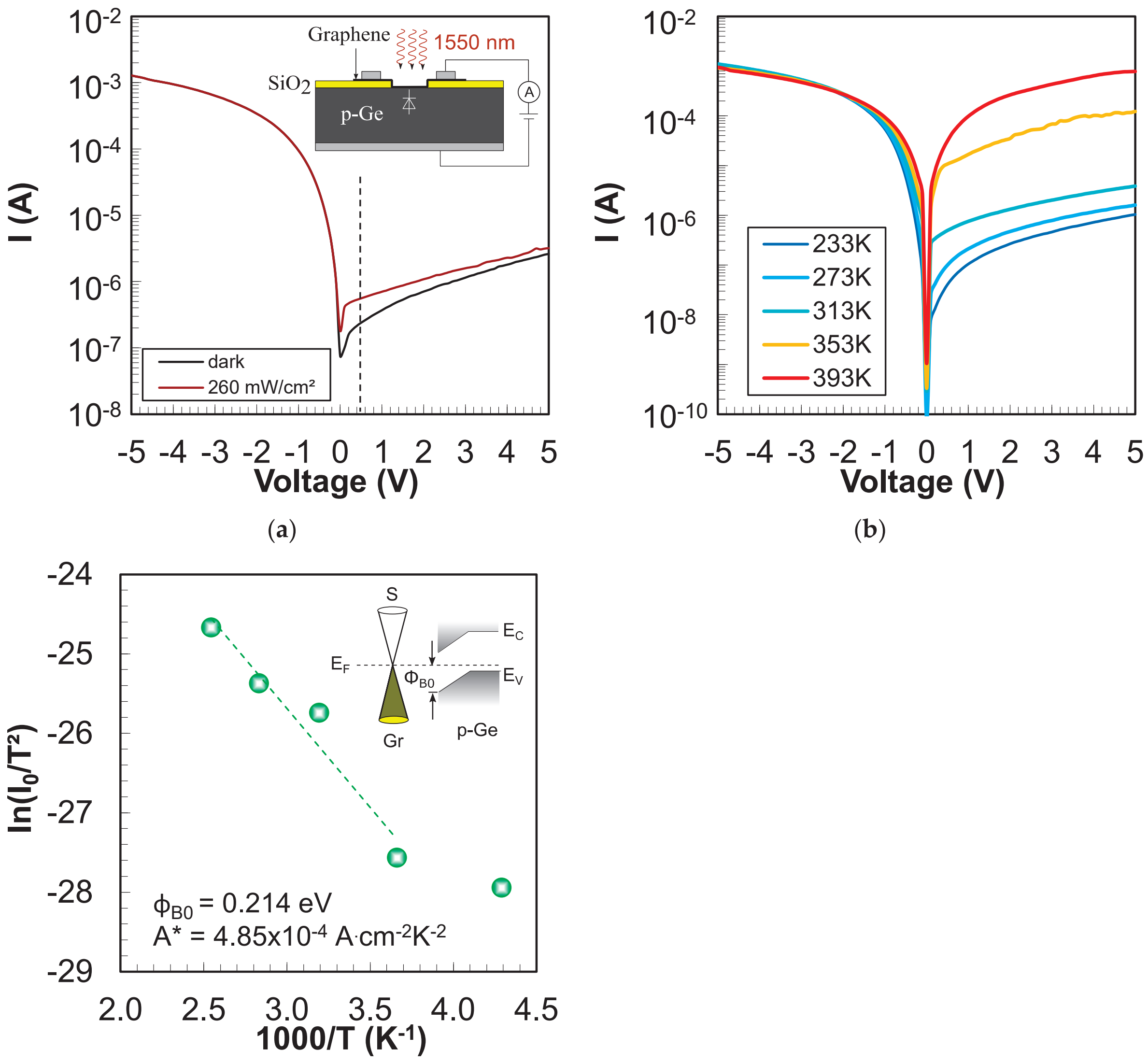

(**a**)

(**b**)

(**c**)

Figure 3. p-Type Schottky contact characterization of graphene on p-Ge (**a**) I-V curve of the Gr/p-Ge Schottky junction in the dark (black curve) and under illumination with a wavelength of 1550 nm (brown curve), dashed line represents the reference point for net photocurrent calculation, inset: biasing of the junction. (**b**) I-V-T plot of the Gr/p-Ge junction measured in the dark. (**c**) Richardson plot of the Gr/p-Ge junction with the extracted Schottky barrier height Φ_{B0} and Richardson constant A*.

Figure 3c shows the Richardson plot of $\ln\left(I_0/T^2\right)$ versus 1000/T. The barrier height of the Gr/p-Ge junction is deduced from a linear fit to the data and represents 0.214 eV (±0.02 eV). This barrier height is comparable to Gr/n-Ge junctions where values between 0.2–0.3 eV have been reported [8,11]. The inset in Figure 3c illustrates the band bending at the Gr/p-Ge junction with the Schottky barrier Φ_{B0} toward the valence band. The Richardson constant is calculated to 4.85×10^{-4} A·cm^{-2}·K^{-2} which is consistent with previous reports about Gr/n-Ge junctions [20]. The $\ln\left(I_0/T^2\right)$—1000/T plot deviates from linearity at very low temperatures which indicates a strong temperature dependence of the barrier height. A decreased Schottky barrier at very low temperatures could also affect the performance of the photo-GABT. However, as the targeted photo-GABT device should perform well at increased temperatures (i.e., 293 K), the deviation from linearity at very low temperatures can be neglected.

The net photocurrent of the Gr/p-Ge diode at a wavelength of 1550 nm is $I_{net} = I_{photo} - I_{dark}$ and represents 3.21×10^{-7} A at a voltage of +0.5 V (see dashed line in Figure 3a). This means that about 2×10^9 electrons are accumulating in Gr on the timescale of a millisecond. This translates to a change in the Fermi energy level in Gr of 0.052 eV, and at the drain of the GABT phototransistor with an n-Si top semiconductor, the current would increase by about one order of magnitude. However, to fully turn on the photo-GABT, further improvements are required to increase the photocurrent at the Gr/p-Ge junction. This could be achieved by, e.g., passivation of the p-Ge surfaces and implementation of an aluminum-based back surface field at the p-Ge back contact [21].

3.2.2. p-Silicon on Graphene

(A) Transfer method

As a first attempt to investigate the p-Si/Gr Schottky contact for the VIS configuration of the photo-GABT, 550 μm thick monocrystalline p-silicon is transferred onto Gr (see methods section). Figure 4a shows the resulting test structure and biasing scheme with p-Si illuminated through a transparent conductive oxide (TCO—here: ZnO:Al). Thereby, graphene is insulated from the substrate through a SiO_2 layer. The I-V curves in the dark and under illumination are illustrated in Figure 4b.

A distinctive rectification with an on–off ratio of 1.2×10^3 (mean 5.7×10^2 at ± 5 V) could be observed for the p-type Schottky contact between p-Si and Gr. Unfortunately, the current under illumination is the same as in the dark, which means that no significant photoresponse could be verified for this device. To better understand the lack of a photocurrent for the p-Si/Gr device, a reference p-Si/metal structure was fabricated and illuminated from the front side and from the back side (see Appendix B, Figure A3). This reference test structure reveals a much stronger photoresponse when illuminated from the back side. When illuminated through the front side with a short wavelength of 450 nm, most of the carriers are absorbed near the surface of the wafer. This indicates that there is a problem with the diffusion of carriers from the front side to the back side of the wafer in case of front side illumination. However, at least a slight photoresponse could be expected for the p-Si/Gr junction under front side illumination as observed for the reference metal/p-Si device (see Figure A3b). This slight photoresponse shown in Figure A3b also demonstrates that the diffusion length in our p-Si wafers is higher than the wafer thickness of 500 μm. It can be speculated that an increased recombination at the wire-sawed surfaces of the transferred p-Si slice impedes any photoeffect for the p-Si/Gr device. The as-cut wafer's front side could also be a source of high recombination, especially when considering that most of the blue light is absorbed near the surface. The boron-oxygen complex [22] could also lead to high recombination in p-Si, which could substantially reduce photoresponse. Novel p-Si transfer techniques based on silicon-on-insulator (SOI) wafers [11] with strongly reduced p-Si thicknesses and improved p-Si membrane surfaces might be suitable to strongly increase the photoresponse of future devices.

The p-Si/Gr Schottky junction was also measured at different temperatures (Figure 4c) to extract the Schottky barrier height from the Richardson plot (Figure 4d). A Schottky barrier height of 0.37 eV (mean 0.3 eV) was drawn for the transferred p-Si/Gr junction. In the literature, Schottky barrier heights between 0.18 eV and 0.47 eV for graphene transferred on top of p-silicon have been reported [18,23,24]. Thus, with the present work, similar barrier heights could be demonstrated for the first time for p-Si transferred on top of Gr. The inset of Figure 4d shows the band bending at the p-Si/Gr junction which fulfills the requirements for the photo-GABT.

(B) Deposition of p-Si

The second, more scalable approach to investigate the p-Si/Gr Schottky contact for the VIS configuration (p-Si/Gr/n-Ge) of the photo-GABT is to deposit and crystallize p-type amorphous silicon (p-a-Si) on top of graphene (see methods section). Thereby, p-a-Si is deposited by RF-sputtering and crystallized through high temperature annealing at 1000 °C. Moreover, the annealing was either executed with a slow heating rate in a furnace from ATV Technologie GmbH or with fast ramps in a rapid thermal processing (RTP) tool. Figure 5 shows the I-V curves of p-Si deposited and crystallized on top of graphene. As can be seen, the I-V curves for the slow annealing process (Figure 5a) show a distinct rectification with a p-type Schottky contact behavior between p-Si and Gr.

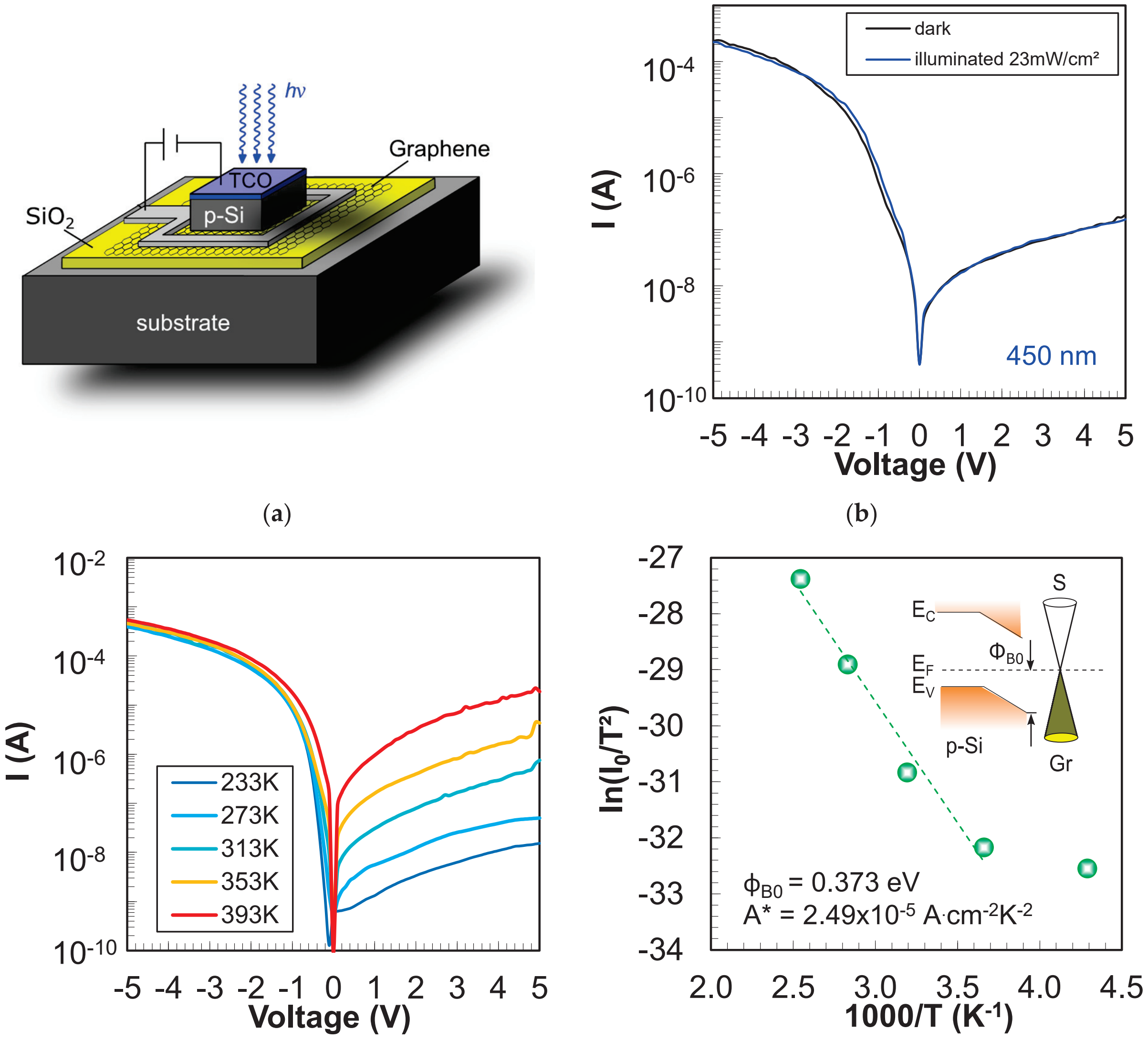

(**a**) (**b**)

(**c**) (**d**)

Figure 4. Investigation of the p-Si/Gr junction utilized for the VIS configuration of the photo-GABT. (**a**) Test structure for the evaluation of the p-Si/Gr p-type Schottky contact. (**b**) I-V curves of the p-Si/Gr junction in the dark and under illumination. (**c**) I-V-T plot of the p-Si/Gr junction measured in the dark. (**d**) Richardson plot of the p-Si/Gr junction with the extracted Schottky barrier height Φ_{B0} and Richardson constant A*.

However, a photoresponse in the reverse direction (blue vs. black curve in Figure 5a), as required for the p-Si/Gr/n-Ge photo-GABT, could not be observed. Furthermore, even if the reverse currently shows saturation, the I-V curve does not pass through the origin, and the forward current is rather low. In contrast, the forward current for the fast RTP anneal (Figure 5b) is much higher, and a distinct photoresponse in the reverse direction can be observed. The shape of the curve also indicates a p-type Schottky contact between p-Si and Gr. However, the reverse current of the RTP anneal curve shows no saturation so far. The reason for the observed photoresponse in the case of the fast annealing could be an increased crystalline volume fraction (see Raman spectra in Appendix B, Figure A4) for the RTP material. It can be speculated that different crystallization dynamics lead to an increased crystallinity for the material annealed with fast heating rates. Although currently, the fast annealing seems more promising toward a functional p-Si/Gr/n-Ge photo-GABT, further optimizations are required to improve the p-Si/Gr junction.

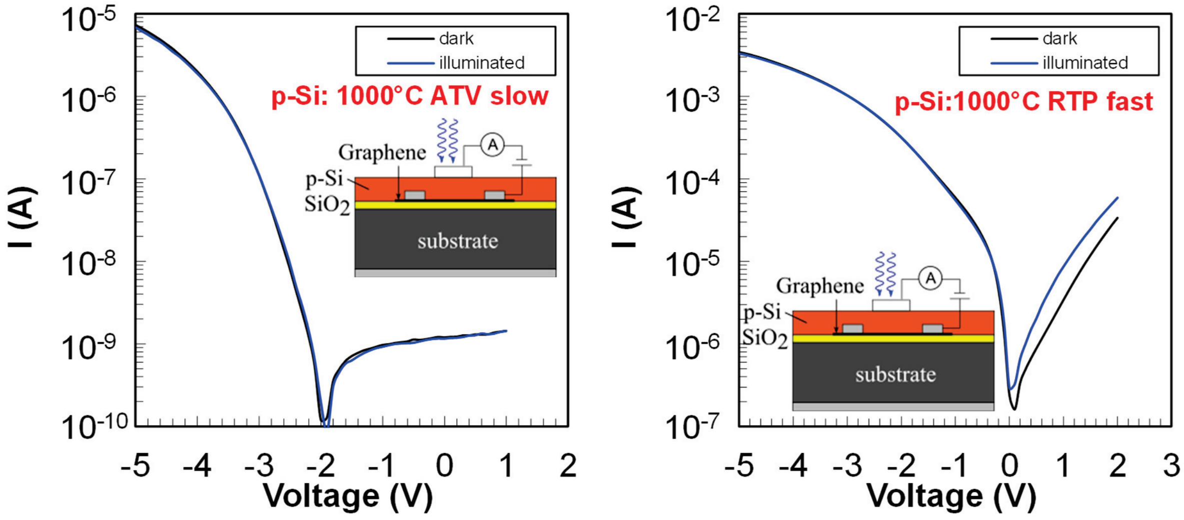

(**a**) (**b**)

Figure 5. p-Si to Gr contact characterization for different p-Si deposition techniques (**a**) I-V curves of the p-Si/Gr junction in the dark and under illumination for p-Si annealed with slow heating rates at 1000 °C in an ATV furnace. (**b**) I-V curves of the p-Si/Gr junction in the dark and under illumination for p-Si annealed with fast heating rates at 1000 °C in an RTP furnace.

3.3. Comparison of Phototransistor Performances

Silicon bipolar phototransistors for the visible range are readily available on the market. These Si npn phototransistors are comparable to those presented more than 20 years ago by Dalla Betta et al., reaching responsivities close to 0.6 A/W at wavelengths of ~850 nm, falling close to zero at ~1000 nm and showing a 3 dB bandwidth of 55 kHz [25]. In the short-wavelength infrared, outstanding results have been shown recently for Si/Ge waveguide phototransistors by Gao et al. [26], reaching responsivities at over 1000 A/W and a 3 dB bandwidth of 1.5 GHz for a wavelength of 1550 nm. It can be noted that even with such high responsivities, waveguide-based photodetection still requires light to be coupled to the waveguide, with, e.g., a grating coupler, thus increasing the overall insertion losses of this strategy. To improve the spectral range, responsivity, and bandwidth, other materials have been investigated. Son Ko et al. [27] used InP Nanopillars directly grown on Si, reporting a responsivity of 9.5 A/W and a bandwidth of 7 GHz for a 785 nm wavelength. Han et al. [28] used a combination of organic semiconductor crystals and nanoparticles to achieve a broadband responsivity over 1.2×10^5 A/W from 410 to 740 nm in wavelength. Besides the CMOS incompatibility of organic semiconductors, the response times are usually in the ms range. Thus, very low bandwidths are expected. 2D materials have also been investigated as phototransistors. Xu et al. [29] reported a responsivity of $\sim 2.5 \times 10^4$ A/W for dual gate phototransistors based on WSe_2. Moudgil et al. [30] used In_2S_3 on Si, achieving a responsivity of 12 A/W and 41 A/W for illumination at 405 nm and 800 nm wavelengths, respectively. Using black phosphorous (BP) on Si-doped Ga_2O_3, Chen et al. [31] reported a responsivity of 2390 A/W and 0.53 A/W under 254 nm and 808 nm illumination, respectively. A p-WSe_2/n-Ge heterojunction transistor was investigated by Li et al. [32], which achieves responsivities of 55 A/W, 95 A/W, and 120 A/W at illuminations of 405 nm, 1310 nm, and 1550 nm, respectively. The aforementioned 2D approaches mainly used exfoliated sheets, which are known to lack upscaling fabrication capabilities. Furthermore, the reported response times range from µs to s, and thus, limited to very limited bandwidths are expected. Further information on photodetection based on graphene transistors can be found elsewhere [33]. In the specific case of the dual barrier

Si/Gr/Ge phototransistor (photoGABT) approach, a plausible advantage is the possibility of the direct growth of Gr on Ge reported by several research groups [34–36]. In addition, analytical calculations (see Appendix A) show that bandwidths in the GHz range could be expected. A comparative table of selected phototransistors is shown in Table 1.

Table 1. Comparison of phototransistor performances for various transistor architectures. Last row is marked in grey and represents "proposed in this work".

Ref.	Phototransistor Type	Responsivity (AW^{-1})	Spectral Range	Bandwidth	CMOS Compatibility
[25]	Si npn	0.6 (at 850 nm)	Broadband (400–1000 nm)	55 kHz	High
[26]	SiGe waveguide	1032	IR (1550 nm)	1.5 GHz	High
[27]	InP nanopillars on Si	9.5	Visible (785 nm)	7 GHz	Medium
[28]	Organic semiconductors	1.2×10^5	Broadband (410–740 nm)	Limited	Low
[29]	WSe_2 on hBN	2.5×10^4	Visible (532 nm)	Limited	Low
[30]	In_2Se_3 on Si	41 (at 800 nm)	Broadband (405–800 nm)	Limited	Low
[31]	BP on Ga_2O_3	2390 (at 254 nm)	Broandband (254–808 nm)	Limited	Low
[32]	WSe_2 on Ge	120 (at 1550 nm)	Broadband (405–1550 nm)	Limited	Low
	Double barrier Si/Gr/Ge	2.8×10^8	Broadband (532–1550 nm)	25 GHz	Medium

4. Conclusions

As a prerequisite for the novel, potentially high-performance graphene adjustable-barrier phototransistor, p-type Schottky contacts between graphene and p-Ge or p-Si are required. In this study, we demonstrate a rectifying p-Ge/Gr p-type Schottky junction with a significant photoresponse at telecommunication wavelengths of 1550 nm, which is against theoretical expectations. The Schottky barrier height for the Gr/p-Ge diode is determined to be 0.214 eV. Furthermore, the transfer and deposition of p-Si on top of graphene have also been investigated. We found a rectifying behavior for all studied p-Si/Gr test structures. The mean Schottky barrier height for the transferred p-Si on Gr devices is 0.3 eV. A distinct photoresponse at a wavelength of 450 nm is observed for the p-Si/Gr junction when p-Si is deposited and crystallized at 1000 °C in a rapid thermal processing tool. These results pave the way for the realization of first functional graphene adjustable-barrier phototransistor devices.

5. Patents

C. Strobel, "Halbleiterbauelement, Verfahren zum Herstellen eines Halbleiterbauelements und Verfahren zum Betreiben eines Halbleiterbauelements", DPMA P83689, vol. Patent 10 2022 106 012.8 DE, Mar. 2023.

C. Strobel, "Photodetektor und Verfahren zum Betreiben eines Photodetektors", DPMA P87474, vol. Patent 10 2023 113 982.7 DE, May 2023.

Author Contributions: Conceptualization, C.S., C.A.C., M.A., C.W. and T.M.; supervision, T.M., A.H. and M.A.; writing—original draft preparation, review, and editing, formal analysis, methodology, C.S.; methodology, M.K. and L.G. All authors discussed the results and commented on the paper. All authors have read and agreed to the published version of the manuscript.

Funding: This research received no external funding.

Data Availability Statement: Data are contained within the article.

Conflicts of Interest: The authors declare no conflicts of interest.

Appendix A

Calculation of main photo-GABT device metrics

The calculated output currents of the new n-Si/Gr/p-Ge photo-GABT in the dark and under 1550 nm illumination (50 μW) are shown in Figure A1. High output currents above 10^4 A/mm^2 are achieved under SWIR illumination. The high output current density is derived from the following considerations. The number of photons from a SWIR laser (1550 nm, 50 μW, 1 mm^2, 1 ms) impinging on the phototransistor can be calculated as 3.9×10^{11}. Assuming a moderate external quantum efficiency of 37%, this results in about 1.4×10^{11} electrons moving to the graphene. The charge carrier-induced increase in the Fermi level in graphene can be calculated to 0.44 eV using the relationship $\Delta E_F = \hbar v_F \sqrt{\pi n}$ [19] with the Dirac constant $\hbar$, the Fermi velocity of graphene v_F and the charge carrier density n. Furthermore, in the initial state the graphene/n-silicon Schottky barrier height is 0.49 eV [12] and then decreases to 0.05 eV due to the SWIR illumination. If one now takes the diode equation for the thermionic emission via the Schottky barrier with $q\Phi_D = 0.05$ eV:

$$J = A^{**}T^2 exp\left(-\frac{q\phi_D}{kT}\right)\left[exp\left(\frac{qV_{DS}}{nkT}\right) - 1\right] \tag{A1}$$

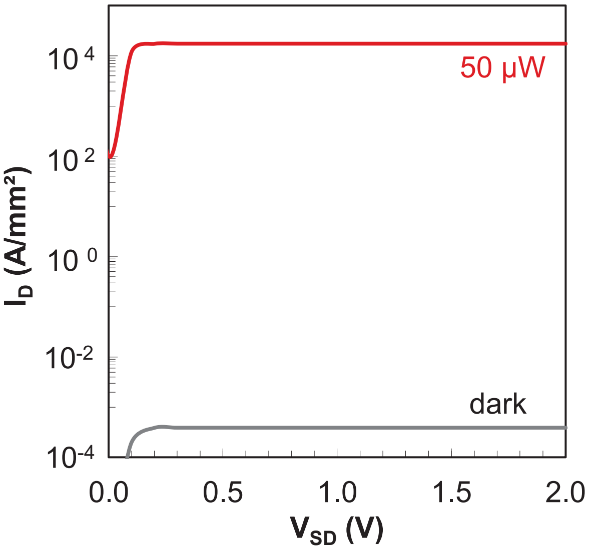

Figure A1. Calculated drain current density in the dark (grey curve) and with 50 μW illumination of 1550 nm (red curve).

With A^{**} being the Richardson constant (120 A cm^{-2} K^{-2}), T being the temperature, and k being the Boltzmann constant. Then, a reverse saturation current density of 1.4×10^4 A/mm^2 is calculated. This corresponds to the illumination-induced ON-current as observed in Figure A1 (red curve). Currents of this magnitude are indeed predicted for germanium-based GABTs [8]. This means that about 1×10^{20} electrons per millisecond flow across the drain Schottky barrier, and, based on the incoming photons, there is an ultra-high gain of about 2.5×10^8 and a responsivity of 2.8×10^8 A W^{-1} at this operating point. This would be amongst the highest reported gains of photodetectors.

Moreover, the speed of such a Schottky barrier-based phototransistor is determined by the transit time of the carriers through the depletion layer, the sheet resistances, the resistance of the bulk material, and the capacitance of the junction. The electron transit time τ_{el} can be calculated from the relation [37]: $\tau_{el} = d/v_s$, with d the thickness of the space charge region, and v_s the saturation velocity. The latter is 1×10^7 cm/s and 0.6×10^7 cm/s for electrons in silicon and germanium, respectively. In order to absorb about 40% of light in p-Ge (see required EQE), a minimum p-Ge thickness of about 1 μm can be derived from Lambert–Beer's law. The calculated space charge region thickness of a Gr/p-Ge junction is also about 1 μm if a slightly negative voltage of about −0.5 V is applied to the gate. In this case, the device operation only relies on a fast drift process as no carriers must slowly diffuse toward the depletion region. In addition, as already discussed above, the minimum n-Si thickness corresponds to 0.3 μm. Thus, a good approximation for the minimum required space charge region thickness an electron must travel in total through the device is $d = 1.3$ µm. This yields a $\tau_{el} \sim 20$ ps and a cutoff frequency of 51 GHz. Furthermore, based on the capacitance C per unit area and the sheet resistance R_s, the frequency response of a Schottky detector can be calculated [37]:

$$w_c = \frac{3}{R_s C b^2} \tag{A2}$$

with w_c being the 3-db cutoff frequency and b being the width of the device. With a capacitance of about 7.5×10^{-3} F/m^2 [38] (area 4×10^{-4} cm^2), a total resistance of 50 Ohm, and a device width of 10 µm, a cutoff frequency $f_c = w_c/2\pi \approx 25$ GHz seems feasible. This cutoff frequency is of the same order as the cutoff frequency obtained from transit time considerations. Thus, the photo-GABT potentially offers a very high bandwidth.

Image of the Gr/p-Ge devices

In Figure A2, the top view of eight individual Gr/p-Ge devices is illustrated. We use a 100 nm thick underlying SiO$_2$ layer to realize a good optical contrast in order to visualize the graphene layer in the optical microscope. Thereby, Gr is patterned to islands of 350 × 350 µm^2 by O$_2$-plasma.

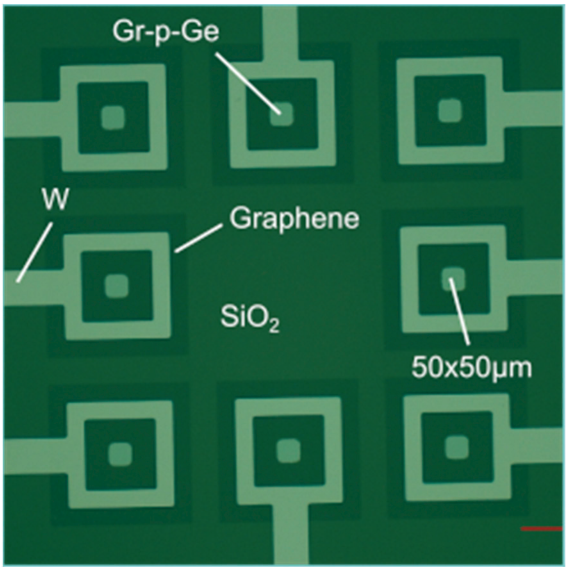

Figure A2. Optical microscope image of eight 50 × 50 µm^2 Gr/p-Ge devices.

Appendix B

A reference device that resembles the p-Si/Gr structure (see Figure 4a) was fabricated. Figure A3 shows the design of this test structure. The 550 µm thick p-type silicon wafer is metalized from the back side through a shadow mask. The size of the metal contact is of the same order as the transferred p-Si flake of the device shown in Figure 4a). It can be assumed that the metal/p-Si contact (see Figure A3a) approximately resembles the semi-metallic graphene/p-Si contact of the test structure in Figure 4a. The front contact of the test structure consists of a full area Al/TCO deposit. Next, the p-Si/metal device is illuminated from the front side and from the back side via a 450 nm LED. The I-V curves of the p-Si/metal test structure are shown in Figure A3b. It can be seen that a strong photoresponse is present under back side illumination even though the metal contact is non-transparent. Thus, a strong lateral diffusion of photo-induced carriers must be available. However, under front side illumination, only a very low photoresponse could be observed. As most of the light of 455 nm wavelength is absorbed near the surface of the wafer, this indicates an insufficient diffusion of carriers from the front to the back side of the p-Si wafer.

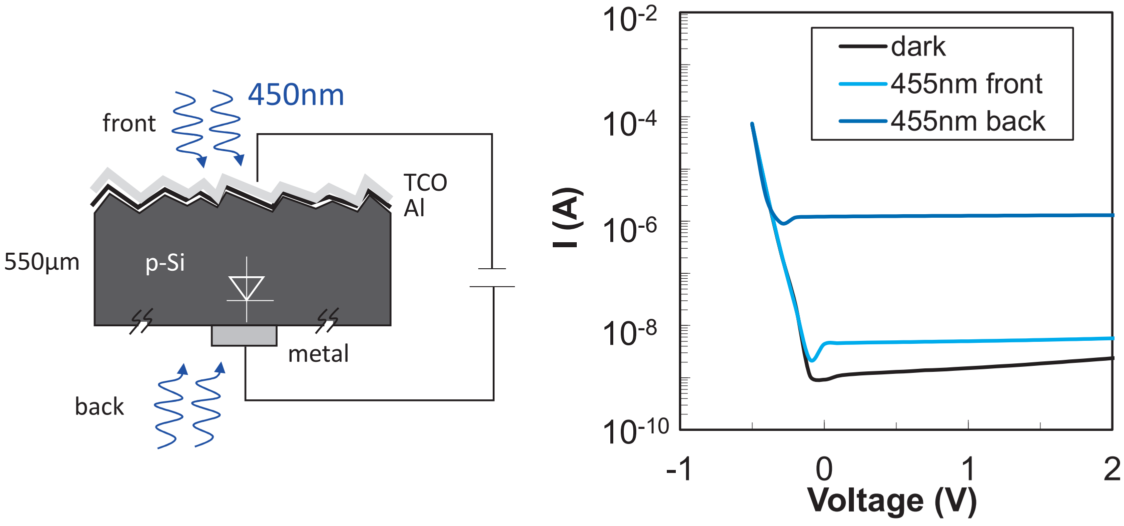

(**a**) (**b**)

Figure A3. p-Si/metal reference device under front and backside illumination (**a**) Cross section of a test structure and the measurement setup for the evaluation of front and back side illumination. (**b**) I-V curves of the p-Si/metal test structure in the dark (black curve), under front illumination (light blue curve), and under back side illumination (dark blue curve).

Raman measurement of sputter deposited and annealed p-Si

The Raman spectra of sputter deposited and crystallized p-Si were measured for material annealed fast (RTP) and slowly (ATV) at 1000 °C. Figure A4 shows the corresponding curves with a distinctive peak at 520 cm^{-1}, which can be attributed to the crystalline phase of p-Si. The Raman spectra demonstrate that both the materials that were annealed with fast (2 K/s) and slow (10 K/min) ramps were successfully crystallized. However, the Raman intensity for the RTP material is almost double as high as for the ATV material.

We attribute the increased Raman intensity to an increased crystalline volume fraction of the RTP material. This could be due to different crystallization dynamics when annealed with fast ramps compared to slow ramps.

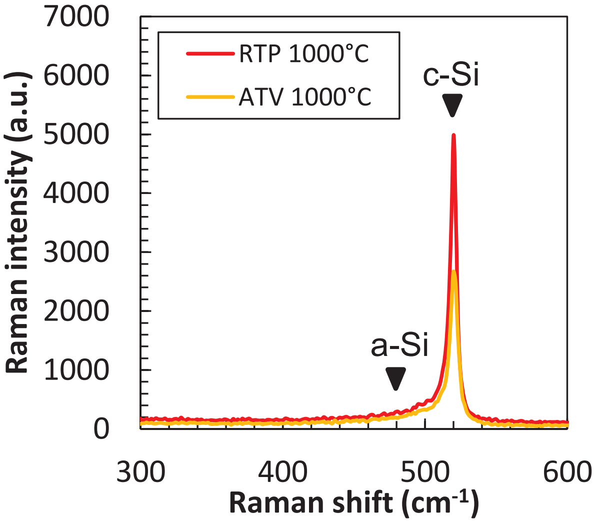

Figure A4. Raman spectrum of sputter deposited p-Si annealed at 1000 °C with a rapid thermal processing (RTP) treatment (red curve) or with a slow process in an ATV furnace (orange curve).

References

1. Chen, G.; Yu, Y.; Shi, Y.; Li, N.; Luo, W.; Cao, L.; Danner, A.J.; Liu, A.-Q.; Zhang, X. High-Speed Photodetectors on Silicon Photonics Platform for Optical Interconnect. *Laser Photonics Rev.* **2022**, *16*, 2200117. [CrossRef]
2. Rouvalis, E.; Chtioui, M.; van Dijk, F.; Lelarge, F.; Fice, M.J.; Renaud, C.C.; Carpintero, G.; Seeds, A.J. 170 GHz Uni-Traveling Carrier Photodiodes for InP-Based Photonic Integrated Circuits. *Opt. Express OE* **2012**, *20*, 20090–20095. [CrossRef] [PubMed]
3. Lischke, S.; Peczek, A.; Morgan, J.S.; Sun, K.; Steckler, D.; Yamamoto, Y.; Korndörfer, F.; Mai, C.; Marschmeyer, S.; Fraschke, M.; et al. Ultra-Fast Germanium Photodiode with 3-dB Bandwidth of 265 GHz. *Nat. Photon.* **2021**, *15*, 925–931. [CrossRef]
4. Koepfli, S.M.; Baumann, M.; Koyaz, Y.; Gadola, R.; Güngör, A.; Keller, K.; Horst, Y.; Nashashibi, S.; Schwanninger, R.; Doderer, M.; et al. Metamaterial Graphene Photodetector with Bandwidth Exceeding 500 Gigahertz. *Science* **2023**, *380*, 1169–1174. [CrossRef] [PubMed]
5. Li, W.; Liu, M.; Cheng, S.; Zhang, H.; Yang, W.; Yi, Z.; Zeng, Q.; Tang, B.; Ahmad, S.; Sun, T. Polarization Independent Tunable Bandwidth Absorber Based on Single-Layer Graphene. *Diam. Relat. Mater.* **2024**, *142*, 110793. [CrossRef]
6. Jiang, B.; Hou, Y.; Wu, J.; Ma, Y.; Gan, X.; Zhao, J. In-Fiber Photoelectric Device Based on Graphene-Coated Tilted Fiber Grating. *OES* **2023**, *2*, 230012. [CrossRef]
7. Konstantatos, G.; Badioli, M.; Gaudreau, L.; Osmond, J.; Bernechea, M.; de Arquer, F.P.G.; Gatti, F.; Koppens, F.H.L. Hybrid Graphene–Quantum Dot Phototransistors with Ultrahigh Gain. *Nat. Nanotech* **2012**, *7*, 363–368. [CrossRef] [PubMed]
8. Strobel, C.; Chavarin, C.A.; Richter, K.; Knaut, M.; Reif, J.; Völkel, S.; Jahn, A.; Albert, M.; Wenger, C.; Kirchner, R.; et al. Novel Graphene Adjustable-Barrier Transistor with Ultra-High Current Gain. *ACS Appl. Mater. Interfaces* **2022**, *14*, 39249–39254. [CrossRef] [PubMed]
9. Strobel, C.; Chavarin, C.A.; Wenger, C.; Albert, M.; Mikolajick, T. Vertical Graphene-Based Transistors for Power Electronics, Optoelectronics and Radio-Frequency Applications. In Proceedings of the 2023 IEEE Nanotechnology Materials and Devices Conference (NMDC), Paestum, Italy, 23–25 October 2023; pp. 196–201.
10. Strobel, C.; Chavarin, C.A.; Knaut, M.; Völkel, S.; Albert, M.; Hiess, A.; Max, B.; Wenger, C.; Kirchner, R.; Mikolajick, T. High Gain Graphene Based Hot Electron Transistor with Record High Saturated Output Current Density. *Adv. Electron. Mater.* **2024**, *10*, 2300624. [CrossRef]
11. Liu, C.; Ma, W.; Chen, M.; Ren, W.; Sun, D. A Vertical Silicon-Graphene-Germanium Transistor. *Nat. Commun.* **2019**, *10*, 4873. [CrossRef]
12. Strobel, C.; Chavarin, C.A.; Völkel, S.; Jahn, A.; Hiess, A.; Knaut, M.; Albert, M.; Wenger, C.; Steinke, O.; Stephan, U.; et al. Enhanced Electrical Properties of Optimized Vertical Graphene-Base Hot Electron Transistors. *ACS Appl. Electron. Mater.* **2023**, *5*, 1670–1675. [CrossRef]
13. Strobel, C.; Chavarin, C.A.; Kitzmann, J.; Lupina, G.; Wenger, C.; Albert, M.; Bartha, J.W. Towards High Frequency Heterojunction Transistors: Electrical Characterization of N-Doped Amorphous Silicon-Graphene Diodes. *J. Appl. Phys.* **2017**, *121*, 245302. [CrossRef]
14. Strobel, C.; Chavarin, C.A.; Leszczynska, B.; Leszczynski, S.; Winkler, F.; Killge, S.; Völkel, S.; Richter, K.; Hiess, A.; Knaut, M.; et al. Demonstration of a Graphene-Base Heterojunction Transistor with Saturated Output Current. *J. Appl. Phys.* **2019**, *125*, 234501. [CrossRef]
15. Bartolomeo, A.D.; Luongo, G.; Iemmo, L.; Urban, F.; Giubileo, F. Graphene–Silicon Schottky Diodes for Photodetection. *IEEE Trans. Nanotechnol.* **2018**, *17*, 1133–1137. [CrossRef]
16. Song, S.; Kim, S.-H.; Han, K.-H.; Kim, H.; Yu, H.-Y. In-Depth Analysis on Self Alignment Effect of the Fermi-Level Using Graphene on Both n- and p-Type Semiconductors. *ACS Appl. Mater. Interfaces* **2023**, *15*, 57879–57889. [CrossRef] [PubMed]
17. Pea, M.; De Seta, M.; Di Gaspare, L.; Persichetti, L.; Scaparro, A.M.; Miseikis, V.; Coletti, C.; Notargiacomo, A. Submicron Size Schottky Junctions on As-Grown Monolayer Epitaxial Graphene on Ge(100): A Low-Invasive Scanned-Probe-Based Study. *ACS Appl. Mater. Interfaces* **2019**, *11*, 35079–35087. [CrossRef] [PubMed]
18. Luongo, G.; Bartolomeo, A.D.; Giubileo, F.; Chavarin, C.A.; Wenger, C. Electronic Properties of Graphene/p-Silicon Schottky Junction. *J. Phys. D Appl. Phys.* **2018**, *51*, 255305. [CrossRef]
19. Yang, H.; Heo, J.; Park, S.; Song, H.J.; Seo, D.H.; Byun, K.-E.; Kim, P.; Yoo, I.; Chung, H.-J.; Kim, K. Graphene Barristor, a Triode Device with a Gate-Controlled Schottky Barrier. *Science* **2012**, *336*, 1140–1143. [CrossRef] [PubMed]
20. Khurelbaatar, Z.; Kil, Y.-H.; Shim, K.-H.; Cho, H.; Kim, M.-J.; Kim, Y.-T.; Choi, C.-J. Temperature Dependent Current Transport Mechanism in Graphene/Germanium Schottky Barrier Diode. *JSTS J. Semicond. Technol. Sci.* **2015**, *15*, 7–15. [CrossRef]
21. Narasinha, S.; Rohatgi, A. Optimized Aluminum Back Surface Field Techniques for Silicon Solar Cells. In Proceedings of the Conference Record of the Twenty Sixth IEEE Photovoltaic Specialists Conference-1997, Anaheim, CA, USA, 29 September–3 October 1997; pp. 63–66.
22. Voronkov, V.V.; Falster, R.; Bothe, K.; Lim, B.; Schmidt, J. Lifetime-Degrading Boron-Oxygen Centres in p-Type and n-Type Compensated Silicon. *J. Appl. Phys.* **2011**, *110*, 063515. [CrossRef]
23. Chen, C.-C.; Aykol, M.; Chang, C.-C.; Levi, A.F.J.; Cronin, S.B. Graphene-Silicon Schottky Diodes. *Nano Lett.* **2011**, *11*, 1863–1867. [CrossRef]
24. An, Y.; Behnam, A.; Pop, E.; Bosman, G.; Ural, A. Forward-Bias Diode Parameters, Electronic Noise, and Photoresponse of Graphene/Silicon Schottky Junctions with an Interfacial Native Oxide Layer. *J. Appl. Phys.* **2015**, *118*, 114307. [CrossRef]

25. Dalla Betta, G.F.; Pignatel, G.U.; Verzellesi, G.; Bellutti, P.; Boscardin, M.; Ferrario, L.; Zorzi, N.; Maglione, A. Design and Optimization of an Npn Silicon Bipolar Phototransistor for Optical Position Encoders. *Microelectron. J.* **1998**, *29*, 49–58. [CrossRef]
26. Gao, Y.; Das, R.; Xie, Y.; Guo, F.; Mascher, P.; Knights, A.P. Si/Ge Phototransistor with Responsivity > 1000 A/W on a Silicon Photonics Platform. *Opt. Express OE* **2024**, *32*, 2271–2280. [CrossRef]
27. Ko, W.S.; Bhattacharya, I.; Tran, T.-T.D.; Ng, K.W.; Adair Gerke, S.; Chang-Hasnain, C. Ultrahigh Responsivity-Bandwidth Product in a Compact InP Nanopillar Phototransistor Directly Grown on Silicon. *Sci. Rep.* **2016**, *6*, 33368. [CrossRef]
28. Han, T.; Shou, M.; Liu, L.; Xie, Z.; Ying, L.; Jiang, C.; Wang, H.; Yao, M.; Deng, H.; Jin, G.; et al. Ultrahigh Photosensitive Organic Phototransistors by Photoelectric Dual Control. *J. Mater. Chem. C* **2019**, *7*, 4725–4732. [CrossRef]
29. Xu, J.; Luo, X.; Hu, S.; Zhang, X.; Mei, D.; Liu, F.; Han, N.; Liu, D.; Gan, X.; Cheng, Y.; et al. Tunable Linearity of High-Performance Vertical Dual-Gate vdW Phototransistors. *Adv. Mater.* **2021**, *33*, 2008080. [CrossRef]
30. Moudgil, A.; Sharma, S.; Das, S. In_2Se_3/Silicon-on-Insulator Heterojunction Phototransistor for Low Noise Dual-Band Detection. *IEEE Electron Device Lett.* **2021**, *42*, 755–758. [CrossRef]
31. Chen, T.; Zhang, J.; Zhang, X.; Chen, C.; Zhang, L.; Hu, Y.; Ma, Y.; Wei, X.; Zhou, X.; Tang, W.; et al. Ultrahigh Responsivity β-Ga2O3/BP Junction Field Effect Phototransistors for UV/IR Dual-Band Detection. *IEEE Sens. J.* **2023**, *23*, 15504–15511. [CrossRef]
32. Li, S.; Wu, Q.; Ding, H.; Wu, S.; Cai, X.; Wang, R.; Xiong, J.; Lin, G.; Huang, W.; Chen, S.; et al. High Gain, Broadband p-WSe2/n-Ge van Der Waals Heterojunction Phototransistor with a Schottky Barrier Collector. *Nano Res.* **2023**, *16*, 5796–5802. [CrossRef]
33. Li, J.; Niu, L.; Zheng, Z.; Yan, F. Photosensitive Graphene Transistors. *Adv. Mater.* **2014**, *26*, 5239–5273. [CrossRef]
34. Pasternak, I.; Wesolowski, M.; Jozwik, I.; Lukosius, M.; Lupina, G.; Dabrowski, P.; Baranowski, J.M.; Strupinski, W. Graphene Growth on Ge(100)/Si(100) Substrates by CVD Method. *Sci. Rep.* **2016**, *6*, 21773. [CrossRef]
35. Wang, G.; Zhang, M.; Zhu, Y.; Ding, G.; Jiang, D.; Guo, Q.; Liu, S.; Xie, X.; Chu, P.K.; Di, Z.; et al. Direct Growth of Graphene Film on Germanium Substrate. *Sci. Rep.* **2013**, *3*, 2465. [CrossRef]
36. Jacobberger, R.M.; Savage, D.E.; Zheng, X.; Sookchoo, P.; Rojas Delgado, R.; Lagally, M.G.; Arnold, M.S. Effect of Germanium Surface Orientation on Graphene Chemical Vapor Deposition and Graphene-Induced Germanium Nanofaceting. *Chem. Mater.* **2022**, *34*, 6769–6778. [CrossRef]
37. Schneider, M.V. Schottky Barrier Photodiodes with Antireflection Coating. *Bell Syst. Tech. J.* **1966**, *45*, 1611–1638. [CrossRef]
38. Luongo, G.; Giubileo, F.; Genovese, L.; Iemmo, L.; Martucciello, N.; Di Bartolomeo, A. I-V and C-V Characterization of a High-Responsivity Graphene/Silicon Photodiode with Embedded MOS Capacitor. *Nanomaterials* **2017**, *7*, 158. [CrossRef]

nanomaterials

Article

Self-Powered Broadband Photodetector Based on NiO/Si Heterojunction Incorporating Graphene Transparent Conducting Layer

Bhishma Pandit, Bhaskar Parida, Hyeon-Sik Jang * and Keun Heo *

School of Semiconductor and Chemical Engineering, Semiconductor Physics Research Center, Jeonbuk National University, Jeonju 54896, Republic of Korea; bhim2046@jbnu.ac.kr (B.P.); bhaskar.parida@dewa.gov.ae (B.P.)
* Correspondence: hsjang88@jbnu.ac.kr (H.-S.J.); kheo@jbnu.ac.kr (K.H.)

Abstract: In this study, a self-powered broadband photodetector based on graphene/NiO/n-Si was fabricated by the direct spin-coating of nanostructured NiO on the Si substrate. The current–voltage measurement of the NiO/Si heterostructure exhibited rectifying characteristics with enhanced photocurrent under light illumination. Photodetection capability was measured in the range from 300 nm to 800 nm, and a higher photoresponse in the UV region was observed due to the wide bandgap of NiO. The presence of a top graphene transparent conducting electrode further enhanced the responsivity in the whole measured wavelength region from 350 to 800 nm. The photoresponse of the NiO/Si detector at 350 nm was found to increase from 0.0187 to 0.163 A/W at −1 V with the insertion of the graphene top layer. A high photo-to-dark current ratio ($\simeq 10^4$) at the zero bias indicates that the device has advantageous application in energy-efficient high-performance broadband photodetectors.

Keywords: graphene/NiO/Si; nanostructure; heterojunction; self-powered; photodetector

1. Introduction

Photodetector devices have become a key component for environmental monitoring, light wave communication, military applications such as missile plum detection, medical treatment, and astronomical observation [1–8]. Instead of single-band detectors, broadband photodetectors such as UV-visible, visible-infrared, and UV-visible-infrared photodetectors are preferred in order to meet the ever-increasing multifunctional requirements. The formation of heterojunction between two materials is advantageous in terms of the suppression of photocarrier recombination and can benefit from different materials' properties, thus resulting in excellent stability, fast response/recovery time, high responsivity, and enhanced external quantum efficiency [9–12]. Wide-bandgap metal oxides such as TiO_2, NiO, WO_3, Ga_2O_3, ZnO, InO, In_2O_3, SnO_2, and their heterostructures with existing semiconductors are also promising for such a wide range of photodetection and sensing application [11–16]. The advances in theoretical studies with well-supported experimental results further improve the extended application of metal oxide-based systems [14,15,17]. In addition, high thermal and chemical stability, easy chemical modification, and the availability of both the p-type and n-type lead to the stable operation of metal oxide-based heterojunction in light harvesting, gas sensing, photovoltaics, and photodetection [18–20]. Among them, NiO has a wide bandgap (3.4–4.3 eV) and can fulfill such requirements in combination with Si, as reported previously [13,21,22]. Thermal/UV oxidation, e-beam evaporation, RF-magnetron sputtering, pulsed laser deposition, and chemical processes are mainly used to prepare the NiO [23–27]. It was reported that the NiO prepared by a cost-effective sol-gel process has a high performance due to its damage-free construction compared to RF sputtering and others. Parida et al. [27] demonstrated the rectifying characteristics of the nanostructured NiO/p-Si diode showing a photoresponse at wavelengths of 385, 515, and 620 nm. The responsivity of the NiO/Si diode was subsequently enhanced by

Zhang et al. using the P (NiO) and n-Si (111) structures, showing the broadband detection from 350 to 600 nm [28]. In another study, Kuru et al. investigated the enhancement of the graphene/Si solar cell using NiO doping [29]. On the other hand, Yang et al. enhanced the power conversion efficiency of the dye-sensitized solar cell using the graphene/NiO composite film and suggested that the loss of photogenerated holes in NiO is due to its low intrinsic electric conductivity and hole diffusion coefficient [30]. Kim et al. reported the high performance of perovskite solar cells by enhancing the electrical conductivity of NiO via copper doping [31]. In this respect, the photoresponse of such a device fabricated using NiO needs a good carrier collecting layer which can enhance the carrier separation and extraction rate.

A 2-dimensional honeycomb array of a carbon atom, i.e., graphene, has been used as a transparent conducting layer in various optoelectronic and photovoltaic devices, due to its high conductivity, high optical transmittance, and low sheet resistance, thus replacing the expensive transparent conducting metal oxide layer [32,33]. The broadband absorption, ease of functionalization, controlled fabrication process, incorporation of nanomaterials, and formation of heterostructures with existing semiconductors and 2D layers result in the exciting performance of the graphene-based devices [34–37]. In this study, we have used graphene as a transparent conducting electrode on a NiO/Si heterostructure. The responsivity of the NiO/Si photodiode increased by more than one order by using graphene for all the measured regions at wavelengths of 350–800 nm. The photodiode exhibited a high response at the zero bias, clearly indicating the self-powered performance; furthermore, with increasing bias voltage, the responsivity was increased significantly, which can be attributed to the efficient carrier collection enabled by the graphene top layer.

2. Experiment

The NiO nanoparticles are prepared by a sol-gel process [27]; briefly, $Ni(NO_3)_2{\cdot}6H_2O$ (0.5 mol) was dispersed in 100 mL of deionized (DI) water, and the PH was adjusted to 10 by adding a NaOH solution. When the obtained green solution had been stirred for 5 min, $Ni(OH)_2$ precipitated on the bottom of the flask and was thoroughly washed five times with DI water. The collected green precipitate was dried at 80 °C overnight and ground using a mortar and pestle. Finally, the product was calcinated in a hot tube furnace for 3 h. A prepared nanopowder was mixed in water assisted by sonication for 20 min, and then spin-coated in n-Si [100] with a resistivity of 1–10 Ω cm and annealed for 10 min at 200 °C. The spin-coating process was repeated three times to obtain the desired thickness. Before spin-coating, the Si samples were cleaned with acetone, methanol, IPA, and DI rinse water, each for 5 min. The native SiO_2 was removed using a buffer oxide etchant, and finally, inorganic particles were removed using a piranha solution (1:1, H_2SO_4:H_2O_2). Afterward, the graphene was transferred to the NiO/Si sample using a PMMA sacrificial layer. In brief, the PMMA was spin-coated on graphene which was grown on a copper foil and annealed for 5 min at 200 °C. Further, the back-side graphene was removed using 1 M nitric acid solution for 3 min. The copper foil was dissolved completely using ammonium persulfate solution for ~7 h. Further, the PMMA/graphene stack was cleaned with DI water three times, for 20 min each time. Later, the PMMA/graphene stack was transferred to the NiO/Si and allowed to dry naturally; afterward, the sample was annealed for 30 min at 200 °C. Finally, the PMMA was removed by dipping the sample in acetone at 60 °C overnight. By completing the graphene transfer, the back and front contacts were made by an InGa eutectic solution and silver paste, respectively. The schematic diagram of the NiO/Si and graphene/NiO/Si diodes is shown in Figure 1a. Figure 1b shows the Raman spectroscopic measurement of the graphene. Three graphene-related Raman peaks were found around wavenumbers 1580, 2668, and 1340, corresponding to the in-plane vibrational mode G peak, the double resonant 2D peak, and the defect-induced D peak. The calculated intensity ratio of the 2D peaks shows a value higher than unity, implying the monolayer nature of the graphene. The thickness of the NiO was confirmed to be 120 nm by SEM measurements, as shown in Figure 1c.

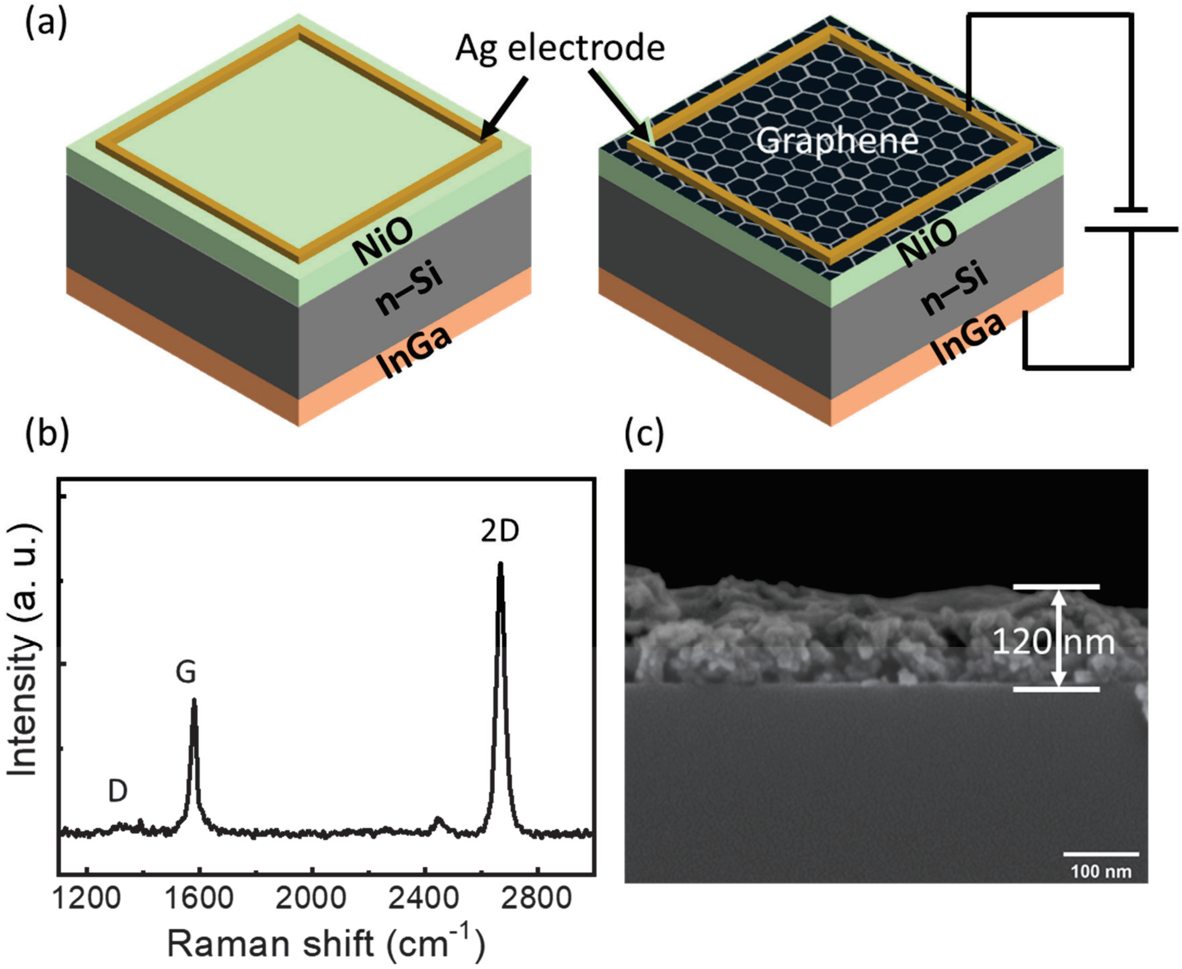

Figure 1. (**a**) Schematic diagram of the fabricated NiO/n-Si diode without (**left**) and with the graphene layer (**right**); (**b**) Raman spectroscopic measurement of graphene; (**c**) SEM image of NiO on the Si substrate for thickness measurement.

The current–voltage (I–V) under dark and illuminated conditions was measured using a 2400 Keithley source meter (Tektronix, Seoul, Republic of Korea) in combination with a Bentham SSM150Xe switching monochromator (Bentham, Seoul, Republic of Korea). The transmittance/absorbance of NiO film was measured using a UV/VIS spectrometer (model: JASCO ARSN-917) with the spin-coated NiO on both sides of the polished sapphire substrate. An FESEM image was taken to confirm the nanostructure of the NiO on the sapphire substrate. All electrical characteristics were measured at room temperature and normal ambient conditions.

3. Results and Discussion

Figure 2a shows an FESEM image of the NiO nanoparticles spin-coated on both sides of the polished sapphire substrate, illustrating that the NiO nanoparticles were uniformly distributed across the substrate. The size of the NiO nanosheets being lower than 100 nm was confirmed as in the previous study [27]. The 23 nm of RMS roughness of the spin-cast NiO observed from the AFM image indicates that the NiO nanosheet has a mean thickness higher than that of 23 nm, as shown in Figure 2b. The XPS spectra of the NiO before and after graphene transfer, as presented in Figure 2c, shows the two distinct Ni 2p$^{3/2}$ and Ni 2p$^{1/2}$ peaks observed at around 855 and 873.2 eV, respectively; in addition, their corresponding satellite peaks observed at a slightly higher binding energy for the NiO nanoparticles confirms that the NiO quality remains the same after the graphene transfer process [38–40]. Figure 2d shows the transmittance spectra of the spin-coated

NiO nanoparticles on both sides of the polished sapphire substrate from 300 to 800 nm by considering both sides of the polished sapphire substrate as a reference baseline. The transparency of NiO is much higher in the visible region and shows a gradual increase in transmittance with increasing the wavelength towards the near-infrared region. However, the transparency sharply dropped towards the lower value in the UV region, due to the absorption of light from the higher energy level. Figure 2e shows the absorption spectra of the NiO nanoparticles spin-coated on both sides of the polished sapphire substrate. The absorption increases exponentially when it enters into the UV region (i.e., for lower than 350 nm). This drastic increase in absorption is due to the strong bandgap absorption from the NiO layer, where the energy of the incident photon lies near or higher than the bandgap of NiO [41]. In order to calculate the bandgap energy of NiO, we further plotted the $(\alpha h\nu)^2$ versus energy (eV) curve (Tauc plot) and fitted the linear region as shown in Figure 2f. This confirms the corresponding bandgap energy of 3.57 eV that falls on the bandgap region of the NiO (3.4–4.3 eV) reported by various previous studies [13,21,22].

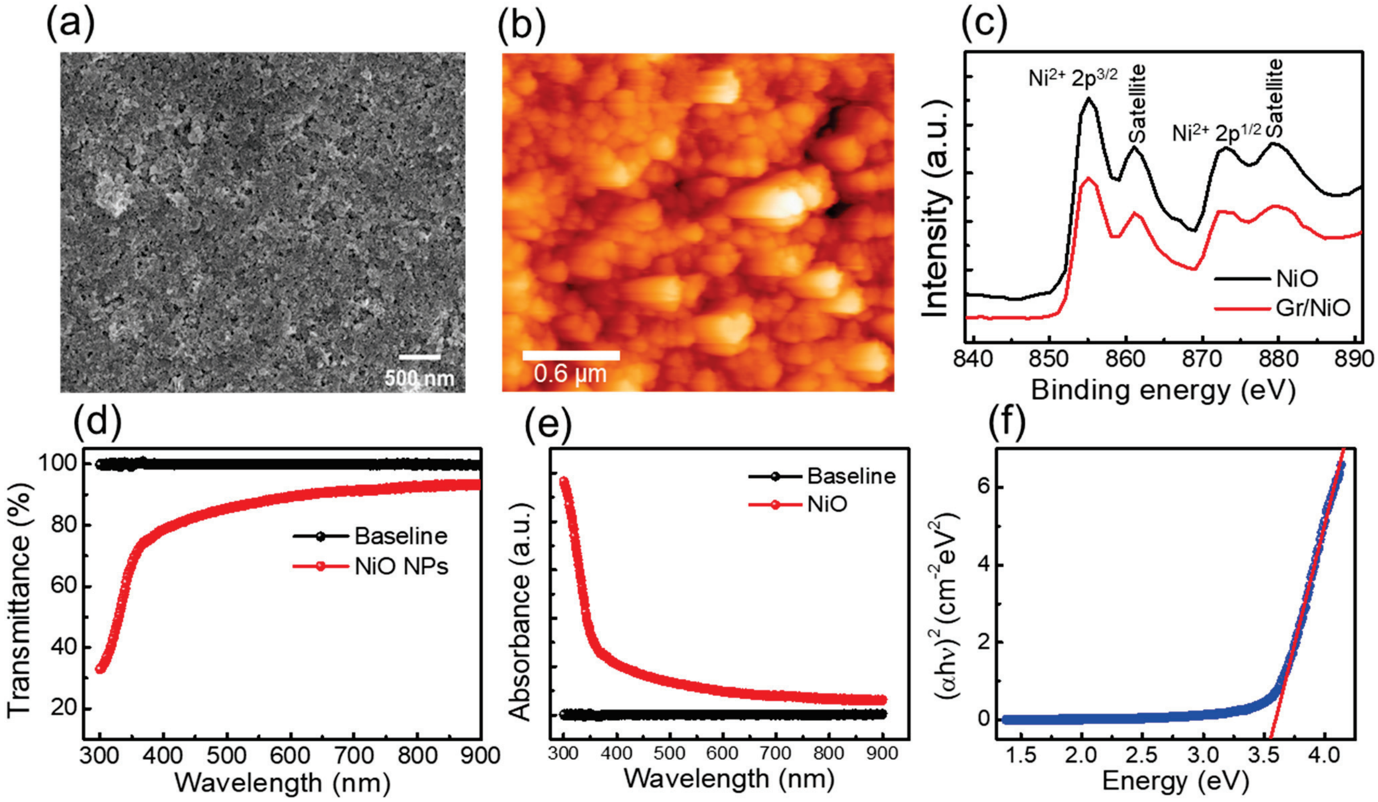

Figure 2. (**a**) FESEM image of the NiO nanoparticles coated on the Si surface; (**b**) AFM image of the NiO nanoparticles; (**c**) XPS analysis of the NiO nanoparticles before and after the graphene transfer; (**d**) transmittance spectra and (**e**) absorption spectra of the NiO coated on both sides of the polished sapphire substrate as a baseline; and (**f**) Tauc plot of the NiO nanoparticles with linear fitting (red line).

Figure 3 shows the current–voltage (I–V) characteristics measured from the NiO/Si (a) and graphene/NiO/Si (b) diodes in the range of −5 to +5 V under dark conditions and with the illumination of 350 nm. The I–V characteristics curve under dark and illuminated conditions shows clear rectifying properties. Around four orders of the rectification ratio were measured at the forward and reverse bias of 1 V. A low reverse leakage current and a high rectification ratio were observed in comparison to the previous studies on the NiO/Si diode, NiO fabricated by UV oxidation, and sputtering techniques [24,42]. A dark current at 0 V was observed in the range of tens of nano-amperes and gradually increased with increasing the reverse voltage. Further, the increase in the reverse current with the illumination of light at a wavelength 350 nm implies that the UV illumination-induced current was added to the external circuit. The use of graphene on the top of the NiO/Si diode shows a further increase in the total amount of photocurrent in comparison to the device fabricated by using NiO/Si only. For the illumination of light at a wavelength of 350 nm, the photocurrent typically increased from 14 µA to 73 µA in the diode with graphene as the top electrode. The higher conductivity of graphene seems to be much more supportive for the collection of the carrier generated by an incident photon before the electron–hole pair recombination. Figure 3c represents the I–V characteristics of the graphene/NiO/Si photodetector under dark and 300 to 800 nm of illumination with an interval of 50 nm. The enhanced photocurrent under illumination confirms the broadband photodetection characteristics of the fabricated device.

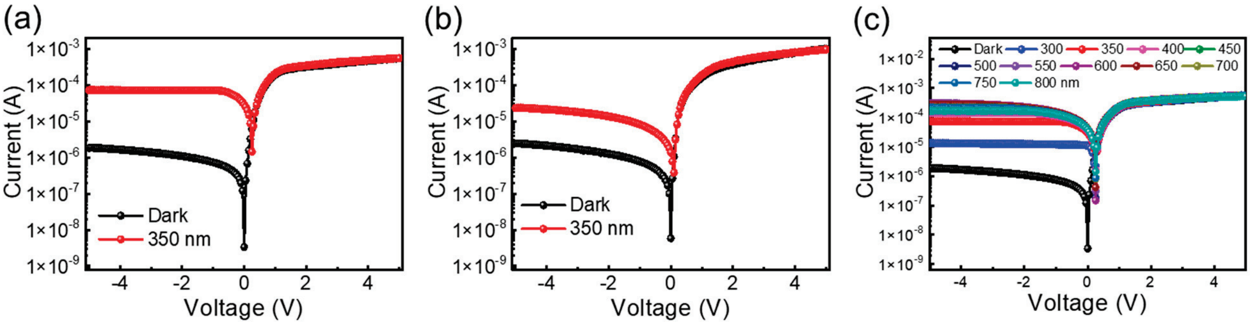

Figure 3. Current–voltage (I–V) characteristics of the (**a**) graphene/NiO/Si and (**b**) NiO/Si diodes under dark and illuminated (350 nm) conditions; (**c**) I–V characteristics of the graphene/NiO/Si photodetector under various illumination wavelengths.

Further, the responsivity of the photodiode was calculated by using the relation $R = (I_{photo} - I_{dark})/P_{inc}$ where I_{photo} is the photocurrent, I_{dark} is the dark current, and P_{inc} is the incident optical power. Here, in our measurement system, the incident optical power was measured as 1.68, 2.31, 3.21, 3.84, 3.61, 3.2, 2.69, 2.1, 1.91, and 1.45 mW/cm^2 for 350, 400, 450, 500, 550, 600, 650, 700, 750, and 800 nm, respectively. Figures 4a and 4c show the calculated photoresponse values from 350 nm to 800 nm with an interval of 50 nm for the graphene/NiO/Si and NiO/Si photodetectors, respectively. The high responsivity of the graphene/NiO/Si diode in comparison to the NiO/Si diode might be due to the enhanced carrier separation and collection through a fully spanned top graphene electrode [43,44]. The responsivity in terms of wavelength for the graphene/NiO/Si diode shows a decrease in responsivity from higher to lower wavelength regions, which is a similar trend observed by previous groups [27,45]. Different from those previous studies, we observed some elevation in the responsivity curve when it enters the UV region. The variation in the responsivity might be due to the band edge of the materials used. A sharp elevation in responsivity for each measured wavelength was observed for the device containing a graphene top electrode. The amount of responsivity gets reduced when the wavelength reduces, according to the relation $R = \frac{\eta\lambda}{1.24}$ where R is the responsivity, η is the quantum efficiency (QE), and λ is the wavelength in µm. The modified form of the previous equation was used to calculate the efficiency $\eta = \frac{R \times 1.24}{\lambda\ (\mu\mathrm{m})}$ of the photodetector. Therefore, it seems that the plot of QE with respect to λ might be valuable for the comparative study. Figure 4b,d show the QE versus λ plot of the graphene/NiO/Si and NiO/Si photodetectors, respectively, which clearly shows an increase in the bias leading to the higher QE. The higher QE of the NiO/Si photodetector in the UV region implied that the NiO layer mainly contributed to the photocurrent generation. The insertion of the top graphene layer further improved the QE of the device, as shown numerically in Figure 4b; the graphene layer improved the QE from 1.18 to 19.5% at zero bias under the illumination condition of 350 nm. The electron–hole pair produced during the illumination should be collected before the recombination; in this sense, the graphene acted as the carrier transport layer and enhanced the device performance. The highest QE of about 20% at the zero bias condition implies that the efficient self-operating device in the UV region was much higher than previously mentioned. The single detector covering the broad spectral range is promising for a low-cost optical communication system.

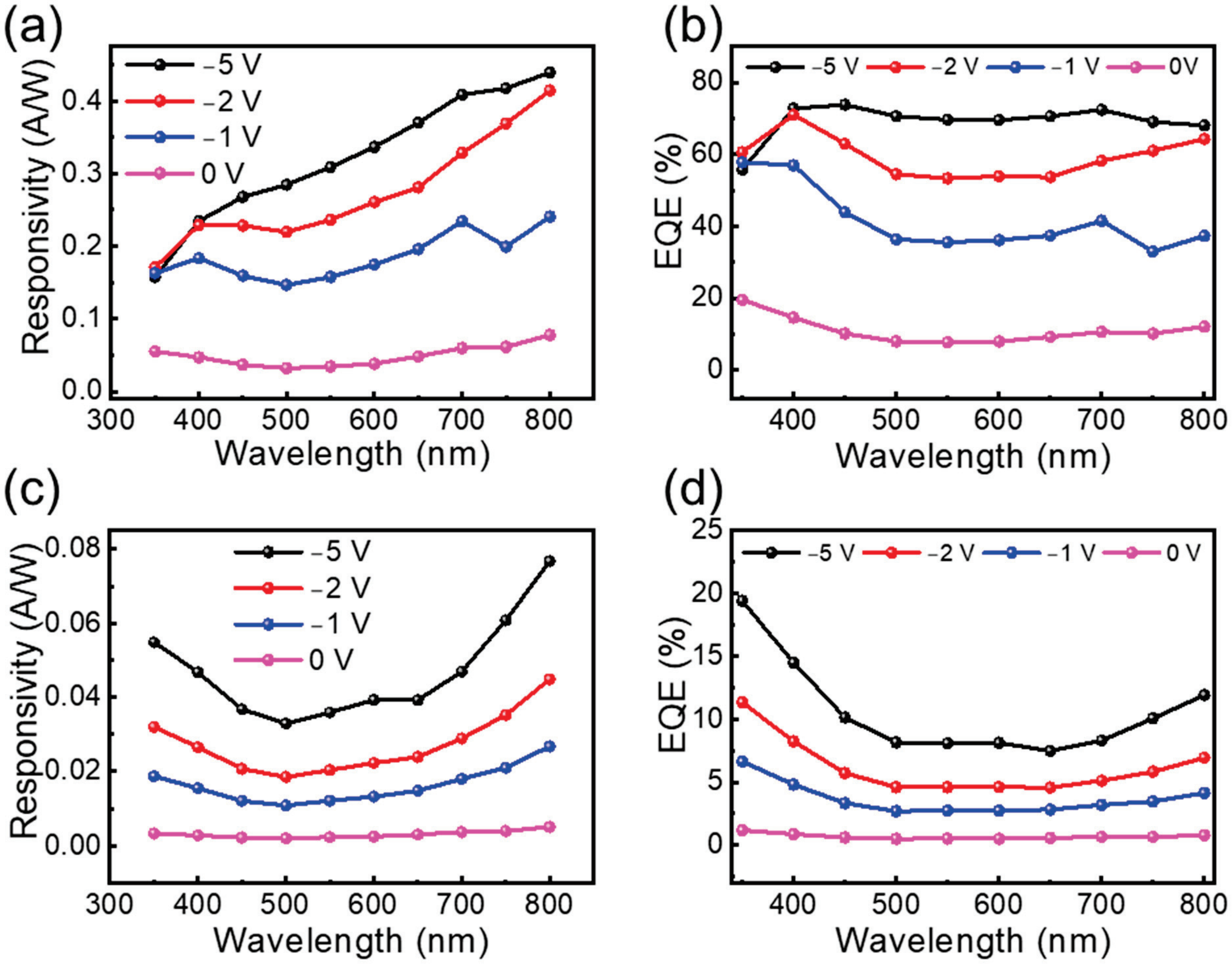

Figure 4. The responsivity (**a**) and corresponding QE (**b**) of the graphene/NiO/Si diode, and the responsivity (**c**) and QE (**d**) of the NiO/Si diode, at various reverse bias conditions.

Figure 5a shows the current on–off properties of both the NiO/Si and graphene/NiO/Si diodes at zero volts from 350 to 600 nm with an interval of 50 nm. The photocurrent on–off characteristics observed at 0 V refer to the self-operation of the device without applying any external bias. The self-powered device responding to the broad spectral region has many advantages in the field of energy-efficient optical communication, sensing, and detection. Rapid electron–hole transport and a lower recombination rate were also essential to achieve a high-performance photodetector. Here, by inserting the graphene as a transparent conducting electrode, the value amount of collected photocurrent is increased for all measured wavelengths. The stable switching response to various wavelengths was confirmed under normal ambient conditions from 350 to 600 nm with repetitive on–off cycles. Furthermore, the 50 repetitive on–off cycles were tested under 1 V of reverse bias with the illumination condition of a 500 nm light source, as presented in Figure 5b. Consistent photoresponse without any distortion was observed through all repeated cycles. Figure 5c shows the on–off properties of diodes at the different biasing values of −1, −2, −3, and −5 V, where the increase in photocurrent leads to an increase in the photoresponse value, although the dark current also increased with respect to increasing the reverse bias voltage. Figure 5d presents the current on–off ratio of the photodetector under the illumination of 350 nm and with a bias voltage ranging from 0 to −5 V. The current on–off ratio increases as the applied reverse bias voltage is reduced. The highest on–off ratio of ~10^5% was observed at 0 V, indicating the high switching ratio under self-powered conditions. The self-powered operation of the NiO/Si photodetector can be understood clearly from the band diagram presented in Figure 6. Once the p-type NiO comes in contact with n-Si, the band bending occurs to meet the equilibrium position and fermi level aligned by the diffusion of the majority of carriers to the lower concentration regions. The band bending at the interface leads to the formation of a depletion region and a built-in electric field directed from the Si to the NiO. Upon the illumination of light having an energy higher than the Si or NiO bandgap energy, the electron and holes are generated and separated by the field present at the interface. The photogenerated holes are moved toward the valence band of the NiO, and the electrons are moved toward the conduction band of the Si and contribute to the enhanced current in the external circuit. Under reverse bias conditions, the external electric field is aligned with the built-in electric field and significantly increases the depletion region, hence enhancing the carrier generation and increasing the photocurrent.

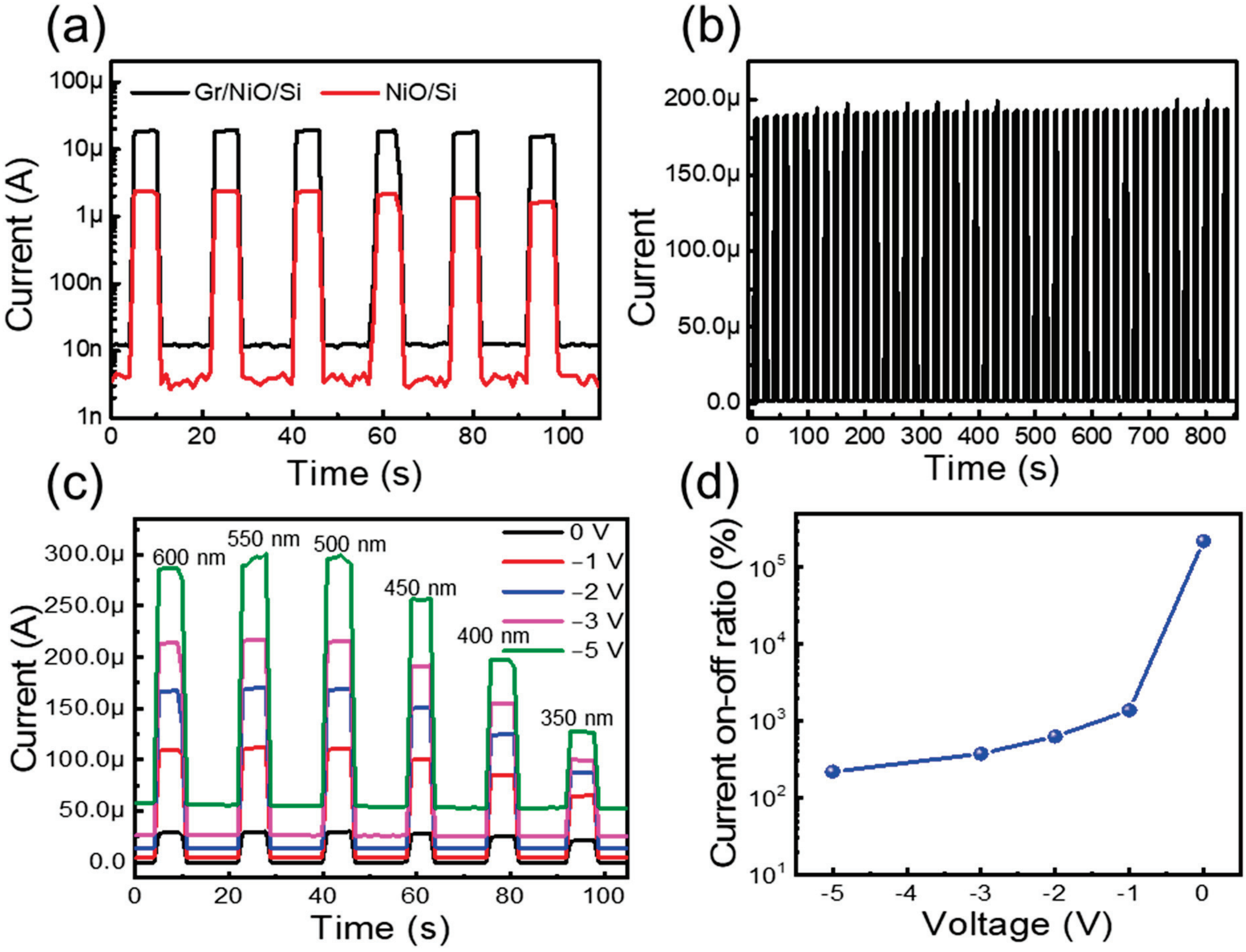

Figure 5. Temporal current on–off characteristics measurement of the (**a**) NiO/Si and graphene/NiO/Si diodes under a zero bias condition; (**b**) the 50 times-repeated cycle of the graphene/NiO/Si diode at −2 V bias under 500 nm illumination; (**c**) the on–off response with various reverse bias conditions from 350 to 600 nm; (**d**) the current on–off ratio under the illumination of 350 nm light at various bias conditions.

Detectivity, one of the most important merits of photodetection, signifies the minimum signal of a photon that can be detected by the photodetector and is given by the following relation [46,47]: $D = \frac{A^{\frac{1}{2}} R}{(2qI_D)^{\frac{1}{2}}}$ where A is the active area of PD, q is the unit electronic charge, and I_D is the dark current. Under 350 nm of illumination, the detectivity of 1.66×10^{12}, 2.71×10^{11}, 2.23×10^{11}, 1.98×10^{11}, and 1.78×10^{11} cmHz$^{1/2}$W^{-1} was observed at biases of 0, −1, −2, −3, and −5 V, respectively. The decrease in the detectivity of the photodetector with increasing the reverse bias voltage corresponds to the effective increase in the dark current in comparison to the photocurrent. Maximum detectivity of the photodetector at 0 V signifies the efficient operation under self-powered conditions. The conductivity of NiO nanoparticles by doping, or by optimizing the device structure for the performance of the graphene/NiO/Si diode, can be improved further [47–52]. In our study, we discuss fruitful information about the graphene conducting layer's effects on the NiO/Si diode, which provides essential information for future investigation. The photodetection characteristics and parameters of the NiO/Si photodetectors along with the previous studies are summarized in Table 1 [53–61].

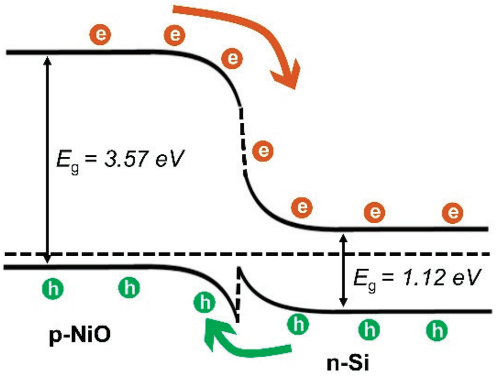

Figure 6. The energy band diagram of the NiO/Si heterojunction.

Table 1. Comparison of the NiO/Si photodetectors with previous studies.

PD	Responsivity (A/W)	Dark Current (A)	Wavelength (nm)	Photocurrent	T_{rise} (s)	T_{fall} (s)	Detectivity (cmHz$^{1/2}$W^{-1})	Bias (V)	Ref.
Al/NiO/Si/Al	0.7	NA	330	NA	NA	NA	63×10^{12}	−3	[53]
NiO/n-Si	~0.15@0 V ~0.17@30 V	NA	290	NA	NA	NA	NA	0	[45]
Ni/NiO/p-Si/InGa	0.156 1 V	3.9×10^{-8}	385	7.1×10^{-7}	0.5	NA	NA	−3	[27]
Au/NiO/Si MSM	~6.5	2.32 μA	365	NA	0.11	NA	NA	5	[54]
Au/NiO/Si MSM	4.5	~5 μA	365	NA	226 ms	200 ms	NA	5	[55]
Ag/Zn:NiO/p-Si/Ag	0.249	~13 μA cm^{-2} (−1 V)	350	79 μA cm^{-2}	0.3	NA	2.3×10^{11} (−1 V)	−4	[56]
Ag/NiO/n-Si/Ag	0.43	7 μA cm^{-2} (−0.2 V)	600	2.5×10^{5}	30 ms	NA	1.5×10^{10} (0 V)	−2	[28]
NiO/n-Si	0.013	3.9×10^{-9}	365	NA	85 ms	85 ms	1.03×10^{11}	0	[57]
Al/NiO/Si MSM	91 μA/mW	59 μA	350	NA	750 ms	800 ms	NA	0.2	[58]
NiO/n-Si PD	0.83	9.1×10^{-12}	365	2.8×10^{-8}	0.1	0.1	NA	0	[59]
NiO NW/n-Si(100)	9.1 mA W^{-1}	NA	350	NA	0.4	NA	1.8×10^{9}	0	[60]
NiO/n-Si	160 mA W^{-1}	NA	365	NA	1.5	NA	NA	5	[61]
graphene/NiO/n-Si	0.055 0.15	3.35×10^{-9} 1.82×10^{-6}	350	2.9×10^{-5} 7.3×10^{-5}	<0.8	<0.8	1.66×10^{12} 1.78×10^{11}	0 −5	This work

4. Conclusions

In conclusion, we successfully employed graphene as a transparent electrode in the NiO/Si broadband photodetector by using the CVD graphene, NiO nanoparticles, and n-type Si. Both the NiO/Si and graphene/NiO/Si diodes show rectifying properties and photoresponse towards the broad spectral region. I–V characteristics were measured with different illumination conditions ranging from 350 to 800 nm, representing the enhanced performance of the photodetector. The high conductivity of the graphene electrode enhances the carrier collection efficiency before the recombination of induced carriers and enhances the QE by up to 78%. The ~20% of QE at 0 V bias for a wavelength of 350 nm illustrates the efficient self-powered performance of the graphene/NiO/Si heterojunction photodetector.

Author Contributions: Conceptualization, K.H.; Resources, B.P. (Bhaskar Parida); Writing—original draft, B.P. (Bhishma Pandit); Writing—review & editing, H.-S.J.; Visualization, H.-S.J.; Supervision, K.H.; Funding acquisition, H.-S.J. All authors have read and agreed to the published version of the manuscript.

Funding: This research was funded by a National Research Foundation of Korea (NRF) Grant funded by the Korean government (MSIT) (No. 2022R1C1C2004541) (No. RS-2023-00221295) (No. 2022R1I1A307258212).

Data Availability Statement: Data are contained within the article.

Conflicts of Interest: The authors declare no conflict of interest.

References

1. García de Arquer, F.P.; Armin, A.; Meredith, P.; Sargent, E.H. Solution-processed semiconductors for next-generation photodetectors. *Nat. Rev. Mater.* **2017**, *2*, 16100. [CrossRef]
2. Chen, H.; Liu, K.; Hu, L.; Al-Ghamdi, A.A.; Fang, X. New concept ultraviolet photodetectors. *Mater. Today* **2015**, *18*, 493–502. [CrossRef]
3. Monroy, E.; Omnès, F.; Calle, F. Wide-bandgap semiconductor ultraviolet photodetectors. *Semicond. Sci. Technol.* **2003**, *18*, R33. [CrossRef]
4. Long, M.; Wang, P.; Fang, H.; Hu, W. Progress, challenges, and opportunities for 2D material based photodetectors. *Adv. Funct. Mater.* **2019**, *29*, 1803807. [CrossRef]
5. Zou, Y.; Zhang, Y.; Hu, Y.; Gu, H. Ultraviolet detectors based on wide bandgap semiconductor nanowire: A review. *Sensors* **2018**, *18*, 2072. [CrossRef]
6. Razeghi, M.; Rogalski, A. Semiconductor ultraviolet detectors. *J. Appl. Phys.* **1996**, *79*, 7433–7473. [CrossRef]
7. Xie, C.; Lu, X.T.; Tong, X.W.; Zhang, Z.X.; Liang, F.X.; Liang, L.; Luo, L.B.; Wu, Y.C. Recent progress in solar-blind deep-ultraviolet photodetectors based on inorganic ultrawide bandgap semiconductors. *Adv. Funct. Mater.* **2019**, *29*, 1806006. [CrossRef]
8. Sang, L.; Liao, M.; Sumiya, M. A comprehensive review of semiconductor ultraviolet photodetectors: From thin film to one-dimensional nanostructures. *Sensors* **2013**, *13*, 10482–10518. [CrossRef]
9. Pandit, B.; Schubert, E.F.; Cho, J. Dual-functional ultraviolet photodetector with graphene electrodes on AlGaN/GaN heterostructure. *Sci. Rep.* **2020**, *10*, 22059. [CrossRef]
10. Pandit, B.; Jang, H.S.; Jeong, Y.; An, S.; Chandramohan, S.; Min, K.K.; Won, S.M.; Choi, C.J.; Cho, J.; Hong, S. Highly Sensitive Ultraviolet Photodetector Based on an AlGaN/GaN HEMT with Graphene-On-p-GaN Mesa Structure. *Adv. Mater. Interfaces* **2023**, *10*, 2202379. [CrossRef]
11. Tsao, J.; Chowdhury, S.; Hollis, M.; Jena, D.; Johnson, N.; Jones, K.; Kaplar, R.; Rajan, S.; Van de Walle, C.; Bellotti, E. Ultrawide-bandgap semiconductors: Research opportunities and challenges. *Adv. Electron. Mater.* **2018**, *4*, 1600501. [CrossRef]
12. Chen, J.; Ouyang, W.; Yang, W.; He, J.H.; Fang, X. Recent progress of heterojunction ultraviolet photodetectors: Materials, integrations, and applications. *Adv. Funct. Mater.* **2020**, *30*, 1909909. [CrossRef]
13. Lany, S. Semiconducting transition metal oxides. *J. Phys. Condens. Matter* **2015**, *27*, 283203. [CrossRef]
14. dos Santos, R.B.; Rivelino, R.; Gueorguiev, G.K.; Kakanakova-Georgieva, A. Exploring 2D structures of indium oxide of different stoichiometry. *CrystEngComm* **2021**, *23*, 6661–6667. [CrossRef]
15. Kakanakova-Georgieva, A.; Giannazzo, F.; Nicotra, G.; Cora, I.; Gueorguiev, G.K.; Persson, P.O.; Pécz, B. Material proposal for 2D indium oxide. *Appl. Surf. Sci.* **2021**, *548*, 149275. [CrossRef]
16. Kim, S.; Lim, H.; Kim, S.; Pandit, B.; Cho, J.; Kang, H.C. Synthesis of SnO_2 nanowires using thermal chemical vapor deposition with SnO powder and their application as self-powered ultraviolet photodetectors. *J. Alloys Compd.* **2023**, *963*, 171265. [CrossRef]
17. Shin, H.; Luo, Y.; Ganesh, P.; Balachandran, J.; Krogel, J.T.; Kent, P.R.; Benali, A.; Heinonen, O. Electronic properties of doped and defective NiO: A quantum Monte Carlo study. *Phys. Rev. Mater.* **2017**, *1*, 073603. [CrossRef]
18. Shi, J.; Zhang, J.; Yang, L.; Qu, M.; Qi, D.C.; Zhang, K.H. Wide bandgap oxide semiconductors: From materials physics to optoelectronic devices. *Adv. Mater.* **2021**, *33*, 2006230. [CrossRef]
19. Chai, H.; Zheng, Z.; Liu, K.; Xu, J.; Wu, K.; Luo, Y.; Liao, H.; Debliquy, M.; Zhang, C. Stability of metal oxide semiconductor gas sensors: A review. *IEEE Sens. J.* **2022**, *22*, 5470–5481. [CrossRef]
20. Desissa, T.D. NiO–ZnO based junction interface as high-temperature contact materials. *Ceram. Int.* **2021**, *47*, 8053–8059. [CrossRef]
21. Jlassi, M.; Sta, I.; Hajji, M.; Ezzaouia, H. Synthesis and characterization of nickel oxide thin films deposited on glass substrates using spray pyrolysis. *Appl. Surf. Sci.* **2014**, *308*, 199–205. [CrossRef]
22. Jarzębski, Z.M. *Oxide Semiconductors*; Pergamon Press: Oxford, UK, 1973.

23. Forin, C.C.; Purica, M.; Budianu, E.; Schiopu, P. p-NiO/ITO transparent heterojunction—Preparation and characterization. In Proceedings of the CAS 2012 (International Semiconductor Conference), Sinaia, Romania, 15–17 October 2012; IEEE: New York, NY, USA, 2012; pp. 131–134.
24. Zhang, D.; Nozaki, S.; Uchida, K. NiO/Si heterostructures formed by UV oxidation of nickel deposited on Si substrates. *J. Vac. Sci. Technol. B* **2014**, *32*, 031202. [CrossRef]
25. Hsu, F.H.; Wang, N.F.; Tsai, Y.Z.; Cheng, Y.S.; Houng, M.P. A new p-Ni1–xO: Li/n-Si heterojunction solar cell fabricated by RF magnetron sputtering. *J. Phys. D Appl. Phys.* **2013**, *46*, 275104. [CrossRef]
26. Irwin, M.D.; Servaites, J.D.; Buchholz, D.B.; Leever, B.J.; Liu, J.; Emery, J.D.; Zhang, M.; Song, J.-H.; Durstock, M.F.; Freeman, A.J. Structural and electrical functionality of NiO interfacial films in bulk heterojunction organic solar cells. *Chem. Mater.* **2011**, *23*, 2218–2226. [CrossRef]
27. Parida, B.; Kim, S.; Oh, M.; Jung, S.; Baek, M.; Ryou, J.-H.; Kim, H. Nanostructured-NiO/Si heterojunction photodetector. *Mater. Sci. Semicond. Process.* **2017**, *71*, 29–34. [CrossRef]
28. Zhang, Y.; Ji, T.; Zhang, W.; Guan, G.; Ren, Q.; Xu, K.; Huang, X.; Zou, R.; Hu, J. A self-powered broadband photodetector based on an n-Si(111)/p-NiO heterojunction with high photosensitivity and enhanced external quantum efficiency. *J. Mater. Chem. C* **2017**, *5*, 12520–12528. [CrossRef]
29. Kuru, C.; Yavuz, S.; Kargar, A.; Choi, D.; Choi, C.; Rustomji, C.; Jin, S.; Bandaru, P.R. Enhanced power conversion efficiency of graphene/silicon heterojunction solar cells through NiO induced doping. *J. Nanosci. Nanotechnol.* **2016**, *16*, 1190–1193. [CrossRef]
30. Yang, H.; Guai, G.H.; Guo, C.; Song, Q.; Jiang, S.P.; Wang, Y.; Zhang, W.; Li, C.M. NiO/graphene composite for enhanced charge separation and collection in p-type dye sensitized solar cell. *J. Phys. Chem. C* **2011**, *115*, 12209–12215. [CrossRef]
31. Kim, J.H.; Liang, P.W.; Williams, S.T.; Cho, N.; Chueh, C.C.; Glaz, M.S.; Ginger, D.S.; Jen, A.K.Y. High-performance and environmentally stable planar heterojunction perovskite solar cells based on a solution-processed copper-doped nickel oxide hole-transporting layer. *Adv. Mater.* **2015**, *27*, 695–701. [CrossRef]
32. Geim, A.K.; Novoselov, K.S. The rise of graphene. *Nat. Mater.* **2007**, *6*, 183–191. [CrossRef]
33. Bonaccorso, F.; Sun, Z.; Hasan, T.; Ferrari, A. Graphene photonics and optoelectronics. *Nat. Photonics* **2010**, *4*, 611–622. [CrossRef]
34. Li, W.; Liu, M.; Cheng, S.; Zhang, H.; Yang, W.; Yi, Z.; Zeng, Q.; Tang, B.; Ahmad, S.; Sun, T. Polarization independent tunable bandwidth absorber based on single-layer graphene. *Diam. Relat. Mater.* **2024**, *142*, 110793. [CrossRef]
35. Jiang, B.; Hou, Y.; Wu, J.; Ma, Y.; Gan, X.; Zhao, J. In-fiber photoelectric device based on graphene-coated tilted fiber grating. *Opto-Electron. Sci.* **2023**, *2*, 230012-1–230012-10. [CrossRef]
36. Zeng, C.; Lu, H.; Mao, D.; Du, Y.; Hua, H.; Zhao, W.; Zhao, J. Graphene-empowered dynamic metasurfaces and metadevices. *Opto-Electron. Adv.* **2022**, *5*, 200098. [CrossRef]
37. Lin, S.; Lu, Y.; Xu, J.; Feng, S.; Li, J. High performance graphene/semiconductor van der Waals heterostructure optoelectronic devices. *Nano Energy* **2017**, *40*, 122–148. [CrossRef]
38. Dubey, P.; Kaurav, N.; Devan, R.S.; Okram, G.; Kuo, Y. The effect of stoichiometry on the structural, thermal and electronic properties of thermally decomposed nickel oxide. *RSC Adv.* **2018**, *8*, 5882–5890. [CrossRef]
39. Ramkumar, R.; Dhakal, G.; Shim, J.-J.; Kim, W.K. NiO/Ni Nanowafer Aerogel Electrodes for High Performance Supercapacitors. *Nanomaterials* **2022**, *12*, 3813. [CrossRef]
40. Chen, Y.; Kang, J.; Chen, B.; Gao, B.; Liu, L.; Liu, X.; Wang, Y.; Wu, L.; Yu, H.; Wang, J. Microscopic mechanism for unipolar resistive switching behaviour of nickel oxides. *J. Phys. D Appl. Phys.* **2012**, *45*, 065303. [CrossRef]
41. El-Kemary, M.; Nagy, N.; El-Mehasseb, I. Nickel oxide nanoparticles: Synthesis and spectral studies of interactions with glucose. *Mater. Sci. Semicond. Process.* **2013**, *16*, 1747–1752. [CrossRef]
42. Nishi, Y.; Iwata, T.; Kimoto, T. Correlation between oxygen composition and electrical properties in NiO thin films for resistive random access memory. *Jpn. J. Appl. Phys.* **2011**, *50*, 015802. [CrossRef]
43. Puspharajah, P.; Radhakrishna, S.; Arof, A. Transparent conducting lithium-doped nickel oxide thin films by spray pyrolysis technique. *J. Mater. Sci.* **1997**, *32*, 3001–3006. [CrossRef]
44. Jang, W.-L.; Lu, Y.-M.; Hwang, W.-S.; Chen, W.-C. Electrical properties of Li-doped NiO films. *J. Eur. Ceram. Soc.* **2010**, *30*, 503–508. [CrossRef]
45. Choi, J.-M.; Im, S. Ultraviolet enhanced Si-photodetector using p-NiO films. *Appl. Surf. Sci.* **2005**, *244*, 435–438. [CrossRef]
46. Pandit, B.; Cho, J. AlGaN Ultraviolet Metal–Semiconductor–Metal Photodetectors with Reduced Graphene Oxide Contacts. *Appl. Sci.* **2018**, *8*, 2098. [CrossRef]
47. Pandit, B.; Cho, J. Solar-blind ultraviolet photodetectors with thermally reduced graphene oxide formed on high-Al-content AlGaN layers. *AIP Adv.* **2021**, *11*, 115322. [CrossRef]
48. Khusayfan, N.M. Electrical and photoresponse properties of Al/graphene oxide doped NiO nanocomposite/p-Si/Al photodiodes. *J. Alloys Compd.* **2016**, *666*, 501–506. [CrossRef]
49. Gupta, R.; Hendi, A.; Cavas, M.; Al-Ghamdi, A.A.; Al-Hartomy, O.A.; Aloraini, R.; El-Tantawy, F.; Yakuphanoglu, F. Improvement of photoresponse properties of NiO/p-Si photodiodes by copper dopant. *Phys. E Low-Dimens. Syst. Nanostruct.* **2014**, *56*, 288–295. [CrossRef]
50. Chen, W.; Wu, Y.; Fan, J.; Djurišić, A.B.; Liu, F.; Tam, H.W.; Ng, A.; Surya, C.; Chan, W.K.; Wang, D. Perovskite Solar Cells: Understanding the Doping Effect on NiO: Toward High-Performance Inverted Perovskite Solar Cells. *Adv. Energy Mater.* **2018**, *8*, 1870091. [CrossRef]

51. Li, G.; Liu, L.; Wu, G.; Chen, W.; Qin, S.; Wang, Y.; Zhang, T. Self-powered UV–near infrared photodetector based on reduced graphene oxide/n-Si vertical heterojunction. *Small* **2016**, *12*, 5019–5026. [CrossRef]
52. Kim, H.-S.; Seo, J.-Y.; Xie, H.; Lira-Cantu, M.; Zakeeruddin, S.M.; Gratzel, M.; Hagfeldt, A. Effect of Cs-incorporated NiOx on the performance of perovskite solar cells. *ACS Omega* **2017**, *2*, 9074–9079. [CrossRef]
53. Hadi, A.A.; Badr, B.A.; Mahdi, R.O.; Khashan, K.S. Rapid laser fabrication of Nickel oxide nanoparticles for UV detector. *Optik* **2020**, *219*, 165019. [CrossRef]
54. Ahmed, A.A.; Hashim, M.; Abdalrheem, R.; Rashid, M. High-performance multicolor metal-semiconductor-metal Si photodetector enhanced by nanostructured NiO thin film. *J. Alloys Compd.* **2019**, *798*, 300–310. [CrossRef]
55. Ahmed, A.A.; Devarajan, M.; Afzal, N. Fabrication and characterization of high performance MSM UV photodetector based on NiO film. *Sens. Actuators A Phys.* **2017**, *262*, 78–86. [CrossRef]
56. Zhang, Y.; Ji, T.; Zou, R.; Ha, E.; Hu, X.; Cui, Z.; Xu, C.; Xu, K.; Zhang, Y.; Hu, J. An efficiently enhanced UV-visible light photodetector with a Zn: NiO/p-Si isotype heterojunction. *J. Mater. Chem. C* **2020**, *8*, 3498–3508. [CrossRef]
57. Ahmed, A.A.; Hashim, M.; Qahtan, T.F.; Rashid, M. Preparation and characteristics study of self-powered and fast response p-NiO/n-Si heterojunction photodetector. *Ceram. Int.* **2022**, *48*, 20078–20089. [CrossRef]
58. Salih, E.Y.; Bashir, M.B.A.; Rajpar, A.H.; Badruddin, I.A.; Bahmanrokh, G. Rapid fabrication of NiO/porous Si film for ultra-violate photodetector: The effect of laser energy. *Microelectron. Eng.* **2022**, *258*, 111758. [CrossRef]
59. Castillo-Saenz, J.; Nedev, N.; Valdez-Salas, B.; Bernechea, M.; Martínez-Guerra, E.; Mendivil-Palma, I.; Curiel-Alvarez, M.; Mateos, D.; Perez-Landeros, O. Effect of oxidation temperature on the properties of NiO_x layers for application in optical sensors. *Thin Solid Film.* **2021**, *734*, 138849. [CrossRef]
60. Reddy, K.C.S.; Sahatiya, P.; Santos-Sauceda, I.; Cortázar, O.; Ramírez-Bon, R. One-step fabrication of 1D p-NiO nanowire/n-Si heterojunction: Development of self-powered ultraviolet photodetector. *Appl. Surf. Sci.* **2020**, *513*, 145804. [CrossRef]
61. Al-Hardan, N.H.; Ahmed, N.M.; Almessiere, M.A.; Aziz, A.A. Low-intensity UV light sensor based on p-NiO/n-Si heterojunction. *Mater. Res. Express* **2020**, *6*, 126332. [CrossRef]

nanomaterials

Article

Fabrication and Enhanced Performance Evaluation of TiO_2@Zn/Al-LDH for DSSC Application: The Influence of Post-Processing Temperature

Altaf Hussain Rajpar [1], Mohamed Bashir Ali Bashir [1,*], Ethar Yahya Salih [2] and Emad M. Ahmed [3]

[1] Department of Mechanical Engineering, College of Engineering, Jouf University, Sakaka 72388, Saudi Arabia; ahrajpar@ju.edu.sa
[2] Department of Renewable Energy, College of Renewable Energy and Environmental Sciences, Al-Karkh University of Science, Baghdad 10081, Iraq; ethar988@gmail.com
[3] Department of Electrical Engineering, College of Engineering, Jouf University, Sakaka 72388, Saudi Arabia
* Correspondence: mbashir@ju.edu.sa

Abstract: A sequence of dye-sensitized solar cells is proposed, utilizing TiO_2@Zn/Al-layered double hydroxide (LDH) as their starting materials, in which Ruthenizer N719 was used as a photon absorber. The anticipated system was turned into sheet-like TiO_2@mixed metal oxide (MMO) via post-processing treatment. The crystal quality indicated a relation to power conversion efficiency (PCE); this was combined with a comparable morphology profile. In detail, the optimum DSSC device exhibited average sheet-like thickness and a dye loading amount of 43.11 nm and 4.28×10^{-3} mM/cm^{-2}, respectively. Concurrently, a considerable PCE enhancement of the optimum DSSC device (TiO_2@MMO-550°) was attained compared to pristine MMO (0.91%), which could be due to boosted electron transfer efficiency. Of the fabricated devices, DSSC fabricated at 550° exhibited the highest PCE (1.91%), with a 35.6% enhancement compared to that obtained at 450°, as a result of its increased open-circuit voltage (3.29 mA/cm^2) and short-circuit current (0.81 V). The proposed work delivers an enhanced efficiency as compared to similar geometries.

Keywords: TiO_2; dye-sensitized solar cell; layered double hydroxide; mixed metal oxide

1. Introduction

The increased demands for petroleum and fossil fuels as the main source of energy, as well as the environmental awareness of their uses, are continuing to exert pressure on the already-existing world energy infrastructure. Therefore, a suitable replacement for sunlight conversion into electrical energy is of great need [1–3]. The technology of dye-sensitized solar cells (DSSCs) has attracted substantial consideration among the research and industrial societies because of its encouraging potential for relatively low production cost and high outcome efficiency [4–8]. However, the need for easy production and cost-effectiveness techniques of semiconductor photo-electrodes is of crucial significance when considering DSSC fabrication [9]. Herein, the utilization of mixed metal oxide (MMO) acquired via the calcination of layered double hydroxide (LDH) has demonstrated promising behavior as a photo-anode material for DSSC application; this is mainly attributed to the tunable composition, high stability, large surface area, and relatively low production cost as well as forthright preparation approaches [10–12]. Herein, LDH is utilized in variety of applications, particularly in the optoelectronic field [13,14]. Interestingly, the calcination of the addressed structure results in LDH's interlayer collapse, after which a variety of MMO structures can be attained, depending on the divalent and trivalent metal ions employed [15,16]. MMOs have revealed significant interest for a diverse field of applications, such as super capacitors, gas sensors, photodetectors, ultraviolet and visible light photocatalysts, etc. For the fabrication of DSSCs, MMOs are used as an active photo-electrode material due to a high electron injection efficiency, a high specific area for dye loading, rapid photo-response behavior, and a comparable energy band gap to TiO_2 and ZnO [17–20].

Several reports demonstrated the utilization of MMO-based Zn/Al-LDH as a precursor in DSSCs applications, through which a particular emphasis was placed on the active part of ZnO in the MMO matrix [10,21–23]. Moreover, the addition of metal and metal oxide nanoparticles, such as G, Cu, GO, CuO, and TiO_2, to the MMO matrix, was also investigated [24–28]. Herein, the proposed study delivers an investigation concerning the addition of TiO_2 to the matrix of MMO-based Zn/Al-LDH. Furthermore, the effect of post-processing temperature was also systematically deliberated, where an enhancement of 35.6% was acquired in the PCE profile at 550° (1.91) compared to that at 450° (1.41). Furthermore, an addition of TiO_2 to the utilized MMO anode materials with cautious control of the post-processing temperature showed a 109.9% increase in the overall output efficiency. The attained efficiency was found to be higher than other outcomes, in similar geometries.

2. Materials and Methods

2.1. Preparation of TiO_2 and TiO_2@LDH

TiO_2 nanoparticles were synthesized via a typical hydrothermal process. Particularly, titanium (IV) *iso*-propoxide, as a precursor, and ethanol were mixed with a ratio of 10/100 under a constant stirring rate of 800 rpm for 30 min. The resultant mixture was then autoclaved under 200 °C for 18 h. The achieved mixture was multi-washed and dried in an air oven at 65 °C. Hereinafter, the obtained powder was annealed at 450 °C for 1 h in a furnace. Concurrently, TiO_2@Zn(Al)O-MMO utilizing Zn^{2+}/Al^{3+}-LDH as a starting material was produced using both a co-precipitation method as well as a thermal treatment temperature approach. Typically, $Zn(NO_3)_2{\cdot}6H_2O$ and $Al(NO_3)_2{\cdot}9H_2O$ were mixed with a ratio of 8:1 in 150 mL of distilled water at 27 °C, with a continuous stirring rate of 600 rpm for 30 min; a precise homogenous growth was attained via the addition of NaOH (1.25 M), wherein a pH of 7.5 was obtained. Subsequently, TiO_2 (0.1 gm) was added to the Zn/Al-LDH solution and left to stir for 2 h, after which the resultant solution was multi-washed and centrifuged to remove any undesired impurities. The resultant paste was diluted using a few drops of EtOH and then transferred to a freshly washed fluorine-doped tin oxide (FTO) substrate via a three-cycles spin coating technique, with an area of 1 cm^2; the thin film was annealed at 150° for 10 min after each deposition. The attained film/s were treated at a post-processing temperature of 450 °C, 550 °C, and 650 °C for 1 h with a heating rate of 5 °C/min in a muffle furnace; the films were designated as TiO_2@MMO-T, with T signposts to indicate the employed post-processing temperatures.

2.2. Fabrication of DSSC

Herein, 5 mM of dye N719 (535-bisTBA Ruthenizer, Solaronix, Aubonne, Switzerland) was adsorbed by the attained MMO-550° and TiO_2@MMO-T layers via immersion for a duration of 3 h at room temperature. Synchronously, the Pt electrode was acquired using a DC sputtering technique on the FTO glass, and later sandwiched with the fabricated photo-anode with polymer film (100 μm) as a spacer. Next, Iodolyte (iodide/triiodide, Z50, Solaronix, Aubonne, Switzerland) was inserted between the photo-anode and the Pt electrode through capillarity.

2.3. Characterizations

The thermal properties of the LDH layer were investigated using thermogravimetric and differential thermal approaches (SBTA851-Mettler Toledo, TGA/DTG, Columbus, OH, USA), while the structural characteristics of the fabricated films were recorded using an X-ray diffractometer (XRD, AXS D8, Bruker, Billerica, MA, USA) under CuKα radiation and a 1.54 nm wavelength. Furthermore, the surface morphologies of the deposited films were inspected using field emission scanning electron microscopy (SU8030, FE-SEM, HITACHI, Tokyo, Japan). The optical analyses were conducted using two different approaches, namely, photoluminescence (PL, LS-50B, PerkinElmer, Waltham, MA, USA, excitation wavelength of 350 nm) and ultraviolet visible light (UV–Vis, Shimadzu, Kyoto, Japan) spectroscopies. The photovoltaic characteristics behavior of the fabricated DSSC was assessed using SMU Keithley 2400 (Cleveland, OH, USA) with a 1.5 G sunlight stimulator as a light source. Finally, an incident photon to current conversion efficiency (IPCE) test was performed using a monochromatic set-up in conjunction with an Xe-lamp (Newport, Shah Alam, Malaysia).

3. Results and Discussion

The thermal behavior of TiO_2@LDH through the TGA/DTG technique is elucidated in Figure 1, which revealed the three foremost stages of weight loss with an overall degradation profile of $\Delta m \approx 37\%$. Specifically, the loss in Δm_1, at around 100–150 °C, is mainly because of the release of the bound water as well as moisture disappearance; this in turn was substantiated with the peak of the DTG profile at 75 °C. Instinctively, a significant weight loss ($\Delta m_2 \approx 23\%$) was perceived, ranging between 200 °C and 500 °C, which is due to the structural collapse of the LDH interlayer as well as MMO formation [29]; this was found to be in good accordance with the DTG peak at 191 °C. Thermal putrefaction, attained at 500 °C and beyond, is attributed to the CO_2 release and possible recrystallization of TiO_2 nanoparticles [24].

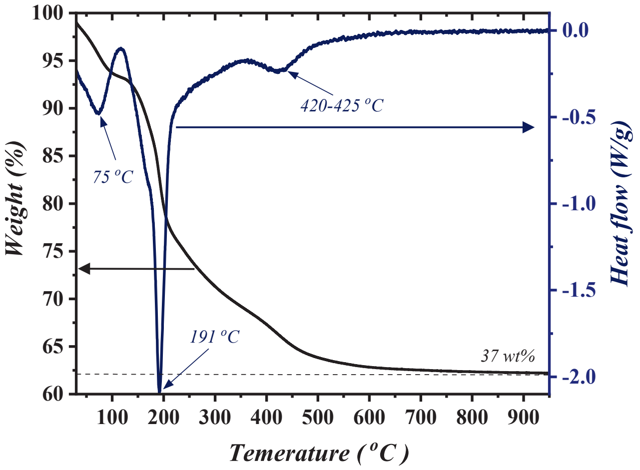

Figure 1. TGA/DTG profile of TiO_2@LDH.

The XRD patterns of the deposited layers are demonstrated in Figure 2. Pristine LDH revealed the occurrence of three distinguished peaks at 2θ = 9.9°, 19.8°, 33.8°, 37.86°, and 51.7°, which correspond to the basal planes (003) and (006) and the non-basal planes (101), (104), and (110), respectively; Additionally, the peaks attained between 30° and 37° are attributed to the formation of ZnO nanoparticles within the LDH matrix [30,31]. The XRD patterns of TiO_2@LDH exhibited similar behavior to that of pristine LDH, with one additional peak at around 26.5° due to the existence of the TiO_2 (101) plane [30]. The post-processing treatment (annealing) of TiO_2@LDH at 550 °C resulted in the collapse of LDH geometry and MMO peaks formation. These peaks correspond to the crystal formation of ZnO in accordance with PDF 89-1397; in particular, the peaks obtained at around 32°, 34.6°, and 36.5° correspond to planes of (100), (002), and (101). Moreover, patterns of TiO_2@MMO-T revealed the higher crystallinity of TiO_2 compared to that attained in the TiO_2@LDH spectrum (Table 1); this could be due to the effect of post-processing treatment at relatively high temperatures. It was proven that FWHM, obtained using XRD analysis, can be utilized as a crystal quality indicator, wherein FWHM is inversely proportional to the crystallite size [32]. Herein, the results presented in Table 1, in accordance with the (100) plane of ZnO hexagonal structure, indicate a higher crystal quality at relatively higher post-processing temperatures. Such a singularity was not clearly observed in the TiO_2 profile.

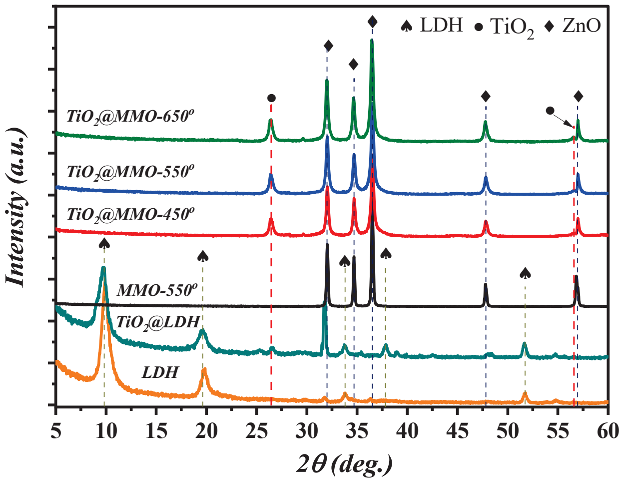

Figure 2. XRD patterns of pristine LDH, TiO_2@LDH, MMO-450°, and TiO_2@MMO-T.

Table 1. XRD characteristics of the deposited films.

	Material	2θ (deg.)	FWHM (deg.)	Crystallite Size (nm)
ZnO (100)	MMO-550°	32.05°	0.201	41.29
	TiO_2@MMO-450°	32.05°	0.333	24.89
	TiO_2@MMO-550°	32.10°	0.307	26.95
	TiO_2@MMO-650°	32.08°	0.331	25.04
TiO_2 (101)	TiO_2@MMO-450°	26.48°	0.493	16.59
	TiO_2@MMO-550°	26.35°	0.481	17.00
	TiO_2@MMO-650°	26.51°	0.487	16.81

The FE-SEM features of the fabricated layers are illustrated in Figure 3a–d, through which the topographies, in general, indicated the occurrence of an upright arrangement sheet-like morphology; this can be clearly observed at a temperature of 450° (Figure 3b). Moreover, the attained morphology showed a slight distortion at higher post-processing temperatures, such as temperatures of 550° and above (Figure 3a,c,d). The thickness of the attained sheet-like formation was found to be 48.7 nm, 52.75 nm, 43.11, and 38.71 nm, respectively, for the MMO prepared at 550° as well as TiO_2-MMO-T, where T represents the post-processing temperatures (450°, 550°, and 650°).

Figure 4 depicts the optical performance of the attained MMO-550 as well as the TiO_2@MMO-T films. A clear cut-off phenomenon was noticed at around 390 nm, concerning the optical behavior of ZnO attained within the MMO matrix (Figure 4a). The addition of TiO_2 within the MMO matrix resulted in a hypso-chromic shift towards lower wavelength (TiO_2@MMO-450°). Interestingly, the post-processing temperature resulted in a deeper hypso-chromic shift; this in turn can be verified via the bandgap investigation (inset into Figure 4a) which was estimated using Tauc relation [33,34]. A noticeable alteration in the attained optical band gap was noticed as the post-processing temperature progressed. The attained optical phenomenon was also investigated using PL spectroscopy (Figure 4b). A similar trend was noticed, where higher post-processing temperatures showed blue-shift behavior with respect to the optical bend gap values obtained.

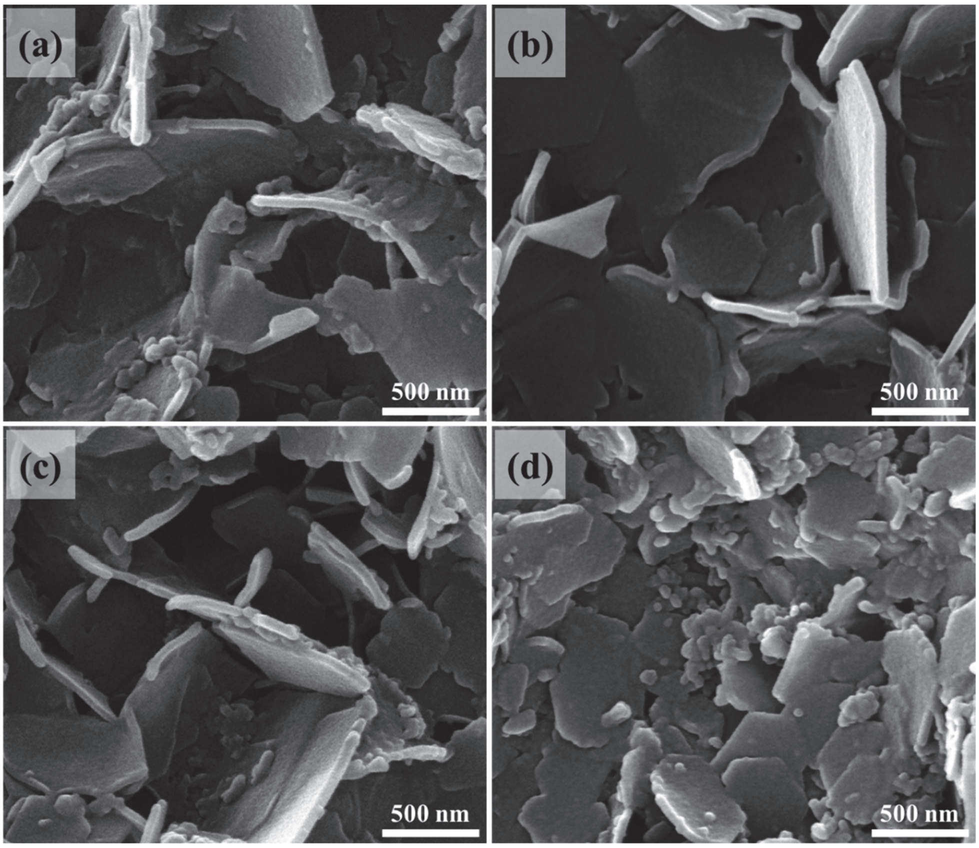

Figure 3. Topographies of the deposited layers (**a**) MMO, (**b**) TiO_2@MMO-450°, (**c**) TiO_2@MMO-550°, and (**d**) TiO_2@MMO-650°.

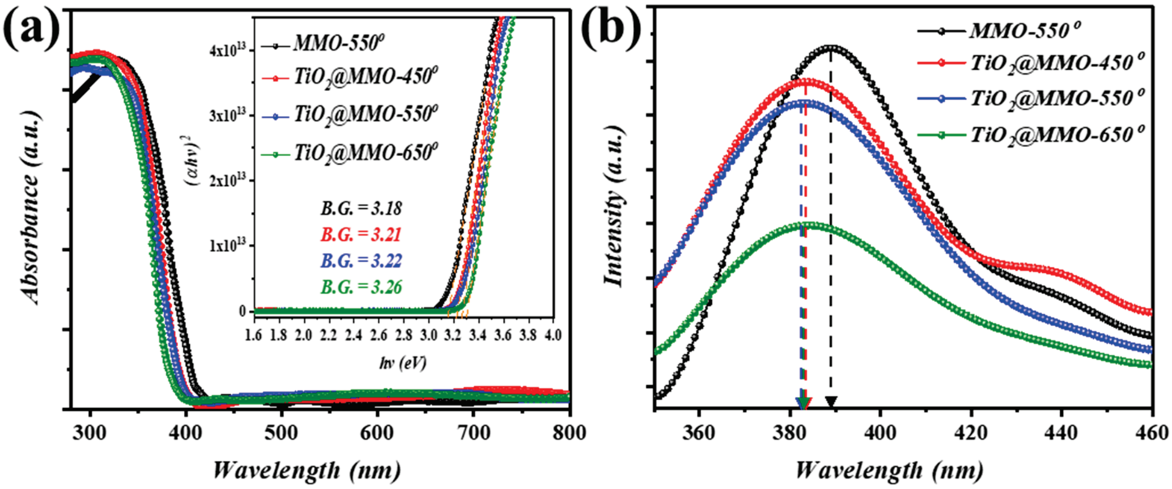

Figure 4. Optical characteristics of the deposited MMO-450° and TiO_2@MMO-T layers; (**a**) UV–Vis and (**b**) PL.

Figure 5a illustrates the band diagram geometry of the proposed work, wherein stimulated sunlight is absorbed via N719 as the main absorption layer and consequently excited electron/s, from HOMO to LUMO, are injected within the semiconductor layer, leading to current circulation [24]. The current density–voltage (J–V) characteristics of the proposed MMO-450° and TiO_2@MMO-T DSSC devices are shown in Figure 5b, where T represents the post-processing temperature. As presented in Table 2, the fabricated devices exhibited a short circuit current ranging from 1.74 to 3.29 (mA/cm^{-2}), while an almost similar open circuit voltage of $\sim$0.80 (V) was observed for all devices. Synchronously, the highest power conversion efficiency (PCE) was noticed, with the TiO_2@MMO layer post-processed at 550°, with a value of 1.91%. This indicates an enhancement of 109.9% compared to MMO-550° DSSC (0.91%), which in turn reveals the active role of TiO_2 in boosting the electron transportation efficiency within the MMO matrix [35]. The latter could be explained through a superior surface area, which successively allows higher dye N719 absorption through the surface for TiO_2@MMO-450° and TiO_2@MMO-550°. The attained J–V outcomes are in an uptight agreement with the XRD investigation and the FWHM profile, as shown in Table 1; a higher crystal quality could lead to easier electron mobility through which faster electron transfer is attained [36]. The dye loading amount (Figure 5d) reveals a relatively up-right agreement with devices attained at 450 °C and 550 °C; however, such an observation was not noticed for DSSC obtained at 650 °C; further details are presented in the Supplementary Materials. Figure 5c depicts the incident photon-to-current efficiency (IPCE) profile of the fabricated DSSC devices in which two foremost peaks were observed at around 375 nm and 530 nm. The former can be attributed to the MMO and TiO_2@MMO self-excitation within the UV spectrum, while the latter is chiefly caused by incident photons absorbed through dye N719 in the fabricated geometry. The quench in the IPCE curves at around 450 nm and the wavelengths above 600 nm suggest the low absorption of incident photons by the utilized dye N719. The proposed system, concerning the utilization of metal doped MMO, demonstrated a comparable overall efficiency in comparison to similar geometries (Table 3). It is worth mentioning that the demonstrated IPCE revealed slightly different peak positions compared to that attained during UV–Vis analysis, which could be due to the presence of dye N719 within the latter arrangement.

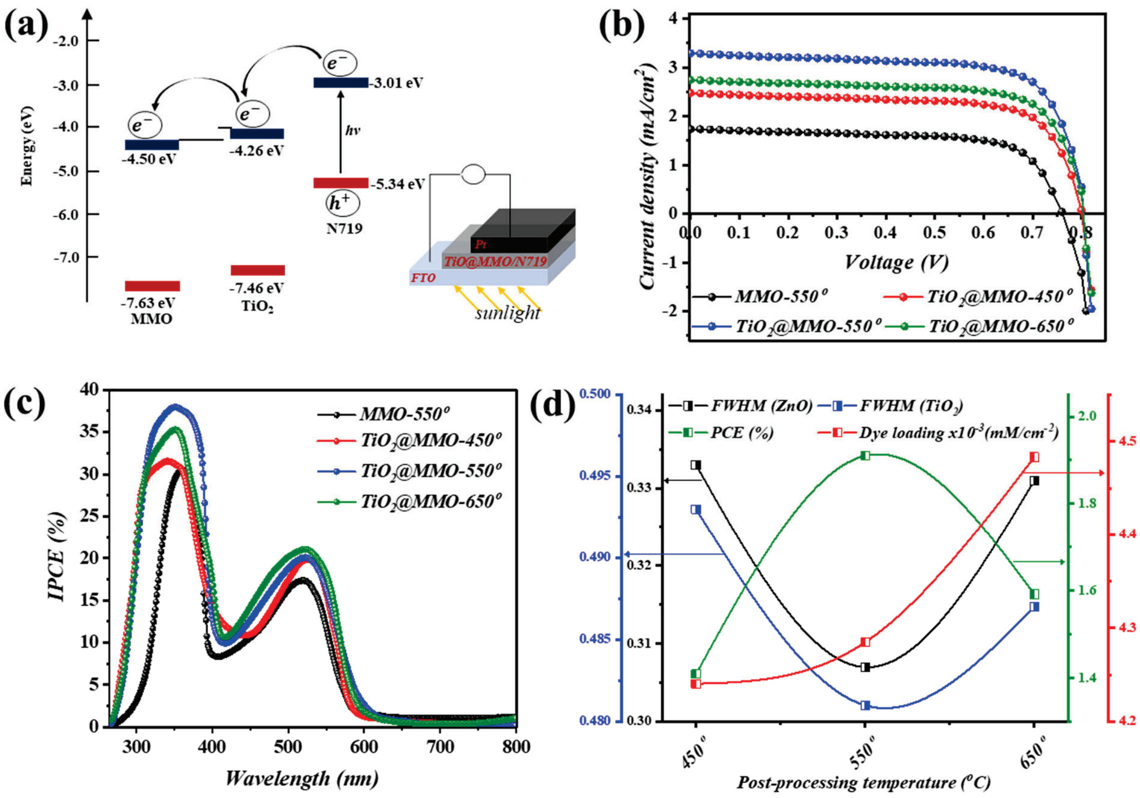

Figure 5. (**a**) band diagram geometry, (**b**) J–V characteristics, and (**c**) IPCE of the fabricated DSSCs, while (**d**) demonstrates a variation in FWHM of ZnO and TiO_2 phases, PCE, and dye loading amount.

Table 2. In-depth photovoltaic and surface features of the fabricated DSSCs.

Sample	J_{sc} (mA/cm^{-2})	V_{oc} (V)	FF	PCE (%)	Dye Load (mM/cm^{-2})
MMO-550°	1.74	0.76	0.69	0.91	3.71×10^{-3}
TiO_2@MMO-450°	2.47	0.80	0.71	1.41	4.24×10^{-3}
TiO_2@MMO-550°	3.29	0.81	0.72	1.91	4.28×10^{-3}
TiO_2@MMO-650°	2.74	0.80	0.73	1.59	4.48×10^{-3}

Table 3. Parameters attained in the proposed work compared to other reports in similar geometries.

Materials	J_{sc} (mA/cm^{-2})	V_{oc} (V)	FF	PCE (%)	Ref.
TiO_2@MMO	3.29	0.81	0.72	1.91	This study
TiO_2@MMO	2.63	0.81	0.70	1.50	[24]
CuO@MMO	3.42	0.67	0.55	1.24	[25]
CuO@MMO	7.21	0.46	0.45	1.50	[26]
G@MMO	0.36	3.62	0.39	0.51	[27]
GO@MMO	0.37	4.46	0.34	0.44	[28]

4. Conclusions

A series of sheet-like TiO_2@Zn/Al-MMO was efficaciously prepared via co-precipitation and hydrothermal techniques, in which TiO_2@Zn/Al-LDH was utilized as a precursor. Simultaneously, the attained TiO_2@Zn/Al-MMO sheets were used for DSSC application by means of post-treatment. The microstructural and optical characteristics of the fabricated sheets were systematically elaborated. Specifically, a sheet-like thickness of 43.11 nm delivered a considerable dye loading value of 4.28 $\times 10^{-3}$ mM/cm^{-2} for the optimum device (TiO_2@MMO-550°), which in turn lead to a relatively efficient overall PCE. In detail, the optimum device exhibited J_{sc} and V_{oc} values of 0.81 V and 3.29 mA/cm^2, respectively; the overall PEC was found to be 1.91%. This in turn resulted in a 35.6% enhancement for DSSC fabricated at a post-processing temperature of 550° compared to that attained at 450°.

Supplementary Materials: The following supporting information can be downloaded at: https://www.mdpi.com/article/10.3390/nano14110920/s1, Figure S1: Regression equation; Table S1: Variables of regression equation.

Author Contributions: Software, E.M.A.; Investigation, A.H.R., M.B.A.B. and E.Y.S.; Writing—original draft, A.H.R.; Writing—review & editing, M.B.A.B., E.Y.S. and E.M.A.; Project administration, A.H.R. All authors have read and agreed to the published version of the manuscript.

Funding: This work was funded by the Deanship of Scientific Research at Jouf University under Grant Number (DSR2022-RG-0115).

Data Availability Statement: The data presented in this study are available on request from the corresponding author due to research further enhancement.

Conflicts of Interest: The authors declare no conflict of interest.

References

1. Mohammed, M.K.; Al-Mousoi, A.K.; Majeed, S.M.; Singh, S.; Kumar, A.; Pandey, R.; Madan, J.; Ahmed, D.S.; Dastan, D. Stable Hole-Transporting Material-Free Perovskite Solar Cells with Efficiency Exceeding 14% via the Introduction of a Malonic Acid Additive for a Perovskite Precursor. *Energy Fuels* **2022**, *36*, 13187–13194. [CrossRef]
2. Kumar, A.; Singh, S.; Mohammed, M.K.; Shalan, A.E. Effect of 2D perovskite layer and multivalent defect on the performance of 3D/2D bilayered perovskite solar cells through computational simulation studies. *Sol. Energy* **2021**, *223*, 193–201. [CrossRef]
3. Albdiri, A.D.; Mohammed, A.A.; Hussein, M.; Koter, S. Modeling of lead ions transport through a bulk liquid membrane. *Desalination Water Treat.* **2020**, *181*, 213–220. [CrossRef]
4. Chiba, Y.; Islam, A.; Watanabe, Y.; Komiya, R.; Koide, N.; Han, L. Dye-sensitized solar cells with conversion efficiency of 11.1%. *Jpn. J. Appl. Phys.* **2006**, *45*, L638. [CrossRef]
5. Abdulghani, S.O.; Salih, E.Y.; Mohammed, A.S. Fabrication and photo-responsive characteristics of GeO_2 doped SnO_2/porous Si film for ultraviolet photodetector application. *Mater. Chem. Phys.* **2023**, *303*, 127859. [CrossRef]

6. O'regan, B.; Grätzel, M. A low-cost, high-efficiency solar cell based on dye-sensitized colloidal TiO_2 films. *Nature* **1991**, *353*, 737–740. [CrossRef]
7. Najm, A.S.; Alwash, S.A.; Sulaiman, N.H.; Chowdhury, M.; Techato, K. N719 dye as a sensitizer for dye-sensitized solar cells (DSSCs): A review of its functions and certain rudimentary principles. *Environ. Prog. Sustain. Energy* **2023**, *42*, e13955. [CrossRef]
8. Sekaran, P.D.; Marimuthu, R. An extensive analysis of dye-sensitized solar cell (DSSC). *Braz. J. Phys.* **2024**, *54*, 28. [CrossRef]
9. Richhariya, G.; Meikap, B.C.; Kumar, A. Review on fabrication methodologies and its impacts on performance of dye-sensitized solar cells. *Environ. Sci. Pollut. Res.* **2022**, *29*, 15233–15251. [CrossRef]
10. Fasolini, A.; Sangiorgi, N.; Brandi, E.T.; Sangiorgi, A.; Mariani, F.; Scavetta, E.; Sanson, A.; Basile, F. Increased efficiency and stability of Dye-Sensitized Solar Cells (DSSC) photoanode by intercalation of Eosin Y into Zn/Al layered double hydroxide. *Appl. Clay Sci.* **2021**, *212*, 106219. [CrossRef]
11. Salih, E.Y.; Abbas, Z.; Al Ali, S.H.H.; Hussein, M.Z. Dielectric behaviour of Zn/Al-NO_3 LDHs filled with polyvinyl chloride composite at low microwave frequencies. *Adv. Mater. Sci. Eng.* **2014**, *2014*, 647120. [CrossRef]
12. Feng, X.; Long, R.; Wang, L.; Liu, C.; Bai, Z.; Liu, X. A review on heavy metal ions adsorption from water by layered double hydroxide and its composites. *Sep. Purif. Technol.* **2022**, *284*, 120099. [CrossRef]
13. Salih, E.Y.; Sabri, M.F.M.; Sulaiman, K.; Hussein, M.Z.; Said, S.M.; Usop, R.; Salleh, M.F.M.; Bashir, M.B.A. Thermal, structural, textural and optical properties of ZnO/$ZnAl_2O_4$ mixed metal oxide-based Zn/Al layered double hydroxide. *Mater. Res. Express* **2018**, *5*, 116202. [CrossRef]
14. Abdelrahman, A.A.; Bendary, S.H.; Mahmoud, S.A. Synthesis and electrochemical properties of NiAl LDH@ RGO hierarchical nanocomposite as a potential counter electrode in dye sensitized solar cells. *Diam. Relat. Mater.* **2023**, *134*, 109738. [CrossRef]
15. Gabriel, R.; De Carvalho, S.H.; da Silva Duarte, J.L.; Oliveira, L.M.; Giannakoudakis, D.A.; Triantafyllidis, K.S.; Soletti, J.I.; Meili, L. Mixed metal oxides derived from layered double hydroxide as catalysts for biodiesel production. *Appl. Catal. A Gen.* **2022**, *630*, 118470. [CrossRef]
16. Lahkale, R.; Sadik, R.; Elhatimi, W.; Bouragba, F.; Assekouri, A.; Chouni, K.; Rhalmi, O.; Sabbar, E. Optical, electrical and dielectric properties of mixed metal oxides derived from Mg-Al Layered Double Hydroxides based solid solution series. *Phys. B Condens. Matter* **2022**, *626*, 413367. [CrossRef]
17. Mohammed, M.K.; Al-Mousoi, A.K.; Singh, S.; Younis, U.; Kumar, A.; Dastan, D.; Ravi, G. Ionic liquid passivator for mesoporous titanium dioxide electron transport layer to enhance the efficiency and stability of hole conductor-free perovskite solar cells. *Energy Fuels* **2022**, *36*, 12192–12200. [CrossRef]
18. Mohammed, M.K.; Jabir, M.S.; Abdulzahraa, H.G.; Mohammed, S.H.; Al-Azzawi, W.K.; Ahmed, D.S.; Singh, S.; Kumar, A.; Asaithambi, S.; Shekargoftar, M. Introduction of cadmium chloride additive to improve the performance and stability of perovskite solar cells. *RSC Adv.* **2022**, *12*, 20461–20470. [CrossRef] [PubMed]
19. Naji, A.M.; Kareem, S.H.; Faris, A.H.; Mohammed, M.K. Polyaniline polymer-modified ZnO electron transport material for high-performance planar perovskite solar cells. *Ceram. Int.* **2021**, *47*, 33390–33397. [CrossRef]
20. Bashir, M.B.A.; Said, S.M.; Sabri, M.F.M.; Miyazaki, Y.; Shnawah, D.A.; Shimada, M.; Salleh, M.F.M.; Mahmood, M.S.; Salih, E.Y.; Fitriani, F. In-filled $La_{0.5}Co_4Sb_{12}$ skutterudite system with high thermoelectric figure of merit. *J. Electron. Mater.* **2018**, *47*, 2429–2438. [CrossRef]
21. Zhang, L.; Liu, J.; Xiao, H.; Liu, D.; Qin, Y.; Wu, H.; Li, H.; Du, N.; Hou, W. Preparation and properties of mixed metal oxides based layered double hydroxide as anode materials for dye-sensitized solar cell. *Chem. Eng. J.* **2014**, *250*, 1–5. [CrossRef]
22. Xu, Z.; Shi, J.; Haroone, M.S.; Chen, W.; Zheng, S.; Lu, J. Zinc-aluminum oxide solid solution nanosheets obtained by pyrolysis of layered double hydroxide as the photoanodes for dye-sensitized solar cells. *J. Colloid Interface Sci.* **2018**, *515*, 240–247. [CrossRef] [PubMed]
23. Liu, S.; Liu, J.; Wang, T.; Wang, C.; Ge, Z.; Liu, J.; Hao, X.; Du, N.; Xiao, H. Preparation and photovoltaic properties of dye-sensitized solar cells based on zinc titanium mixed metal oxides. *Colloids Surf. A Physicochem. Eng. Asp.* **2019**, *568*, 59–65. [CrossRef]
24. Foruzin, L.J.; Rezvani, Z.; Nejati, K. Fabrication of TiO_2@ ZnAl-layered double hydroxide based anode material for dye-sensitized solar cell. *RSC Adv.* **2016**, *6*, 10912–10918. [CrossRef]
25. Bashir, M.B.A.; Rajpar, A.H.; Salih, E.Y.; Ahmed, E.M. Preparation and Photovoltaic Evaluation of CuO@Zn(Al)O-Mixed Metal Oxides for Dye Sensitized Solar Cell. *Nanomaterials* **2023**, *13*, 802. [CrossRef]
26. Ge, Z.; Wang, C.; Chen, T.; Chen, Z.; Wang, T.; Guo, L.; Qi, G.; Liu, J. Preparation of Cu-doped ZnO nanoparticles via layered double hydroxide and application for dye-sensitized solar cells. *J. Phys. Chem. Solids* **2021**, *150*, 109833. [CrossRef]
27. Ge, Z.; Zhu, Y.; Wang, C.; Xia, L.; Guo, L.; Wu, Y.; Liu, J. Investigation of the photoanode based on graphene/zinc aluminum mixed metal oxide for dye-sensitized solar cell. *J. Sol-Gel Sci. Technol.* **2020**, *95*, 432–438. [CrossRef]
28. Wang, C.; Zhu, Y.; Ge, Z.; Shi, R.; Chen, T.; Chen, Z.; Liu, J. The feasible photoanode of graphene oxide/zinc aluminum mixed metal oxides for the dye-sensitized solar cell. *Colloid Interface Sci. Commun.* **2020**, *39*, 100313. [CrossRef]
29. Antoniak-Jurak, K.; Kowalik, P.; Bicki, R.; Michalska, K.; Próchniak, W.; Wiercioch, P. Cu substituted $ZnAl_2O_4$ ex-LDH catalysts for medium-temperature WGS–effect of Cu/Zn ratio and thermal treatment on catalyst efficiency. *Int. J. Hydrog. Energy* **2019**, *44*, 27390–27400. [CrossRef]
30. Mohammad, M.R.; Ahmed, D.S.; Mohammed, M.K. Synthesis of Ag-doped TiO_2 nanoparticles coated with carbon nanotubes by the sol–gel method and their antibacterial activities. *J. Sol-Gel Sci. Technol.* **2019**, *90*, 498–509. [CrossRef]

31. Mohammad, M.R.; Ahmed, D.S.; Mohammed, M.K. ZnO/Ag nanoparticle-decorated single-walled carbon nanotubes (SWCNTs) and their properties. *Surf. Rev. Lett.* **2020**, *27*, 1950123. [CrossRef]
32. Bashir, M.B.A.; Salih, E.Y.; Sabri, M.F.M.; Rajpar, A.H.; Badruddin, I.A.; Hussein, M.Z.; Al-Jumaili, B.E. In-depth thermal, microstructural and photoluminescence analysis of mesoporous ZnO/$ZnAl_2O_4$-MMO: The effect of molar ratio. *ECS J. Solid State Sci. Technol.* **2021**, *10*, 106006. [CrossRef]
33. Ahmed, N.M.; Ramizy, A.; Hassan, Z.; Amer, A.; Omar, K.; Al-Douri, Y.; Alattas, O.S. Nano and micro porous GaN characterization using image processing method. *Optik* **2012**, *123*, 1074–1078. [CrossRef]
34. Ramizy, A.; Aziz, W.J.; Hassan, Z.; Omar, K.; Ibrahim, K. The effect of porosity on the properties of silicon solar cell. *Microelectron. Int.* **2010**, *27*, 117–120. [CrossRef]
35. Boro, B.; Gogoi, B.; Rajbongshi, B.; Ramchiary, A. Nano-structured TiO_2/ZnO nanocomposite for dye-sensitized solar cells application: A review. *Renew. Sustain. Energy Rev.* **2018**, *81*, 2264–2270. [CrossRef]
36. Tao, R.; Tomita, T.; Wong, R.A.; Waki, K. Electrochemical and structural analysis of Al-doped ZnO nanorod arrays in dye-sensitized solar cells. *J. Power Sources* **2012**, *214*, 159–165. [CrossRef]

nanomaterials

Article

Asymmetric Schottky Barrier-Generated MoS_2/WTe_2 FET Biosensor Based on a Rectified Signal

Xinhao Zhang [1,†], Shuo Chen [1,†], Heqi Ma [1], Tianyu Sun [1], Xiangyong Cui [1], Panpan Huo [1], Baoyuan Man [1,*] and Cheng Yang [1,2,*]

[1] School of Physics and Electronics, Shandong Normal University, Jinan 250014, China; zhangxh0050@163.com (X.Z.); shuochen1119@gmail.com (S.C.); heqima9@163.com (H.M.); s15169093367@126.com (T.S.); CXY2023025549@outlook.com (X.C.); hpp6780@163.com (P.H.)

[2] Shandong Provincial Engineering and Technical Center of Light Manipulations, Shandong Normal University, Jinan 250014, China

* Correspondence: byman@sdnu.edu.cn (B.M.); chengyang@sdnu.edu.cn (C.Y.)

† These authors contributed equally to this work.

Abstract: Field-effect transistor (FET) biosensors can be used to measure the charge information carried by biomolecules. However, insurmountable hysteresis in the long-term and large-range transfer characteristic curve exists and affects the measurements. Noise signal, caused by the interference coefficient of external factors, may destroy the quantitative analysis of trace targets in complex biological systems. In this report, a "rectified signal" in the output characteristic curve, instead of the "absolute value signal" in the transfer characteristic curve, is obtained and analyzed to solve these problems. The proposed asymmetric Schottky barrier-generated MoS_2/WTe_2 FET biosensor achieved a 10^5 rectified signal, sufficient reliability and stability (maintained for 60 days), ultra-sensitive detection (10 aM) of the Down syndrome-related DYRK1A gene, and excellent specificity in base recognition. This biosensor with a response range of 10 aM–100 pM has significant application potential in the screening and rapid diagnosis of Down syndrome.

Keywords: Schottky junction; field-effect transistor; biosensor; rectified signal; ultra-sensitive detection

1. Introduction

Low-dimensional materials-based field-effect transistor (FET) biosensors have the advantages of high sensitivity, fast detection, miniaturization, low cost, and compatibility with integrated circuits [1–3]. However, the commonly used signals in FET biosensors are referred to as "absolute value signals". These include Dirac voltage, threshold voltage V_{th}, source-drain current I_{ds}, and others [4–7]. These "absolute value signals" directly collect and process the specific changes in biomolecules. Although these signals carry the biomolecules' charge information [8–10], they have the drawbacks of incomplete, unstable, and unreliable detection. Kulkarni et al. reported that the detection range of FET-based biosensors was limited by the Debye length due to the Debye screening effect. Consequently, molecular charge information outside the Debye length cannot be detected [11]. Sadighbayan et al. reported that ions in water or an electrolyte solution affected the surface potential or electric field of the sensor, causing fluctuations in the "absolute value signal". The fluctuations made the stable detection of the charge information of biomolecules challenging [12]. Xu et al. reported that non-target molecules on the sensor surface can generate non-specific signals, affecting the charge density or potential on the sensor surface. This non-specific signal makes the detected "absolute value signal" unreliable [13,14].

A series of signal optimization models and signal processing methods for the "absolute value signals" have been proposed by researchers to accurately express the charge information carried by biomolecules. Fathi-Hafshejani, Parvin and coworkers combined density functional theory (DFT) and the collected "absolute value signals". They optimized the calculation model of the interaction energy and charge transfer between MUA (mercaptoundecanoic acid) and WSe_2, achieving the rapid and sensitive detection of the novel coronavirus (SARS-CoV-2) [15]. By adding a MoS_2 layer on graphene, Chen et al. suppressed the interference caused by the Debye screening effect on charge information detection. Consequently, they achieved the high integrity of charge information detection under physiological environment conditions [16]. Hajian, Reza et al. used the double exponential function and linear regression model to determine the relationship between the signal change curve and DNA concentration, and then cross-checked the theoretical results with the experimental "absolute value signals" to improve the detection stability [17]. Sarah Balderston et al. identified an insurmountable hysteresis phenomenon in measuring the transfer characteristic curve. They proposed a signal-processing model based on the average transconductance of small-range scanning gate voltage to minimize the interference of the hysteresis phenomenon on the measurement results, achieving single-base mutation detection in the BRCA1 and KRAS genes [18]. These models and strategies have significantly promoted signal accuracy. However, due to the inherent defects of the sensing materials, measurements still suffer from the interference of the hysteresis phenomenon while determining the influence of biomolecules on the intrinsic electric field of the sensing materials.

This study, for the first time, reports a strategy of using a "rectified signal" in the output characteristic curve instead of the "absolute value signal" in the transfer characteristic curve. A Schottky barrier-based MoS_2/WTe_2 FET biosensor was prepared to generate a "rectified signal" in the output characteristic curve. The low work function semimetal WTe_2 electrode replaced the Au electrode and formed a Schottky junction with MoS_2, reducing the Schottky barrier height at the WTe_2/MoS_2 interface and increasing carrier mobility. The Schottky barrier difference between the WTe_2/MoS_2 electrode and MoS_2/Au electrode caused the rectification ratio. Furthermore, the MoS_2/WTe_2 FET biosensor was used as a sensing platform to detect the Down syndrome-related DYRK1A gene, achieving a detection limit of 10 aM and high specificity. The linear response range was 10 aM–100 pM, indicating that the MoS_2/WTe_2 FET biosensor has broad application potential in the screening and rapid diagnosis of Down syndrome.

2. Materials and Methods

2.1. Materials

PBS (pH~7.0–7.2), 1-pyrenebutanoic acid succinimidyl ester (PBASE), DMSO, and ethanolamine were procured from Aladdin Co., Ltd. (Shanghai, China). SiO_2/Si substrates, bulk MoS_2, 1T′-WTe_2, blue film tape, and PDMS (polydimethylsiloxane) film were purchased from Shanghai Onway Technology Co., Ltd. (Shanghai, China). Other reagents were procured from Sinopharm Chemical Reagent Co., Ltd. (Shanghai, China). Deionized water (DI water) was collected from a Millipore water purification system (Milli-Q Direct8). The partial DNA/RNA sequences were purchased from Sangon Biotech (Shanghai) Co., Ltd. (Shanghai, China) (Table S1).

2.2. Device Fabrication

MoS_2 and 1T′-WTe_2 films were peeled off from their crystal blocks using blue film tape and then transferred to the PDMS film using a two-dimensional material transfer platform. Finally, MoS_2 and 1T′-WTe_2 films with the optimal thickness, size, and morphology were transferred to the SiO_2/Si substrates with pre-lithographed electrodes, forming 1T′-WTe_2/MoS_2 devices (Figure S1).

2.3. Device Functionalization and Immobilization

Before the detection of the target DNA molecule, the constructed MoS_2/WTe_2 needed to be functionalized and immobilized. PBASE was selected to functionalize MoS_2 and immobilize the probe DNA as a linker between MoS_2 and probe DNA. PBASE, when dissolved in DMSO, stacks its pyrene group on the surface of MoS_2, binds to MoS_2, and immobilizes the probe DNA via the coupling reaction between the amine of the probe DNA and the amine-reactive succinimide group of PBASE (Figure S2). During functionalization, the PBASE solution, placed in an Eppendorf tube (EP tube), reacted with the MoS_2/WTe_2 FET biosensor at 37 °C for 20 min in a constant temperature box to deposit the pyrene groups in PBASE on the MoS_2 surface by π-π stacking. After reaction completion, the unreacted samples on the surface were washed off with DMSO solution. During the probe DNA immobilization, the probe DNA solution (1 pM) was placed in an EP tube and reacted with the MoS_2/WTe_2 FET biosensor at 37 °C for 2 h in a constant temperature box to immobilize the probe DNA via a conjugation reaction between the amine group of the probe DNA and the amine-reactive succinimide group of PBASE. The shift of the Mo3d peak and S2p peak positions confirmed that PBASE and the probe DNA were successfully combined on the MoS_2/WTe_2 surface (Figure S3). After reaction completion, the unreacted gene samples on the surface were washed off with 1×PBS solution. In the target DNA detection process, 200 µL of the DYRK1A gene sample was placed in an EP tube, followed by a reaction with the MoS_2/WTe_2 FET biosensor at 37 °C for 2 h in a constant temperature box to allow more target DNA to diffuse to the MoS_2 surface and be captured by the probe DNA on the surface. After completion, the unreacted gene samples on the surface were washed off with 1×PBS solution, and the performance of the MoS_2/WTe_2 FET biosensor was tested after drying.

2.4. Characterization

The electrical properties of the MoS_2/WTe_2 FET biosensor were determined using a Keithley 4200-SCS semiconductor parameter analyzer at room temperature and in atmospheric pressure, dry, dark, and well-ventilated conditions. A constant stride interval of 20 mV was applied to the V_{DS}–I_{DS} curve. The structure and morphologies of the prepared samples were analyzed using SEM (Zeiss Gemini Ultra-55, 3.0 kV, Oberkochen, Germany) and EDS. AFM was used to determine the roughness of the MoS_2/WTe_2 surface. The Raman spectrometer used in this study was a Horiba HR Evolution 800 with a 532 nm excitation laser. The XPS characterization was conducted using a Thermo Fisher Scientific Escalab 250Xi instrument (Waltham, MA, USA) with an Al K X-ray source at 150 W and a spot size of 500. The spectra were acquired with an operating voltage of 12.5 kV and a spectrometer pressure of 8×10^{-10} mbar. The XPS spectra were calibrated by the peak of C 1 s at 282 eV, normalized by the baseline level, and curve-fitted by smart function.

3. Results and Discussion

3.1. The Advantages and Generation Mechanisms of the Rectified Signal

The rectified signal is a kind of response signal, which is composed of two currents with opposite directions. It effectively reflects the specific changes in the biomolecules. Taking the current variation (ΔI) and rectification ratio variation (ΔR) as examples, the accuracy of the "absolute value signal" and "rectified signal" can be discussed in detail.

Figure 1A shows that, when the "absolute value signal" (such as source-drain current) is used as the response signal, which can be expressed as [19]

$$\Delta I = I_2 - I_1, \tag{1}$$

I_1 and I_2 are the measured source-drain currents at different biomolecular concentrations.

$$I_1 = C_1 \cdot I_{1\cdot True};\ I_2 = C_2 \cdot I_{2\cdot True}, \tag{2}$$

$I_{1\cdot True}$ and $I_{2\cdot True}$ are the accurate values of the source-drain current at different biomolecular concentrations without interference from external factors. The constant C_i (i = 1, 2) represents the interference coefficient of external factors at different biomolecular concentrations. Since I_2 and I_1 are "absolute value signals" at different biomolecular concentrations, each external factor affects them differently $(C_2 \neq C_1)$, which implies that the charge information carried by biomolecules cannot be accurately determined by using an "absolute value signal" as a response signal.

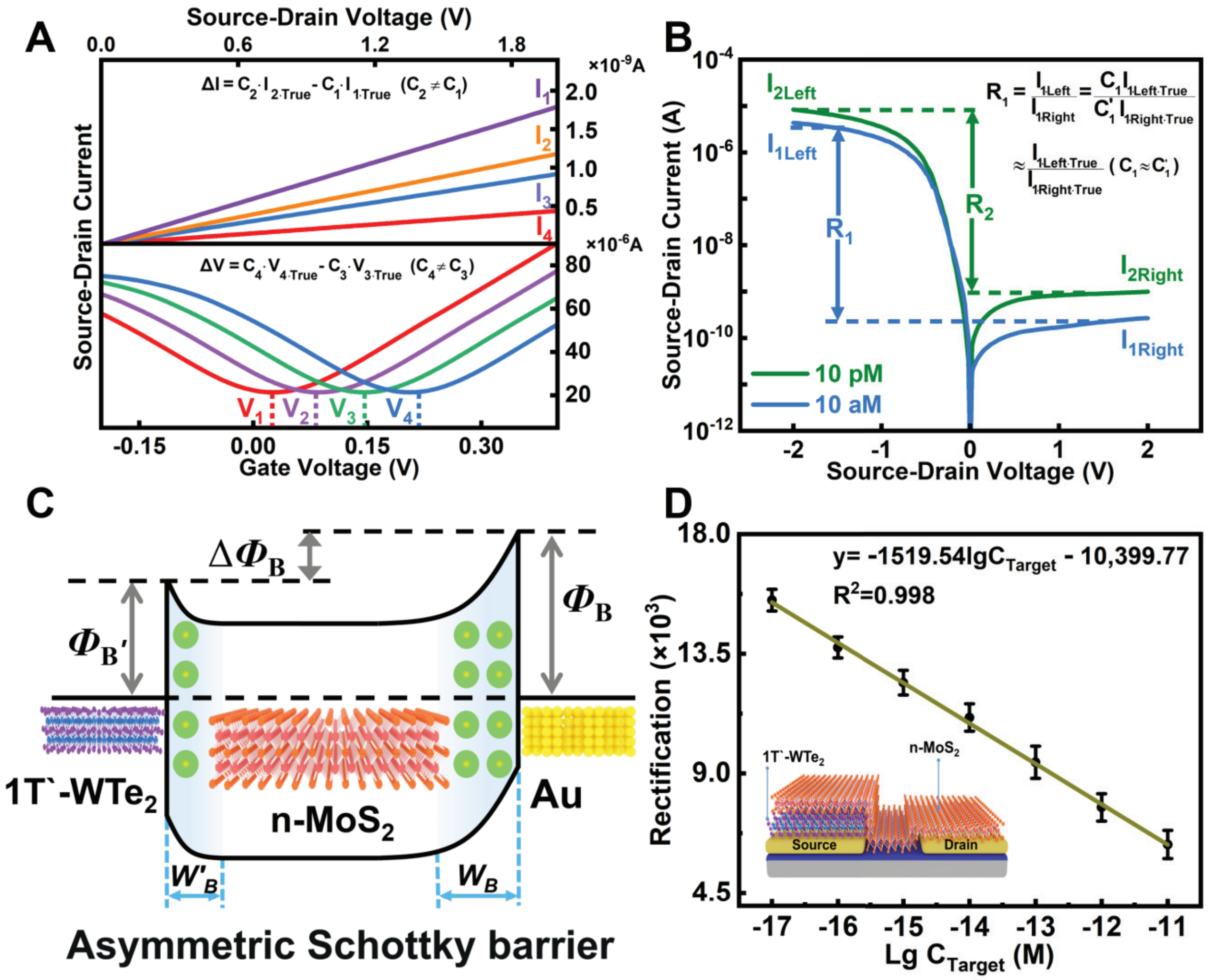

Figure 1. (**A**) Current–voltage images using the source-drain current, Dirac voltage, and other absolute value signals as response signals. (**B**) Current–voltage image when the rectification ratio, a rectified signal, is used as a response signal. (**C**) The band diagram of the structure generating the rectification ratio signal. (**D**) The linear relationship between the rectification ratio signal and the concentration of biomolecules. The inset shows a schematic diagram of the structure.

Figure 1B shows that, when the "rectified signal" is used as a response signal, the rectification ratio can be expressed as [20]:

$$\Delta \mathrm{R} = \mathrm{R}_2 - \mathrm{R}_1, \tag{3}$$

where R_1 and R_2 are the rectification ratios at different biomolecular concentrations.

$$\mathrm{R}_1 = \frac{\mathrm{I}_{1\cdot\ \mathrm{Left}}}{\mathrm{I}_{1\cdot\ \mathrm{Right}}} = \frac{\mathrm{C}_1{\cdot}\mathrm{I}_{1\cdot\ \mathrm{Left\cdot True}}}{\mathrm{C}_1'{\cdot}\mathrm{I}_{1\cdot\ \mathrm{Right\cdot True}}} \approx \frac{\mathrm{I}_{1\cdot\ \mathrm{Left\cdot True}}}{\mathrm{I}_{1\cdot\ \mathrm{Right\cdot True}}}\left(\mathrm{C}_1 \approx \mathrm{C}_1'\right), \tag{4}$$

$$\mathrm{R}_2 = \frac{\mathrm{I}_{2\cdot\ \mathrm{Left}}}{\mathrm{I}_{2\cdot\ \mathrm{Right}}} = \frac{\mathrm{C}_2{\cdot}\mathrm{I}_{2\cdot\ \mathrm{Left\cdot True}}}{\mathrm{C}_2'{\cdot}\mathrm{I}_{2\cdot\ \mathrm{Right\cdot True}}} \approx \frac{\mathrm{I}_{2\cdot\ \mathrm{Left\cdot True}}}{\mathrm{I}_{2\cdot\ \mathrm{Right\cdot True}}}\left(\mathrm{C}_2 \approx \mathrm{C}_2'\right), \tag{5}$$

$I_{i\ Left}$ (i = 1,2) and $I_{i\ Right}$ are the source-drain currents under the sweep negative and positive voltages, respectively. Since $I_{i.\ Left}$ and $I_{i.\ Right}$ are measured at the same biomolecular concentration, they should be affected by external factors approximately equally ($C_i \approx C_i^{'}$), which means that R_2 and R_1 values are approximately accurate. Thus, the variation in the "rectified signal" ($\Delta R = R_2 - R_1$) is approximately accurate. Using the "rectified signal" as a response signal accurately reflects the charge information carried by biomolecules.

A MoS_2/WTe_2 FET biosensor with an asymmetric Schottky barrier was constructed to measure the rectification ratio signal. Figure 1C shows the schematic diagram of its energy band structure. High-quality n-type MoS_2 and low-work function semimetal 1T′-WTe_2 were obtained by mechanical exfoliation and built into heterojunctions by a transfer platform [21]. In the MoS_2/WTe_2 FET biosensor, MoS_2 forms asymmetric Schottky junctions with 1T′-WTe_2 and Au, with barrier heights of $\Phi_B^{'}$ and Φ_B and barrier widths of $W_B^{'}$ and W_B, respectively. The Schottky barrier height can be obtained from the Schottky–Mott relation [22]:

$$\Phi_B = \Phi_M - \chi_S, \tag{6}$$

where Φ_B is the Schottky barrier height, Φ_M is the work function of the metal electrodes, and χ_S represents the electron affinity of the n-type semiconductor. The Schottky barrier width can be obtained by the following formula [23]:

$$W = \sqrt{\frac{2\mathcal{E}_s V_{bi}}{qN_A}}, \tag{7}$$

where $\mathcal{E}_s$ is the dielectric constant of the semiconductor; $V_{bi} = (\Phi_M - \Phi_S)/q$ is the built-in potential of the Schottky junction; q is the elementary charge; and N_A is the bulk charge density of the channel material.

Because of the lower work function of WTe_2 compared to that of Au, the Schottky barrier height and width of the MoS_2/Au junction is larger than those of the MoS_2/1T′-WTe_2 junction in the WTe_2/MoS_2/Au FET biosensor. The asymmetric Schottky barrier height between the two junctions leads to the generation of a rectification ratio signal in the heterojunction FET. As we know, the smaller the barrier width, the larger the tunneling current. In addition, the widths of the two junctions are different; thus, the smaller the W, the larger the tunneling current. Then, the tunneling currents of the two junctions are definitely not the same, which finally causes source-drain current changes at both ends, resulting in rectification ratio changes, as shown in Figure 1D.

3.2. Schematic Diagram of the MoS_2/WTe_2 FET Biosensor

The functionalization of the sensing surface, probe DNA immobilization, and target DNA hybridization were performed using the MoS_2/WTe_2 FET biosensor to generate a more stable response signal. In Figure 2A, 1-pyrenebutyric acid succinimidyl ester (PBASE) in the N,N-dimethylformamide solution was used as a linker between MoS_2 and the probe DNA, ensuring that the probe DNA could effectively bind to MoS_2 [24]. The pyrene group of PBASE was fixed on the MoS_2 surface by π-π stacking. The succinimide part of PBASE protruded from the MoS_2 surface and coupled with the amine group of the 5′-amine-modified DNA probe, as shown in Figure 2B [25]. Next, the target DNA complementary was added to the probe DNA. Consequently, the target DNA was hybridized with the probe DNA by base complementary pairing, as shown in Figure 2C. Notably, the different Schottky barrier widths of the MoS_2/WTe_2 FET biosensors can be obtained with the different steps, affecting the probability of tunneling current [26].

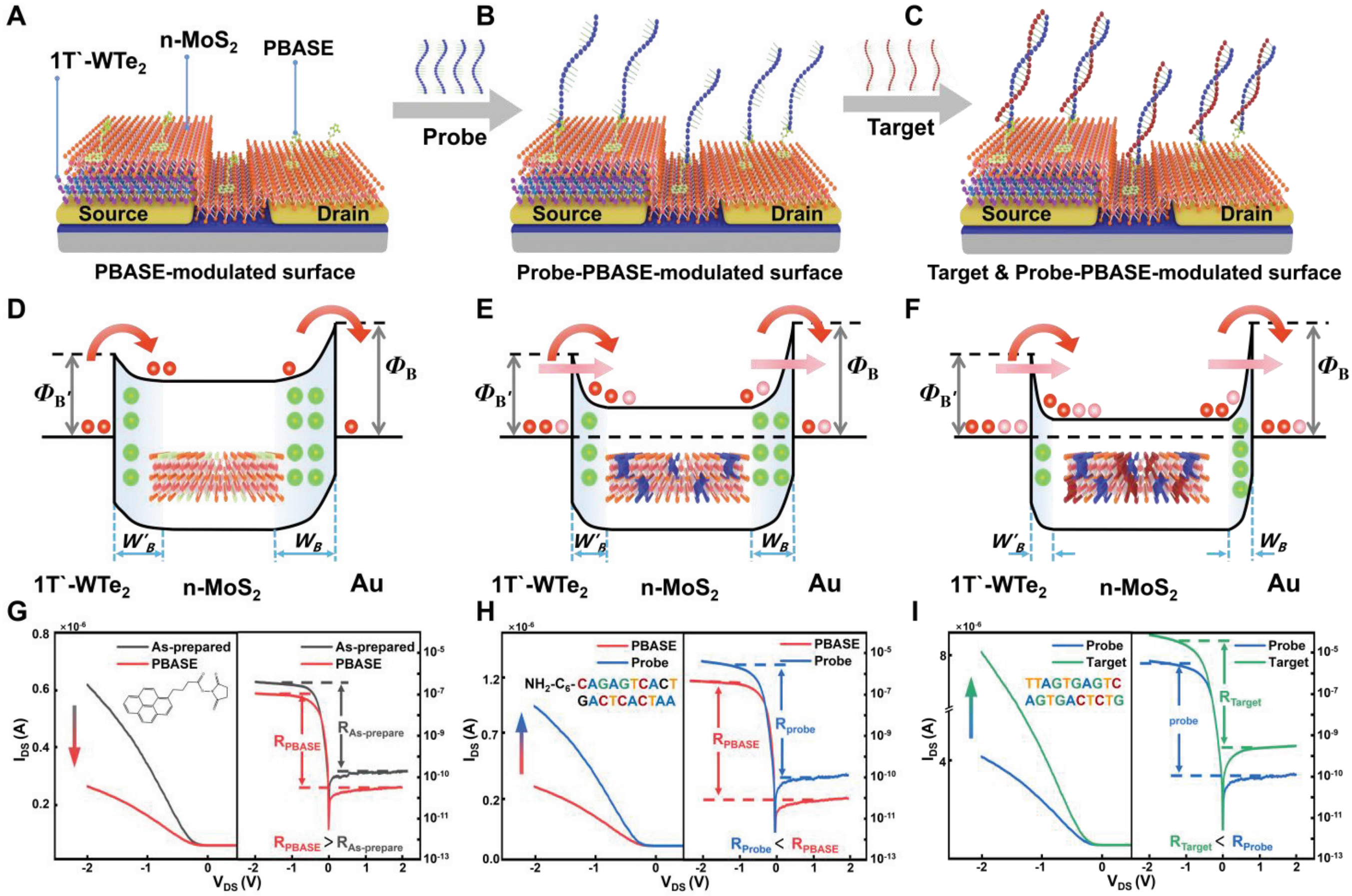

Figure 2. Schematic diagram of the MoS_2/WTe_2 FET biosensor. (**A**) Functionalization of the MoS_2/WTe_2 surface using the PBASE solution. (**B**) Immobilization of the probe DNA implied an interaction between PBASE and the probe DNA, achieving the binding of the probe DNA and the MoS_2/WTe_2 FET biosensor. (**C**) Interaction between the probe DNA and target DNA to form a double-stranded DNA. Schematic diagram of the band gap changes in the MoS_2/WTe_2 FET biosensor in the three processes: (**D**) functionalization of the sensing surface, (**E**) immobilization of the probe DNA, and (**F**) binding of the target DNA, where the charge injection mode modulated by PBASE on the surface is thermionic emission (TE), and the charge injection mode modulated by probe-PBASE on the surface and by target & probe–PBASE on the surface is tunneling. Absolute value signal I_{DS} (left) and rectified signal R (right) of the MoS_2/WTe_2 FET biosensor in the (**G**) functionalization, (**H**) immobilization of probe DNA, and (**I**) binding of target DNA.

In the functionalization process of MoS_2, the pyrene groups in PBASE fixed on the surface of MoS_2 by π-π stacking add a small amount of holes to the MoS_2/WTe_2 FET biosensor. Hole doping also effectively widens the Schottky barrier width of the MoS_2/WTe_2 FET biosensor. At this time, thermionic emission (TE) is the main charge injection mode, as shown in Figure 2D. That is to say, although the decrease in the forward bias current dominated by the MoS_2/Au junction is small, its relative decrease rate is larger, resulting in the increase in the rectification ratio R, as shown in Figure 2G. In the process of probe DNA immobilization, the succinimide part of the MoS_2 surface couples with the probe DNA, which fixes the probe DNA on MoS_2 and adds a small amount of electrons to the MoS_2/WTe_2 FET biosensor. Electron doping also effectively reduces the Schottky barrier width of the MoS_2/WTe_2 FET biosensor. At this time, the charge injection mode is electron tunneling and TE, as shown in Figure 2E. According to the conclusion, after fixing the probe DNA, the barrier width of the MoS_2/Au Schottky junction is reduced more and the relative current growth rate is higher than that of the $MoS_2/1T'$-WTe_2 Schottky junction. That is to say, although the increase in the forward bias current dominated by the MoS_2/Au junction is small, its current growth rate is larger, resulting in the decrease in the rectification rate R, as shown in the right inset of Figure 2H. Similarly, target DNA hybridizes with probe DNA through base complementary pairing, which also adds electron doping to the MoS_2/WTe_2 FET biosensor. It increases the current and reduces the Schottky barrier width at the same time, and the barrier width of the MoS_2/Au junction is reduced more and the relative current growth rate is higher, resulting in the increase in the current and decrease in the rectification ratio R, as shown in Figure 2F,I.

The equation of the Schottky barrier width was used to calculate the change in the barrier width before and after doping. Their effects on the forward, reverse current, and rectification ratio signal were analyzed using Equations (2)–(4) [22]. The rectification ratio signal was found to effectively eliminate the interference of external factors on the molecular signal because it depends only on the ratio of the forward and reverse currents rather than the absolute value of the single-direction current. Therefore, the rectification ratio signal is not affected significantly, and an accurate expression of the charge information carried by biomolecules is obtained.

In addition, the rectification ratio signal not only reflects the changes in both Schottky junctions but also avoids the interference of the hysteresis phenomenon (Figure 2G–I). Since the forward and reverse source-drain currents are affected by the charge information on DNA molecules, the rectification ratio signal can detect weak charge information under the conditions of a low concentration DNA solution. In contrast, the forward or reverse source-drain current, which is used as the response signal, is difficult to separate from the noise signal [27], reducing the sensing sensitivity. Therefore, the rectification ratio signal as a kind of "response signal" is a promising biosensing signal, which can play a key role in biosensors and other sensing devices.

3.3. Structure and Characterization Analyses of the MoS_2/WTe_2 FET Biosensor

Figure 3A shows an optical image of the fabricated MoS_2/WTe_2 FET biosensor, consisting of a MoS_2/WTe_2 heterostructure and two electrodes on a SiO_2/Si substrate; the electrode spacing is 20 μm. Figure 3B shows the SEM image and the optical image of the area marked in Figure 3A. The corresponding EDS mapping of this area, showing the uniform distribution of each element [28], is shown in Figure S4. The EDS mapping shows that the atomic ratio of S to Mo in the MoS_2/WTe_2 FET biosensor is 2:1, and the atomic ratio of Te to W is 2:1, indicating the elements' uniform distribution. Figure 3C shows the image of the MoS_2/WTe_2 heterojunction measured by an atomic force microscope (AFM). The line scan profile of the heterojunction height was extracted from the AFM image, while the thicknesses of the MoS_2 and WTe_2 flakes were measured to be 5.72 nm and 20.41 nm. The Raman spectrum of the heterojunction (Figure 3D) was measured using a 532 nm laser. The Raman spectrum revealed the characteristic peak $E_{2g}{}^1$ representing the in-plane vibration mode was located at 383 cm^{-1} and the characteristic peak A_{1g} representing the out-of-plane vibration mode was located at 407.79 cm^{-1}, consistent with the thickness of the MoS_2 flake [29,30]. The characteristic peaks ${}^3A_2$, ${}^4A_1$, ${}^8A_1$, and ${}^{10}A_1$ of WTe_2 were located near 116.4, 133.7, 163.9, and 211.8 cm^{-1}, respectively, consistent with the crystal structure of WTe_2 [31].

The electrical properties of MoS_2 and WTe_2 were measured [32]. Figure 3E shows the Schottky contact between the MoS_2 and Au electrodes and the Ohmic contact between the WTe_2 and Au electrodes. Figure 3F depicts the transfer characteristic curves of the MoS_2 and WTe_2 devices at a source-drain voltage V_{DS} = 0.5 V, where MoS_2 showed conventional n-type semiconductor characteristics [33] and the current of WTe_2 was unaffected by gate voltage, showing semimetal characteristics [34].

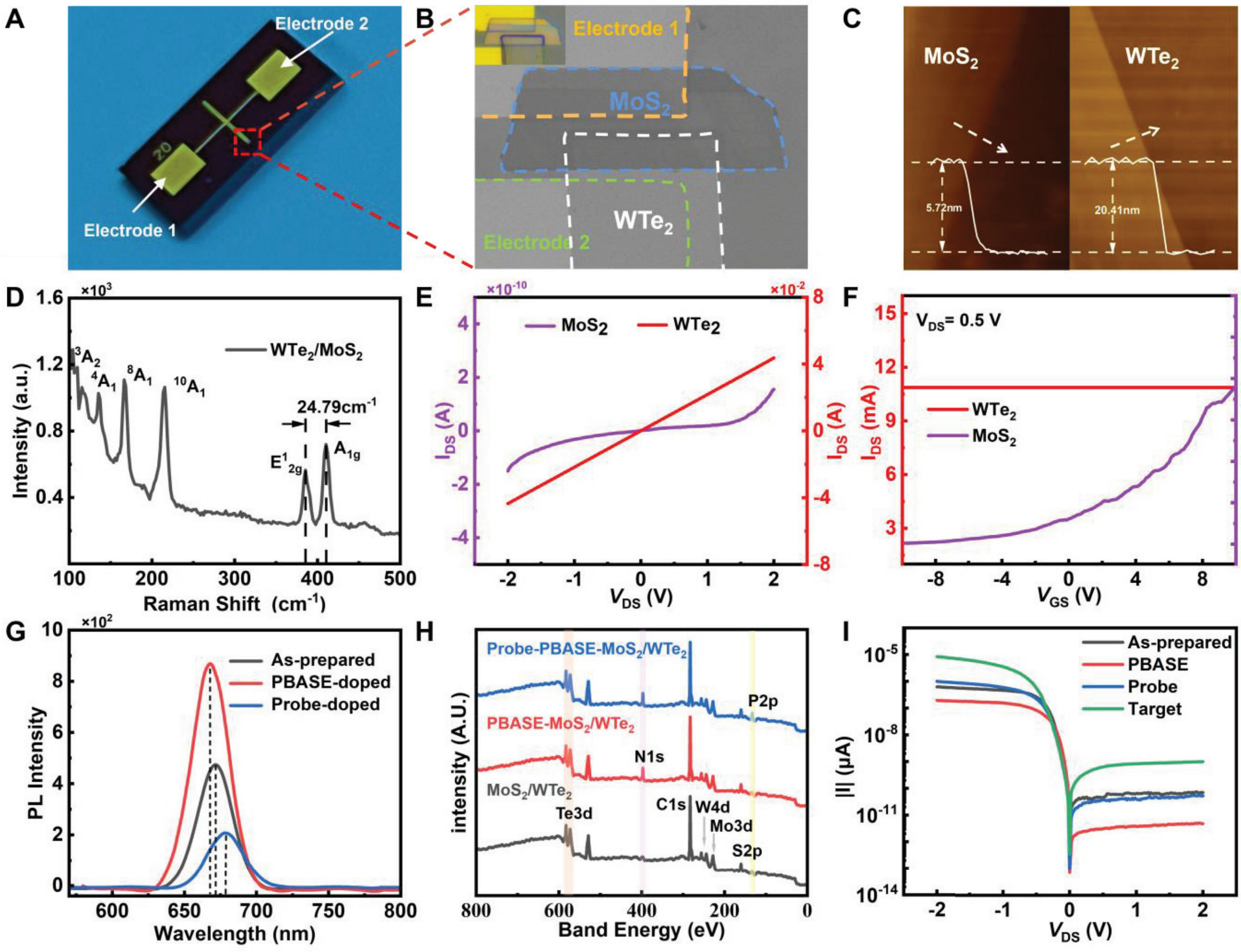

Figure 3. (**A**) A typical MoS_2/WTe_2 FET biosensor device. (**B**) SEM image of the MoS_2/WTe_2 FET biosensor, with its optical image in the inset. (**C**) AFM images of the MoS_2 and WTe_2 films. (**D**) Raman spectra of the MoS_2/WTe_2 heterojunction. (**E**,**F**) I_{DS}-V_{DS} and I_{DS}-V_{GS} characteristics of MoS_2 and WTe_2 at room temperature. The inset in (**E**) is the whole I_{DS}-V_{DS} characteristics of WTe_2. (**G**) Photoluminescence spectra with and without biomolecules. (**H**) X-ray photoelectron spectra before adding the target DYRK1A. (**I**) Current output characteristics after adding different biomolecules.

Photoluminescence (PL) and X-ray photoelectron spectroscopy (XPS) were used to verify that this biosensor can be successfully functionalized [35]. After functionalizing with MoS_2, the PL peak intensity increased, and the peak underwent a blue shift (See Figure 3G). After immobilizing the probe DNA, its PL peak intensity decreased, and the peak red-shifted. The peak intensity enhancement and the blue shift can be attributed to the following: The functionalized MoS_2 was affected by PBASE, where the electrons, trions A^-, and foreign holes combined to form several neutral excitons A^0, increasing the proportion of neutral excitons A^0 and an enhancement in radiative transition. Consequently, the dominant exciton in the A peak changed from trion A^- to neutral exciton A^0, leading to a PL peak intensity enhancement and the blue shift of the peak position. The peak intensity reduction and red shift can be attributed to the following: The immobilized MoS_2 was affected by the probe DNA, where foreign electrons and neutral excitons A^0 combined to form trions A^-. This was followed by the dominant exciton in the A peak changing from neutral exciton A^0 to trion A^-, while the radiative transition weakened, reducing the PL peak intensity and yielding the red shift of the peak position [36]. Figure 3H shows the N1s peak of PBASE and the P2p peak of the probe DNA, confirming the functionalization and immobilization of the probe DNA. The XPS measurements revealed that PBASE and the probe DNA were successively bound to the MoS_2/WTe_2 surface. Furthermore, the change in the source-drain current in Figure 3I can be explained by the following reasoning: The adsorption of PBASE on the MoS_2/WTe_2 surface caused p-doping, resulting in a decrease in the overall source-drain current. The binding of the probe DNA with PBASE caused n-doping, increasing the source-drain current. Similarly, the complementary pairing of the target DNA with probe DNA caused n-doping, increasing the overall source-drain current [37,38].

3.4. Sensing Performance of the MoS_2/WTe_2 FET Biosensor

Down syndrome [39] is one of the most common chromosomal diseases and one of the main causes of human intellectual disability. The DYRK1A gene on chromosome 21 was chosen as the target DNA to study the sensitivity of the MoS_2/WTe_2 FET biosensor (Figure 4A). The functionalized and immobilized MoS_2/WTe_2 FET biosensor in different concentrations of the target DNA solution was studied to obtain the relationship between the target concentration and the response signal [40]. Figure 4B shows that the output characteristic curve gradually shifted upward as the concentration of the target DNA (DYRK1A) gradually increased from 10 aM to 100 pM. The current results of the different concentrations of the target DNA (DYRK1A) under positive and negative bias voltages are shown in Figure S5. Since the band gap width of MoS_2 was not zero [41], the noise signal of the MoS_2-based FET biosensor was much lower than that of the graphene FET biosensor [42,43]. When the target DNA concentration was as low as 10 aM, the detected source-drain current was much larger than that without adding the target DNA. Therefore, it can be confirmed that the 10 aM target DNA was successfully detected. Figure 4C shows the rectification ratio response with the increasing concentrations of the target DNA, which is attributed to the change in the Schottky barrier width caused by charge doping. Specifically, the change in the source-drain current dominated by the MoS_2/Au junction is larger than that dominated by the MoS_2/WTe_2 junction. Figure 4D shows that the rectification ratio gradually decreased as the concentration increased from 10 aM to 100 pM. Furthermore, the rectification ratio signal had a linear relationship with the concentration gradient ($y = -1519.54 \lg C_{Target} - 10,399.77$). These results indicate that the rectification ratio can serve as a kind of detection indicator in the MoS_2/WTe_2 FET biosensors.

Four kinds of biomarkers (N_1–N_4) diffused into the MoS_2/WTe_2 FET biosensor with the immobilized probe DNA were chosen to demonstrate the specificity of the MoS_2/WTe_2 FET biosensors. Figure 4E,F show that there is no obvious current change after adding 1 fM N_1–N_4 samples, and the inset of Figure 4E is the current after local magnification. The complete current diagram after adding the N_1–N_4 samples is shown in Figure S6. In addition, there is a higher response after adding the 10 aM target DNA than that after adding 1 fM N_1–N_4 samples. Figure 4F shows a comparison of the response ratios between the target DNA and non-target DNA samples, with N_1, N_2, N_3, and N_4 representing non-target DNA samples and P representing the target DNA sample. Thus, the proposed MoS_2/WTe_2 FET biosensor has a good specificity. As shown in Figure 4G, the biosensing performance of the MoS_2/WTe_2 FET biosensor did not decrease significantly after sixty days and the peak to valley value (PV) was still within an acceptable error range (PV = 9.86%). Thus, the MoS_2/WTe_2 FET biosensor demonstrated excellent stability and durability.

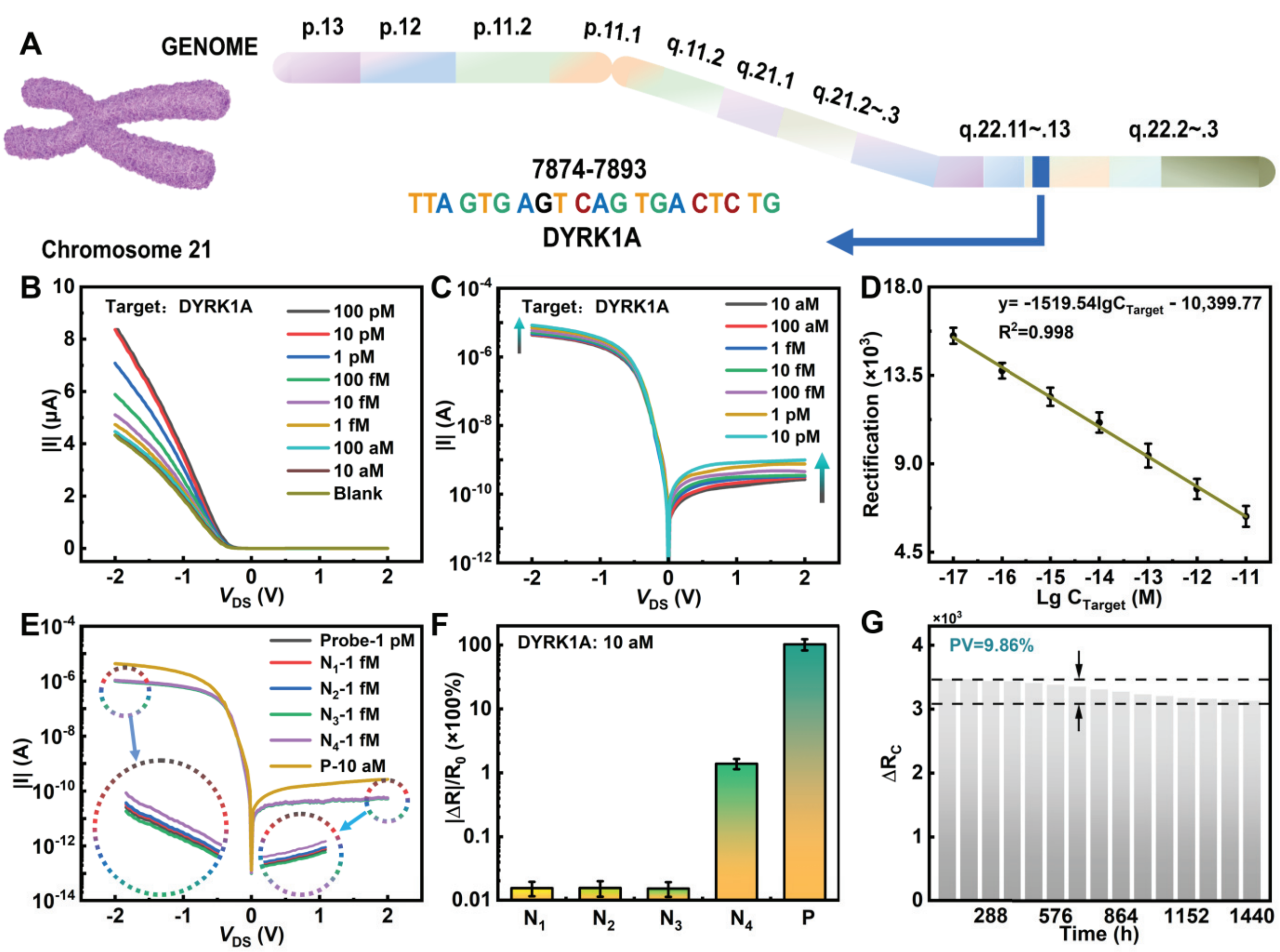

Figure 4. Sensing performance of the MoS_2/WTe_2 FET biosensor. (**A**) Target site of Down syndrome in chromosome 21 genome map. (**B**) Response of the output characteristic curve of the target DNA (DYRK1A gene). (**C**) Effect of the target DNA (DYRK1A gene) on the rectification ratio. (**D**) Statistics of the rectification ratio response of the DYRK1A gene. (**E**) Specificity response of the MoS_2/WTe_2 FET biosensor. (**F**) A comparison of the target DNA and non-target DNA. (**G**) The rectification ratio signal change values for the two concentrations during the sixty days; the peak to valley value is 9.87%.

3.5. Comparison of Similar Structures

The advantage of the “rectified signal” (rectification ratio) was demonstrated by constructing three kinds of FETs: $Au/MoS_2/Au$ FET (Figure 5A), $WTe_2/MoS_2/Au$ FET (Figure 5B), and $WTe_2/MoS_2/WTe_2$ FET (Figure 5C). Except for the reported $WTe_2/MoS_2/Au$ FET, the other two FETs only showed “absolute value signal” (source-drain current) as the response signal. Due to the presence of a large symmetric barrier in $Au/MoS_2/Au$ FET [44], the obtained current was about 1×10^{-10} A, as shown in Figure 5D. In contrast, due to the presence of an asymmetric barrier in $WTe_2/MoS_2/Au$ FET, the forward source-drain current dominated by MoS_2/Au junction was about 1×10^{-10} A, while the reverse source-drain current dominated by WTe_2/MoS_2 junction was about 1×10^{-6} A (See Figure 5E). Furthermore, Figure 5F shows that, due to the presence of a symmetric small-barrier $WTe_2/MoS_2/WTe_2$ FET, the source-drain current was about 1×10^{-6} A. Figure S7 shows the changes in the transfer characteristic curves after introducing biomolecules in three different structures.

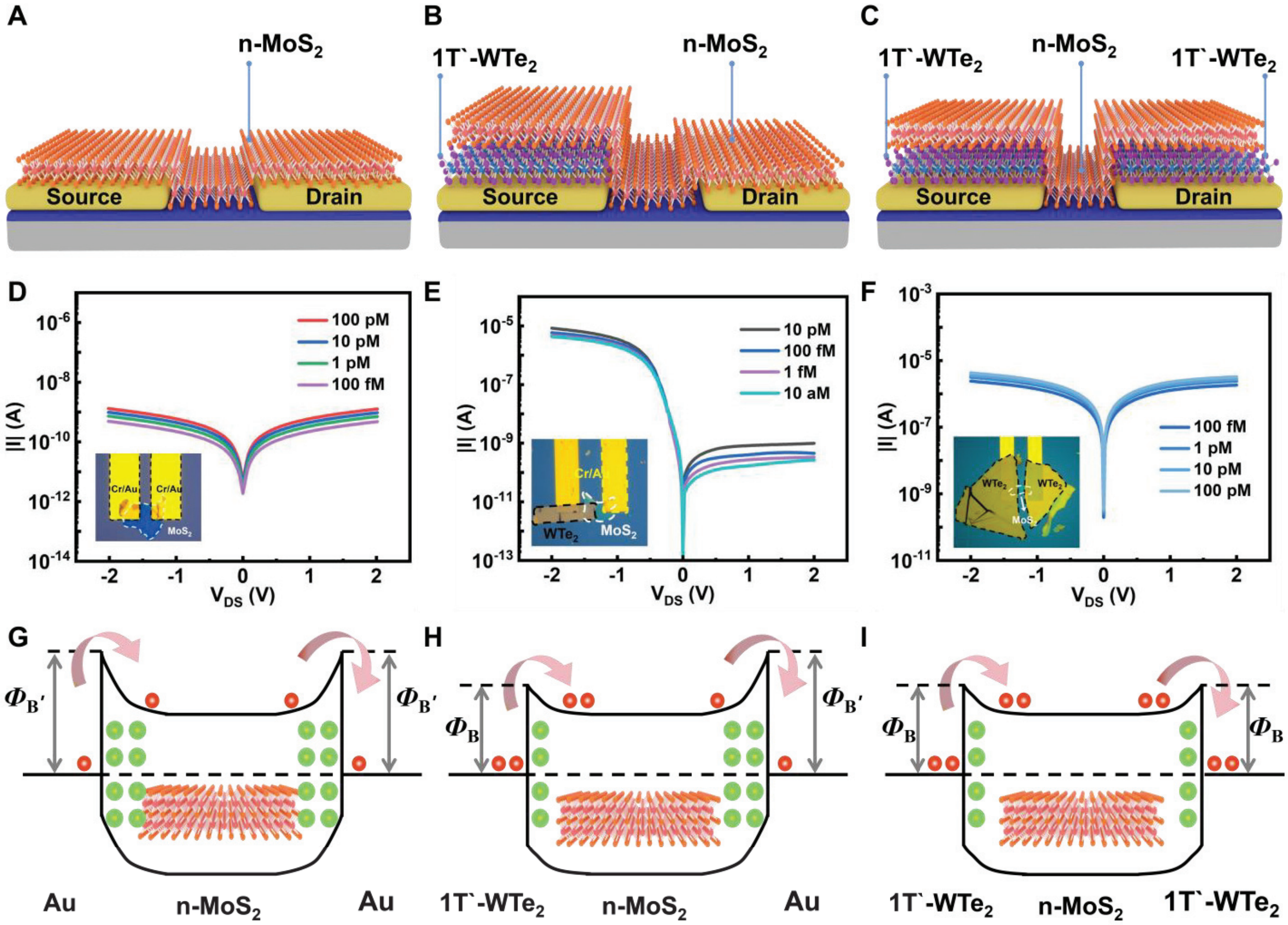

Figure 5. Comparison of similar structures. Schematic diagrams (**A**–**C**), output characteristic curves (**D**–**F**), and band diagrams (**G**–**I**) of the Au/MoS_2/Au, WTe_2/MoS_2/Au, and WTe_2/MoS_2/WTe_2 structures, respectively.

The source-drain current signals of the three structures were very weak, but the rectification ratio signal of the WTe_2/MoS_2/Au FET biosensor had significant variations. This indicates that the rectification ratio signal effectively amplifies the molecular signal variation and improves molecular signal sensitivity. Figure 5G–I shows the band diagram of the three structures. When the target biomolecules modified the sensing materials, the Schottky barrier widths were modulated. As shown in Figure 5G, when the target DNA caused electron doping [22], the Schottky barrier width of the MoS_2/Au junction decreased and the source-drain current increased. As shown in Figure 5H, the asymmetric barrier decreased after adding the target DNA, resulting in an increased current and a decreased rectification ratio (Figure S8). Figure 5I shows that, when the target DNA was added into WTe_2/MoS_2/WTe_2 FET, it caused electron doping and decreased the Schottky barrier width, increasing the source-drain current.

Moreover, the rectification ratio signal of the WTe_2/MoS_2/Au FET biosensor is stable for long periods of time (Figure S9), indicating that the "rectified signal" (the rectification ratio) is not affected by the solution environment and is a promising biosensing signal in FET biosensors.

4. Conclusions

This study developed a novel strategy using the "rectified signal" in the output characteristic curve to detect biomolecules. The strategy effectively avoided the interference of external factors and was suitable for the quantitative analysis of trace targets in complex biological systems. Based on this strategy, a highly reliable and stable MoS_2/WTe_2 FET biosensor with an asymmetric Schottky barrier was developed. The experiments showed that the prepared biosensor achieved an ultra-sensitive and specific detection of the DYRK1A gene in the range of 10 aM–100 pM, indicating that the MoS_2/WTe_2 FET biosensor has great application potential in the prenatal screening of Down syndrome. This study demonstrated the importance of using a "rectified signal" in FET biosensors and provided a novel perspective for designing and optimizing biosensors based on two-dimensional materials.

Supplementary Materials: The following supporting information can be downloaded at: https://www.mdpi.com/article/10.3390/nano14020226/s1. Figure S1: Fabrication process diagram of the MoS_2/WTe_2 FET biosensor; Figure S2: The functionalization and immobilization process of the device; Figure S3: High-resolution XPS spectra of Mo 3d and S 2p; Figure S4: EDS images mentioned in Figure 3B; Figure S5: The current results of different concentrations of the target DNA (DYRK1A) under (A) positive and (B) negative bias voltages; Figure S6: The complete current diagram after adding the N_1–N_4 samples; Figure S7: The transfer characteristic curves of the $Au/MoS_2/Au$, $WTe_2/MoS_2/Au$, and $WTe_2/MoS_2/WTe_2$ structures; Figure S8: Output characteristic curves measured at different biomolecular concentrations in the MoS_2/WTe_2 FET biosensor; Figure S9: Stability comparison of the "rectified signal" and "absolute value signal"; Table S1: The DNA sequences purchased from Sangon Biotech (Shanghai) Co., Ltd.; Table S2: Comparison of the biosensing performances of the various FET biosensors. References [45–52] are cited in the supplementary materials.

Author Contributions: Conceptualization, X.Z. and S.C.; methodology, H.M.; software, T.S.; validation, X.Z., S.C. and H.M.; formal analysis, T.S.; investigation, X.C.; resources, S.C.; data curation, P.H.; writing—original draft preparation, X.Z.; writing—review and editing, C.Y.; visualization, C.Y.; supervision, B.M.; project administration, B.M.; funding acquisition, C.Y. All authors have read and agreed to the published version of the manuscript.

Funding: This research was funded by the National Natural Science Foundation of China (11974222) and the Shandong Provincial Natural Science Foundation (ZR2023MA087).

Data Availability Statement: Data are contained within the article and Supplementary Materials.

Acknowledgments: The authors acknowledge the anonymous referees for their helpful comments and constructive remarks on this manuscript.

Conflicts of Interest: The authors declare no conflicts of interest.

References

1. Wang, L.; Wang, X.; Wu, Y.; Guo, M.; Gu, C.; Dai, C.; Kong, D.; Wang, Y.; Zhang, C.; Qu, D. Rapid and ultrasensitive electromechanical detection of ions, biomolecules and SARS-CoV-2 RNA in unamplified samples. *Nat. Biomed. Eng.* **2022**, *6*, 276–285. [CrossRef]
2. Wang, C.; Li, W.; Drabek, D.; Okba, N.M.; van Haperen, R.; Osterhaus, A.D.; van Kuppeveld, F.J.; Haagmans, B.L.; Grosveld, F.; Bosch, B.-J. A human monoclonal antibody blocking SARS-CoV-2 infection. *Nat. Commun.* **2020**, *11*, 2251. [CrossRef]
3. Ji, H.; Wang, Z.; Wang, S.; Wang, C.; Chu, Y.; Liu, H.; Zhang, Y.; Han, L. A Novel InSe-FET Biosensor based on Carrier-Scattering Regulation Derived from the DNA Probe Assembly-Determined Electrostatic Potential Distribution. *Adv. Funct. Mater.* **2023**, *33*, 2213277. [CrossRef]
4. von Lüders, L.; Tilmann, R.; Lee, K.; Bartlam, C.; Stimpel-Lindner, T.; Nevanen, T.K.; Iljin, K.; Knirsch, K.C.; Hirsch, A.; Duesberg, G.S. Functionalisation of Graphene Sensor Surfaces for the Specific Detection of Biomarkers. *Angew. Chem. Int. Ed.* **2023**, *62*, e202219024. [CrossRef] [PubMed]
5. Gilpatrick, T.; Lee, I.; Graham, J.E.; Raimondeau, E.; Bowen, R.; Heron, A.; Downs, B.; Sukumar, S.; Sedlazeck, F.J.; Timp, W. Targeted nanopore sequencing with Cas9-guided adapter ligation. *Nat. Biotechnol.* **2020**, *38*, 433–438. [CrossRef]
6. Li, B.; Deng, A.; Li, K.; Hu, Y.; Li, Z.; Shi, Y.; Xiong, Q.; Liu, Z.; Guo, Q.; Zou, L. Viral infection and transmission in a large, well-traced outbreak caused by the SARS-CoV-2 Delta variant. *Nat. Commun.* **2022**, *13*, 460. [CrossRef]
7. Zhang, X.; Liu, T.; Boyle, A.; Bahreman, A.; Bao, L.; Jing, Q.; Xue, H.; Kieltyka, R.; Kros, A.; Schneider, G.F. Dielectric-Modulated Biosensing with Ultrahigh-Frequency-Operated Graphene Field-Effect Transistors. *Adv. Mater.* **2022**, *34*, 2270055. [CrossRef]
8. Jiang, J.; Chu, Z.; Yin, Z.; Li, J.; Yang, Y.; Chen, J.; Wu, J.; You, J.; Zhang, X. Red Perovskite Light-Emitting Diodes with Efficiency Exceeding 25% Realized by Co-Spacer Cations. *Adv. Mater.* **2022**, *34*, 2204460. [CrossRef]
9. Hou, S.; Wu, M.; Li, H.; Gong, H.R.; Gao, Z.; Shi, R.; Huang, X.; Li, D.; Huang, J.D.; Yu, J. Ultrasensitive Detection of SARS-CoV-2 by Flexible Metal Oxide Field-Effect Transistors. *Adv. Funct. Mater.* **2023**, *33*, 2301268. [CrossRef]

10. Sen, A.; Shim, J.; Bala, A.; Park, H.; Kim, S. Boosting Sensitivity and Reliability in Field-Effect Transistor-Based Biosensors with Nanoporous MoS_2 Encapsulated by Non-Planar Al_2O_3. *Adv. Funct. Mater.* **2023**, *33*, 2301919. [CrossRef]
11. Kulkarni, G.S.; Zhong, Z. Detection beyond the Debye screening length in a high-frequency nanoelectronic biosensor. *Nano Lett.* **2012**, *12*, 719–723. [CrossRef]
12. Sadighbayan, D.; Hasanzadeh, M.; Ghafar-Zadeh, E. Biosensing based on field-effect transistors (FET): Recent progress and challenges. *TrAC Trends Anal. Chem.* **2020**, *133*, 116067. [CrossRef] [PubMed]
13. Xu, S.; Zhan, J.; Man, B.; Jiang, S.; Yue, W.; Gao, S.; Guo, C.; Liu, H.; Li, Z.; Wang, J. Real-time reliable determination of binding kinetics of DNA hybridization using a multi-channel graphene biosensor. *Nat. Commun.* **2017**, *8*, 14902. [CrossRef] [PubMed]
14. Di Bartolomeo, A.; Kumar, A.; Durante, O.; Sessa, A.; Faella, E.; Viscardi, L.; Intonti, K.; Giubileo, F.; Martucciello, N.; Romano, P. Temperature-dependent photoconductivity in two-dimensional MoS_2 transistors. *Mater. Today Nano* **2023**, *24*, 100382. [CrossRef]
15. Fathi-Hafshejani, P.; Azam, N.; Wang, L.; Kuroda, M.A.; Hamilton, M.C.; Hasim, S.; Mahjouri-Samani, M. Two-dimensional-material-based field-effect transistor biosensor for detecting COVID-19 virus (SARS-CoV-2). *ACS Nano* **2021**, *15*, 11461–11469. [CrossRef]
16. Chen, S.; Sun, Y.; Xia, Y.; Lv, K.; Man, B.; Yang, C. Donor effect dominated molybdenum disulfide/graphene nanostructure-based field-effect transistor for ultrasensitive DNA detection. *Biosens. Bioelectron.* **2020**, *156*, 112128. [CrossRef]
17. Hajian, R.; Balderston, S.; Tran, T.; DeBoer, T.; Etienne, J.; Sandhu, M.; Wauford, N.A.; Chung, J.-Y.; Nokes, J.; Athaiya, M. Detection of unamplified target genes via CRISPR–Cas9 immobilized on a graphene field-effect transistor. *Nat. Biomed. Eng.* **2019**, *3*, 427–437. [CrossRef] [PubMed]
18. Balderston, S.; Taulbee, J.J.; Celaya, E.; Fung, K.; Jiao, A.; Smith, K.; Hajian, R.; Gasiunas, G.; Kutanovas, S.; Kim, D. Discrimination of single-point mutations in unamplified genomic DNA via Cas9 immobilized on a graphene field-effect transistor. *Nat. Biomed. Eng.* **2021**, *5*, 713–725. [CrossRef]
19. Mei, J.; Li, Y.-T.; Zhang, H.; Xiao, M.-M.; Ning, Y.; Zhang, Z.-Y.; Zhang, G.-J. Molybdenum disulfide field-effect transistor biosensor for ultrasensitive detection of DNA by employing morpholino as probe. *Biosens. Bioelectron.* **2018**, *110*, 71–77. [CrossRef]
20. Hu, S.; An, M.; Yang, N.; Li, B. A series circuit of thermal rectifiers: An effective way to enhance rectification ratio. *arXiv* **2016**, arXiv:1605.01806. [CrossRef]
21. Zhao, Q.; Jie, W.; Wang, T.; Castellanos-Gomez, A.; Frisenda, R. InSe Schottky diodes based on van der Waals contacts. *Adv. Funct. Mater.* **2020**, *30*, 2001307. [CrossRef]
22. Zhang, X.; Liu, B.; Gao, L.; Yu, H.; Liu, X.; Du, J.; Xiao, J.; Liu, Y.; Gu, L.; Liao, Q. Near-ideal van der Waals rectifiers based on all-two-dimensional Schottky junctions. *Nat. Commun.* **2021**, *12*, 1522. [CrossRef] [PubMed]
23. Li, B.; Xing, T.; Zhong, M.; Huang, L.; Lei, N.; Zhang, J.; Li, J.; Wei, Z. A two-dimensional Fe-doped SnS_2 magnetic semiconductor. *Nat. Commun.* **2017**, *8*, 1958. [CrossRef] [PubMed]
24. Khosravi, F.; Loeian, S.M.; Panchapakesan, B. Ultrasensitive label-free sensing of IL-6 based on PASE functionalized carbon nanotube micro-arrays with RNA-aptamers as molecular recognition elements. *Biosensors* **2017**, *7*, 17. [CrossRef]
25. Hwang, C.; Park, N.; Kim, E.S.; Kim, M.; Kim, S.D.; Park, S.; Kim, N.Y.; Kim, J.H. Ultra-fast and recyclable DNA biosensor for point-of-care detection of SARS-CoV-2 (COVID-19). *Biosens. Bioelectron.* **2021**, *185*, 113177. [CrossRef]
26. Tan, C.; Yin, S.; Chen, J.; Lu, Y.; Wei, W.; Du, H.; Liu, K.; Wang, F.; Zhai, T.; Li, L. Broken-gap PtS_2/WSe_2 van der Waals heterojunction with ultrahigh reverse rectification and fast photoresponse. *ACS Nano* **2021**, *15*, 8328–8337. [CrossRef]
27. Le, V.X.; Lee, H.; Pham, N.S.; Bong, S.; Oh, H.; Cho, S.-H.; Shin, I.-S. Stainless steel 304 needle electrode for precise glucose biosensor with high signal-to-noise ratio. *Sens. Actuators B Chem.* **2021**, *346*, 130552. [CrossRef]
28. Mao, J.; Zhang, B.; Shi, Y.; Wu, X.; He, Y.; Wu, D.; Jie, J.; Lee, C.S.; Zhang, X. Conformal MoS_2/silicon nanowire array heterojunction with enhanced light trapping and effective interface passivation for ultraweak infrared light detection. *Adv. Funct. Mater.* **2022**, *32*, 2108174. [CrossRef]
29. Zhang, D.; Yang, Z.; Li, P.; Pang, M.; Xue, Q. Flexible self-powered high-performance ammonia sensor based on Au-decorated MoSe2 nanoflowers driven by single layer MoS_2-flake piezoelectric nanogenerator. *Nano Energy* **2019**, *65*, 103974. [CrossRef]
30. Li, H.; Zhang, Q.; Yap, C.C.R.; Tay, B.K.; Edwin, T.H.T.; Olivier, A.; Baillargeat, D. From bulk to monolayer MoS_2: Evolution of Raman scattering. *Adv. Funct. Mater.* **2012**, *22*, 1385–1390. [CrossRef]
31. Wei, Y.; Deng, C.; Zheng, X.; Chen, Y.; Zhang, X.; Luo, W.; Zhang, Y.; Peng, G.; Liu, J.; Huang, H. Anisotropic in-plane thermal conductivity for multi-layer WTe_2. *Nano. Res.* **2022**, *15*, 401–407. [CrossRef]
32. Chen, Y.; Liu, H.; Yu, G.; Ma, C.; Xu, Z.; Zhang, J.; Zhang, C.; Chen, M.; Li, D.; Zheng, W. Defect Engineering of 2D Semiconductors for Dual Control of Emission and Carrier Polarity. *Adv. Mater.* **2023**, e2312425. [CrossRef] [PubMed]
33. Kumar, A.; Viscardi, L.; Faella, E.; Giubileo, F.; Intonti, K.; Pelella, A.; Sleziona, S.; Kharsah, O.; Schleberger, M.; Di Bartolomeo, A. Black phosphorus unipolar transistor, memory, and photodetector. *J. Mater. Sci.* **2023**, *58*, 2689–2699. [CrossRef]
34. Zhou, C.; Raju, S.; Li, B.; Chan, M.; Chai, Y.; Yang, C.Y. Self-driven metal–semiconductor–metal WSe2 photodetector with asymmetric contact geometries. *Adv. Funct. Mater.* **2018**, *28*, 1802954. [CrossRef]
35. Sheta, S.M.; El-Sheikh, S.M.; Abd-Elzaher, M.M.; Salem, S.R.; Moussa, H.A.; Mohamed, R.M.; Mkhalid, I.A. A novel biosensor for early diagnosis of liver cancer cases using smart nano-magnetic metal–organic framework. *Appl. Organomet. Chem.* **2019**, *33*, e5249. [CrossRef]
36. Mouri, S.; Miyauchi, Y.; Matsuda, K. Tunable photoluminescence of monolayer MoS_2 via chemical doping. *Nano Lett.* **2013**, *13*, 5944–5948. [CrossRef] [PubMed]

37. Rabchinskii, M.K.; Saveliev, S.D.; Stolyarova, D.Y.; Brzhezinskaya, M.; Kirilenko, D.A.; Baidakova, M.V.; Ryzhkov, S.A.; Shnitov, V.V.; Sysoev, V.V.; Brunkov, P.N. Modulating nitrogen species via N-doping and post annealing of graphene derivatives: XPS and XAS examination. *Carbon* **2021**, *182*, 593–604. [CrossRef]
38. Taklu, B.W.; Su, W.-N.; Nikodimos, Y.; Lakshmanan, K.; Temesgen, N.T.; Lin, P.-X.; Jiang, S.-K.; Huang, C.-J.; Wang, D.-Y.; Sheu, H.-S. Dual CuCl doped argyrodite superconductor to boost the interfacial compatibility and air stability for all solid-state lithium metal batteries. *Nano Energy* **2021**, *90*, 106542. [CrossRef]
39. Hüls, A.; Costa, A.C.; Dierssen, M.; Baksh, R.A.; Bargagna, S.; Baumer, N.T.; Brandão, A.C.; Carfi, A.; Carmona-Iragui, M.; Chicoine, B.A. Medical vulnerability of individuals with Down syndrome to severe COVID-19–data from the Trisomy 21 Research Society and the UK ISARIC4C survey. *EClinicalMedicine* **2021**, *33*, 100769. [CrossRef]
40. Wang, S.; Sun, M.; Zhang, Y.; Ji, H.; Gao, J.; Song, S.; Sun, J.; Liu, H.; Zhang, Y.; Han, L. Ultrasensitive antibiotic perceiving based on aptamer-functionalized ultraclean graphene field-effect transistor biosensor. *Anal. Chem.* **2022**, *94*, 14785–14793. [CrossRef]
41. Mak, K.F.; Lee, C.; Hone, J.; Shan, J.; Heinz, T.F. Atomically thin MoS_2: A new direct-gap semiconductor. *Phys. Rev. Lett.* **2010**, *105*, 136805. [CrossRef] [PubMed]
42. Song, P.; Ou, P.; Wang, Y.; Yuan, H.; Duan, S.; Chen, L.; Fu, H.; Song, J.; Liu, X. An ultrasensitive FET biosensor based on vertically aligned MoS_2 nanolayers with abundant surface active sites. *Anal. Chim. Acta* **2023**, *1252*, 341036. [CrossRef] [PubMed]
43. Marconcini, P.; Macucci, M. Envelope-function-based transport simulation of a graphene ribbon with an antidot lattice. *IEEE Trans. Nanotechnol.* **2016**, *16*, 534–544. [CrossRef]
44. Liu, J.; Hao, Q.; Gan, H.; Li, P.; Li, B.; Tu, Y.; Zhu, J.; Qi, D.; Chai, Y.; Zhang, W. Selectively Modulated Photoresponse in Type-I Heterojunction for Ultrasensitive Self-Powered Photodetectors. *Laser-Photon. Rev.* **2022**, *16*, 2200338. [CrossRef]
45. Khan, N.I.; Mousazadehkasin, M.; Ghosh, S.; Tsavalas, J.G.; Song, E. An integrated microfluidic platform for selective and real-time detection of thrombin biomarkers using a graphene FET. *Analyst* **2020**, *145*, 4494–4503. [CrossRef]
46. Park, D.; Kim, J.H.; Kim, H.J.; Lee, D.; Lee, D.S.; Yoon, D.S.; Hwang, K.S. Multiplexed femtomolar detection of Alzheimer's disease biomarkers in biofluids using a reduced graphene oxide field-effect transistor. *Biosens. Bioelectron.* **2020**, *167*, 112505. [CrossRef]
47. Danielson, E.; Sontakke, V.A.; Porkovich, A.J.; Wang, Z.; Kumar, P.; Ziadi, Z.; Yokobayashi, Y.; Sowwan, M. Graphene based field-effect transistor biosensors functionalized using gas-phase synthesized gold nanoparticles. *Sens. Actuators B Chem.* **2020**, *320*, 128432. [CrossRef]
48. Li, Y.; Peng, Z.; Holl, N.J.; Hassan, M.R.; Pappas, J.M.; Wei, C.; Izadi, O.H.; Wang, Y.; Dong, X.; Wang, C. MXene–graphene field-effect transistor sensing of influenza virus and SARS-CoV-2. *ACS Omega* **2021**, *6*, 6643–6653. [CrossRef]
49. Park, H.; Lee, H.; Jeong, S.H.; Lee, E.; Lee, W.; Liu, N.; Yoon, D.S.; Kim, S.; Lee, S.W. MoS_2 field-effect transistor-amyloid-β1–42 hybrid device for signal amplified detection of MMP-9. *Anal. Chem.* **2019**, *91*, 8252–8258. [CrossRef]
50. Liu, J.; Chen, X.; Wang, Q.; Xiao, M.; Zhong, D.; Sun, W.; Zhang, G.; Zhang, Z. Ultrasensitive monolayer MoS_2 field-effect transistor based DNA sensors for screening of down syndrome. *Nano Lett.* **2019**, *19*, 1437–1444. [CrossRef]
51. Chan, C.; Shi, J.; Fan, Y.; Yang, M. A microfluidic flow-through chip integrated with reduced graphene oxide transistor for influenza virus gene detection. *Sens. Actuators B Chem.* **2017**, *251*, 927–933. [CrossRef]
52. Islam, S.; Shukla, S.; Bajpai, V.K.; Han, Y.-K.; Huh, Y.S.; Kumar, A.; Ghosh, A.; Gandhi, S. A smart nanosensor for the detection of human immunodeficiency virus and associated cardiovascular and arthritis diseases using functionalized graphene-based transistors. *Biosens. Bioelectron.* **2019**, *126*, 792–799. [CrossRef] [PubMed]

MDPI AG
Grosspeteranlage 5
4052 Basel
Switzerland
Tel.: +41 61 683 77 34

Nanomaterials Editorial Office
E-mail: nanomaterials@mdpi.com
www.mdpi.com/journal/nanomaterials

Academic Open
Access Publishing

mdpi.com

ISBN 978-3-7258-4468-5